

Integrating Structural Mechanics Into Microstructure Solidification Modelling

Peter Mathews Soar

A thesis submitted in partial fulfilment of the requirements of the
University of Greenwich for the degree of Doctor of Philosophy

September 2021

DECLARATION

I certify that the work contained in this thesis, or any part of it, has not been accepted in substance for any previous degree awarded to me or any other person, and is not concurrently being submitted for any other degree other than that of Doctor of Philosophy which has been studied at the University of Greenwich, London, UK.

I also declare that the work contained in this thesis is the result of my own investigations, except where otherwise identified and acknowledged by references. I further declare that no aspects of the contents of this thesis are the outcome of any form of research misconduct.

I declare any personal, sensitive or confidential information/data has been removed or participants have been anonymised. I further declare that where any questionnaires, survey answers or other qualitative responses of participants are recorded/included in the appendices, all personal information has been removed or anonymised. Where University forms (such as those from the Research Ethics Committee) have been included in appendices, all handwritten/scanned signatures have been removed.

Student Name:

Student Signature:

Date:

First Supervisor's Name:

First Supervisor's Signature:

Date:

DEDICATION

I would like to dedicate this this thesis to my family and friends for
their constant support throughout my PhD.

ABSTRACT

The objective of this work is to investigate how the development of a solidifying microstructure can be altered by the consideration of structural mechanical behaviour. To this end a bespoke structural mechanics code utilising a staggered grid finite volume method was developed and verified before being coupled to pre-existing solidification models.

Concurrently resolving the physical processes of structural mechanics and microstructure solidification within a combined modelling framework required considerations of how to identify the solid structure, how to keep track of the extant deformation and investigation of how the calculated deformations can alter both the growth orientation and physical position of a solidifying dendrite. Once fully coupled, this numerical method was used to generate results which demonstrate physical mechanisms which could not be simulated using models which neglect the concurrent interactions between microstructure solidification and structural mechanics.

The importance of this behaviour is highlighted in the literature, with there being a wide selection of practical experiments which showcase how developing dendritic microstructures are

fundamentally altered due to structural mechanical phenomena. Given that the macroscopic material properties of manufactured alloys are highly dependent on the morphology of the underlying microstructure, if the understanding of these phenomena can be improved there is potential for materials with more desirable properties to ultimately be produced. This provides the motivation for this work, as while the interdependence between structural mechanics and microstructure solidification is known of in industry, it remains an under-explored field with no numerical models currently existing which can capture these behaviours on a scale relevant to industrial processes.

ACKNOWLEDGEMENTS

I would like to thank my first supervisor Dr. Andrew Kao for always being available to discuss my work and provide his invaluable perspective and suggestions. Always enthusiastic about my work and pushing me to become a better researcher, I find it hard to imagine doing my PhD with any other person as my supervisor.

I would also like to acknowledge my second and third supervisors Dr. Georgi Djambazov and Prof. Koulis Pericleous for their support and input throughout the PhD.

I would like to acknowledge my fellow PhD candidate, office mate and good friend Mr. Teddy Gan for helping me find this PhD position at Greenwich University, for using his prior experience to prepare me for the PhD experience and for letting me drink more than my fair share of his tea.

Finally, I would like to thank my father Jem Soar for making my hastily scrawled outlines into the professional technical diagrams used throughout this thesis.

CONTENTS

ABSTRACT	iii
ACKNOWLEDGEMENTS	v
FIGURES	xi
TABLES	xix
NOMENCLATURE	xx
1 INTRODUCTION	1
1.1 Thesis Overview	3
1.2 Thesis Contributions	4
1.3 Thesis Outline	5
2 LITERATURE REVIEW	10
2.1 Overview	10
2.2 Structural Mechanical Behaviour Observed in Microstructure Growth	10
2.3 Existing Solidification Models Considering Structural Mechanical Effects	30

2.4	Using Finite Volume Methods for Structural Mechanics in a Multi-Physics Framework	36
2.5	Summary	39
3	CREATING A STRUCTURAL MECHANICS SOLVER	40
3.1	Overview	40
3.2	Material Model: Linear Elasticity	41
3.2.1	Theory	41
3.2.2	‘Small’ Deformations	43
3.2.3	Quasi-Stationary Approach	46
3.2.4	Displacement Formulation	49
3.3	Variable Material Properties	51
3.4	Staggered Grid Finite Volume Method (SGFVM)	54
3.5	Stress & Strain Outputs	59
3.6	Boundary Conditions	60
3.6.1	Fixed Displacements	60
3.6.2	Fixed Stress & Free Surfaces	61
3.6.3	Slip Domain Boundary	63
3.6.4	Symmetry Domain Boundary	64
3.6.5	Periodic Domain Boundary	65
3.7	Thermal Effects	66
3.8	Structure Identification	68
3.9	Algorithm Overview	73
3.9.1	Stopping Criteria	73
3.9.2	Numerical Scheme	74

3.9.3	Numerical Order of Iterative Scheme	75
3.9.4	Algorithm Description	77
3.10	Model Verification	78
3.10.1	Material Properties & General Problem Setup	80
3.10.2	Block Under Body Force	86
3.10.3	Block Under Facial Force	87
3.10.4	Block With Triangular Face Under Body Force	88
3.10.5	Hemispherical Structure Under Body Force	89
3.10.6	Cantilever Beam With Point Load - Beam Theory Analytic Solution	90
3.10.7	Cantilever Beam With Distributed Load	93
3.10.8	Thermal Expansion of Block Under a Fixed Temperature Change	95
3.10.9	Verification Conclusions	96
3.11	Summary	97
4	COUPLING STRUCTURAL MECHANICS TO	
	SOLIDIFICATION	98
4.1	Overview	98
4.2	TESA Solvers	99
4.3	Solidification Modelling	101
4.3.1	The Enthalpy Method	103
4.3.2	The Cellular Automata (CA) Method	106
4.4	Accounting for Existing Deformation	110
4.5	Solver Performance Enhancements	117

4.5.1	Multi-Scale Modelling with Trilinear Interpolation	117
4.5.2	Parallel Programming	126
4.5.3	Enhancement Speed Impact	128
4.6	Summary	132
5	STRUCTURAL CHANGES TO DENDRITE ORIENTATION	133
5.1	Overview	133
5.2	Local Orientation Tracking	133
5.3	Displacement Driven Orientation Change	136
5.4	Displacement Driven Orientation Change Verification	146
5.5	Summary	153
6	DENDRITE ADVECTION	155
6.1	Overview	155
6.2	Transporting Dendrite Structures	156
6.3	Advection of a Homogeneous Structure	157
6.3.1	Basic Advection	159
6.3.2	Flux Limited Advection	163
6.3.3	Volume of Fluid Methods	168
6.3.4	Concurrent Advection with Solidification	179
6.4	Advection of a Heterogeneous Structure	183
6.5	Complications of Coupling Significant Advection with Solidification	184
6.6	Currently Implemented Advection	193
6.7	Summary	195
7	MODELLING CASES	196
7.1	Overview	196

CONTENTS

7.2	Context and Problem Setup	197
7.3	Thin Sample Fixed Force	200
7.4	Growth Under Thermal Strain	202
7.5	Sinusoidally Changing Force	204
7.6	HPC Thin Sample Cases	208
7.7	3D Dendrites	212
7.8	Rotational Force	214
7.9	Parametric Study	215
7.10	Summary	237
8	CONCLUSION & FUTURE WORK	239
8.1	Conclusions	239
8.2	Future Work	244
	REFERENCES	247
A	Staggered Grid Solver Discretisation	264
B	Structural Mechanics Solver Validation	269
C	Dissemination	315
C.1	Publications	315
C.2	Prizes & Awards	316

FIGURES

2.2	Sliver Defect from Xu <i>et al.</i> (2020) [11].	13
2.3	Dendrite arm rotating under gravity from Reinhart <i>et al.</i> (2008) [19].	15
2.4	Gravity driven mechanical dendrite behaviour from Reinhart <i>et al.</i> (2014) [20].	16
2.5	Dendrites showing misorientation from Aveson (2019) <i>et al.</i> [27].	19
2.6	Dendritic system becoming misorientated along the convergent boundary of dendrite arms from Sun <i>et al.</i> (2019) [28].	20
2.7	Long dendrite arm crossing microstructure becoming misorientated from Sun <i>et al.</i> (2018) [30].	20
2.8	Dendrites showing misorientation from Hallensleben <i>et al.</i> (2019) [29].	21
2.9	Long dendrite arm crossing microstructure becoming misorientated from Hu <i>et al.</i> (2019) [31].	22
2.10	Solidification of a Ga-25 wt%In alloy showing a large misorientation.	26
2.1	Stray grain formation from Zhou (2011) [9].	27
2.11	Solidification of a Ga-25 wt%In alloy showing multiple misorientated dendrites.	27

2.12 Demonstrating stress being calculated during microstructure solidification by Uehara, Fukui and Ohno (2008) [62]	33
2.13 Equivalent stress distributions due to gravity for differently shaped dendrites by Takaki and Kashima (2011) [63].	33
2.14 Example of a coupled microstructure solidification with concurrent structural effects by Yamaguchi and Beckermann (2014) [66]	35
3.1 Limit on L due to eutectic formation.	46
3.2 Approaches to representing a dendritic shape in the SMS.	52
3.3 Heterogeneous dendrite.	53
3.4 Finite volumes using staggered displacements.	55
3.5 Relationship between staggered u and v grids.	56
3.6 Annotated u and v grids.	58
3.7 Fixed displacement boundaries.	61
3.8 Types of Neumann boundary.	63
3.9 Slip boundary.	64
3.10 Symmetry domain boundary.	65
3.11 Periodic domain boundary.	66
3.12 Domain identification for SMS.	72
3.13 Accuracy of 1 st and 2 nd order SMS boundaries against COMSOL.	76
3.14 General problem setup.	82
3.15 Plotted model w displacements.	84
3.16 w displacement grid size comparison.	85
3.17 Case 1 - Floor fixed block under negative body force in z	86

3.18 Case 2 - Floor fixed block under positive facial force in z on High face.	87
3.19 Case 3 - Floor & wall fixed block with triangular corner under negative body force in z	88
3.20 Case 4 - Floor fixed hemispherical structure under negative body force in z	89
3.21 Case 5 - $4 \times 4 \times 20$ cantilever beam with point load.	92
3.22 Case 6 - $4 \times 4 \times 20$ cantilever beam with distributed load.	94
3.23 Case 7 - Floor fixed block structure experiencing thermoelastic expansion under temperature increase.	95
4.1 Flow chart of relationship between TESA modules	101
4.2 Enthalpy method equiaxed dendrite.	104
4.3 Enthalpy method columnar dendrite.	105
4.4 CA method equiaxed dendrite.	107
4.5 CA method Columnar dendrite. (a) 0° dendrite. (b) 25° dendrite.	108
4.6 CA method 3D Columnar dendrite.	109
4.7 CA method 3D equiaxed dendrites. (a) 0° dendrite. (b) Randomly rotated dendrite.	110
4.8 Procedure for applying force to growing structures.	112
4.9 Deformation of a growing beam.	114
4.10 Final deformation of a grown beam.	116
4.11 Overlaid 4×4 cells showing a multi-scaling of 2 and 4.	118
4.12 Copying coarse cell value into constituent fine cells.	120
4.13 2D trilinear interpolation example.	121

4.14 3D trilinear interpolation process.	123
4.15 Accuracy comparisons for a beam using multi-scaled SMS vs COMSOL.	125
4.16 Boundary behaviour for a 2D system of four parallel processors. .	127
4.17 Comparison of cell centred and cell staggered parallel boundaries.	128
4.18 Displacement profiles for test case used to test timing.	130
5.1 Intrinsic rotation example.	135
5.2 Displacements normal to cube faces.	137
5.3 Method of interpolating displacements on all faces of a volume. .	138
5.4 Displacements tangential to volume faces.	138
5.5 Obtaining $\Delta\theta$ from interpolated displacements.	139
5.6 Orientation changes with four-fold symmetry.	141
5.7 Extrinsic rotation example.	143
5.8 Obtaining the local angle of a deformed beam.	148
5.9 Changing orientation of a growing beam.	151
5.10 Final orientation along a grown beam.	153
6.1 Grid used for solid advection process.	159
6.2 Standard 1D advection.	162
6.3 Homogeneous square advected using upwind method.	163
6.4 Homogeneous square advected using Superbee method.	166
6.5 Split vs unsplit advection examples.	167
6.6 Split (left) vs unsplit (right) advection.	168
6.7 VOF 1D advection.	170
6.8 SLIC reconstruction examples.	172

6.9 Six SLIC reconstruction cases used by F_w in equation 6.15.	175
6.10 Homogeneous dendrite advected using VOF with a SLIC reconstruction.	176
6.11 Homogeneous dendrite advected using VOF with a WLIC reconstruction.	179
6.12 Dendrite growth behaviour under external forces showing thermal field T from Soar <i>et al.</i> [93]	180
6.13 Columnar dendrite under constant advection growing using enthalpy method.	182
6.14 Advection of a 3D dendrite using the Superbee flux limiter.	184
6.15 Variables needing advection for CA method. (a)-(c) solid fraction, (d)-(f) equivalent concentration, (g)-(i) liquidus concentration.	185
6.16 Advection using higher grid density.	186
6.17 Regrowth after significant advection.	188
6.18 Rotating dendrite.	190
6.19 Growing equiaxed dendrite advecting using Superbee.	191
6.20 Concurrent solidification with significant deformation.	193
7.1 Thin sample 3D view.	198
7.2 Thin sample dendrite growing under a constant body force.	201
7.3 Dendrite growing under thermal strain.	203
7.4 Dendrite growing under sinusoidal force.	206
7.5 Variable comparisons over time for dendrite under sinusoidal force.	207
7.6 Large scale thin sample solutions from Soar <i>et al.</i> [45].	210
7.7 Converging grain example from Soar <i>et al.</i> [45].	211

7.8 Large thin sample dendritic system.	212
7.9 Dendrite bending out of plane.	213
7.10 Forest of dendrites showing orientation components in pairs to compare behaviour without and with force applied.	214
7.11 Rotational force acting upon a dendrite.	215
7.12 Dendrite structures for cases 1, 10, 25, 50 and 100 in descending order at final time step $t = 250000$	218
7.13 Case 1 microstructure and orientation change (θ°) development at $t = 50000, 100000, 150000, 200000, 250000$	219
7.14 Case 10 microstructure and orientation change (θ°) development at $t = 50000, 100000, 150000, 200000, 250000$	220
7.15 Case 25 microstructure and orientation change (θ°) development at $t = 50000, 100000, 150000, 200000, 250000$	221
7.16 Case 50 microstructure and orientation change (θ°) development at $t = 50000, 100000, 150000, 200000, 250000$	222
7.17 Case 100 microstructure and orientation change (θ°) development at $t = 50000, 100000, 150000, 200000, 250000$	223
7.18 Case comparison plots for largest observed orientation change θ at time step.	227
7.19 Scaled orientation change θ comparing all cases and showing fitted power law of $\theta(t) = -4 \times 10^{-11}t^{1.91}$	228
7.20 Accumulated w displacements (μm) for all cases at final time step $t = 250000$	229
7.21 Case comparison plots for largest observed cumulative w displacement at time step.	231

7.22 Case comparison plots for largest observed single time step w displacement.	234
7.23 Von Mises stress σ_{vm} (Pa) for all cases at final time step $t = 250000$.	236
A.1 2D slice showing information used to obtain u displacement.	265
B.1 Case 1 - Floor fixed block under negative body force in z	285
B.2 Case 2 - Floor fixed block under positive body force in z	286
B.3 Case 3 - Floor fixed block under positive body force in y	287
B.4 Case 4 - Floor fixed block under positive body force in x	288
B.5 Case 5 - Floor fixed block under positive body force in x and y	289
B.6 Case 6 - Floor fixed block under positive body force in x and negative force in y	290
B.7 Case 7 - Floor fixed block under positive body force in x , y and z .	291
B.8 Case 8 - Floor fixed block under positive facial force in z on high face.	292
B.9 Case 9 - Floor fixed block under positive facial force in y on high face.	293
B.10 Block Validation 10 – Floor block under rotational facial forces.	294
B.11 Case 11 - Floor fixed block under opposing facial forces.	295
B.12 Case 12 - Floor fixed block under positive body force in x and a facial force in z on side face.	296
B.13 Case 13 - Floor & wall fixed block under body force in z	297
B.14 Case 14 - Floor block with fixed displacement.	298
B.15 Case 15 - $4 \times 4 \times 10$ cantilever beam with point load.	299
B.16 Case 16 - $4 \times 4 \times 20$ cantilever beam with point load.	300

FIGURES

B.17 Case 17 - $4 \times 4 \times 40$ cantilever beam with point load.	301
B.18 Case 18 - $4 \times 4 \times 10$ cantilever beam with distributed load.	302
B.19 Case 19 - $4 \times 4 \times 20$ cantilever beam with distributed load.	303
B.20 Case 20 - $4 \times 4 \times 40$ cantilever beam with distributed load.	304
B.21 Case 21 - Floor fixed block with diagonal edge under negative body force in z	305
B.22 Case 22 - Floor fixed block with diagonal edge with facial force applied to diagonal edge.	306
B.23 Case 23 - Floor & wall fixed block with triangular corner under negative body force in z	307
B.24 Case 24 - Floor fixed block with curved edge under negative body force in z	308
B.25 Case 25 - Floor fixed block with concave corner under negative body force in z	309
B.26 Case 26 - Floor fixed hemispherical structure under negative body force in z	310
B.27 Case 27 - Floor fixed block structure under uniform temperature increase causing thermoelastic expansion.	311
B.28 Case 28 - Floor fixed block structure under increasing temperature gradient causing thermoelastic expansion.	312
B.29 Case 29 - Floor fixed block structure under decreasing temperature gradient causing thermoelastic contraction.	313
B.30 Case 30 - Floor fixed block structure under temperature gradient causing thermoelastic expansion & contraction.	314

TABLES

2.1	Mechanical orientation changes observed in experiments.	29
3.1	Times to reach steady state	48
3.2	Maximum displacements observed at different grid densities.	83
4.1	Timing data in seconds comparing real time improvements from parallel computing and multi-scale modelling.	132
7.1	Properties used for problem setup.	200
7.2	Comparison of orientation change (θ°) values.	225
7.3	Comparison of maximum accumulated deformation (μm) values.	230

NOMENCLATURE

Symbol	Description	Unit
α	Coefficient of Thermal Expansion	K^{-1}
A	FVM Local Material Properties	-
BF	Body Force	N/m^3
C_l, C_s, C_e	Liquid, Solid and Equivalent Concentration	wt%
$\Delta\theta$	Change in Rotation Angle	rad
ΔT	Temperature Change	K
Δt	Time Step	s
Δx	Cell Size	m
D	Solute Diffusivity	-
ϵ	Strain Tensor	-
ε	Normal Strain	-
E	Young's Modulus	Pa
f	Solid Fraction	-
F_x, F_y, F_z	Force Components	N/m^3
F_l	Solid Flux	-
Γ	Thermal Modulus	Pa
γ	Shear Strain	-
g	Gravitational Acceleration	m/s^{-2}
I	Second Moment of Area	m^4
i, j, k	Cartesian Array Indices	-
H	Enthalpy	J
κ	Interface Curvature	m^{-1}
k	Partition Coefficient	-
λ	Lamé's First Parameter	Pa
μ	Shear Modulus (Lamé Constant)	Pa
η	Poisson's Ratio	-
N_x, N_y, N_z	Interface Surface Normals	-
Ω	WLIC Weighting Function	-

NOMENCLATURE

ω	Relaxation Parameter	-
Φ	Flux Limiter Function	-
ϕ	Phase Variable	-
ρ	Density	kg/m ³
\mathbf{R}	Rotation Matrix	rad
R_x, R_y, R_z	Rotation Components	rad
r	Interface Smoothness	-
$\boldsymbol{\sigma}$	Stress Tensor	Pa
σ	Normal Stress	Pa
σ_{vm}	Von Mises' Stress	Pa
S	FVM Source Term	-
τ	Shear Stress	Pa
θ	Generic Rotation Angle	rad
$\theta_x, \theta_y, \theta_z$	Extrinsic Rotation Angles	rad
$\theta_{z1}, \theta_x, \theta_{z2}$	Intrinsic Euler Angle Rotation Angles	rad
θ_p	Flip Flop Parameter	-
T	Temperature	K
T^i	Solid-Liquid Interface Temperature	K
t	Time	s
\mathbf{u}	Displacement Vector	m
u, v, w	Displacement Components	m
U, V, W	Displacement Matrices	m
x, y, z	Cartesian Coordinates	m

Acronyms

CA	Cellular Automata
CFD	Computational Fluid Dynamics
CPU	Central Processing Unit
CTE	Columnar to Equiaxed
FDM	Finite Difference Method
FEM	Finite Element Method
FVM	Finite Volume Method
MPI	Message Passing Interface
SGFVM	Staggered Grid Finite Volume Method
SM	Structural Mechanics
SMS	Structural Mechanics Solver
TEMHD	Thermoelectric Magnetohydrodynamics
TESA	Thermoelectric Solidification Algorithm
VoF	Volume of Fluid

Chapter 1

INTRODUCTION

Discoveries in metallurgy seem to be intrinsically linked with the advance of western civilisation. This relationship between human development and their command over the material resources available to them is such that to this day it is common to refer to the ‘bronze’ and ‘iron’ ages when identifying periods of history spanning millennia. Considering the current focus on the digital in modern life it can be easy to overlook the many advancements occurring in the manufacture of metal parts, even as they remain ubiquitous to myriad activities in modern life. With this in mind, it would seem a reasonable prediction that the creation of metal alloys with superior material properties will remain a key component of human technological development for the foreseeable future.

The microstructures of metal alloys are comprised of crystalline structures called dendrites (from the Greek ‘dendron’ meaning tree) which form as the liquid metal solidifies. How these dendrites grow and interact have a significant impact on the material properties of solidified metal parts, often being highly dependent on the morphology of final state of their underlying microstructure.

1. INTRODUCTION

In some extreme situations, the microstructural development can even lead to the formation of casting defects which render parts unusable.

If industry was able to correctly refine the processes employed in the creation of metal parts, whether casting, welding or 3D printing, the parts produced could be better tailored to their requirements by altering properties such as the strength, ductility or resistance to impact. Furthermore, adjusting the underlying microstructure of parts to be more effective at the macroscopic scale such as this can potentially provide further benefits to the components such as increasing the functional lifespan or lowering the weight while retaining strength.

These are not new observations, with there being large bodies of existing research exploring how solidification processes can be refined to create more desirable alloys. Despite this, one aspect of the process that remains poorly understood is how the growth behaviour of a solidifying microstructure can be altered by structural mechanical behaviour such as deformation and the accumulation of stress. Industrial processes are certainly aware mechanical behaviour is a factor, with cases from many practical experiments indicating this interaction has had a significant impact upon the final microstructure. Nevertheless, the physical relationships underpinning this process remain poorly understood and largely unexplored due to the technically difficult, time consuming and expensive nature of performing practical experiments.

Advances in computer power mean that the numerical modelling of microstructures can now be performed at a scale relevant to some industrial applications, which can provide further insight into physical processes that would be difficult to attain with practical experiments alone. As such, while

numerical modelling has been utilised to explore many key mechanisms relating to the microstructure solidification process, the paucity of extant numerical models capable of doing this concurrently with structural mechanics has left the simulation of this key mechanism a largely underdeveloped topic of research.

1.1 Thesis Overview

The work contained in this thesis describes the development of a numerical model which can couple together and concurrently solve both microstructure solidification and structural mechanics. This allows simulation of behaviours observed in practical experiments where the growth of dendrites is altered by stress accumulation an accumulation causing dendrites to change orientation and deform as they are growing. Given there is a lack of any existing numerical modelling capable of resolving a coupled solidification-structural mechanics scenario such as this at any scale of interest to industrial processes, it was considered the most practicable course to develop a bespoke structural mechanics solver (SMS) which could be coupled with the existing multi-physics code the ThermoElectric Solidification Algorithm (TESA) developed at Greenwich University by the Computational Science and Engineering Group (CSEG). In creating the SMS specifically for integration with TESA, it allowed for a more effective and intimate coupling than would be the case if attempting to use an existing commercial code for this purpose.

Structural mechanics can impact solidification in a number of ways, with cases of large deformations, impacts and even fracturing observed experimentally. However, due to the lack of existing numerical work in this field

and the requirement to develop a new model, it seemed prudent to focus on only the most fundamental mechanical behaviour and verify that this approach can be implemented effectively while ascertaining if this process has a meaningful impact on microstructural development.

Consequently, the SMS uses a linear elastic material model to examine scenarios where ‘small’ deformations cause changes to dendrite orientation, where these small alterations to orientation can accumulate and cause significant changes to growth behaviour. The coupled solver is used to generate results which explore some of these scenarios, providing insight into the fundamental mechanisms dictated by this effect and highlighting the need for further research on this topic.

1.2 Thesis Contributions

Both microstructure solidification and structural mechanics are topics which have been actively researched for decades, with a wide selection of models already existing which can be potentially applied to either phenomena. However, the combination of these two phenomena so they can act concurrently upon the same structure is a relatively unexplored area of research which necessitated the construction of a bespoke structural mechanics solver capable of being effectively coupled to the existing microstructure solidification code TESA.

The objective of this work is to implement this novel coupled solver to allow an examination of fundamental mechanisms which could not be captured using existing modelling. This provides the motivation for the work contained within

this thesis, where the subsequent chapters will endeavour to answer the following questions:

What is the most effective way to couple the separate structural mechanics and microstructure solidification models within a single interdependent process?

Can numerical modelling of concurrent microstructure solidification and structural mechanics predict the fundamental behaviours observed in practical experiments?

1.3 Thesis Outline

Chapter 1 provides context for the thesis by introducing the research topic of coupling microstructure solidification to concurrently occurring structural mechanical behaviour. An overview of the thesis is provided along with the research questions the thesis sets out to answer. A brief outline of the thesis chapters is also given.

Chapter 2 provides a review of the relevant literature currently available on this topic. This starts by providing a summary of practical experiments where structural mechanics can be seen to significantly impact the development of microstructure solidification. Then an exploration is provided of existing research which has addressed the topic of numerically modelling structural mechanics and microstructure solidification within the same simulation. This

1. INTRODUCTION

identifies that while structural mechanics is often a consideration in solidification modelling, there is vanishingly little research where the models operate concurrently to have an impact on one another, with even fewer cases where this modelling occurs on a microstructure level. Finally, research exploring the viability of modelling structural mechanics as a finite volume method process is examined and contrasted with potential approaches utilising the finite element method.

Chapter 3 outlines the process of the creation and validation of the structural mechanics solver. The theory and assumptions underlining the linear elastic material model used are outlined and justified, demonstrating how the stress based formulation of the equilibrium equations can be converted to a displacement formulation. The requirement for a variable material property formulation of the equations is discussed, with this form of the equilibrium equations being discretised into a staggered grid finite volume method numerical scheme. How the stress within the structure can be obtained from the displacement outputs is outlined and the boundary conditions this solver will use are described in detail. It is demonstrated how thermal strains are incorporated in the equilibrium equations, and how this alters the numerical scheme. This issue of identifying the structure within the larger problem domain is introduced and various important aspects to implementing this solver as a numerical scheme are discussed. Finally, the solver is verified by comparing the behaviour and accuracy against 7 test cases testing the key functionality of the solver against results obtained from a commercial code and an analytic solution.

Chapter 4 describes how the SMS is coupled to the existing multi-physics microstructure solidification code TESA. This starts out by providing a brief

summary of the existing TESA solvers, how they relate to one another and how the SMS fits into this framework. The solidification models which have been used in this research are also described in more detail. The method which allows the quasi-stationary SMS to account for existing deformation is explained. Finally, multi-scale modelling and parallel computing were introduced in the context of the solver to act as performance enhancements implemented to improve solution times.

Chapter 5 introduces deformation driven orientation changes as the primary method employed for using structural mechanics to influence solidification. This describes how the Cellular Automata method uses Euler angles to describe the orientations which dictate the growth behaviour of the dendrites modelled, explaining that it will be a requirement to alter the solver so that local orientations for each cell are used to allow different parts of the same dendrite to grow at differing orientations. The method to obtain a change in a structures orientation based on the deformations obtained from the SMS is outlined. Finally this method is verified in a test case being compared against an analytic solution.

Chapter 6 describes the methods used to explore solid structure advection, which was examined in depth as a potential method for using structural mechanics to influence microstructure solidification. The utility in having a method to physically move a dendrite through the problem domain is introduced, which is a necessity for large deformation, while also having applications in related topics of research. Advection of a binary structure is explored, outlining the limitations of basic advection in this context and introducing flux limiters and Volume of Fluid methods as a means to mitigate these shortcomings. These same

considerations are made for the heterogeneous structure of the dendrites produced by the CA method which possess internal concentration patterns which need to be maintained. For this reason, along with other concerns, the difficulties presented in attempting to model structure advection alongside solidification within the current framework are explored. Finally, the degree to which solid advection behaviour has been implemented in the current version of the research is defined and justified within the wider context of the model assumptions.

Chapter 7 presents a wide selection of cases modelled using the coupled SMS with microstructure solidification. These cases have been chosen as they highlight fundamental behaviours which can be captured but which would be missed using any existing solidification modelling. This starts by examining thin sample cases under different modelling conditions where the orientation change is effectively two dimensional. This is expanded to full three-dimensional models where dendrites can bend out of plane and rotate. Finally, a small parametric study is ran to highlight the complexity of coupled structural mechanics and solidification which renders simple approximations ineffective, necessitating the modelling approaches presented in this research.

Chapter 8 contains the conclusions which can be drawn from the work presented in this thesis along with a discussion of potential avenues for future work which would expand upon this research.

Appendix A provides the full process of discretising the linear elasticity equilibrium equation to a staggered grid finite volume method numerical scheme. This was only shown for the u displacement as the process is identical for the three equilibrium equations.

Appendix B supplements the validation cases shown in chapter 3 by showing

1. INTRODUCTION

30 verification cases (including the 7 from chapter 3 which are repeated for context) accompanied with a brief assessment where the fundamental mechanical behaviour and the numerical accuracy of the SMS is validated.

Appendix C lists publications by the thesis author which have been based upon this research along with any prizes or awards the work has received.

Chapter 2

LITERATURE REVIEW

2.1 Overview

This chapter will provide a review of the existing relevant research. This review will focus on three areas: observations and explanations of structural mechanical behaviour found in practical microstructure solidification experiments, existing solidification models which consider the impact of structural mechanics and the use of the Finite Volume method for modelling structural mechanics.

2.2 Structural Mechanical Behaviour Observed in Microstructure Growth

Structural mechanical behaviour has been widely observed in practical experiments as one of the many factors which can impact microstructural development during the casting process of metal alloys. This makes it a factor of interest in industry as the final composition of the dendritic microstructure has been widely observed to have a significant impact on the macroscopic

2. LITERATURE REVIEW

material properties, with primary spacing being found to be intrinsically linked with the mechanical properties of a structure [1] and the crystallographic orientation of the dendrites being found to change the anisotropic behaviour [2] and make the material more resistant to scratches and deformation [3].

Consequently, mechanical effects are generally taken into consideration when producing parts to ensure a good grain structure forms, which generally means encouraging a finer grain structure as this improves many important structural properties. This is due to fine grained structures being less susceptible to a crystallographic defect known as dislocation which changes the arrangement of atoms along the grain boundaries, as described by the Hall-Petch relationship which demonstrates an increase in yield strength as the grain sizes become smaller. Causing a finer grain structure is often the aim of production processes also far more actively utilise mechanical behaviour such as pulling [4], stirring [5] and macroscopic deformation [6]. This can even go so far as inducing cavitation [7] to cause the fragmentation of dendrite arms and encourage Columnar to Equiaxed (CTE) transition to occur, which significantly changes the growth behaviour and generally leads to a structure having material properties with reinforced tensile strength and hardness.

Structural mechanical effects have also been observed in a wide variety of casting methods as a key factor to consider when attempting to prevent the formation of casting defects. When examining the process of aluminium twin roll casting Westengen and Nes (1984) [8] found structural inhomogeneities and defects could be induced by the deformation imparted on the solidifying metal while passing through the twin rollers.

The process of making single crystal superalloys is now widely employed for

2. LITERATURE REVIEW

fabricating parts such as turbine blades which must possess high tensile strength even at high temperature despite having a complex structure. Single crystal structures represent the opposite extreme to the fine-grained structures mentioned prior, with the lack of grain boundaries in fact lowering the yield strength when compared to an otherwise identical fine-grained structure, as would be expected from the Hall-Petch relationship (though directional solidification is often exploited to give the single crystal strong anisotropic material properties which can mitigate this in practice). Nevertheless, the lack of grain boundaries causes these single crystal structures to be highly resistant to creep and thermal shock when compared to other grain morphologies, making them ideal for working under the extreme temperature conditions turbine blades must constantly endure. However, the process of making single crystal superalloys is prone to the formation of misaligned grains, often referred to as a ‘stray grain’ defect, which unsurprisingly ruin these beneficial properties and generally require the part with the defect to be scrapped.

Zhou (2011) [9] examines the formation of stray grains using a bi-crystal superalloy, where the converging and diverging grain boundaries encourage the formation of stray grains as seen in figure 2.1, concluding that a likely cause is the deformation and detachment of secondary arms rather than the initial nucleation of the grain. It was further observed by Yang *et al.* (2014) [10] that even in cases where no large local deformations occur, a gradual change in dendrite orientation can encourage the growth of stray grains.

2. LITERATURE REVIEW

Slivers are a similar defect where a misoriented grain extends through the microstructure as a thin strip such as can be observed in figure 2.2. One mechanism for this was proposed by Xu (2020) [11] where macro and micro scale stresses caused brittle dendrite fragmentation, generally occurring near the mould wall, where one of these misaligned fragments is able to develop into a sliver which can span the structure. Huang *et al.* (2020) [12] also noted a high incidence of slivers at the mould wall, but posited deformation driven by thermal contraction as the root cause of the defect for the case being examined.

Slivers were also found to arise as a secondary consequence of the formation of freckle defects as was highlighted by Han *et al.* (2021) [13], where thermal stress accumulating at the freckle channel caused mechanical deformation of surrounding dendrites which then developed into slivers.

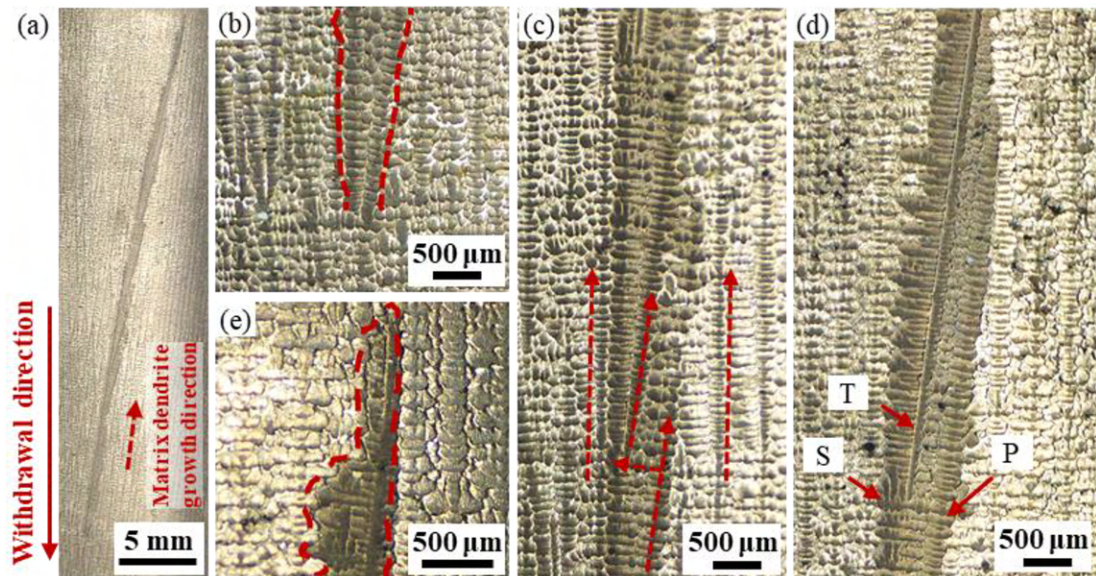


Figure 2.2: Sliver Defect from Xu *et al.* (2020) [11]. Licensed for reproduction under Creative Commons.

2. LITERATURE REVIEW

Defects have been seen occurring due to the interaction of dendrites with the dendrite wall as highlighted in two papers by Bogdanowicz *et al.* (2019) [14, 15] and continued by Krawczyk *et al.* (2021) [16], where the wall caused the dendrite to deflect and form low angle grain boundaries which act as a preferential site for the accumulation of residual strain and additional defects.

When examining a 3D printed metal superalloy, Li *et al.* (2015) [17] observed dendritic deformation to be a factor in the formation of both high (harming resistance to creep and thermal fatigue) and low angle grain boundary defects, becoming regions of high residual strains and encouraging the formation of further structural inhomogeneity defects.

Reviewing experimental results has indicated that there are three main structural behaviours which impact upon the development of a microstructure: deformation of dendrites, changes to dendrite orientation and fragmentation of dendrites. Though it must be noted that the distinction being drawn between these cases is often inter-related and can be somewhat imprecise, as deformation will almost always cause a corresponding change in the orientation of the dendrite and may be observed prior to fragmentation. However, visible deformation does not seem to be a pre-requisite for either a notable orientation change or a fragmentation even to occur.

Small deformations in the region of 1° - 10° were claimed by Doherty (2003) [18] to be a ubiquitous feature within conventionally solidified grains. A proposed solution for the significant orientation change observed by Billia *et al.* (2004) was the accumulated gravity driven bending moments and torque in the thin neck of the dendrite. A similar conclusion was drawn by Reinhart *et al.* (2008) [19] when observing an *in situ* example of a secondary arm bending under gravity (figure

2. LITERATURE REVIEW

2.3), claiming that the stresses in the solid neck attaching secondary arms to the primary trunk can accumulate until visible bending occurs.

A more extreme example of this behaviour was later captured by Reinhart *et al.* (2014) [20] where multiple examples of dendrites bending under by gravity could be observed (figure 2.4), making the analogy that the dendrite arms behaved similarly to a cantilever beam.

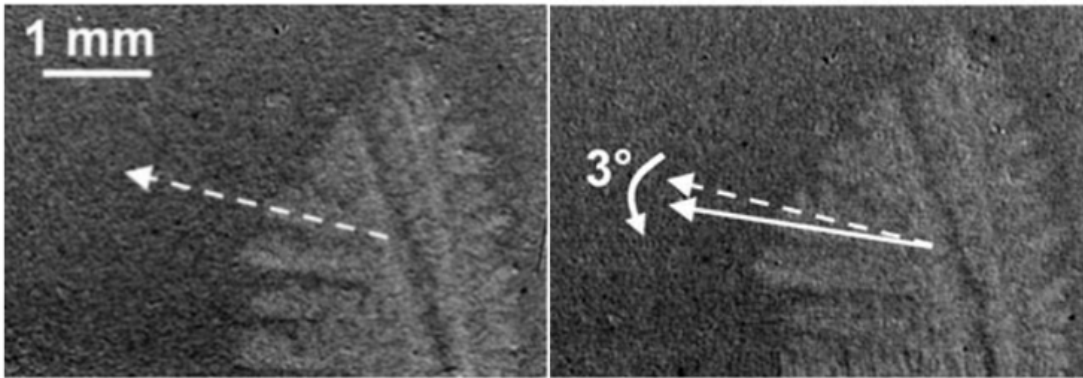


Figure 2.3: Dendrite arm rotating under gravity from Reinhart *et al.* (2008) [19]. Licensed for reproduction under Creative Commons.

2. LITERATURE REVIEW

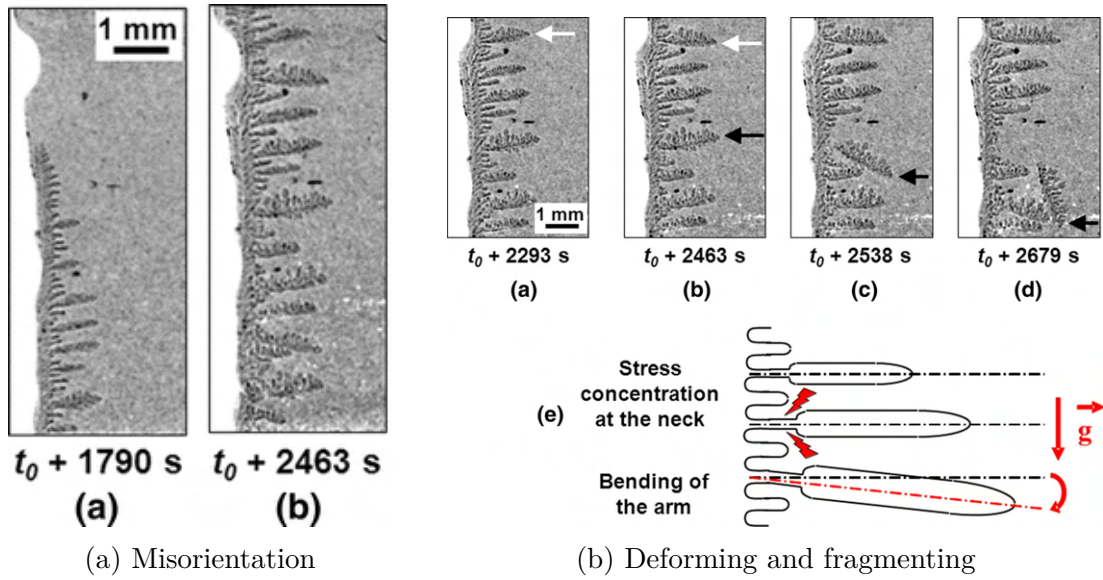


Figure 2.4: Gravity driven mechanical dendrite behaviour from Reinhart *et al.* (2014) [20]. Licensed for reproduction under Creative Commons.

2. LITERATURE REVIEW

As previously noted, it is almost certain that any significant deformation will also change the crystallographic orientation of the dendrite. The orientation of a dendrite can have a significant impact on many behaviours dictating the development of a dendritic system beyond simply defining the angle at which it preferentially grows, such as changing the behaviour of primary dendrite arm spacing [21], side-branching [22] and competitive growth [23, 24]. As such, mechanical effects which cause a dendrite to change orientation can have a large impact on the development of the microstructure, even in cases where little to no visible deformation occurs.

A local orientation change such as this was observed in experiments performed by Aveson *et al.* (2012, 2014) [25, 26], where the mechanism posited was that elastic deformation could occur at the solidifying tip of a dendrite which behaves like a cantilever beam, which would then become locked in as the solidification front advanced.

A very clear example of this localised behaviour was later presented by Aveson *et al.* (2019) [27], where it can be observed in figure 2.5a that a dendrite received a sharp change in orientation, purportedly driven by gravity. Growth then continues straight along the new bearing with no further orientation changes, allowing it to outcompete a neighbouring dendrite. A less extreme example of local orientations from this paper can also be observed in figure 2.5b, believed to be caused by thermal contraction.

Sun *et al.* (2019) [28] highlighted the local nature of orientation changes within entire grain systems, as the orientation of dendrites within a grain was found to change across the length of a convergent boundary of dendrite arms, with dendrites attaining a significantly different orientation when comparing one

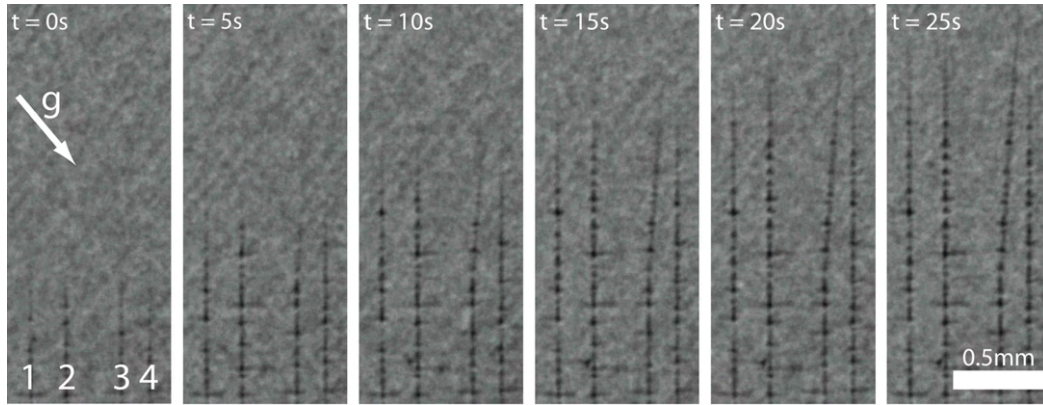
2. LITERATURE REVIEW

end of the grain to the other (figure 2.6). Hallensleben *et al.* (2019) [29] also observed sudden bending events occurring part way through a long dendrite arm 2.8a.

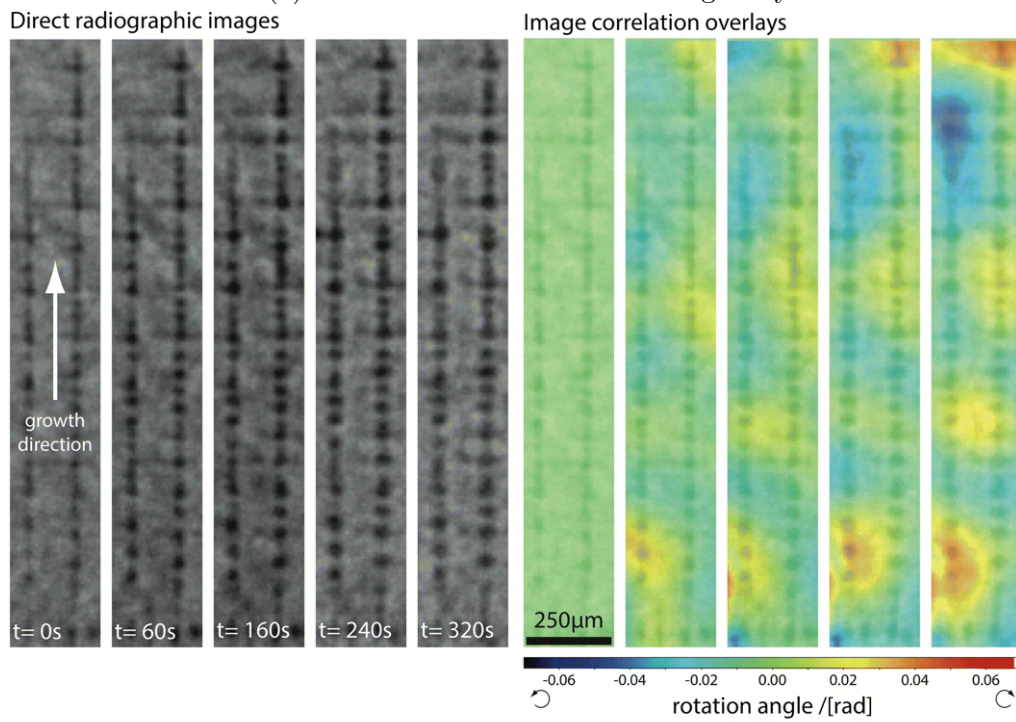
However, in the same paper it was noted that misaligned dendrites found in the microstructure were more generally cases featuring continuous bending across the length of the domain 2.8b. Continuous bending was observed by Sun *et al.* (2018) [30] where deformation is driving a monotonic orientation change in a long dendrite arm (again likened to a cantilever beam) as it grows through a single crystal casting (figure 2.7), with the microstructural development seeming to be dominated by this orientation change rather than any visible deformation.

A similar phenomenon was described by Hu *et al.* (2019) [31], where in figure 2.9 a 7.6° orientation change of a dendrite can be observed gradually occurring as it crosses the microstructure of a single crystal superalloy.

2. LITERATURE REVIEW



(a) Localised misorientation from gravity



(b) Localised misorientations from thermal contraction

Figure 2.5: Dendrites showing misorientation from Aveson (2019) *et al.* [27]. Licensed for reproduction under Creative Commons.

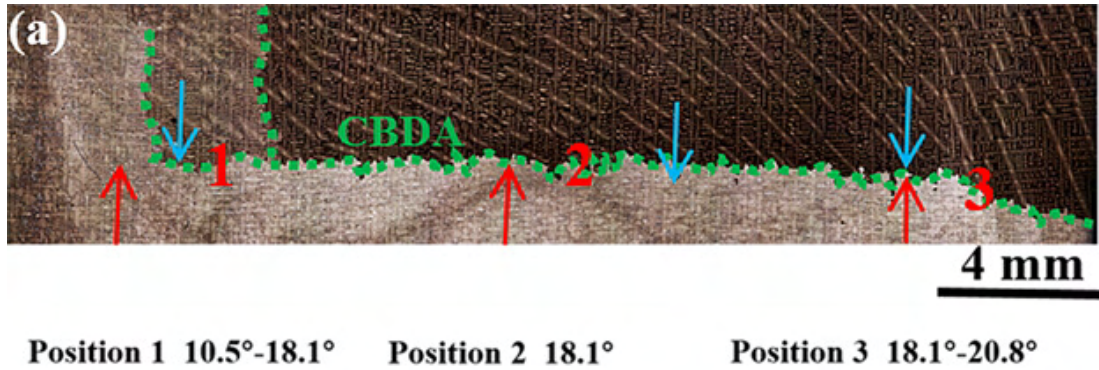


Figure 2.6: Dendritic system becoming misorientated along the convergent boundary of dendrite arms from Sun *et al.* (2019) [28]. Licensed for reproduction under Creative Commons.

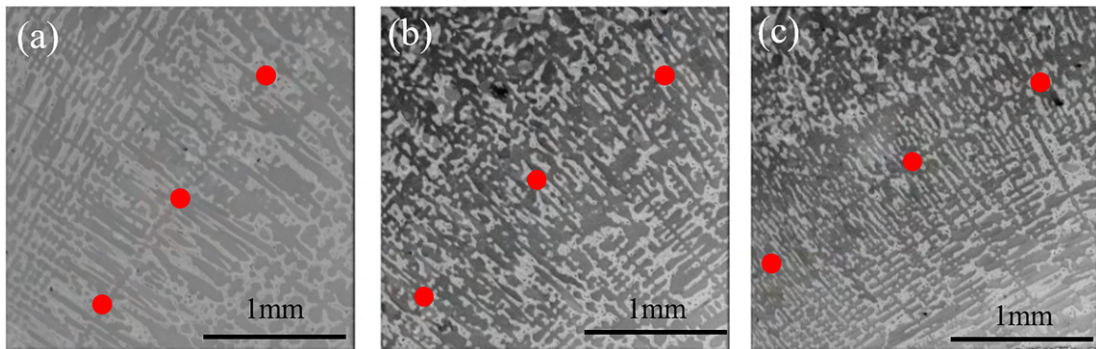
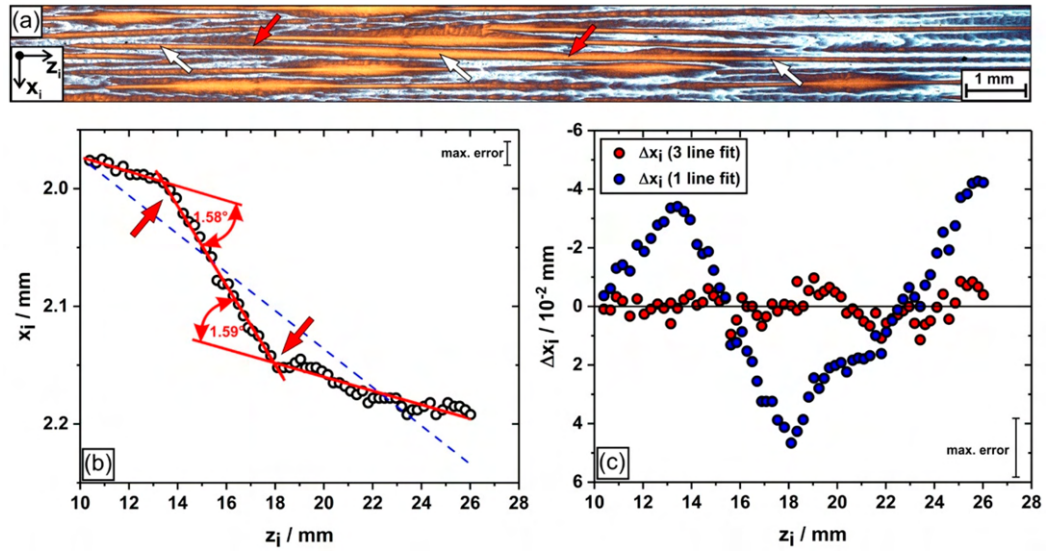
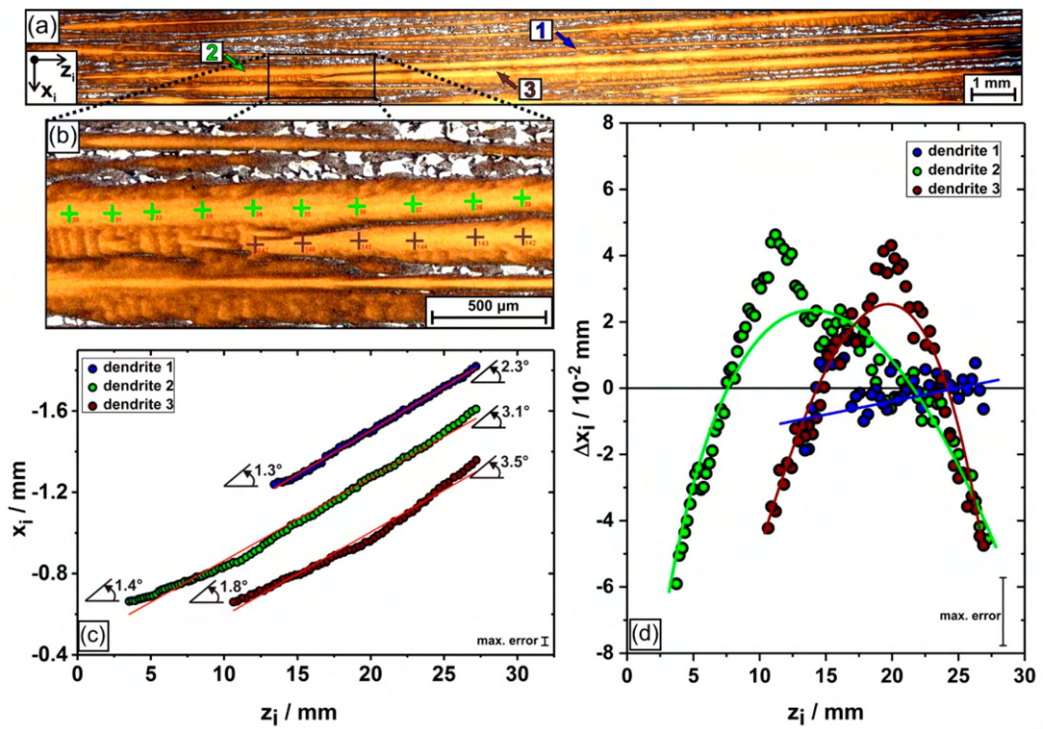


Figure 2.7: Long dendrite arm crossing microstructure becoming misorientated from Sun *et al.* (2018) [30]. Licensed for reproduction under Creative Commons.

2. LITERATURE REVIEW



(a) Morphological misorientations



(b) Stress based misorientations

Figure 2.8: Dendrites showing misorientation from Hallensleben *et al.* (2019) [29]. Licensed for reproduction under Creative Commons.

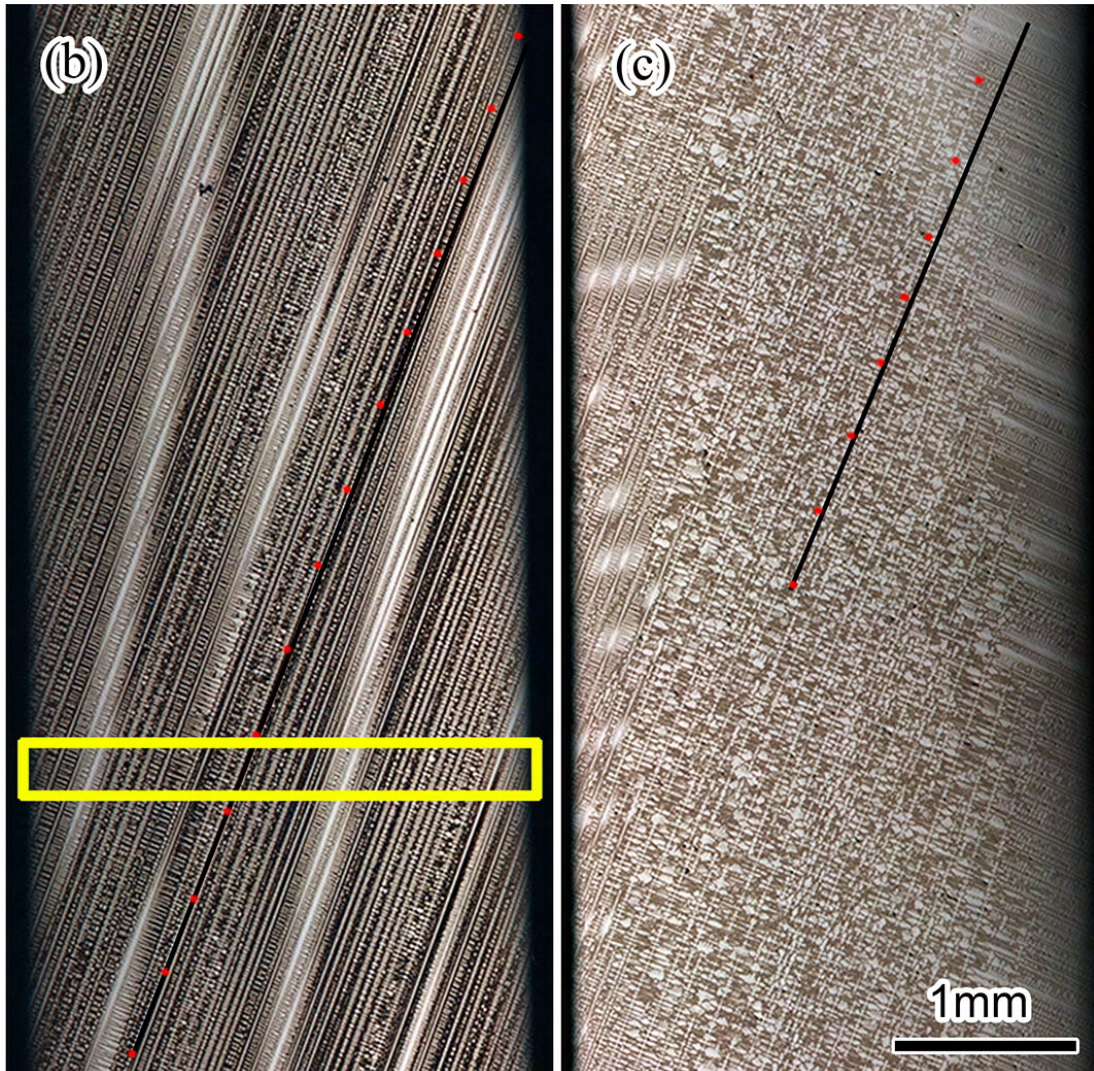


Figure 2.9: Long dendrite arm crossing microstructure becoming misorientated from Hu *et al.* (2019) [31]. Reproduced from Springer Nature under licence number 5091500230555.

2. LITERATURE REVIEW

The fragmentation of dendrite arms has been found to occur under a variety of different solidification conditions. The deformation of dendrites observed by Reinhart *et al.* [20] culminated in a dendrite fracturing due to gravity and falling to the bottom of the sample (figure 2.4b). Gravity driven fragmentation was also observed by Gibbs *et al.* (2016) [32], demonstrating that fragmentation may not always be easy to identify, as fragmented arms may remain trapped in the solidifying dendritic system and be unable to float away.

Fragmentation can also occur after a system has finished growing, such as in the case of the cumulative shrinkage stress observed by Zhou (2011) [33] to break up a dendritic network. However, structural mechanics can also be a source of fragmentation without any observable deformation occurring, as observed by Ananiev *et al.* (2009) [34] where the accumulated elastic energy in the neck of a dendrite arm may induce sudden remelting, causing the arm to detach.

An issue with attempting to describe the interactions between structural mechanics and solidification is the inherent interdependence between different physical phenomena, often meaning there may be no single factor which can be solely attributed as the cause of the final composition of a microstructure. A case of fragmentation was described by Mathiesen *et al.* (2006) [35] which does not consider structural mechanics as a factor in arm detachment, despite finding very different fragmentation behaviour depending on the direction of gravity relative to the growth direction.

While there are certainly numerous cases where fragmentation is purely a factor of temperature or concentration instabilities causing remelting, it cannot be established if the arm simply separated as the region of fragmentation liquefies, or if the structure being weakened by the ongoing remelting actually mechanically

fails before the remelting is complete.

This interdependence also makes the observed behaviours very problem specific, where an examination of magnetic field induced fragmentation by Li *et al.* (2012) [36] concludes the magnetic field induced a torque which was breaking dendrites, whereas Liotti *et al.* (2014) [37] claimed that direct mechanical action from the Lorentz force was not a primary cause of fragmentation for their sample, being primarily driven by the movement of inter-dendritic liquid which caused remelting.

This problem dependence is particularly troublesome in the somewhat contentious case of ascertaining the structural effects of fluid flow during solidification. A model developed by Pilling *et al.* (1996) [38] concluded that inter-dendritic flow could not cause bending or fragmentation by itself, though Dahle *et al.* (1999) [39] posits that under the right solidification conditions this could occur in processes where the flow rate is very high.

Dragnevski *et al.* (2002) [40] concludes that the likelihood of mechanical damage from fluid flow is remote, though concedes it may be a possibility for fine dendrites under high flow velocities. Later modelling would seem to go against this, with Hanlon *et al.* (2006) [41] suggesting that convective velocities may be strong enough to bend primary arms and Kashina *et al.* (2011) [42] finding the influence of fluid flow to be more dominant than gravity in the stress build-up of the neck of a dendrite.

Even if the fluid flow is not sufficient to cause visible bending, Xu *et al.* (2018) [43] observed that stress caused by fluid flow may lead to remelting and fragmentation. Certainly fluid flow can cause morphological changes to the growth orientation as the solute concentration is changed to induce growth into

2. LITERATURE REVIEW

the flow, even if that leads to growth deflecting from the starting orientation [44], but it is not clear what effect forces imparted by the fluid flow or gravity on the now lopsided dendrites may have on the continuing orientation changes.

Experimental results using a on a solidifying Gallium 25%wt. Indium alloy undertaken by N. Shevchenko and S. Eckert from Helmholtz-Zentrum Dresden-Rossendorf (HZDR) help to further highlight this complexity, where in figure 2.10 the development of a long dendrite arm deforming and accruing misorientations, which eventually dominate the impact of any observable deformation.

Further results using a similar problem setup were published by Soar *et al.* (2021) [45] and can be seen in figure 2.11, wherein irregular observable misorientations can be observed throughout the system of dendrites. Whether the key driver of these misorientations were gravity, pressure from the flow velocities, remelting weakening the root of the dendrites, morphological orientation changes induced by the flow or a combination of all of these factors is unclear, with more work into the interdependence between these physical processes being required.

2. LITERATURE REVIEW

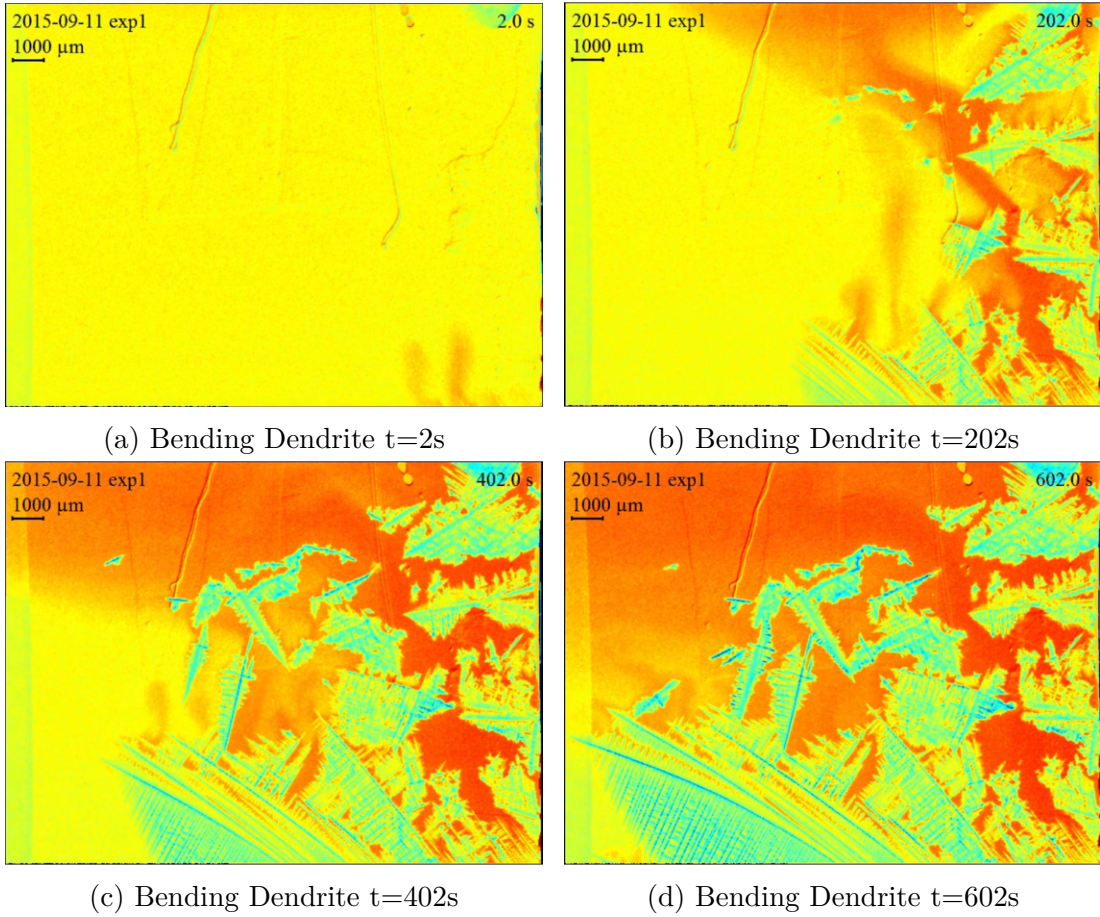
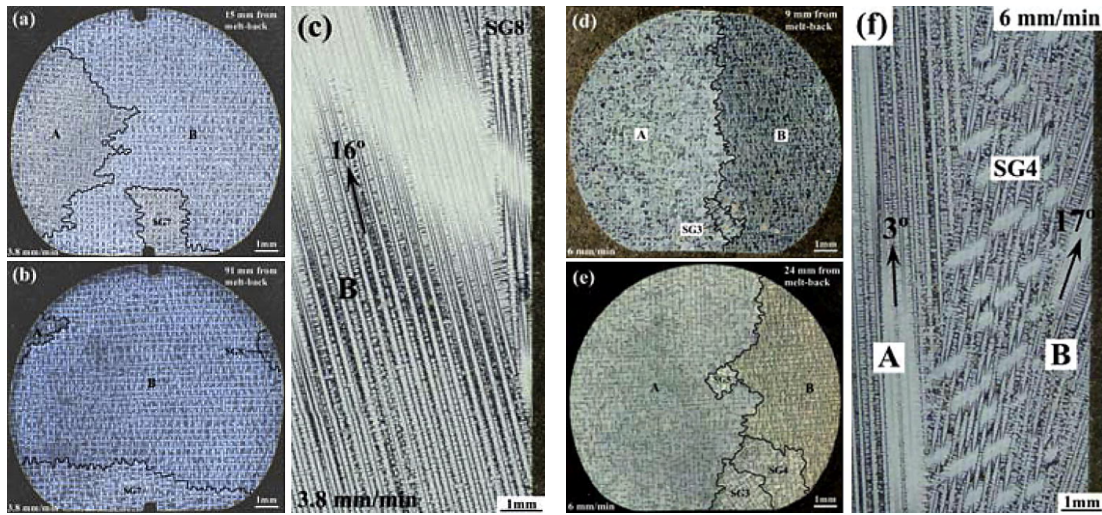


Figure 2.10: Solidification of a Ga-25 wt.%In alloy showing a large misorientation. Images courtesy of N. Shevchenko and S. Eckert at HZDR.

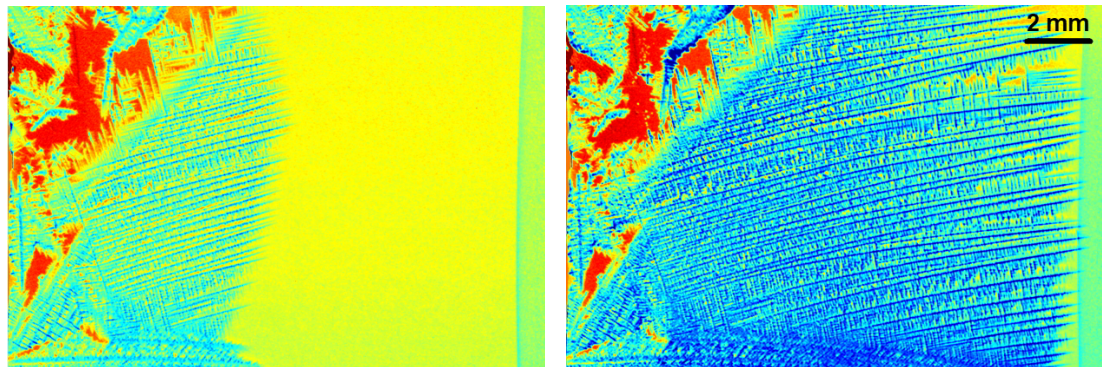
2. LITERATURE REVIEW



(a) Converging Grain Boundary

(b) Diverging Grain Boundary

Figure 2.1: Stray grain formation from Zhou (2011) [9]. Reproduced from Springer Nature under licence number 5091500996151.



(a) Dendritic system grown partway through the domain

(b) Dendritic system grown across the domain

Figure 2.11: Solidification of a Ga-25 wt.%In alloy showing multiple misoriented dendrites. Images courtesy of N. Shevchenko and S. Eckert at HZDR and published by Soar *et al.* (2021) [45].

2. LITERATURE REVIEW

Many of the key examples described have been summarised in table 2.1, where the source of the experiment and a reference to the image (if considered relevant enough to reproduce in this chapter) is provided. The observed maximum misorientation has been provided as well as the ‘rate’ of orientation change if the experiment showed a slowly misorientating long dendrite arm, where a ‘local’ change indicated a sudden deformation causing the change.

These observations come with the caveat that due to the complex nature of the process, there can be instances where both gradual and localised orientation changes can contribute to the final orientation angle. When orientation numbers have been provided by the author, they were used, but for some cases estimates of misorientation were made based on the provided figures. Finally the table also contains the material used in the experiment along with the cause of the orientation change as proposed by the authors.

2. LITERATURE REVIEW

	Paper	Image	Misorientation		Material	Proposed Cause
			Max	Rate/mm		
1	Aveson <i>et al.</i> (2014) [26]	–	20°	Local	Ni-based superalloy	Thermal contraction
2	Aveson <i>et al.</i> (2019) [27]	2.5a	5°	Local	Ni-based superalloy	Gravity
3	Aveson <i>et al.</i> (2019) [27]	2.5b	3.5°	Local	Ni-based superalloy	Thermal contraction
4	Billia <i>et al.</i> (2004) [46]	–	3.5°	Local	Al-73 wt.%Cu alloy	Gravity, shear stress and collisions
5	Doherty (2003) [18]	–	10°	Local	Multiple	Thermal contraction
6	Hallensleben <i>et al.</i> (2019) [29]	2.8a	1.7°	0.07°	Ni-based superalloy	Contraction or convection
7	Hallensleben <i>et al.</i> (2019) [29]	2.8b	1.59°	Local	Ni-based superalloy	Morphological chemical interactions
8	Hu <i>et al.</i> (2019) [31]	2.9	7.6°	0.07°	Ni-based superalloy	Thermal contraction
9	Reinhart <i>et al.</i> (2008) [19]	2.3	3°	Local	Al-3.5 wt.%Ni alloy	Gravity and shear stress
10	Reinhart <i>et al.</i> (2014) [20]	2.4a	9°	Local	Al-7 wt.%Si alloy	Gravity and wall interaction
11	Shevchenko, N and Eckert, S	2.10	20°	2.3°	Ga-25 wt.%In alloy	Gravity, fluid flow and remelting
12	Shevchenko, N and Eckert, S	2.11	10°	1°	Ga-25 wt.%In alloy	Gravity, fluid flow and remelting
13	Strickland <i>et al.</i> (2021) [47]	–	8°	0.1°	Ni-based superalloy	Macro-segregation
14	Sun <i>et al.</i> (2018) [30]	2.7	33.5°	1.6°	Ni-based superalloy	Contraction at mould wall
15	Sun <i>et al.</i> (2019) [28]	2.6	20.8°	Local	Ni-based superalloy	Contraction at mould wall

Table 2.1: Mechanical orientation changes observed in experiments.

2.3 Existing Solidification Models Considering Structural Mechanical Effects

Numerically modelling the evolution of dendritic microstructures has been a wide field of research for decades, generating many industrially relevant insights for large industrial partners such as Rolls-Royce plc, Cannon-Muskegon and Alcoa. Funding from these parties alone have supported cutting edge dendritic microstructure modelling work in fields such as grain selector design [48], preventing casting defects in single crystal castings [49–51], controlling the dendrite arm spacing in the melt pools of direct deposition laser welding [52] and predicting the stress accumulation within twin roll cast strips of Aluminium [53].

Despite the observations of mechanical effects being widespread in experimental results, structural mechanics is an often neglected factor in the numerical modelling of dendritic growth. This particularly seems to be the case when considering the interdependent behaviour where structural mechanics changes dendrite growth in real time as solidification is ongoing, potentially rendering models unable to predict the key mechanisms observed in experiments.

This was identified by Asta *et al.* (2009) [54] as one of the key open questions requiring further research in their review of the field, with the relationship between strain and the misorientation of dendrites still being identified as an area of research needing focus over a decade later by Strickland *et al.* (2020) [1] in a review of directional dendritic growth and primary arm spacing.

This is not to say that the impact of stresses and deformation on cast metal alloys is an unknown factor to modellers, with there indeed being a wide range of

2. LITERATURE REVIEW

work addressing the topic to some degree, but as of yet it almost all falls short of modelling microstructure solidification concurrently with structural mechanics.

Often the models operate at a macroscopic scale and will not allow the mechanical effects to impact the solidification process, such as Gandin *et al.* (2002) who created a model for predicting the yield stress of a cast metal alloy. This can often take the form of applying a structural mechanics model to post process an already solidified part, as can be observed in the work of Thorborg, Klinkhammer and Heitzer (2012) [55] where the temperature driven stresses were predicted in a 3D cast iron part.

A similar task was undertaken by Palumbo *et al.* (2015) [56], where post processing was again applied to a 3D representation of a sand-cast stainless steel part to find the heat driven residual stresses. There are also examples of this being applied to the deformation of semi-solid material, such as the level-set based finite element model developed by Sun *et al.* (2017) [57], which is functionally a post processing of a structure in the process of solidifying.

While there have been examinations of how the stresses change transiently in a solidifying system, the structural mechanics being applied often remains post processing to observe how the stresses change as the structure develops. Seetharamu *et al.* (2001) [58] used a finite element macroscopic model of an solidifying ingot to find how the heat driven stresses change over time.

Similar experiments were undertaken by Srinivasan *et al.* (2016) [59] again exploring a macroscopic problem which was post processed at various growth stages to find the temperature driven stresses, concluding that the stress, thermal field and deformation are interlinked and have a clear impact on the quality of the final ingot produced.

Moj *et al.* (2017) [60] proposed a micro-macro modelling of solidifying steel, where the thermal forces drove both the micro-scale phase transition and macro-

2. LITERATURE REVIEW

scale mechanical deformation, but this deformation only occurred after the phase transition from liquid to solid, meaning it had no effects on future solidification.

While still being technically a macroscopic scale model Fackeldey, Ludwig and Sahm (2002) [61] presented a method considering the mechanical interaction between the casting and mould which coupled solidification to the temperatures, stresses and the microstructure composition. However, in this case the microstructure was characterised by parameters describing the primary and secondary arm spacing and the eutectic fraction, as opposed to truly modelling the dendrites comprising the microstructure.

While solidification modelling which considers structural mechanics often works at the macroscopic level, there have been examples looking into the structural behaviour of microstructures. Uehara, Fukui and Ohno (2008) [62] present a phase field simulation of dendritic solidification where a finite element method was used to obtain a stress profile which evolved as the system solidified (figure 2.12). However, while the authors did highlight a relationship between stress dependence and phase transformation, that aspect was ultimately neglected for the sake of simplicity, leaving this as another case of transient post processing.

Structural post processing of a single growing dendrite can be found in the work undertaken by Takaki and Kashima (2011) [63] and Kashima *et al.* (2011) [42], where the impact of convection and gravity on the stress variation in the narrow neck of a single growing dendrite was evaluated (figure 2.13).

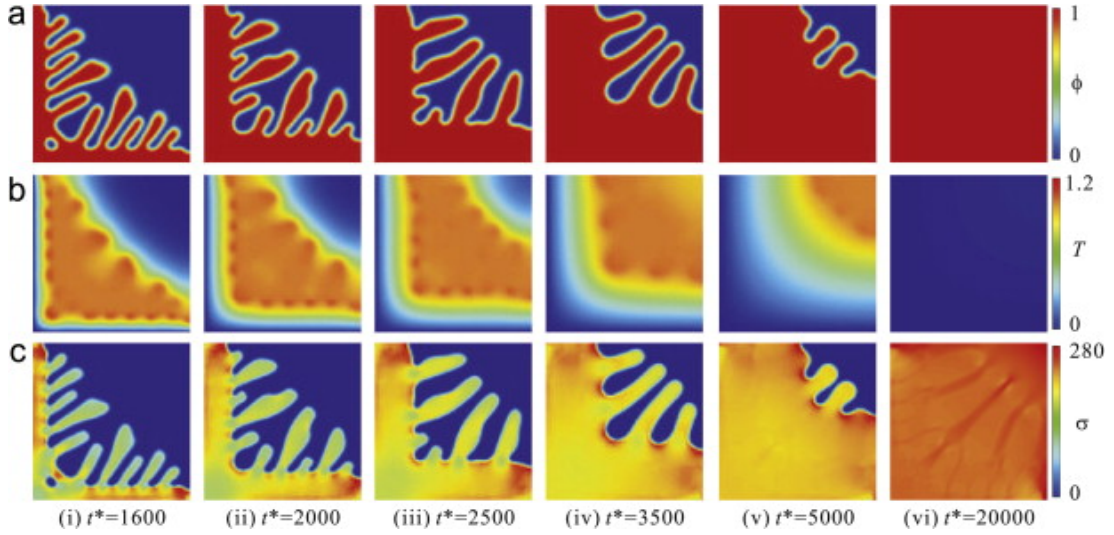


Figure 2.12: Variation of (a) phase field, (b) temperature and (c) equivalent stress during cooling process. Demonstrating stress being calculated during microstructure solidification by Uehara, Fukui and Ohno (2008) [62]. Reproduced from Springer Nature under licence number 5093760693894.

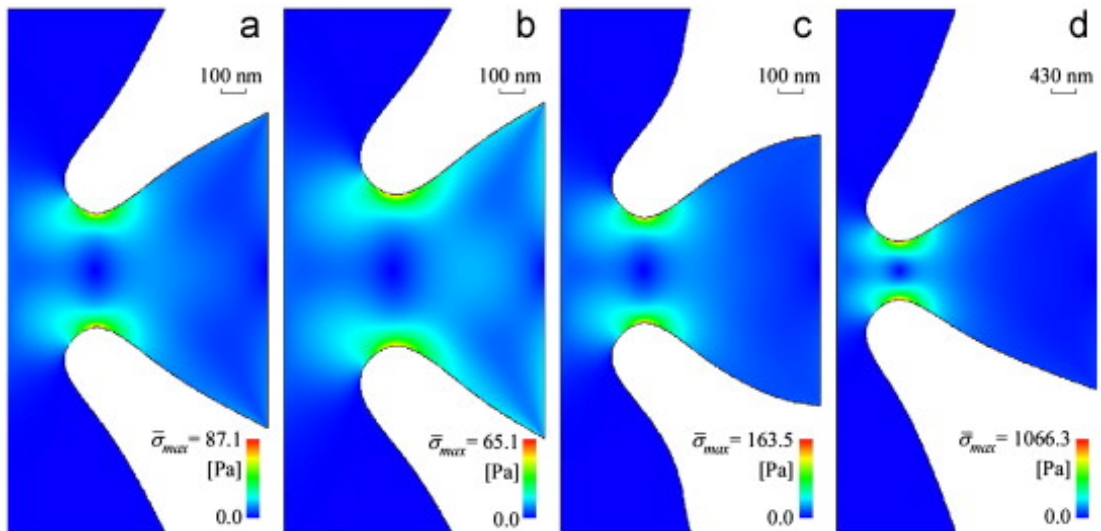


Figure 2.13: Equivalent stress distributions due to gravity for differently shaped dendrites by Takaki and Kashima (2011) [63]. Reproduced from Springer Nature under licence number 5093760526071.

An example of a truly coupled approach considering the interdependence of

2. LITERATURE REVIEW

solidification and structural mechanics was developed by Yamaguchi and Beckermann (2013, 2014) [64–66], where a phase field model was coupled to a structural mechanics solver while also considering the impact deformation has on the crystallographic orientation as the system develops (figure 2.14).

However, there were several shortcomings identified by the author which could make this model impracticable for modelling many situations, most notably that the approach was currently only able to simulate a pure substance and that the only way to impose structural effects on the system was to apply fixed displacements at the domain boundaries of the simulation.

Another example of a fully coupled microstructure solidification system can be found in the thesis of Victor (2018) [67] which coupled phase field solidification to multiple plasticity models to explore different deformation processes on the developing microstructure, but as the unique microstructure of the Ni-base superalloy being modelled is comprised of dislocated globular crystals, the approach undertaken does not seem appropriate for the modelling of dendritic systems.

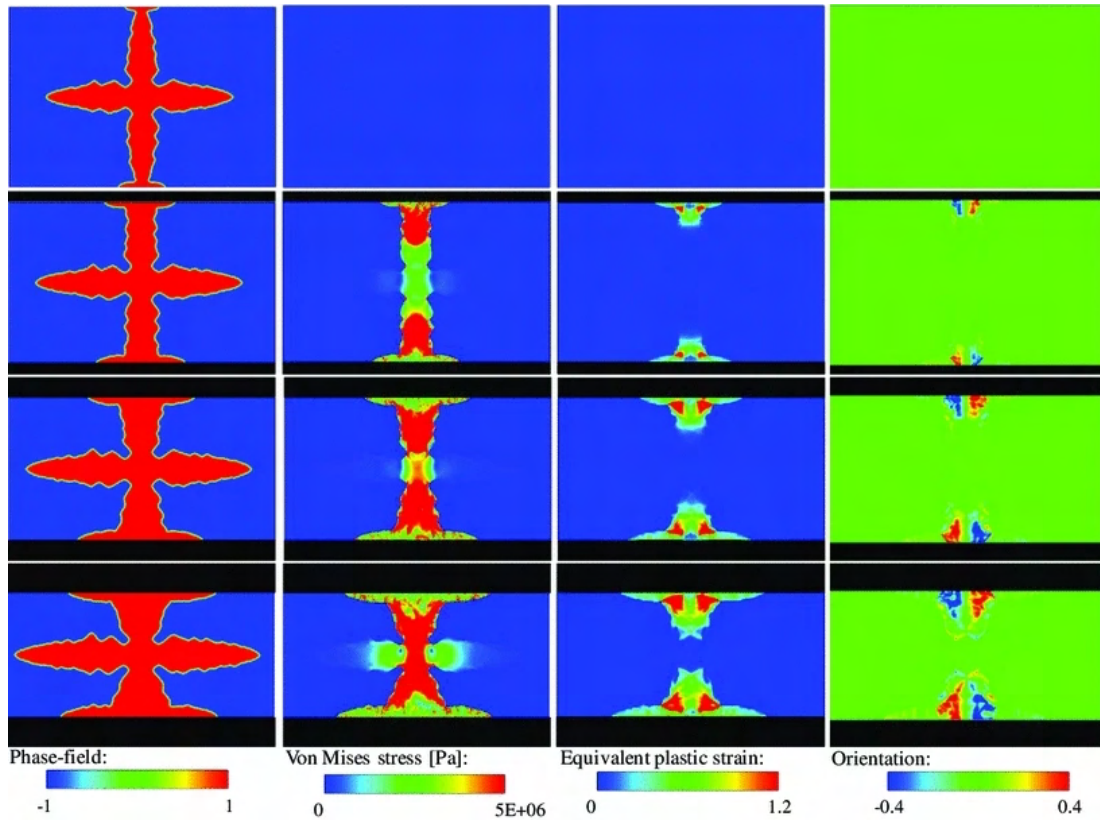


Figure 2.14: Predicted phase field (left column), von Mises stress (center left column), equivalent plastic strain (center right column), and crystallographic orientation angle relative to an arbitrary coordinate system (right column) contours for elasto-perfectly plastic compression of a single dendrite growing into an undercooled melt. Example of a coupled microstructure solidification with concurrent structural effects by Yamaguchi and Beckermann (2014) [66]. Reproduced from Springer Nature under licence number 5093760308304.

2.4 Using Finite Volume Methods for Structural Mechanics in a Multi-Physics Framework

When solving Structural Mechanics (SM) problems of a given level of complexity it is generally taken for granted that the Finite Element Method (FEM) or one of its expanded forms will be the most appropriate choice of model. The FEM is a method of numerically solving differential equations which operates by fitting a mesh to the structure being analysed, with the corners of these mesh cells being the nodes solved to obtain a solution. Fitting a mesh which closely matches the structure being modelled can be a very effective way of solving SM problems for complex structures.

However, this process of meshing the structure can present a problem in the framework of coupled solidification with SM, where after every change to the structure by solidification it would require re-meshing to continue providing accurate results, which has potential to become a highly computationally expensive part of the modelling process. This problem has been mitigated for some cases of a developing microstructure by resolving SM on a fixed grid fitted to the entire domain, updating the material properties of the nodes as the system develops [62] or by electing to use a Cartesian mesh to simplify the process [42, 63]. However, as making compromises such as these can work against some of the inherent strength of the FEM, it was natural to consider other approaches to resolve structural mechanics in a multi-physics framework.

Consequently, the viability of applying the Finite Volume Method (FVM) to this problem was examined. The FVM is another expansion of the Finite Difference Method that likewise has a long history of use, being used to solve PDEs by representing the problem domain as a collection of volumes with a node

2. LITERATURE REVIEW

in the centre where the values are calculated. This method is usually applied to Computational Fluid Dynamics (CFD) problems as the formulation provides better mass conservation in general, however this is merely a convention, with it being possible to apply the FEM to CFD problems and the FVM to SM problems. The adoption of FEM for CFD is currently a more common transition, with commercial packages such as COMSOL Multiphysics using the FEM for their CFD solver, though FVM solvers initially intended for use in CFD such as OpenFOAM have also been successfully implemented to solve SM problems [68].

While often overlooked, the FVM has been applied to SM problems for around three decades as was examined by Cardiff and Demirdžić (2021) [69] in their comprehensive review of developments in the field. It has been long indicated by many of these studies that a comparable level of accuracy for FEM solutions can be attained using the FVM, such as was presented by Oñate, Cervera and Zienkiewicz (1994) [70] where for a simple 2D structure under constant loads both the FEM and FVM produce the same results. A two-dimensional vertex based FVM approach presented by Taylor, Bailey and Cross (1995) [71] also make note of the comparable solution accuracy and computational efficiency of the FVM while highlighting its beneficial qualities when considered within the framework of an integrated multi-physics solver.

This work was expanded into a three-dimensional formulation used in the multi-physics solver PHYSICA which continued to demonstrate high accuracy was attainable with a FVM approach [72–75]. The case for the use of the FVM to solve SM was further supported by Oliveira and Rente (1999) [76] who showed that on an unstructured grid both transient and stationary problems provide results for the FVM which are comparable to the analytic solution, an observation that was supported further by later research undertaken by Cavalcante and Pindera (2012) [77, 78] who developed a generalised 2D scheme

2. LITERATURE REVIEW

for the finite volume method which was found to be in good agreement with analytic solutions. Overall, there seems to be a significant body of research supporting the notion that when correctly applied the FVM is of comparable accuracy and efficiency to other approaches for solving SM problems, indicating this should not be a principal cause for choosing between these modelling approaches.

The FVM has been widely used for multi-physics problems more generally where the shape and movement of solid structures is being considered, even if structural mechanics is not itself being solved and driving these movements. For example, the technique presented by Udaykumar, Mittal and Rampungoon (2002) [79] uses the FVM to model the flow behaviour around general solidification fronts as well as representing standard fluid-structure interactions. However, when solving multi-physics problems a key consideration must be how models are to be coupled so that data can easily pass between them. While it is certainly possible to couple models using different numerical schemes together, as identified by Yates (2011) [80] in his own review of the literature for fluid-structure interaction, simulating the problem efficiently can be aided by utilising the same numerical method for both the fluid and solid equations.

The advantages of coupling when using a single mesh for fluid-structure interactions had also been highlighted by Slone *et al.* (2004) [75], with a further example being the research of Xia and Lin (2008) [81], which used the FVM to solve both the fluid and solid material, finding it to be a viable alternative to the FEM. This could also be observed in cases where a higher number of physical phenomena require solving on the mesh, as it was for the welding problems examined by Taylor *et al.* (2002) [73], which employed the same FVM mesh to solve phase change, heat transfer, weld pool dynamics and structural mechanics, finding results comparable to reference solutions.

2.5 Summary

This chapter has contained a summary research conducted by other authors that was relevant to the focus of this thesis. A review was made of experimental results which demonstrate cases where structural mechanical behaviour had seemingly changed the development of the microstructure to a significant degree, demonstrating that this is an active concern in industry and area in need of further research. Numerical models related to this topic were then appraised, demonstrating that while this field has been active, with many modelling approaches being applied on a macro and micro level, they all fall short of being able to model microstructure solidification at an industrially relevant size where the growth behaviour is influenced by concurrently solved structural mechanics. To demonstrate why the Finite Volume method was chosen to solve structural mechanics for this research, examples demonstrating the comparable accuracy with the Finite Element method were provided along with examples of how the Finite Volume method had been successfully applied in previous multi-physics models.

Chapter 3

CREATING A STRUCTURAL MECHANICS SOLVER

3.1 Overview

In this chapter a bespoke Structural Mechanics Solver (SMS) capable of being intimately coupled with an existing solidification model is introduced. This process starts by introducing the theory underpinning the linear elastic material model chosen for the solver. The process of identifying structures within the domain is examined and a variable material property approach is introduced to account for the generally heterogeneous nature of the growing dendrites. The discretisation of this approach into a Staggered Grid Finite Volume Method (SGFVM) is presented along with how stress and strain outputs, boundary conditions and thermoelastic behaviour are being accounted for. Considerations for the algorithmic implementation of this approach are then discussed. Finally, the accuracy of the model is verified against test cases replicated in COMSOL and analytic solutions derived using Euler-Bernoulli beam theory.

3.2 Material Model: Linear Elasticity

3.2.1 Theory

Structural Mechanics (SM) is the study of how structures deform and accumulate stresses due to external forces. A key decision when numerically modelling a SM problem is the choice of material model, as this dictates not only how the structure behaves but also under what conditions the model will be valid.

The material model ultimately selected was linear elastic, a foundational material model that has been in use for hundreds of years, with a geometry dependent version of linear elasticity being traceable back to Robert Hooke in the late 17th century, with many textbooks such as the one written by Timoshenko and Goodier (1951) [82] providing comprehensive explorations of the concepts described in this section.

Linear elasticity is itself a simplification of the non-linear theory of elasticity, which is reached by making the following assumptions about the problem:

- The deformations are ‘small’ (infinitesimal strains). See section [3.2.2](#).
- There is a linear relationship between the stress and strain.
- The results of the problem do not demonstrate yielding (plastic behaviour).

While it is clear that these simplifying assumptions cannot be held to be true for all solidification incorporating SM problems which could be explored, with there being examples observed in practical experiments where dendrites demonstrate clear plastic behaviour when bending. This can sometimes reach the point of dendrites breaking and falling, which certainly cannot be accurately represented within a linear elastic framework.

There are undoubtedly many scenarios where these assumptions would make utilising linear elasticity a questionable choice to represent the structure, however

3. CREATING A STRUCTURAL MECHANICS SOLVER

any chosen numerical modelling will necessarily have simplifying assumptions which can make their application questionable for the modelling certain cases, no matter how complex that material model may be.

Consequently, due to the paucity of existing work coupling SM to microstructure solidification there remains an abundance of scenarios which can appropriately be examined which satisfy the assumptions of linear elasticity, with it making intuitive sense to begin this line of research with the implementation of a fundamental material model such as this to see what mechanisms can still be observed under these modelling restrictions. More complex material models will remain open as a possible expansion for future research if these simplifying assumptions become a limiting factor.

The choice of utilising a linear elastic material model was also supported by examples from both practical experiments [26, 30, 34] and numerical modelling [63, 65] which have likened the behaviour of columnar dendrites to that of a cantilever beam fixed at one end. With the behaviour of these beams being described by the Euler-Bernoulli or Timoshenko beam theory analytic solutions, both themselves simplifications of linear elasticity, a diverse selection of other research on the mechanical behaviour of dendrites have been ultimately assuming linear elasticity for the behaviour of single dendrite arms.

The governing equations describing a linear elastic material which any numerical modelling must satisfy are as follows:

1. The Equation of motion, for a 3D material:

$$\rho \frac{\partial^2 u}{\partial t^2} = \frac{\partial \sigma_x}{\partial x} + \frac{\partial \tau_{xy}}{\partial y} + \frac{\partial \tau_{xz}}{\partial z} + F_x \quad (3.1)$$

$$\rho \frac{\partial^2 v}{\partial t^2} = \frac{\partial \sigma_y}{\partial y} + \frac{\partial \tau_{yx}}{\partial x} + \frac{\partial \tau_{yz}}{\partial z} + F_y \quad (3.2)$$

3. CREATING A STRUCTURAL MECHANICS SOLVER

$$\rho \frac{\partial^2 w}{\partial t^2} = \frac{\partial \sigma_z}{\partial z} + \frac{\partial \tau_{zx}}{\partial x} + \frac{\partial \tau_{zy}}{\partial y} + F_z \quad (3.3)$$

where u , v , and w are the displacements in the x , y and z directions respectively; ρ is the density of the material; σ and τ are normal and shear stresses respectively; and F is a body force in the indicated direction.

2. The strain-displacement relationship:

$$\varepsilon_x = \frac{\partial u}{\partial x}; \quad \varepsilon_y = \frac{\partial v}{\partial y}; \quad \varepsilon_z = \frac{\partial w}{\partial z} \quad (3.4)$$

$$\gamma_{xy} = \gamma_{yx} = \frac{1}{2} \left(\frac{\partial u}{\partial y} + \frac{\partial v}{\partial x} \right)$$
$$\gamma_{xz} = \gamma_{zx} = \frac{1}{2} \left(\frac{\partial u}{\partial z} + \frac{\partial w}{\partial x} \right) \quad (3.5)$$

$$\gamma_{yz} = \gamma_{zy} = \frac{1}{2} \left(\frac{\partial v}{\partial z} + \frac{\partial w}{\partial y} \right)$$

where ε and γ are the normal and shear strains respectively.

3. The constitutive equation described by Hooke's Law which states the linear relationship between stress and strain tensors:

$$\boldsymbol{\sigma} = \mathbf{C}\boldsymbol{\epsilon} \quad (3.6)$$

Where \mathbf{C} is the elasticity tensor which maps the linear relationships between $\boldsymbol{\sigma}$ and $\boldsymbol{\epsilon}$ which are respectively the stress and strain tensors for the material. The precise nature of this linear relationship between stress and strain under Hooke's law will be expanded upon in section [3.2.4](#).

3.2.2 'Small' Deformations

Of the three fundamental assumptions for a linear elastic material, the assumptions of 'small' deformations is the most difficult to define and

3. CREATING A STRUCTURAL MECHANICS SOLVER

satisfactorily prove to be satisfied. The assumption of ‘small’ deformations is a mathematical simplification where the deformations (and corresponding strains) obtained from solving SM for a structure are taken to be so much smaller than any relevant dimension of the structure that it can be considered to not have moved spatially. However, in practice establishing what size of deformation is sufficiently ‘small’ enough to satisfy this assumption is not so straight forward, with conventions seeming to change in different disciplines as to what can be treated as an acceptable limit.

There can be no set limit on the magnitude of the deformation as the deformations only need to be ‘small’ in comparison to the size of the structure, which in some scenarios could lead to seemingly non-negligible deformations being considered acceptably ‘small’. With this in mind, in the context of this research a ‘small’ deformation has been taken to be deformations on the order of 1% or less of the longest dimension of the deforming structure.

It may be observed that this condition may potentially be hard to maintain in the framework of solidifying dendrites, as the deformations would be expected to grow in magnitude as the dendrite grows in length. If a dendrite is assumed to behave roughly analogously to a cantilever beam, as has been assumed widely both in practical experiments and numerical modelling, then it would be assumed that the deformation w would increase along with the length L following some power law $w(L^n)$, with $n > 1$. While this may imply a harsh restraint on the problems that can be examined, elements of both the modelling setup and the physical realities of alloy microstructure solidification do mitigate this constraint.

First of all, from a numerical standpoint, the quasi-stationary approach ultimately implemented (section 3.2.3) means that structural mechanics can be resolved as often as required to ensure that deformations occurring since structural mechanics was last resolved remain sufficiently small to satisfy linear

3. CREATING A STRUCTURAL MECHANICS SOLVER

elasticity.

Furthermore, from a physical perspective in many alloy solidification scenarios (see section 4.3 for more information on the solidification models being used in this research) there is in fact an intrinsic problem dependent upper limit on the length L introduced by the different melting temperatures of the elements used in the alloy [83]. The dendrites themselves form due to the morphological instabilities occurring at the solid-liquid interface, where these perturbations become amplified until the tips and depressions become the tree like dendrites. This happens due to the properties of the different elements used in the alloy (as well as the temperature conditions), where the solidifying dendrite will be primarily composed of whichever element solidifies at the higher temperature, with much of the solute being rejected into the liquid. This solute rejection then suppresses growth in the depressions comprising the inter-dendritic region as the liquid here becomes solute enriched while the tips of the dendrites are free to continue solidifying. However, once the temperature in these regions become sufficiently low, the solute enriched liquid will also solidify once the eutectic temperature is reached. A eutectic mixture is one formed by a specific composition of two or more materials which all change phase at a specific temperature, the composition and temperature where this occurs is known as the eutectic point. If the composition of the alloy does not allow this immediate transition in phase to occur for both components, you will have both solid and liquid phases existing at the same temperature (as we are seeing in our cases of dendritic solidification), however once the eutectic temperature is reached all components of the alloy will solidify, as indicated in figure 3.1. Consequently, any part of a dendritic network in a region below the eutectic temperature becomes fully solid, with a correspondingly higher Young's Modulus than the semi-solid dendrites which continue to grow in the region

3. CREATING A STRUCTURAL MECHANICS SOLVER

above this temperature. This leads to comparatively insignificant deformation occurring in this fully solid region which allows the length L to only refer to the length of the structure ahead of this phase, allowing it to become in effect a problem dependent fixed constant.

While it is certainly possible to find cases where the eutectic temperature is sufficiently low that dendrites can grow which experience deformations which would invalidate linear elastic assumptions, say for a vanishing thermal gradient, these problems will be outside of the current intended application of the model, with the expansion of the model to accurately handle larger deformations certainly being a potential avenue of future work.

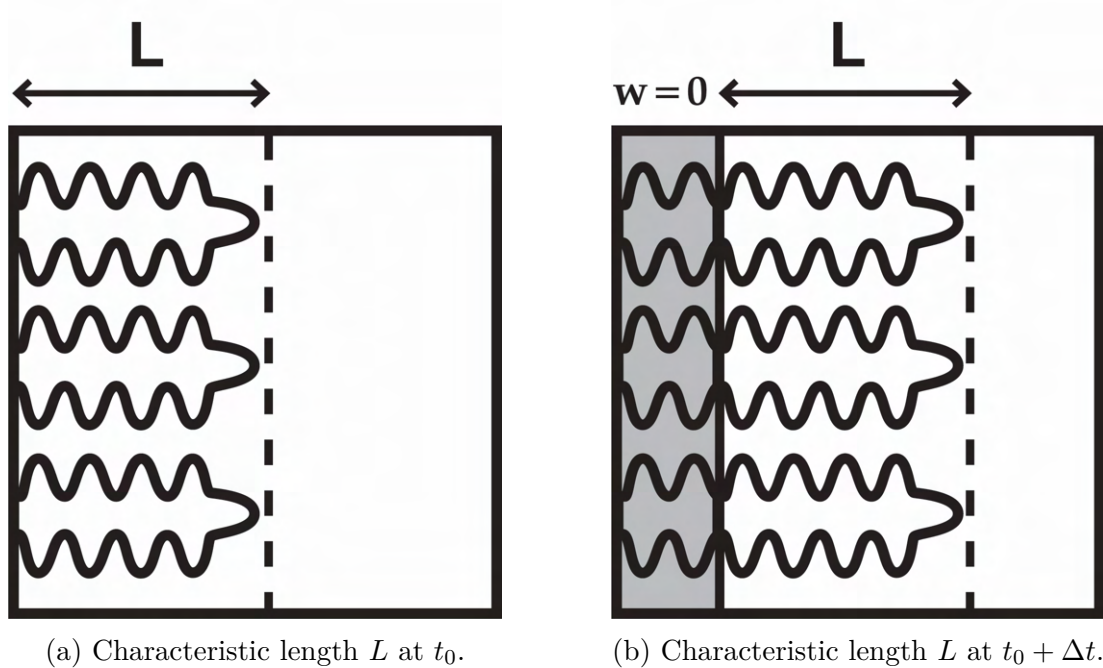


Figure 3.1: Limit on L due to eutectic formation.

3.2.3 Quasi-Stationary Approach

With microstructure solidification being an inherently transient process, there will of course be a correspondingly transient element to any observed structural

3. CREATING A STRUCTURAL MECHANICS SOLVER

mechanical behaviour. This would seemingly imply that the best way to model structural mechanics is also as the transient process described in the equilibrium equations for linear elasticity 3.1 - 3.3. However, capturing this transient behaviour while the volume of the structure continuously changes due to solidification proved to be a non-trivial matter, which led to a quasi-stationary approach being considered wherein SM would be called at successive intervals to obtain a stationary solution, being separated by a problem dependent time interval to allow a small amount of solidification to occur.

It was also considered that even if treated transiently, for the problems being examined SM would generally be converging to a stationary solution orders of magnitude faster than the time steps generally used for solidification. This would mean that any transient structural behaviour being modelled will ultimately have no impact on the solidification process and increase the computational load of the modelling while having no tangible benefit in demonstrating the structural mechanical influence on solidification.

In order to demonstrate this a test was performed on a simplified transient 2D version of the code, wherein a solidification process was mimicked by taking a small cantilever beam structure and solving it transiently until the solution has converged. After convergence, a new column of volumes is added to the end of the structure, force is applied to these volumes and the system is then solved to stationary convergence again. The typical cell size employed by the solidification code of $\Delta x = 10\mu m$ was taken, with this test running to grow a 3×20 volume structure to a 52×20 volume structure one column of volumes at a time under a constant body force.

A snapshot of these convergence times is provided in table 3.1, showing the time it has taken for structures to converge to a steady state after a new column of volumes are added to the structure.

3. CREATING A STRUCTURAL MECHANICS SOLVER

Volumes ($x \times y$)	Time to reach steady state (μs)
10 \times 20	10.04
20 \times 20	10.60
30 \times 20	12.53
40 \times 20	13.27
50 \times 20	15.06

Table 3.1: Times to reach steady state

Comparing these results against the characteristic time to solidify one cell - between 0.1s and 10s, the convergence time for the structures examined in this test are shorter by multiple orders of magnitude. This seems to support the notion that SM can be treated as a stationary process for the purposes of defining how it interacts with the solidification code, as based on these findings it will always have long converged to a steady state within a solidification time step even if treated as a transient process.

This is not necessarily a definite conclusion to the question of transient structural behaviour in this line of research, as it is certainly the case that for large plastic deformations and fracturing that there may be complex and time dependent behaviour that this approach could not account for, while accounting for yielding would require an updated formulation to correctly account for deformation which cannot be undone. However, these scenarios described are already outside of the scope of modelling under the assumptions of linear elasticity and hence represent an avenue of future research. While the test performed here is hardly a perfect analogy for true solidification, given the length of the beam is increased by adding entire new volumes rather than gradually increasing solid contents in the cells, the inaccuracies caused by this simplified approach should only serve to increase the convergence time for any structural behaviour over what would be expected from a truly solidifying structure.

3. CREATING A STRUCTURAL MECHANICS SOLVER

Considering this information, SM was treated as a stationary process to be solved at a problem dependent interval, acting as a quasi-stationary process within the framework of a coupled microstructure solidification process, where the implementation of transient structural behaviour only would add complications without benefiting the quality of the solutions obtained. The implications this choice has on the development of the SMS is that structural problems being solved are *elastostatic*, allowing the equations 3.1 - 3.3 to be simplified to the following stationary form of the linear elastic equilibrium equations:

$$\frac{\partial \sigma_x}{\partial x} + \frac{\partial \tau_{xy}}{\partial y} + \frac{\partial \tau_{xz}}{\partial z} + F_x = 0 \quad (3.7)$$

$$\frac{\partial \sigma_y}{\partial y} + \frac{\partial \tau_{yx}}{\partial x} + \frac{\partial \tau_{yz}}{\partial z} + F_y = 0 \quad (3.8)$$

$$\frac{\partial \sigma_z}{\partial z} + \frac{\partial \tau_{zx}}{\partial x} + \frac{\partial \tau_{zy}}{\partial y} + F_z = 0 \quad (3.9)$$

3.2.4 Displacement Formulation

The stationary equilibrium equations 3.7 - 3.9 describe the structural behaviour by balancing the stresses which arise in a structure experiencing external forces. However, while the internal stresses of the structure are certainly of interest when modelling microstructure solidification, when considering how structural effects will impact solidification behaviour the primary area of interest is how the shape has deformed and the crystallographic orientation has changed.

Obtaining the displacement values required from solutions showing the stresses is a relatively straightforward task, but being the primary output of interest it was considered beneficial to use the displacement formulation of linear elasticity.

3. CREATING A STRUCTURAL MECHANICS SOLVER

These equations can be obtained by first combining the full 3D linear stress-strain relationship described by Hooke's law as summarised in equation 3.6, with the strain-displacement relationship shown in equations 3.4 and 3.5.

This allows the following relationships between the stress components of the equilibrium equations and the displacements in u , v and w to be described:

$$\sigma_x = 2\mu\varepsilon_x + \lambda(\varepsilon_x + \varepsilon_y + \varepsilon_z) = 2\mu \frac{\partial u}{\partial x} + \lambda \left(\frac{\partial u}{\partial x} + \frac{\partial v}{\partial y} + \frac{\partial w}{\partial z} \right) \quad (3.10)$$

$$\sigma_y = 2\mu\varepsilon_y + \lambda(\varepsilon_x + \varepsilon_y + \varepsilon_z) = 2\mu \frac{\partial v}{\partial y} + \lambda \left(\frac{\partial u}{\partial x} + \frac{\partial v}{\partial y} + \frac{\partial w}{\partial z} \right) \quad (3.11)$$

$$\sigma_z = 2\mu\varepsilon_z + \lambda(\varepsilon_x + \varepsilon_y + \varepsilon_z) = 2\mu \frac{\partial w}{\partial z} + \lambda \left(\frac{\partial u}{\partial x} + \frac{\partial v}{\partial y} + \frac{\partial w}{\partial z} \right) \quad (3.12)$$

$$\tau_{xy} = \tau_{yx} = \mu\gamma_{xy} = \mu \left(\frac{\partial u}{\partial y} + \frac{\partial v}{\partial x} \right) \quad (3.13)$$

$$\tau_{xz} = \tau_{zx} = \mu\gamma_{xz} = \mu \left(\frac{\partial u}{\partial z} + \frac{\partial w}{\partial x} \right) \quad (3.14)$$

$$\tau_{yz} = \tau_{zy} = \mu\gamma_{yz} = \mu \left(\frac{\partial v}{\partial z} + \frac{\partial w}{\partial y} \right) \quad (3.15)$$

Where λ and μ are the two Lamé constants defined as the following combinations of the Young's Modulus (E) and Poisson's Ratio (η):

$$\lambda = \frac{\eta E}{(1 + \eta)(1 - 2\eta)} \quad (3.16)$$

$$\mu = \frac{E}{2(1 + \eta)} \quad (3.17)$$

These stress-displacement relationships can then be substituted back into the equilibrium equations 3.7, 3.8 and 3.9 and simplified (only showing the full

3. CREATING A STRUCTURAL MECHANICS SOLVER

expansion for displacement in x for brevity):

$$\begin{aligned} & \frac{\partial}{\partial x} \left(2\mu \frac{\partial u}{\partial x} + \lambda \left(\frac{\partial u}{\partial x} + \frac{\partial v}{\partial y} + \frac{\partial w}{\partial z} \right) \right) \\ & + \frac{\partial}{\partial y} \left(\mu \left(\frac{\partial u}{\partial y} + \frac{\partial v}{\partial x} \right) \right) + \frac{\partial}{\partial z} \left(\mu \left(\frac{\partial u}{\partial z} + \frac{\partial w}{\partial x} \right) \right) + F_x = 0 \end{aligned} \quad (3.18)$$

$$2\mu \frac{\partial^2 u}{\partial^2 x} + \lambda \frac{\partial^2 u}{\partial^2 x} + \lambda \frac{\partial^2 v}{\partial x \partial y} + \lambda \frac{\partial^2 w}{\partial x \partial z} + \mu \frac{\partial^2 v}{\partial x \partial y} + \mu \frac{\partial^2 u}{\partial^2 y} + \mu \frac{\partial^2 w}{\partial x \partial z} + \mu \frac{\partial^2 u}{\partial^2 z} + F_x = 0 \quad (3.19)$$

which is often collected together in the form:

$$(\lambda + \mu) \left(\frac{\partial^2 u}{\partial x^2} + \frac{\partial^2 v}{\partial x \partial y} + \frac{\partial^2 w}{\partial x \partial z} \right) + \mu \left(\frac{\partial^2 u}{\partial x^2} + \frac{\partial^2 u}{\partial y^2} + \frac{\partial^2 u}{\partial z^2} \right) + F_x = 0 \quad (3.20)$$

Using the same principles the corresponding equations for the displacements in y and z can be obtained:

$$(\lambda + \mu) \left(\frac{\partial^2 v}{\partial y^2} + \frac{\partial^2 u}{\partial y \partial x} + \frac{\partial^2 w}{\partial y \partial z} \right) + \mu \left(\frac{\partial^2 v}{\partial x^2} + \frac{\partial^2 v}{\partial y^2} + \frac{\partial^2 v}{\partial z^2} \right) + F_y = 0 \quad (3.21)$$

$$(\lambda + \mu) \left(\frac{\partial^2 w}{\partial z^2} + \frac{\partial^2 u}{\partial z \partial x} + \frac{\partial^2 v}{\partial z \partial y} \right) + \mu \left(\frac{\partial^2 w}{\partial x^2} + \frac{\partial^2 w}{\partial y^2} + \frac{\partial^2 w}{\partial z^2} \right) + F_z = 0 \quad (3.22)$$

Equations 3.20, 3.21 and 3.22 are the three Partial Differential Equations that must be simultaneously solved to find how much a linear elastic structure deforms under applied external forces.

3.3 Variable Material Properties

A dendrite, as the name suggests, often has a broadly tree like morphology where spaces exist between the secondary arms (figure 3.2a). Ensuring that these spaces are interpreted as existing by the SMS is critical to ensure the structural behaviour is accurate to a genuine dendritic system.

3. CREATING A STRUCTURAL MECHANICS SOLVER

However, for grid resolutions that would otherwise be reasonable for modelling microstructure solidification, these spaces can often be too minor to be correctly represented as having physical spaces between arms, with a region of secondary arms often being identified as a continuous region where the concentration rises and falls to match the secondary arms. If this structure was identified as a homogeneous solid, rather than the tree like structure expected, the SMS will instead consider the structure to be in effect a solid cone which will be far less susceptible to deformation (figure 3.2b).

While it would be theoretically possible to lower the grid size further, allowing these spaces to become more pronounced so that the model will truly represent the liquid filled spaces between the arms, this would increase the computational load on both solidification and structural mechanics to a degree that would make this impracticable for many problems.

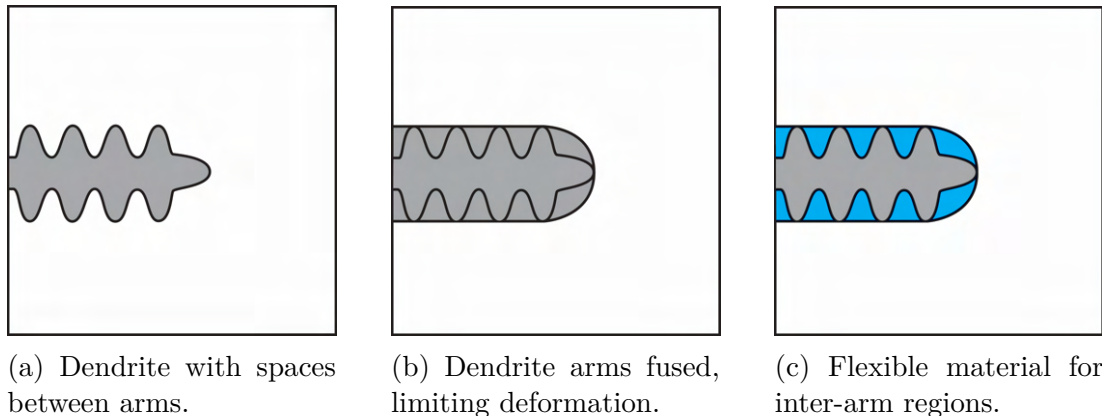


Figure 3.2: Approaches to representing a dendritic shape in the SMS.

This is further complicated by the morphology of the dendritic systems being examined, with alloys generally not being homogeneous in the manner shown in figure 3.2. Often the concentration of the alloy varies inside the dendritic structure, leading to a heterogeneous dendrite morphology more comparable to the example shown in figure 3.3, with the solid fraction gradually diminishing

3. CREATING A STRUCTURAL MECHANICS SOLVER

as it approaches the interface. These variations can also have an effect on the mechanical behaviour of the dendrite, potentially causing the tip and developing secondary arms to be more susceptible to deformation than the core of the primary arm.

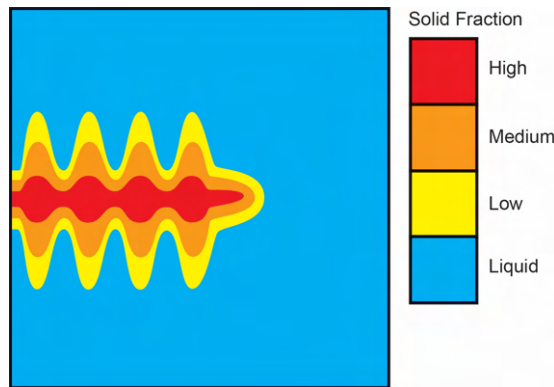


Figure 3.3: Heterogeneous dendrite.

These concerns lead to the inclusion of variable material properties for each computational cell of the structure, allowing the susceptibility to deformation to vary across the structure based on the solid fraction at that location. This allows the previously described tree like morphology to be represented even on lower grid resolutions by allowing there to be bars of much lower resistance to bending to be represented between the secondary arms, or any other region where dendrites are effectively touching due to the grid resolution (figure 3.2c). Considering the formation of the eutectic discussed in section 3.2.2, this approach could also accommodate modelling the deformation of both semi-solid and fully solidified sections regions of the dendritic network within the same problem domain.

Implementing this complicates the equilibrium equations for structural mechanics slightly, as now the Lamé Parameters themselves become variables as opposed to constants, with potentially different values at each location in the equation (only showing u for brevity):

3. CREATING A STRUCTURAL MECHANICS SOLVER

$$\begin{aligned} & \frac{\partial}{\partial x} \left(2\boldsymbol{\mu} \frac{\partial u}{\partial x} + \boldsymbol{\lambda} \left(\frac{\partial u}{\partial x} + \frac{\partial v}{\partial y} + \frac{\partial w}{\partial z} \right) \right) \\ & + \frac{\partial}{\partial y} \left(\boldsymbol{\mu} \left(\frac{\partial u}{\partial y} + \frac{\partial v}{\partial x} \right) \right) + \frac{\partial}{\partial z} \left(\boldsymbol{\mu} \left(\frac{\partial u}{\partial z} + \frac{\partial w}{\partial x} \right) \right) + F_x = 0 \end{aligned} \quad (3.23)$$

As such the material property information cannot be taken outside of the differential terms and collected together to form the elegant equilibrium equations 3.20, 3.21 and 3.22, as the material properties must be accounted for as a spatial variable requiring differencing along with the displacements during the discretisation process. This leaves the following set of equilibrium equations for a linear elastic material with variable material properties:

$$\begin{aligned} & 2 \frac{\partial}{\partial x} \boldsymbol{\mu} \frac{\partial u}{\partial x} + \frac{\partial}{\partial x} \boldsymbol{\lambda} \frac{\partial u}{\partial x} + \frac{\partial}{\partial y} \boldsymbol{\mu} \frac{\partial u}{\partial y} + \frac{\partial}{\partial z} \boldsymbol{\mu} \frac{\partial u}{\partial z} \\ & + \frac{\partial}{\partial x} \boldsymbol{\lambda} \frac{\partial v}{\partial y} + \frac{\partial}{\partial y} \boldsymbol{\mu} \frac{\partial v}{\partial x} + \frac{\partial}{\partial x} \boldsymbol{\lambda} \frac{\partial w}{\partial z} + \frac{\partial}{\partial z} \boldsymbol{\mu} \frac{\partial w}{\partial x} + F_x = 0 \end{aligned} \quad (3.24)$$

$$\begin{aligned} & 2 \frac{\partial}{\partial y} \boldsymbol{\mu} \frac{\partial v}{\partial y} + \frac{\partial}{\partial y} \boldsymbol{\lambda} \frac{\partial v}{\partial y} + \frac{\partial}{\partial x} \boldsymbol{\mu} \frac{\partial v}{\partial x} + \frac{\partial}{\partial z} \boldsymbol{\mu} \frac{\partial v}{\partial z} \\ & + \frac{\partial}{\partial y} \boldsymbol{\lambda} \frac{\partial u}{\partial x} + \frac{\partial}{\partial x} \boldsymbol{\mu} \frac{\partial u}{\partial y} + \frac{\partial}{\partial y} \boldsymbol{\lambda} \frac{\partial w}{\partial z} + \frac{\partial}{\partial z} \boldsymbol{\mu} \frac{\partial w}{\partial y} + F_y = 0 \end{aligned} \quad (3.25)$$

$$\begin{aligned} & 2 \frac{\partial}{\partial z} \boldsymbol{\mu} \frac{\partial w}{\partial z} + \frac{\partial}{\partial z} \boldsymbol{\lambda} \frac{\partial w}{\partial z} + \frac{\partial}{\partial x} \boldsymbol{\mu} \frac{\partial w}{\partial x} + \frac{\partial}{\partial y} \boldsymbol{\mu} \frac{\partial w}{\partial y} \\ & + \frac{\partial}{\partial z} \boldsymbol{\lambda} \frac{\partial u}{\partial x} + \frac{\partial}{\partial x} \boldsymbol{\mu} \frac{\partial u}{\partial z} + \frac{\partial}{\partial z} \boldsymbol{\lambda} \frac{\partial v}{\partial y} + \frac{\partial}{\partial y} \boldsymbol{\mu} \frac{\partial v}{\partial z} + F_z = 0 \end{aligned} \quad (3.26)$$

3.4 Staggered Grid Finite Volume Method (SGFVM)

As discussed in 2.4, a FVM framework was chosen as it provides intrinsic benefits when trying to couple structural mechanics with a solidification process, which was then further expanded into a SGFVM approach [84] where the material properties are stored in the centre of the volumes but displacement/velocity values

3. CREATING A STRUCTURAL MECHANICS SOLVER

are stored at the cell faces.

This approach is quite unusual within the under-explored field of using the FVM for structural mechanics, however SGFVM have been successfully applied to structural mechanics problems in the past [85]. While it is relatively straightforward to interpolate values from the cell centres to cell faces or visa versa, this staggered formation does simplify matters as the values are now generally at the most useful spatial location.

An example of how these staggered displacements would be found on the structure can be seen in figure 3.4a, with a slice through the 3D structure in figure 3.4b showing the location where the cell centred material properties are stored.

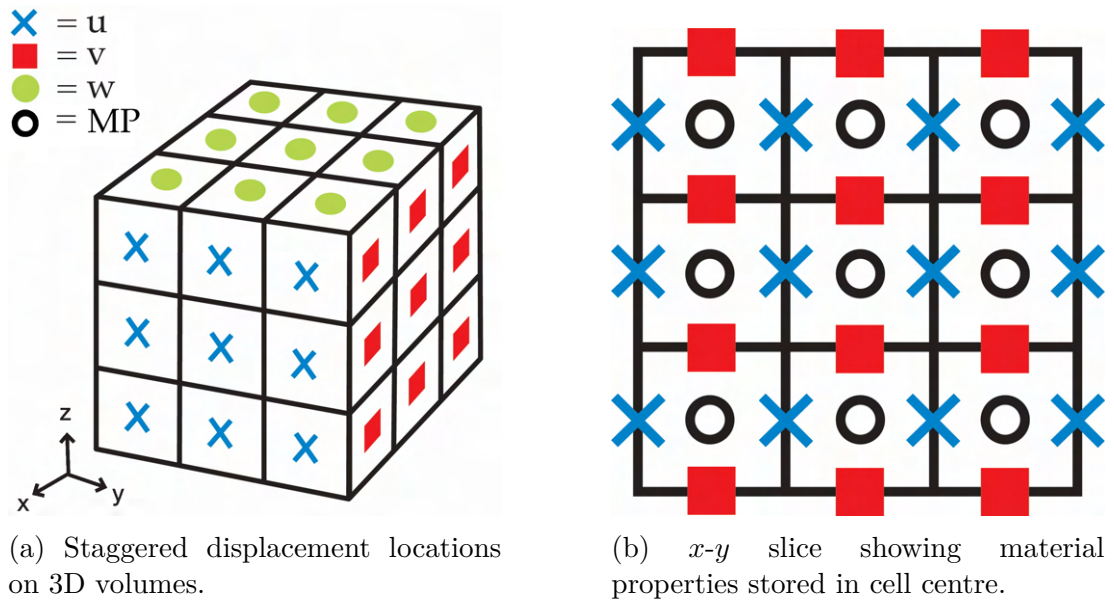


Figure 3.4: Finite volumes using staggered displacements.

For the purposes of developing the SMS, this means that there are three 3D grids of displacements, each staggered in their respective dimensions so they have the correct number of points to line up with the faces of the volumes comprising the domain. In figure 3.5 a slice has been taken through the structure showing

3. CREATING A STRUCTURAL MECHANICS SOLVER

the x - y axis demonstrating the relationship between the u and v displacement grids. It has been simplified into 2D for ease of visual clarity, though in reality there is a third grid of the w displacements going into and out of the page from this slice.

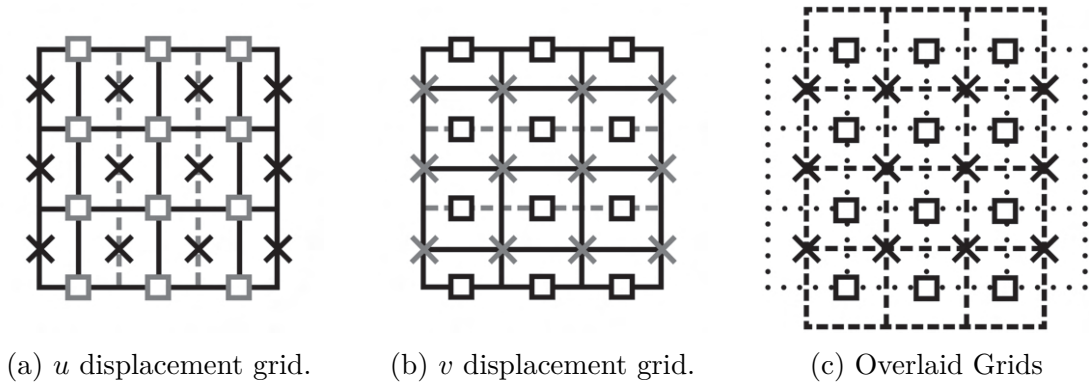


Figure 3.5: Relationship between staggered u and v grids.

Considering the three overlaid displacement grids and the equilibrium equations 3.24 - 3.26, the cross terms relating these three grids together can be observed in each equation, meaning that for a three-dimensional linear elasticity problem these three staggered grids must all be solved simultaneously, as changes on one grid will effect the solution on the the other two.

This SGFVM approach was used to obtain an iterative numerical scheme to calculate the displacements corresponding to the stationary solution of a linear elastic structure experiencing external forces. The full discretisation approach used to obtain this method can be found in Appendix A, arriving at the following set of equations:

3. CREATING A STRUCTURAL MECHANICS SOLVER

$$\begin{aligned}
 u_p &= \frac{1}{-A_P}(A_N u_n + A_S u_s + A_E u_e + A_W u_w + A_H u_h + A_L u_l + S_x) \\
 A_P &= 8\mu_p + 2\lambda_p; \quad A_E = 2\mu_E + \lambda_E; \quad A_W = 2\mu_W + \lambda_W \\
 A_N &= \mu_N; \quad A_S = \mu_S; \quad A_H = \mu_H; \quad A_L = \mu_L \\
 S_x &= \mu_N(v_{ne} - v_{nw}) - \mu_S(v_{se} - v_{sw}) + \mu_H(w_{he} - w_{hw}) - \mu_L(w_{le} - w_{lw}) + \\
 &\quad \lambda_E(v_{ne} - v_{se} + w_{he} - w_{le}) + \lambda_W(v_{nw} - v_{sw} + w_{hw} - w_{lw}) + \Delta x^2 F_x
 \end{aligned} \tag{3.27}$$

$$\begin{aligned}
 v_p &= \frac{1}{-A_P}(A_N v_n + A_S v_s + A_E v_e + A_W v_w + A_H v_h + A_L v_l + S_y) \\
 A_P &= 8\mu_p + 2\lambda_p; \quad A_N = 2\mu_N + \lambda_N; \quad A_S = 2\mu_S + \lambda_S \\
 A_E &= \mu_E; \quad A_W = \mu_W; \quad A_H = \mu_H; \quad A_L = \mu_L \\
 S_y &= \mu_E(v_{en} - v_{es}) - \mu_W(v_{wn} - v_{ws}) + \mu_H(w_{hn} - w_{hs}) - \mu_L(w_{ln} - w_{ls}) + \\
 &\quad \lambda_N(v_{en} - v_{wn} + w_{hn} - w_{ln}) + \lambda_S(v_{es} - v_{ws} + w_{hs} - w_{ls}) + \Delta x^2 F_y
 \end{aligned} \tag{3.28}$$

$$\begin{aligned}
 w_p &= \frac{1}{-A_P}(A_N w_n + A_S w_s + A_E w_e + A_W w_w + A_H w_h + A_L w_l + S_z) \\
 A_P &= 8\mu_p + 2\lambda_p; \quad A_H = 2\mu_H + \lambda_H; \quad A_L = 2\mu_L + \lambda_L \\
 A_E &= \mu_E; \quad A_W = \mu_W; \quad A_N = \mu_N; \quad A_S = \mu_S \\
 S_z &= \mu_E(v_{eh} - v_{el}) - \mu_W(v_{wh} - v_{wl}) + \mu_N(w_{nh} - w_{nl}) - \mu_S(w_{sh} - w_{sl}) + \\
 &\quad \lambda_H(v_{eh} - v_{wh} + w_{nh} - w_{sh}) + \lambda_L(v_{el} - v_{wl} + w_{nl} - w_{sl}) + \Delta x^2 F_w
 \end{aligned} \tag{3.29}$$

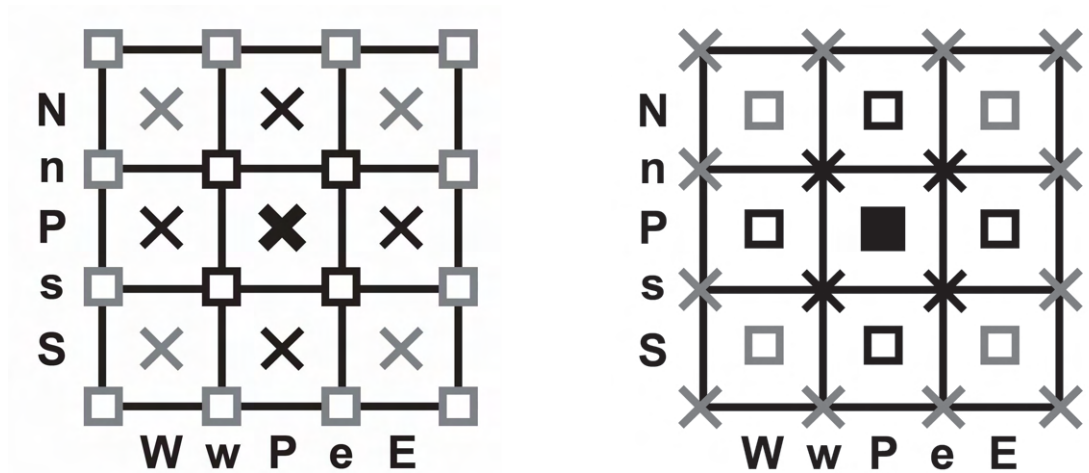
These equations define the displacement at a generic point P on their corresponding staggered grids, with the spatial references e, w, n, s, h, l representing a half grid step in the East, West, North, South, High and Low directions relative to that point P respectively, with the capitalised references E, W, N, S, H, L indicating an entire grid step in the corresponding direction.

For clarity in the scheme, the source term S has been separated from the

3. CREATING A STRUCTURAL MECHANICS SOLVER

main scheme, indicating the influence of the displacements from the other grids brought in by the cross terms and body forces on the differencing scheme. It must also be stressed that due to the nature of the staggered grids, the point P and corresponding directions being referenced for each displacement equations are relative to a generic internal point within their corresponding staggered grid and does **not** represent the same point within the structure. It is in fact impossible for the u , v and w displacements to ever occupy the same spatial locations due to the way in which the grids overlap.

The annotated grids in figure 3.6 should further highlight this relationship and the relative spatial labelling being used in the differencing scheme, highlighting the surrounding displacements which are used to obtain the new value at point P (again only in 2D slices for visual clarity, so w displacements and any volumes in the High and Low directions have been neglected).



(a) Information required to obtain u_P .

(b) Information required to obtain v_P .

Figure 3.6: Annotated u and v grids.

3.5 Stress & Strain Outputs

While the SMS obtains the solution in the form of the displacements due to these being considered the most relevant output to interact with the solidification process, that does not mean that the stress and strain within the structure are of no interest. The concurrent modelling of structural mechanics alongside solidification provides an opportunity to observe where stresses accumulate within a solidifying structure in real time in a novel manner impossible in most modelling frameworks.

At the current stage the stresses and strains are essentially post processed quantities extracted from the displacements to allow observation of how stress accumulates over time, potentially suggesting mechanisms for the build up and locations where fractures may occur. These stresses do not currently have any direct bearing on the development of the solidification process, this being a potential expansion for future work considering the suggestions that stress accumulation can lead to remelting and fragmentation even if no observable deformation has occurred [34, 43].

The elements of the strain at the point P in the cell centre can be easily obtained by taking the strain relationship equations for the normal (equation 3.4) and shear (equation 3.5) strains, discretising them and substituting in the obtained displacement values:

$$\begin{aligned}
 \varepsilon_x(P) &= \frac{u_e - u_w}{\Delta x}; \quad \varepsilon_y(P) = \frac{v_n - v_s}{\Delta x}; \quad \varepsilon_z(P) = \frac{w_h - w_l}{\Delta x} \\
 \gamma_{xy}(P) = \gamma_{yx}(P) &= \frac{1}{2\Delta x} (u_n - u_s + v_e - v_w) \\
 \gamma_{xz}(P) = \gamma_{zx}(P) &= \frac{1}{2\Delta x} (u_h - u_l + w_e - w_w) \\
 \gamma_{yz}(P) = \gamma_{zy}(P) &= \frac{1}{2\Delta x} (v_h - v_l + w_n - w_s)
 \end{aligned} \tag{3.30}$$

These can then be substituted into the stress-strain relationship equations for

3. CREATING A STRUCTURAL MECHANICS SOLVER

linear elasticity in equations 3.10 - 3.15 to obtain the normal and shear stress components of the structure at each point. However, it can often be useful to have this stress information summarised in a single output which can provide a clearer idea of which regions of the structure experience high levels of stress of any kind without having to simultaneously compare all the normal and shear stress outputs.

For this reason, the quantity which will usually be used to demonstrate the stress within the structure will be the Von Mises Stress [86], which describes the yield strength of a material by combining the previously defined stress terms using the following formula:

$$\sigma_{VM} = \sqrt{\frac{1}{2} [(\sigma_x - \sigma_y)^2 + (\sigma_y - \sigma_z)^2 + (\sigma_z - \sigma_x)^2] + 3(\tau_{xy}^2 + \tau_{yz}^2 + \tau_{xz}^2)} \quad (3.31)$$

3.6 Boundary Conditions

There are a wide collection of potential boundary conditions which must be considered by the SMS to allow it to function for the largest selection of modelling scenarios as possible. The boundary conditions described in the following subsections may be applied to either the edges of the structure within the domain, the boundaries of the modelling domain itself or in some cases both.

3.6.1 Fixed Displacements

Fixed displacements are Dirichlet boundary conditions that can be applied at both the domain boundary or the surface of a structure within the domain. This means that any given nodes with a fixed displacement defined will maintain this

3. CREATING A STRUCTURAL MECHANICS SOLVER

value no matter what else happens to the structure in the solver. The way that this is generally applied in the problems being examined is to represent structures connected to a surface using a fixed condition of $u = v = w = 0$ at the domain boundaries, so that any parts of the structure coming into contact with this boundary become fixed at that location (see boundary 2 in figure 3.7).

However, while not used for any of the realistic modelling scenarios currently being examined, functionality for varying Dirichlet conditions along the domain boundaries or the surface of the internal structure was implemented in the event it would later be required. For example, if a fixed displacement was identified from some other physical process these can be defined across the surface of the structure, with potential to all be the same or vary as required by the problem (see boundary 1 in figure 3.7).

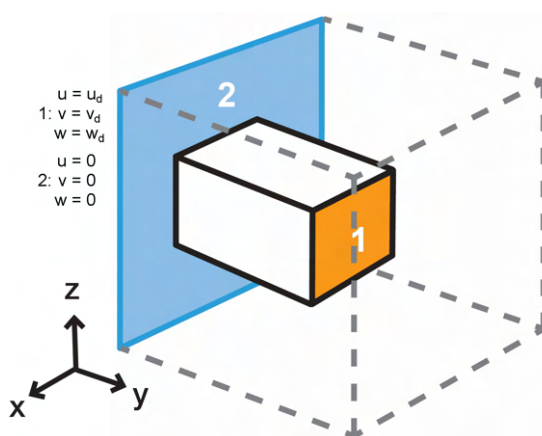


Figure 3.7: Fixed displacement boundaries.

3.6.2 Fixed Stress & Free Surfaces

Fixed stress surfaces (and the subset of ‘free’ surfaces) are a Neumann boundary condition which can be applied on both the domain boundaries and the internal faces of the structure to represent the force (or lack of force) acting at that location. What this means for the equations governing the structural behaviour

3. CREATING A STRUCTURAL MECHANICS SOLVER

is that the normal and shear stresses are a fixed value S .

Using the stress-strain relations from Hooke's Law and the strain-displacement relationship, these boundaries can be converted into the displacement formulation being used elsewhere in the SMS. At each boundary there is one normal and two shear stress conditions that must be satisfied on the three displacement grids, being positive or negative depending on which side of the structure (relative to the direction of the axis) the boundary is on.

How these fixed stress boundaries vary can be observed in figure 3.8a, which will be expanded into a deformation formulation to interact with the rest of the solver, which for brevity will only be replicated below for the boundary at face 1, but the same process would be applied at all faces:

$$F_x = \sigma_x = 2\mu\varepsilon_x + \lambda(\varepsilon_x + \varepsilon_y + \varepsilon_z) = 2\mu\frac{\partial u}{\partial x} + \lambda\left(\frac{\partial u}{\partial x} + \frac{\partial v}{\partial y} + \frac{\partial w}{\partial z}\right) = S_x \quad (3.32)$$

$$F_y = \tau_{xy} = \mu\gamma_{xy} = \mu\left(\frac{\partial u}{\partial y} + \frac{\partial v}{\partial x}\right) = S_y \quad (3.33)$$

$$F_z = \tau_{xz} = \mu\gamma_{xz} = \mu\left(\frac{\partial u}{\partial z} + \frac{\partial w}{\partial x}\right) = S_z \quad (3.34)$$

The forces acting on the faces can vary, so there is no need for different faces to have the same fixed stress defined, and there does not have to be any relationship between the defined normal and shear stresses acting upon a face. The behaviour at these boundaries have been implemented such that all stress elements for a boundary can vary spatially, a crucial requirement for the implementation of surface forces created by other physics, such as a varying pressure field being imparted on the face of a structure by fluid flow.

However, while it is important for the SMS to be able to interpret surface forces acting upon a structures, in practice the setup of this boundary most often

3. CREATING A STRUCTURAL MECHANICS SOLVER

used is $S_x = S_y = S_z = 0$, making this a ‘free’ surface which allows the structure to move unimpeded, only being limited by the elastic behaviour balancing the displacements in u , v and w .

Having these conditions act on the domain boundaries is also computationally useful, as while it may be desirable for a boundary to restrict any further solidification growth, using a ‘free’ surface would allow the domain boundary to impart no physical limitation on the structural movement.

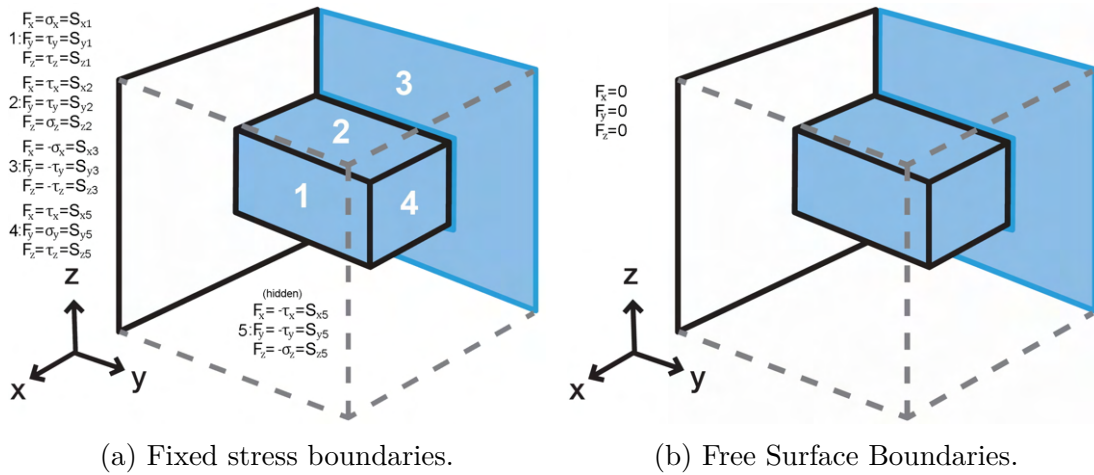


Figure 3.8: Types of Neumann boundary.

3.6.3 Slip Domain Boundary

The slip boundary condition is a combination of fixed displacements and fixed strains with different rules for the different displacement grids. While generally making the most sense to be applied at domain boundaries, it could theoretically be applied at an internal structure boundary also. The combination of these conditions can be useful for mimicking the behaviour at a wall more accurately, as can be seen in figure 3.9.

If a structure touches a wall, it makes sense that movement into the wall will be prevented (so in this case a fixed displacement $u = 0$), but setting the entire

3. CREATING A STRUCTURAL MECHANICS SOLVER

domain boundary to be fixed in all displacements does not make much physical sense, as the structure would immediately fuse with the wall and stop moving once there is a point of contact. By also including free surfaces for displacements in directions parallel on the Cartesian grid to the boundary ($S_y = S_z = 0$ for this example), this allows the structure to continue to move freely in ways that do cause further interaction with the wall.

While clearly not an ideal physical representation of interaction with a wall at the boundary due to it limiting perpendicular movement away from the wall along with lacking any friction to limit parallel movement (though if a sensible value for this could be found and represented as a fixed strain, this could potentially be added rather than the ‘free’ surface indicated in this example). Nevertheless, slip boundaries can allow for more sensible behaviour at the domain boundaries than a surface which is either entirely fixed displacements or fixed stresses for many modelling scenarios.

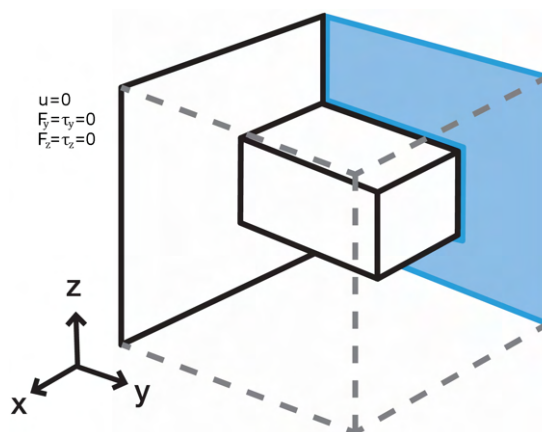


Figure 3.9: Slip boundary.

3.6.4 Symmetry Domain Boundary

The symmetry condition is a purely domain boundary, which represents a mirroring of the structure and behaviour across the defined symmetry

3. CREATING A STRUCTURAL MECHANICS SOLVER

boundary. In practice for the SMS this simply means that the values within this boundary are identical to their neighbouring cells within the domain.

This boundary can be computationally useful as it allows larger cases to be modelled where only a subsection of the domain needs modelling, with the symmetry condition making the results on the other side of the boundary a reflection of any calculated values.

Unfortunately, the kind of structural phenomena being examined in the later modelling cases often makes symmetry in the solutions unreasonable to assume at any given boundary, however it is certainly a useful tool to have access to for situations where it can be justifiably used.

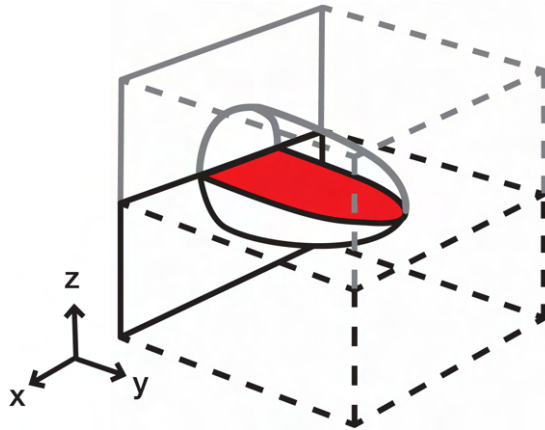


Figure 3.10: Symmetry domain boundary.

3.6.5 Periodic Domain Boundary

The periodic boundary condition is a purely domain boundary where two domain faces are linked such that they are considered to be physically next to one another, allowing continuous movement between the linked boundaries. The example of this concept shown in figure 3.11 has taken the High and Low boundaries to be periodic, but problems could be set up where East-West or North-South are the paired periodic domains.

3. CREATING A STRUCTURAL MECHANICS SOLVER

Within a solidification context, these boundaries can be a useful tool in simulating a slice taken of a continuous solidifying system, where the region being simulated can be considered as being so far from any fixed boundaries that the solidification behaviour acts continuously, meaning that only this small slice requires modelling. This domain boundary was relatively easy to incorporate within the SMS, with displacements within the domain boundaries needing to correspond with the first layer of information in from the domain at the paired boundary, allowing the solution to develop across the boundary as a continuous structure.

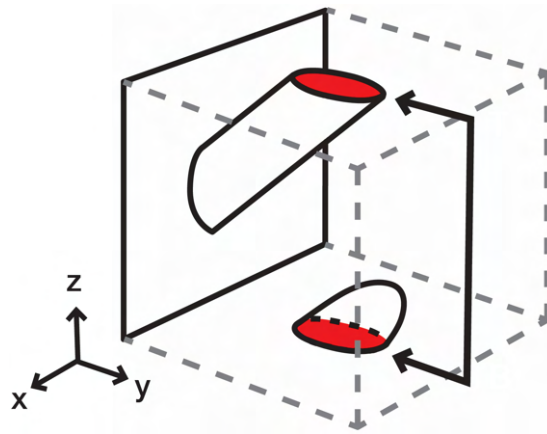


Figure 3.11: Periodic domain boundary.

3.7 Thermal Effects

As identified in section 2.2 of the literature review, many experimental observations of deformation and misorientation of dendrites were attributed to strain caused by thermal expansion. This is of course problem-dependent as many scenarios exist which can be effectively treated as temperature independent, where any impact from thermal expansion is insignificant. However, given the number of experimental cases attributing deformation to

3. CREATING A STRUCTURAL MECHANICS SOLVER

thermal effects the incorporation of thermal effects into the SMS was an obvious expansion which would expand the modelling scenarios that could be accurately represented.

To incorporate thermal strains in the SMS, the strain-displacement relationship for the normal strains (the shear strains remain unchanged) has to be expanded to account for these non-elastic thermal strains:

$$\varepsilon = \varepsilon_e + \varepsilon_{th} \quad (3.35)$$

Where the thermal strains change the relationship to the following:

$$\varepsilon_x = \frac{\partial u}{\partial x} - \alpha\Delta T; \quad \varepsilon_y = \frac{\partial v}{\partial y} - \alpha\Delta T; \quad \varepsilon_z = \frac{\partial w}{\partial z} - \alpha\Delta T \quad (3.36)$$

Where α is the coefficient of thermal expansion for the material and ΔT is the change in temperature at the current time compared to the reference temperature defined for the assumed to be isotropic material.

This update to the strains correspondingly changes the displacement form of the normal stresses after these new values have been substituted in (this will be considering σ_x and the u displacement equation only going forward for brevity, but the same process has to be taken to update the v and w equations):

$$\begin{aligned} \sigma_x &= 2\mu\varepsilon_x + \lambda(\varepsilon_x + \varepsilon_y + \varepsilon_z) \\ &= 2\mu\left(\frac{\partial u}{\partial x} - \alpha\Delta T\right) + \lambda\left(\left(\frac{\partial u}{\partial x} - \alpha\Delta T\right) + \left(\frac{\partial v}{\partial y} - \alpha\Delta T\right) + \left(\frac{\partial w}{\partial z} - \alpha\Delta T\right)\right) \\ &= 2\mu\frac{\partial u}{\partial x} + \lambda\left(\frac{\partial u}{\partial x} + \frac{\partial v}{\partial y} + \frac{\partial w}{\partial z}\right) - (2\mu + 3\lambda)\alpha\Delta T \\ &= 2\mu\frac{\partial u}{\partial x} + \lambda\left(\frac{\partial u}{\partial x} + \frac{\partial v}{\partial y} + \frac{\partial w}{\partial z}\right) - \Gamma\alpha\Delta T \end{aligned} \quad (3.37)$$

3. CREATING A STRUCTURAL MECHANICS SOLVER

Where Γ is being defined as the thermal modulus, which can be simplified in terms of E and η to become:

$$\Gamma = 2\mu + 3\lambda = 2\left(\frac{E}{2(1 + \eta)}\right) + 3\left(\frac{\eta E}{(1 + \eta)(1 - 2\eta)}\right) = \frac{E}{(1 - 2\eta)} \quad (3.38)$$

Incorporating this additional thermal term in the numerical scheme by using the updated definitions of σ_x , σ_y and σ_z into the stationary equilibrium equations 3.7 - 3.9 does not in fact change the numerical scheme a great deal, with the only change to the FVM equations 3.27 - 3.29 being the incorporation of the thermal term into the source term (where S_e is the existing elastic source term defined in the equations which include the cross terms and body force):

$$\begin{aligned} S_x &= S_{xe} + S_{xt} = S_{xe} - \Delta x^2 \frac{\partial}{\partial x} \Gamma \alpha \Delta T \\ S_y &= S_{ye} + S_{yt} = S_{ye} - \Delta x^2 \frac{\partial}{\partial y} \Gamma \alpha \Delta T \\ S_z &= S_{ze} + S_{zt} = S_{ze} - \Delta x^2 \frac{\partial}{\partial z} \Gamma \alpha \Delta T \end{aligned} \quad (3.39)$$

That the thermal behaviour can be incorporated in the source term in this manner serves to make it quite straightforward to activate or deactivate thermal strains as required on a problem by problem basis.

3.8 Structure Identification

One crucial concern for the development of the SMS was deciding how the solidifying dendrites would be identified and interpreted as structures by the solver. While initial tests of the solver simply took the entire domain as the structure, with the domain boundaries simultaneously acting as a boundary for the structure, this would clearly be insufficient for the microstructure solidification problems the solver was being created to interface with.

3. CREATING A STRUCTURAL MECHANICS SOLVER

The solidification methods being used in this research generate a solid fraction profile, where each computational cell has a value between 0 and 1 to indicate the proportion of each cell now comprised of solid material. Using this as an input, an edge detection algorithm was written which performs a sweep through the domain identifying which cells are solid (or solidifying), liquid or at a boundary based on the state of the cells surrounding it.

The most obvious way of defining the problem would be as a collection of volumes matching the solid cells identified in the solid fraction profile, so that the problem domain being solved by the SMS would simply be any individual dendrite structures as can be seen in figure 3.12a, however implementing this presents some problems. The SMS requires at least one cell separating any opposing boundaries (e.g. East-West, North-South, High-Low) on the growing structure, but when simulating solidification of a dendrite it is likely that parts of a dendrite may reach a thickness of a single cell at some points, especially at the tips of the dendrite arms. This means that to account for this for a closely fitted domain, parts of the structure would either have to be ignored or fictitious cells added to satisfy these modelling constraints.

However, the implementation of a variable material property framework previously discussed in 3.3 allows a more flexible approach to the question of structural identification to be taken. Now the liquid in the domain can also be solved by the SMS by treating it as a ‘solid’ with a nominal Young’s Modulus value many orders of magnitude below that used by the true solid structure so that the liquid offers no measurable resistance to the movement of the structure.

While unconventional, this approach is not unique, with Uehara, Fukui and Ohno [62] taking a similar approach within a FEM framework, where the entire domain was solved throughout the solidification process, changing the material properties at the computational nodes from a ‘liquid’ (also represented as a

3. CREATING A STRUCTURAL MECHANICS SOLVER

solid with a very low Young's Modulus) to those of a solidifying metal as the solidification progressed. The entire domain could also be solved in this manner using the SMS, as indicated in the example in figure 3.12b where the blue region is to solved as 'liquid'.

While this means that no concessions have to be made to accurately model the dendrite, an obvious problem arises when the structure is very small relative to the domain as the propagation and convergence of the deformation into the entire 'liquid' region has potential to greatly increase the solution time. While the deformations in the 'liquid' region may be of use as flow fields when coupled to other physical processes, if only modelling structural mechanics and solidification the solution in the liquid will be unused and hence adds to the computational load without improving the solution.

Consequently, a middle ground between solving a closely fitted structure and solving the entire domain was desirable. This was first done by generating a box around any structures to be solved, as indicated in figure 3.12c, so that in theory only a relatively small region of 'liquid' would be solved around the structure. However, as the box is drawn based on the furthest identified solid material in any direction, there are potential ways a microstructure may develop which could end up capturing needlessly large 'liquid' regions. In particular, if there are multiple dendrites at opposite ends of the samples a box drawing approach such as this can lead to almost the entire domain being solved from the start, as in figure 3.12d.

For this reason, a locus method was implemented to define an acceptable 'liquid' region to be solved, where by counting outwards from the solid material a region analogous to a larger and smoother version of the dendrite morphology would be captured and defined as the 'liquid' region of the structure needing to be solved, as indicated in figure 3.12c.

3. CREATING A STRUCTURAL MECHANICS SOLVER

It is true that this locus structure will have more complex boundary conditions than a simple box, so in cases where the box and locus region encompasses a comparable amount of ‘liquid’, it may be possible that the solution using a box will converge slightly faster. However, even in this unusual scenario the locus boundaries would be continuous enough that the solution will be obtained at a comparable speed, while being significantly faster than the box drawing approach in situations where the box would capture large regions of ‘liquid’.

3. CREATING A STRUCTURAL MECHANICS SOLVER

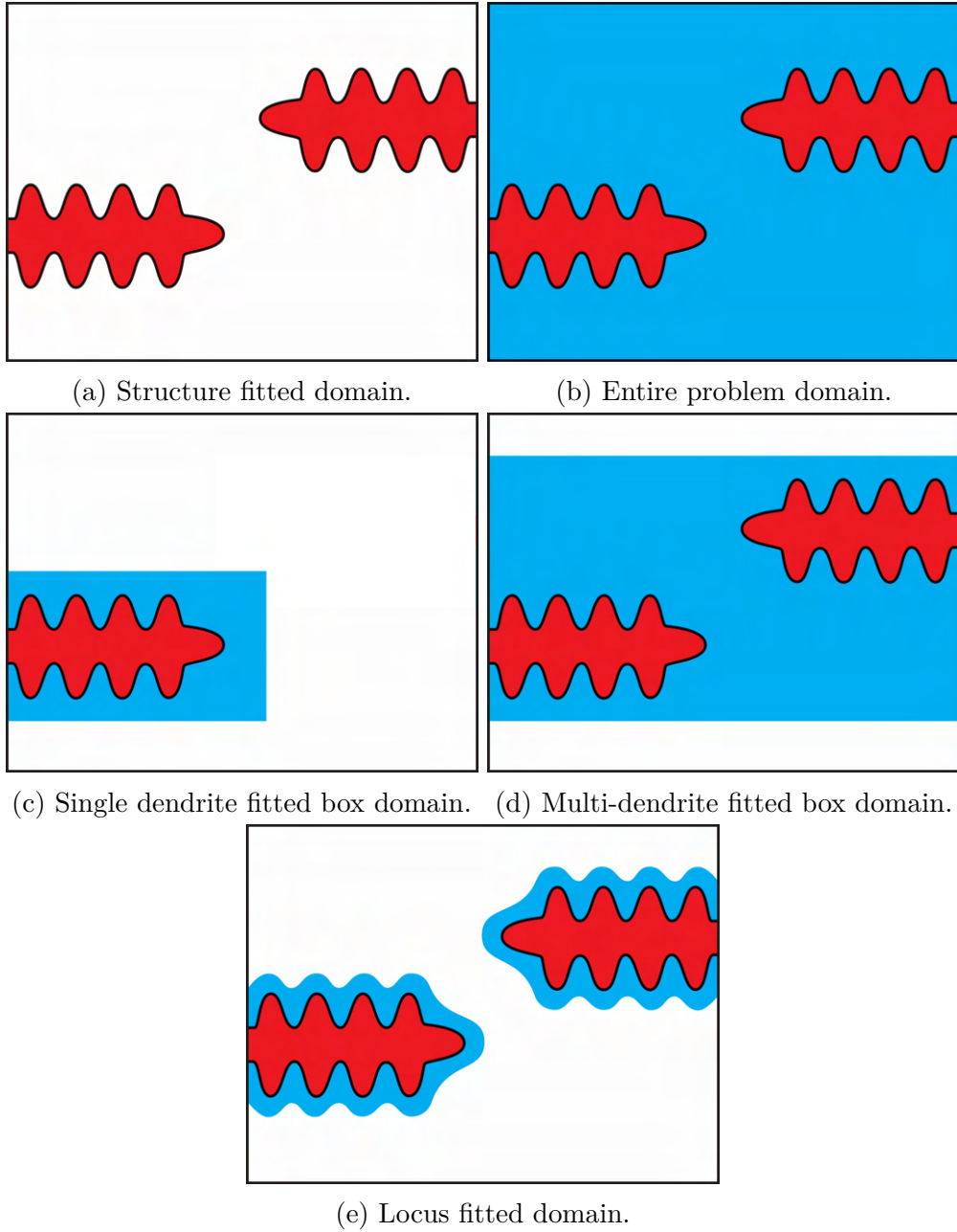


Figure 3.12: Domain identification for SMS.

3.9 Algorithm Overview

This section includes some brief points regarding how the SGFVM outlined in section 3.4 was implemented as an numerical algorithm which converges to find the steady state displacement solution of a three-dimensional structure experiencing external forces.

3.9.1 Stopping Criteria

The first stopping criterion implemented was based on the largest normalised change in displacements between successive time steps being less than a given tolerance (tol). This value is chosen prior to the code being run, but is generally taken as a small number close to the machine precision of the data type of the displacement variables being used to prevent under-converged solutions. Where U , V and W are the matrices containing the displacements in x , y and z directions the stopping criteria for the algorithm at step t are defined as follows:

$$\frac{\|U_t - U_{t-1}\|}{\|U_t\|} < tol \ \& \ \frac{\|V_t - V_{t-1}\|}{\|V_t\|} < tol \ \& \ \frac{\|W_t - W_{t-1}\|}{\|W_t\|} < tol \quad (3.40)$$

where $\|\cdot\|$ is a maximum norm

$$\|A\| = \max_{i,j,k} \{|a_{1,1,1}|, \dots, |a_{n,n,n}|\}$$

However, while usually sufficient, implementing this stopping criteria on very large cases showed that as the rate of change in displacements became very small this method would sometimes register solutions as being converged too soon, no matter how small the tolerance value used as the relative change was identified as being smaller than machine precision, though if allowed to continue these changes could accumulate to a displacement profile with significantly larger values. This

3. CREATING A STRUCTURAL MECHANICS SOLVER

led to residual based convergence criteria being implemented, which checks to see how close the solution at the current time is to balancing the forces acting on the structure, which can be summarised as follows:

$$Res_u < tol \ \& \ Res_v < tol \ \& \ Res_w < tol \quad (3.41)$$

where, for iteration t

$$\begin{aligned} Res_u &= A_N u_n^t + A_S u_s^t + A_E u_e^t + A_W u_w^t + A_H u_h^t + A_L u_l^t + S_x^t - A_P u_p^{t-1} \\ Res_v &= A_N v_n^t + A_S v_s^t + A_E v_e^t + A_W v_w^t + A_H v_h^t + A_L v_l^t + S_y^t - A_P v_p^{t-1} \\ Res_w &= A_N w_n^t + A_S w_s^t + A_E w_e^t + A_W w_w^t + A_H w_h^t + A_L w_l^t + S_z^t - A_P w_p^{t-1} \end{aligned} \quad (3.42)$$

3.9.2 Numerical Scheme

This scheme is currently being solved as a Gauss-Seidel method utilising a Successive Over Relaxation (SOR) approach, which solves point by point to calculate the displacement profiles using the relaxation parameter ω which can be raised or lowered to increase convergence speed or stability as required. While they can be identical, each displacement grid in fact has it's own ω variable, allowing them to vary between the grids if required to reach a solution.

Furthermore a basic framework for ω has been implemented to allow the relaxation parameter for each grid to increase or decrease (within set limits) based on the evolution of the stopping criteria. Due to the nature of the problem requiring all grids to be solved simultaneously, each overall step taken by the model requires a separate iteration to update the entire u , v or w grid, with the most recently calculated values for any displacements between the three grids always being used to calculate the current point, as dictated by the Gauss Seidel method. The incorporation of the relaxation term updates the numerical scheme

3. CREATING A STRUCTURAL MECHANICS SOLVER

as follows:

$$\begin{aligned}
 u_p^i &= (1 - \omega)u_p^{i-1} + \frac{\omega}{A_P}(A_N u_n^{i-1} + A_S u_s^{i-1} + A_E u_e^{i-1} + A_W u_w^{i-1} + A_H u_h^{i-1} + A_L u_l^{i-1} + S_x^{i-1}) \\
 v_p^i &= (1 - \omega)v_p^{i-1} + \frac{\omega}{A_P}(A_N v_n^{i-1} + A_S v_s^{i-1} + A_E v_e^{i-1} + A_W v_w^{i-1} + A_H v_h^{i-1} + A_L v_l^{i-1} + S_y^{i-1}) \\
 w_p^i &= (1 - \omega)w_p^{i-1} + \frac{\omega}{A_P}(A_N w_n^{i-1} + A_S w_s^{i-1} + A_E w_e^{i-1} + A_W w_w^{i-1} + A_H w_h^{i-1} + A_L w_l^{i-1} + S_z^{i-1})
 \end{aligned}
 \tag{3.43}$$

3.9.3 Numerical Order of Iterative Scheme

The SGFVM defined in section 3.4 is accurate to $O(\Delta x^2)$, as demonstrated in the derivation in Appendix A. However, the discretisation of the fixed Stress (and therefore ‘free’ surface) boundary conditions described in section 3.6 are currently only discretised at $O(\Delta x)$. This is primarily due to complications with parallel programming (section 4.5.2) and shape of the structure (section 3.8), as the second order boundary conditions require information up to two cells away from the boundary in question.

This means that boundary conditions near a processor boundary may require more information than is present in the processor boundary, while some structures may attain such a thin profile that there would not be enough cells comprising the structure to accommodate these second order boundaries. Early in development these second order boundaries were implemented, which allowed an investigation to be undertaken to establish how first order boundaries compared in both behaviour and numerical accuracy.

An example of this can be seen in figure 3.13 where a 2D box was fixed to the floor and compressed, which was modelled using the SMS with first order boundaries, second order boundaries and in COMSOL. The displacement profiles generated by COMSOL have been provided with an annotated black line at the eastern edge, indicating the position of the plotted slice of accompanying comparative data.

3. CREATING A STRUCTURAL MECHANICS SOLVER

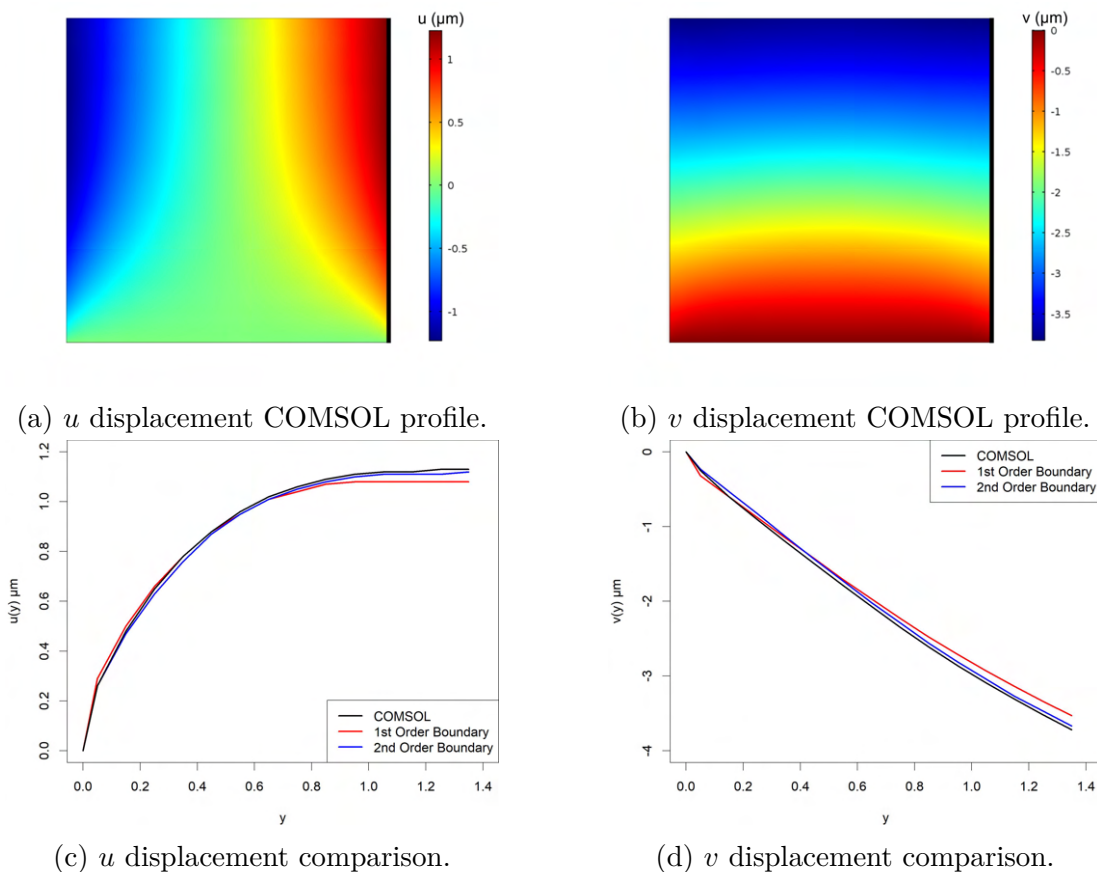


Figure 3.13: Accuracy of 1st and 2nd order SMS boundaries against COMSOL.

Considering these plots, it appears that whilst the first order boundaries undoubtedly have a poorer match to the COMSOL solution than the second order boundaries, the first order boundaries nevertheless still provides a close match both in behaviour and absolute values with the other solutions, still being within a 5% interval of the COMSOL values. Furthermore, this could be considered a worst case scenario for accuracy, with a domain exactly fitting the structure and a relatively low grid density of 14×14 volumes being used.

Consequently, while there are potential measures which could be undertaken to address the complications of implementing second order boundaries, such as the creation of new MPI processes and special logic which only applies boundary

3. CREATING A STRUCTURAL MECHANICS SOLVER

conditions which are appropriate for the structure morphology, only the first order boundaries have been implemented in the parallel code and all following results presented in this Thesis will also be using first order boundaries.

Based on the investigations of this setup, the accuracy of numerical schemes utilising first order boundaries seem to be acceptably high for the problems being examined, however the implementation of higher order boundary conditions remains a potential avenue to expand the solver if the current accuracy ever becomes a limiting factor.

3.9.4 Algorithm Description

Here the process the solver undertakes to solve Structural Mechanics problems is briefly outlined at a high level:

- A matrix of Solid Fraction values generated by solidification is provided, which is used to identify the structural domain to be solved (see section [3.8](#)).
- While the stopping criteria (see section [3.9.1](#)) are unsatisfied, the following steps will continue running:
 1. For the u displacements, the algorithm performs a point by point sweep of the domain.
 2. If a point is identified as part of the structure, depending on the composition of the surrounding cells either the differencing scheme for an internal node (see equation [\(3.43\)](#)) or an appropriate boundary condition is applied to obtain a new value for the displacement at that location, using the v and w values obtained in the prior iteration for their contributions to the source term.

3. CREATING A STRUCTURAL MECHANICS SOLVER

3. For the v displacements, the algorithm performs a point by point sweep of the domain.
4. If a point is identified as part of the structure, depending on the composition of the surrounding cells either the differencing scheme for an internal node (see equation (3.43)) or an appropriate boundary condition is applied to obtain a new value for the displacement at that location, using the u values obtained from this current iteration and w values obtained in the prior iteration for their contributions to the source term.
5. For the w displacements, the algorithm performs a point by point sweep of the domain.
6. If a point is identified as part of the structure, depending on the composition of the surrounding cells either the differencing scheme for an internal node (see equation (3.43)) or an appropriate boundary condition is applied to obtain a new value for the displacement at that location, using the u and v values obtained from this current iteration for their contributions to the source term.
7. Increment iteration number, storing current u , v and w values for use in the following iteration and return to Step 1.

3.10 Model Verification

In this section, the accuracy of the results obtained by the SMS are investigated by examining a selection of idealised modelling scenarios. In these scenarios, the SMS is run to obtain the displacements u, v and w which are compared to the displacements obtained by solving an identical problem setup using the commercial multiphysics software COMSOL as well as analytic solutions when

3. CREATING A STRUCTURAL MECHANICS SOLVER

appropriate. As COMSOL is a commercial program used widely in both academia and industry to generate accurate multiphysics modelling, it has been reasoned that if the SMS generates comparable results to COMSOL it can be taken that the results generated are of an acceptable level of accuracy to realistically represent the underlying structural mechanics behaviour.

The different verification cases examined cannot be truly exhaustive, as all the possible permutations of boundary conditions, forces and shapes would be impractical to both obtain and to sensibly present here. Instead the aim will be to focus on enough distinct cases to demonstrate that for a wide range of setups, the SMS is demonstrating the expected structural mechanical behaviour with values obtained at acceptable levels of accuracy.

In this section, 7 verification cases have been selected to highlight some of the key functionality of the SMS. A more thorough examination testing 30 verification cases can be found in Appendix B.

When presenting the results for comparing the relative accuracy of the SMS vs COMSOL and analytic solutions, as the fundamental behaviour was found to match in all cases, direct visual comparisons with COMSOL plots are not very enlightening for ascertaining the relative accuracy. Therefore, rather than duplicating almost identical displacement plots from the SMS and COMSOL, for each case a plot showing the behaviour of the displacements generated by the SMS only has been provided along with a chart plotting a line of displacement data which has been extracted from the results generated by the SMS, by COMSOL (using a comparably dense FEM mesh) and a beam theory analytic solution when applicable. Dotted lines have also been plotted on these charts to indicate an interval of $\pm 10\%$ from the COMSOL solution to make it easier to appreciate the relative accuracy of the SMS results to COMSOL. Where appropriate to do so, the location of this extracted line of data has been

3. CREATING A STRUCTURAL MECHANICS SOLVER

indicated on the 3D displacement plots with a black dotted line.

3.10.1 Material Properties & General Problem Setup

Every case examined will have any unique aspects of their own setup outlined, but in order to avoid unnecessary repetition, a general problem setup will be outlined which can be taken as true for all of the verification cases being presented unless explicitly stated otherwise. All structures will have the following structural material properties:

$$E = 10 \text{ GPa}$$

$$\eta = 0.3$$

$$\rho = 7020 \text{ kg/m}^3$$

These values have not been chosen to represent any specific material but are similar to those of softer metals such as solid Gallium and Indium. However, for the purpose of verification, so long as the same values are used in both the SMS and COMSOL to generate the results, the choice of material properties is largely arbitrary.

Unless otherwise noted, the body force being used in any of these examinations will be analogous to the magnitude of the gravity force that would act on this structure: $F_b = \rho g = 9.8 \times 7020 \text{ N/m}^3$, although the direction of this force will vary depending on the case being examined. Likewise, for simplicity unless stated otherwise any facial forces will be taken to be the same as the body force, but only being applied on the volume faces: $F_f = 9.8 \times 7020 \text{ N/m}^2$, where again the direction of the force will vary and be stated in the verification case.

3. CREATING A STRUCTURAL MECHANICS SOLVER

Due to the nature of the SMS, the structure being used in the verification cases will exist in a larger domain that does not contain any structure that the code will act upon. The boundary conditions will differ from case to case (as will be explicitly noted), but in general the domain boundaries will be Dirichlet conditions with fixed displacements of $u = 0$, $v = 0$, $w = 0$; with the boundaries of the structure being free surface Neumann boundaries of $\frac{du}{dx} = 0$, $\frac{dv}{dy} = 0$, $\frac{dw}{dz} = 0$ as demonstrated in figure 3.14. This setup means that in general when fixed boundaries are required the structure will touch a domain boundary, and when a Neumann boundary is required that boundary of the structure will be free within the domain.

As discussed earlier in sections 3.8, the SMS has an edge detection that allows for close and accurate fitting of a structure as well as having the option of solving large parts of the domain including the solid structure and large amounts of the surrounding liquid. For these test cases the problems were set up so that the edge detection accurately fits the structure, as due to the use of first order boundary conditions as described in section 3.9.3, solving a closely fitted structure should represent a worst case scenario for the accuracy of the SMS due to these lower order regions being located within the structure rather than in a remote region of the ‘liquid’ which should have little if any meaningful impact on the displacements within the solid.

While generally not using closely fitted SMS domains in the results presented in Chapter 7, for verification it seemed prudent to present this potential worst case accuracy as there may be reasons to use closely fitted problem domains in the future, and even when fitting larger domains including the liquid it is possible for first order boundaries to occur within the structure.

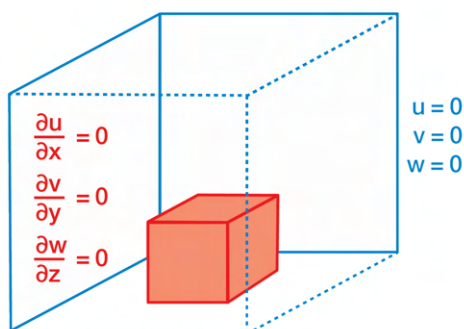


Figure 3.14: General problem setup.

Grid Independence

In order to ascertain what grid resolution should be used to generate these model results, the scenario described in section 3.10.2 was repeated with the grid size Δx halved each time, comparing these results with the same scenario modelled in COMSOL. When an increased grid resolution fails to generate a more accurate solution it can be assumed that grid independence has been achieved and the corresponding value of Δx can be used for the other results for the verification family. What is important is not the actual value of Δx , as this will always very depending on the scale of the problem being worked on, but rather how this value relates to the size of the structure being solved and thereby the number of computational cells the structure will be broken down into.

Results comparing the maximum displacement of a $10\text{m} \times 10\text{m} \times 10\text{m}$ block under gravity using different grid sizes can be observed in table 3.2, comparing the value at a point in the middle of the top face of the cube. Lines running bottom to top of the structure to compare the overall behaviour have been extracted and plotted in figure 3.15 as well extracting slices of the w displacements for

3. CREATING A STRUCTURAL MECHANICS SOLVER

each grid size as presented in figure 3.16. As can be observed from the attached slices showing the results in section 3.10.2, at this point on the structure the u and v displacements are very close to zero with w being the largest displacement dominating this scenario, so the w displacement will be used as the metric for reaching grid independence.

x	y	z	Δx	$w(\max)$ μm
COMSOL				-338
10	10	10	1	-309
20	20	20	0.5	-324
40	40	40	0.25	-331
80	80	80	0.125	-333
160	160	160	0.0625	-331

Table 3.2: Maximum displacements observed at different grid densities.

The displacements being observed stop changing significantly between $\Delta x = 0.25$ and $\Delta x = 0.125$, however choosing an appropriate grid spacing is problem dependent. As such, while a grid spacing of $\Delta x = 0.25$ may be appropriate for a relatively simple case such as tested here, a structure with a more complex geometry or force may require a finer grid to capture the expected behaviour accurately. This was observed to be the case for some of the more complicated tests, where $\Delta x = 0.25$ captured the underlying behaviour, but not to a great deal of accuracy. As such, for the Cases 1,2 and 7 $\Delta x = 0.25$ was used and for Cases 3-6 $\Delta x = 0.125$, which should allow the test cases presented to obtain a solution with the best compromise between accuracy and computation time given the problem setups.

3. CREATING A STRUCTURAL MECHANICS SOLVER

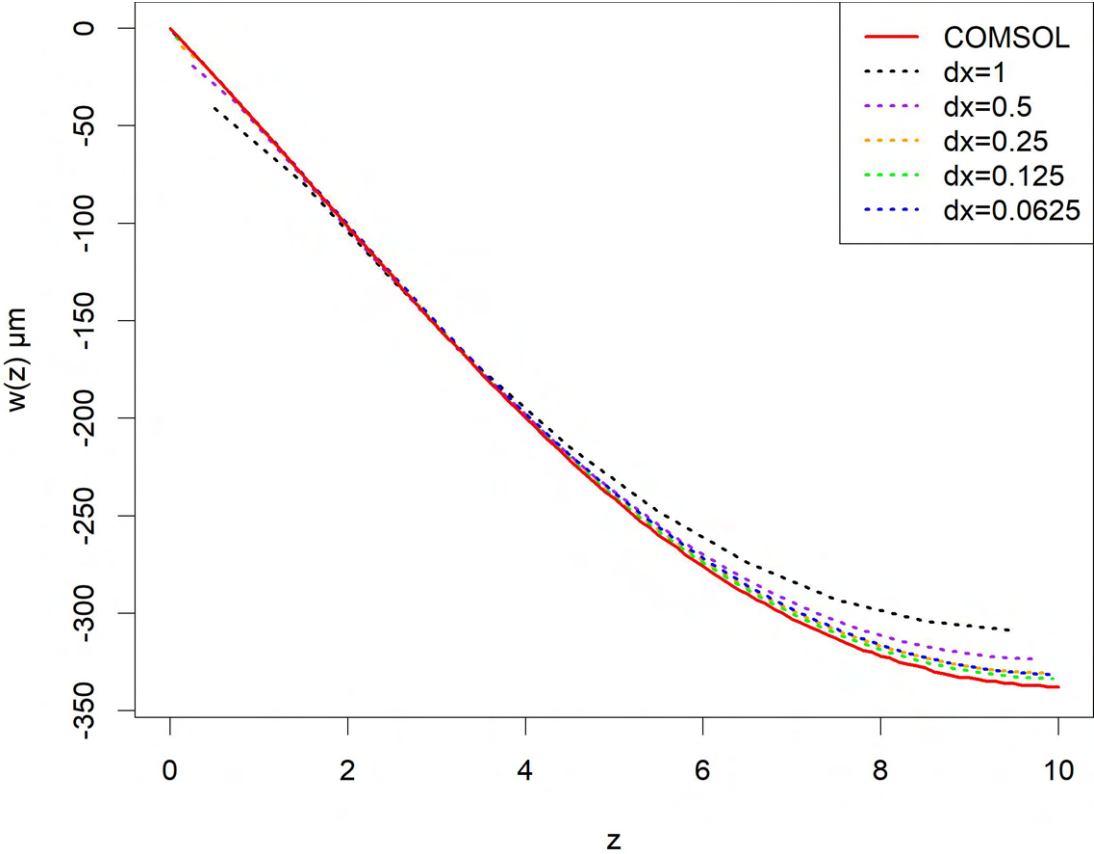


Figure 3.15: Plotted model w displacements.

3. CREATING A STRUCTURAL MECHANICS SOLVER

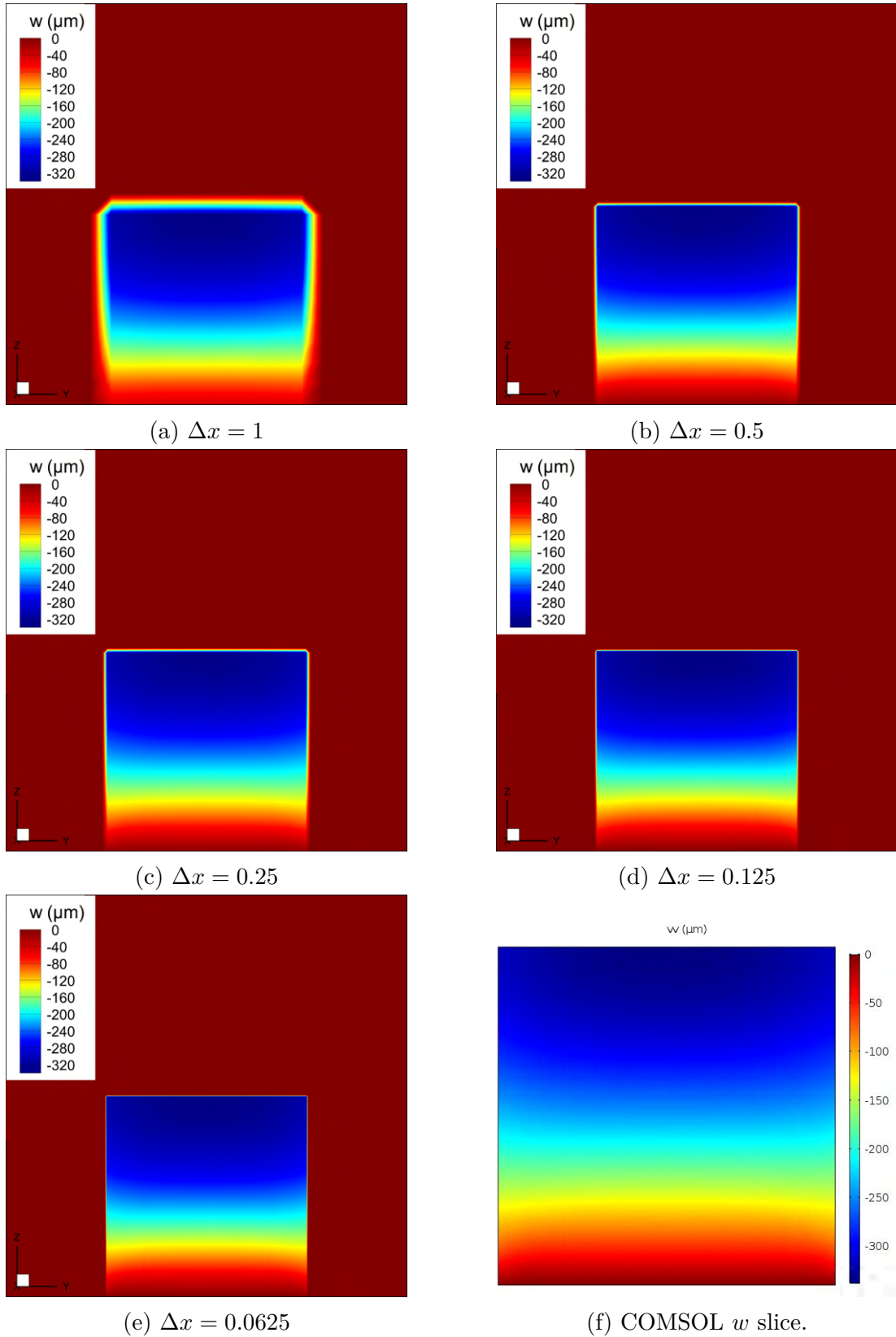


Figure 3.16: w displacement grid size comparison.

3. CREATING A STRUCTURAL MECHANICS SOLVER

3.10.2 Block Under Body Force

This case was chosen to demonstrate that the SMS can accurately model the behaviour of regular 3D structure under a body force load. A block was fixed at the face touching the floor and compressed by a negative body force in the z direction. The data comparisons indicate a close match in accuracy between the SMS and COMSOL for this scenario.

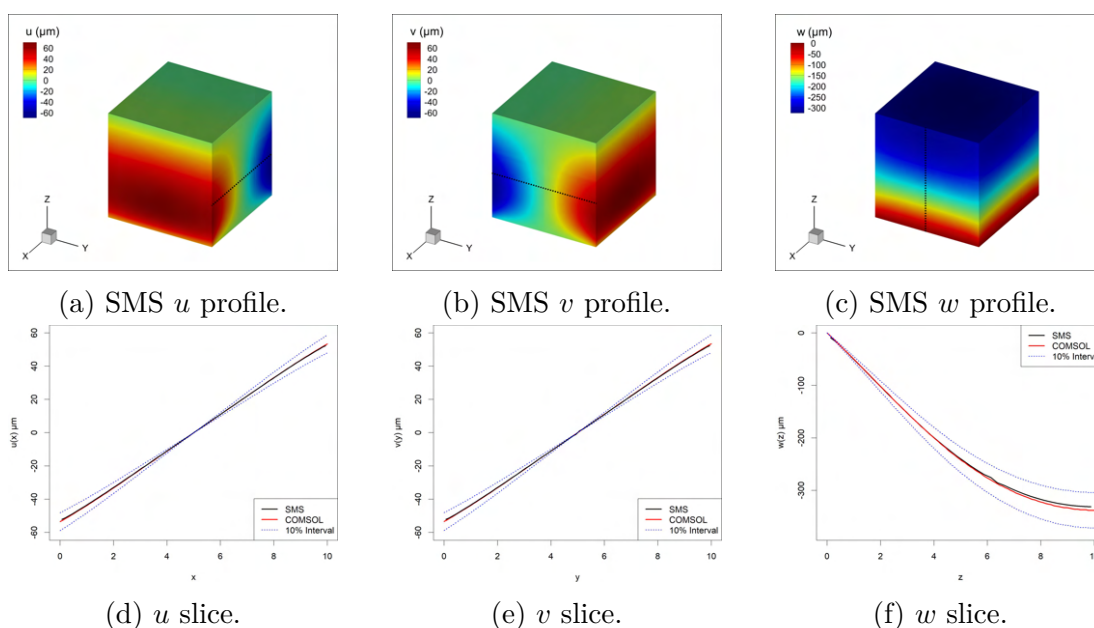


Figure 3.17: Case 1 - Floor fixed block under negative body force in z .

3. CREATING A STRUCTURAL MECHANICS SOLVER

3.10.3 Block Under Facial Force

This case was chosen to demonstrate that the SMS can accurately model the behaviour of regular 3D structure with a force load applied to the face of a structure. A block was fixed at the face touching the floor and stretched by a positive facial force in the z direction. The data comparisons indicate a close match in accuracy between the SMS and COMSOL for this scenario.

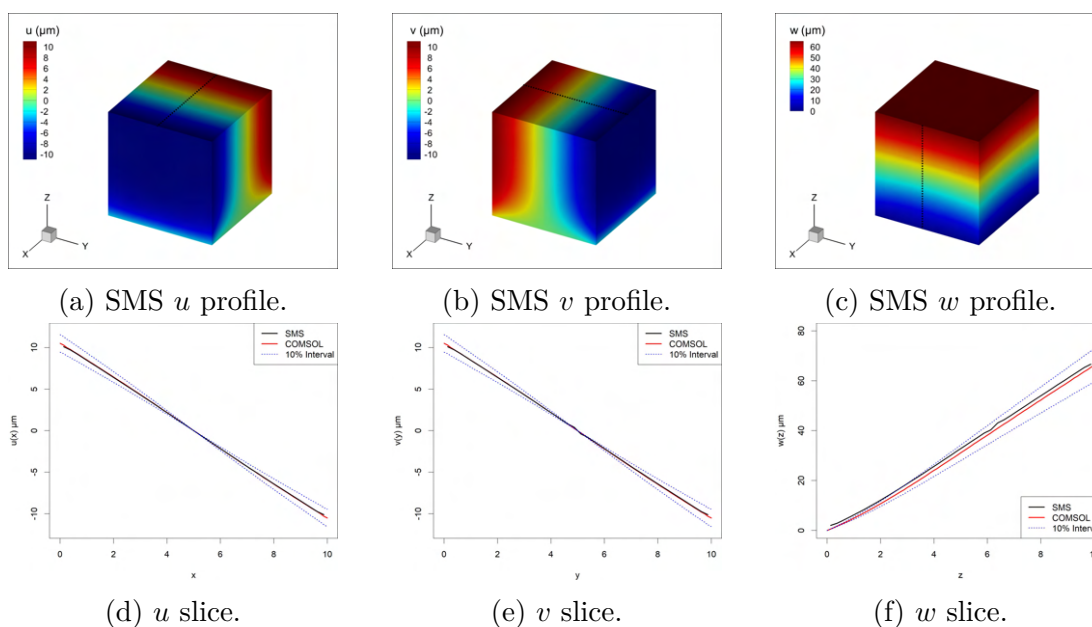


Figure 3.18: Case 2 - Floor fixed block under positive facial force in z on High face.

3. CREATING A STRUCTURAL MECHANICS SOLVER

3.10.4 Block With Triangular Face Under Body Force

This case was chosen to show the SMS can accurately solve structures with diagonal edges, as due to the nature of the SMS any parts not perfectly aligned with the axis will be approximated using cubic volumes. Fixed faces were defined for the West, South and Low faces of a cubic structure missing a corner was uniformly compressed by a negative body force applied in the z direction. The comparisons indicate that while matching the general behaviour observed in COMSOL, the accuracy of the values are not as close as was observed in the two simpler cases, with the values being within a 10% interval for u and w but the v profile providing a less accurate match. While this does demonstrate the fundamental behaviour is captured by the SMS for diagonal faces/edges, it seems to indicate that when modelling these structures the values are less accurate when compared to COMSOL.

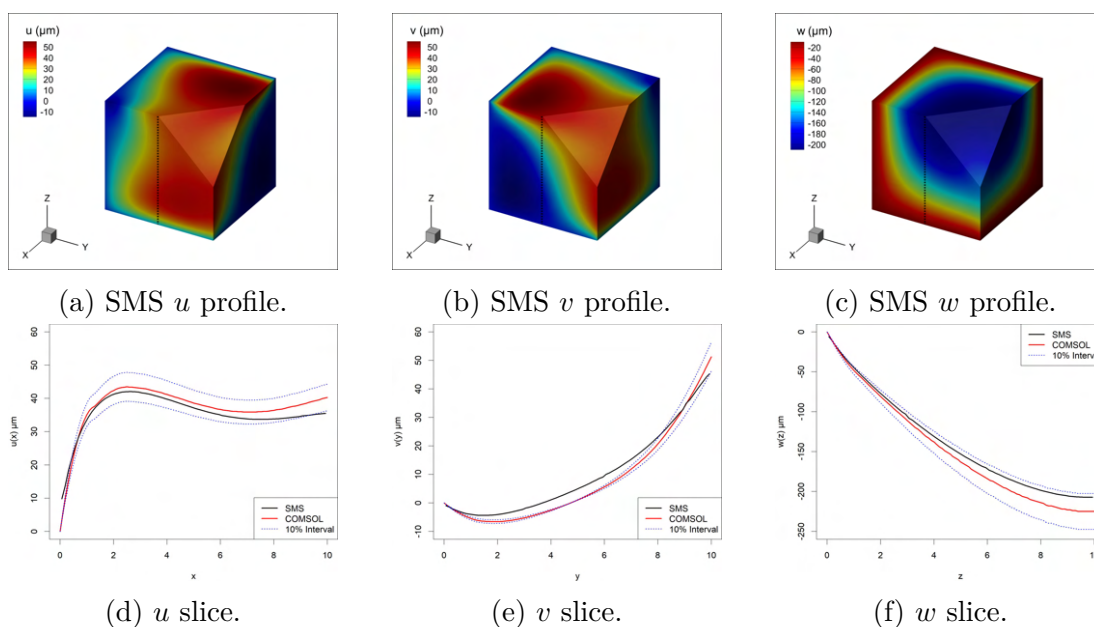


Figure 3.19: Case 3 - Floor & wall fixed block with triangular corner under negative body force in z .

3.10.5 Hemispherical Structure Under Body Force

This case was chosen to demonstrate the SMS can obtain accurate displacements for more complex structures with curved faces and/or edges. As in the prior case any parts of the structure not in line with the axis require approximation using cubic volumes, which for this structure would encompass the entire rounded surface. An extreme case such as this should indicate if the approach used to approximate the structure is appropriate for more complex geometries. The hemispherical structure was fixed by the flat face and subjected to a uniformly compressive negative body force in the z direction. The data comparisons indicate another good match with COMSOL for the general behaviour of the structure, with the values for u and v matching very closely. However, while still within the 10% interval, the w displacement is clearly under predicted when compared to COMSOL.

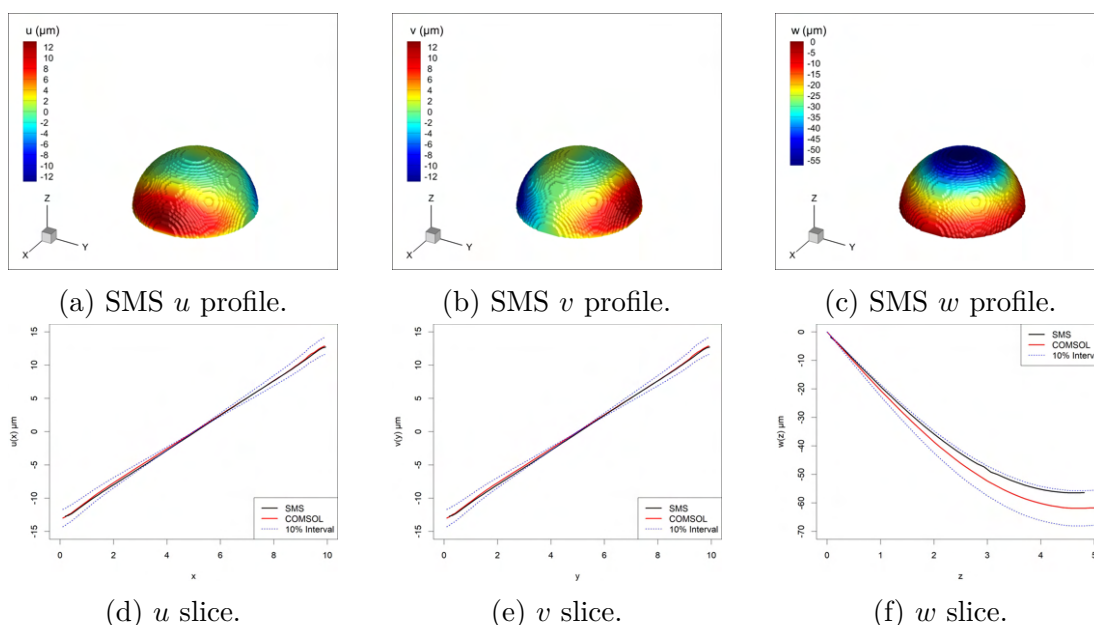


Figure 3.20: Case 4 - Floor fixed hemispherical structure under negative body force in z .

3.10.6 Cantilever Beam With Point Load - Beam Theory Analytic Solution

There were multiple reasons for examining a cantilevered beam as a test case. Firstly, so far the cases have all had comparable ratios of height:length:width, so a beam structure will indicate how well the SMS can simulate the behaviour of structures where this ratio is less balanced, such as the beam where the length is far greater than the thickness of the structure. Furthermore, a beam affixed to a wall subjected to a force perpendicular to the beam provides an example of a shearing force, where the previous verification cases have only tested forces which were normal to the fixed faces of the structure. However, the key benefit of examining this scenario is that it provides an opportunity to validate the accuracy of the SMS against an analytic solution as well as COMSOL.

The Euler-Bernoulli beam theory provides a simplification of the theory of linear elasticity that can be used to obtain the load carrying capacity and deflection of a beam by treating it as a 1D problem with an analytic solution. Beam theory has existed for centuries and correspondingly there is a large amount of existing research and applications utilising it. There are many works which provide a detailed explanation and derivation of this theory, such as [87], but for the purposes of this verification case the key principle is that the deflection (w) of a stationary beam with length L , second moment of area I for the beam cross section and a point load of F applied to the end can be defined as the following problem:

$$EI \frac{\partial^4 w}{\partial x^4} = 0; \quad w_{x=0} = 0; \quad \frac{\partial w}{\partial x}_{x=0} = 0; \quad \frac{\partial^2 w}{\partial x^2}_{x=L} = 0; \quad -EI \frac{\partial^3 w}{\partial x^3}_{x=L} = F \quad (3.44)$$

Which can be solved to yield the following analytic solution for the deflection

3. CREATING A STRUCTURAL MECHANICS SOLVER

at any point along the beam:

$$w(x) = \frac{F}{6EI}(3Lx^2 - x^3) \quad (3.45)$$

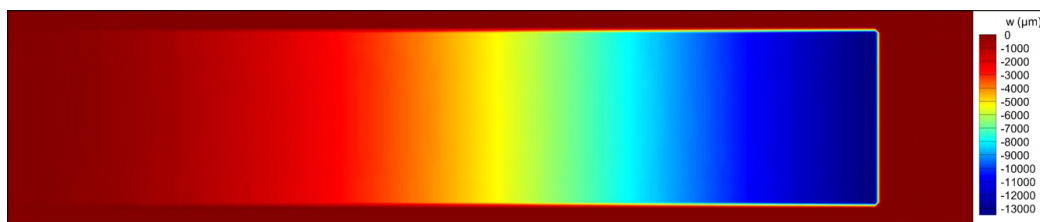
The following Euler-Bernoulli assumptions, in addition to the basic assumptions of linear elasticity, are required for these analytic results to be held accurate:

- The beam cross section does not significantly deform under the load and can be assumed to be rigid.
- The cross section of the beam remains planar and normal to the beam during deformation.

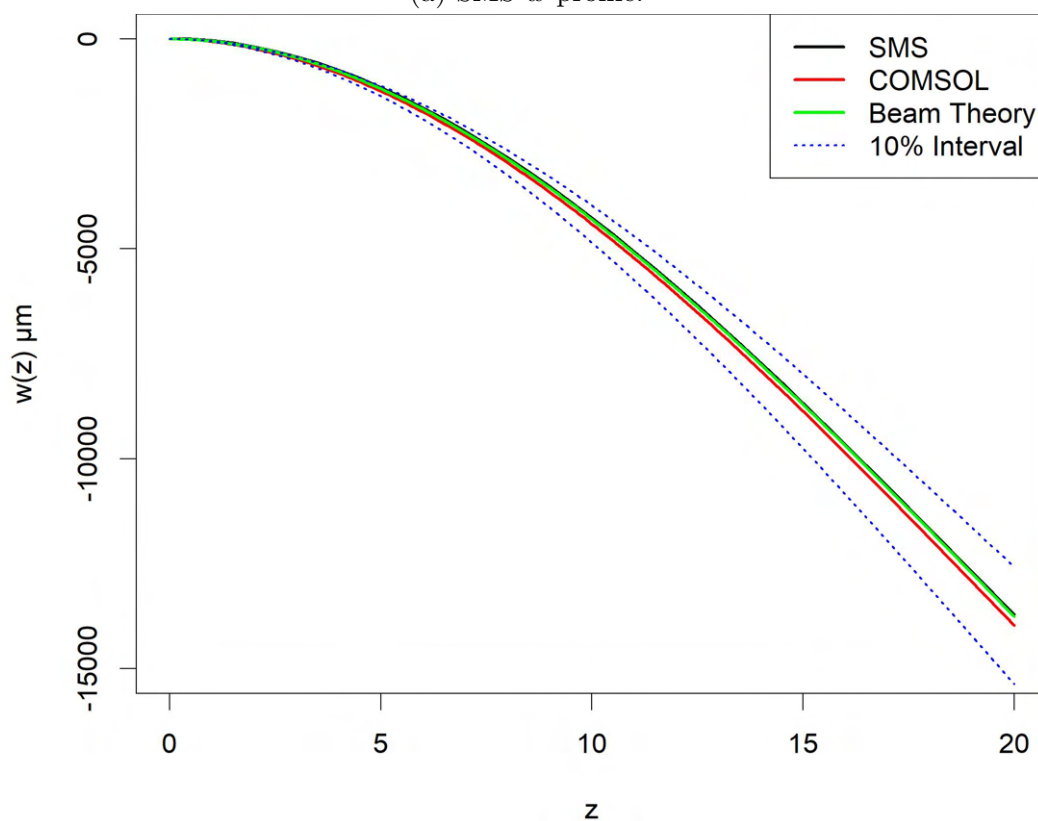
To test this verification case, a cantilever beam with the dimensions $4m \times 4m \times 20m$ was fixed to the wall at one end and had a negative facial (or ‘point’ for the 1D beam theory model) force in z , representing a case where a fixed cantilever beam has a weight applied to the face of its free end.

As beam theory is a 1D approximation, only the deflection w is provided, so while the SMS and COMSOL solutions did provide u and v displacement profiles, these have been omitted to focus on the beam theory comparison. The data comparisons confirm that there is a very close match in values between all three models - beam theory, SMS and COMSOL.

3. CREATING A STRUCTURAL MECHANICS SOLVER



(a) SMS w profile.



(b) w value COMSOL and beam theory comparison.

Figure 3.21: Case 5 - $4 \times 4 \times 20$ cantilever beam with point load.

3.10.7 Cantilever Beam With Distributed Load

This case was chosen to demonstrate that the SMS can model a cantilever beam under a uniform body force (or distributed load), where all of the other benefits of examining a beam structure such as this as were outlined in section 3.10.6 continue to hold true here.

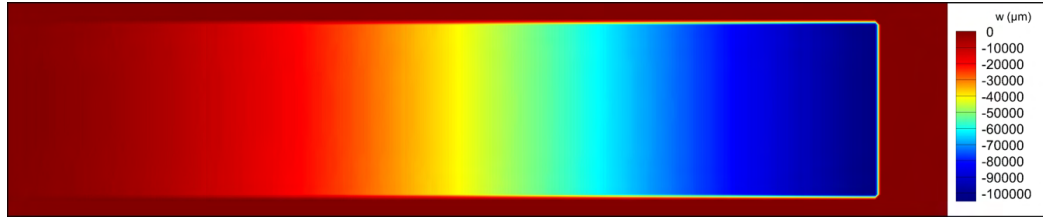
This verification case is identical in setup and assumptions to those outlined in section 3.10.6, with the exception of the definition of the force, which is now distributed along the beam rather than being a point load at the beam end.

Beam theory can also be used to obtain an analytic solution for this problem, describing the deflection (w) of a stationary under a uniformly distributed load of F applied along the length of the beam with the equation:

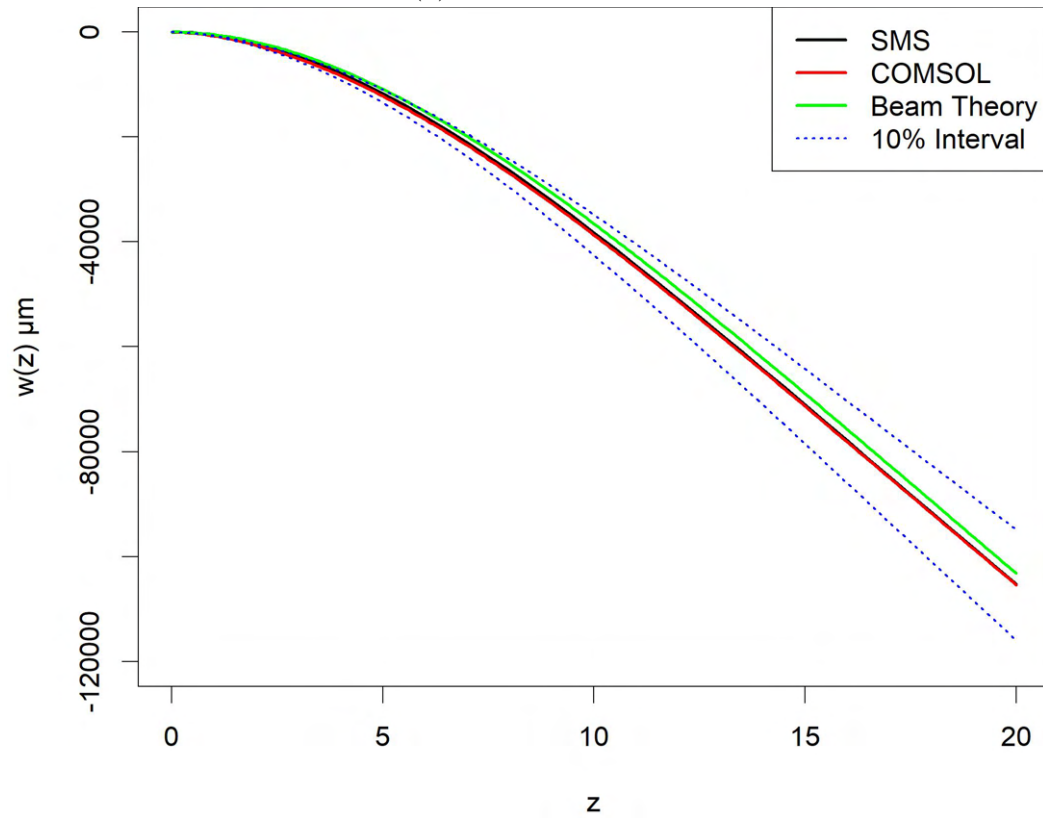
$$w(x) = \frac{F}{24EI}(6L^2x^2 - 4Lx^3 + x^4) \quad (3.46)$$

Again, due to beam theory being a 1D approximation only the deflection w has been provided. The data comparisons confirm that for this case there is also a very close match in values between all three models - beam theory, SMS and COMSOL.

3. CREATING A STRUCTURAL MECHANICS SOLVER



(a) SMS w profile.



(b) w value COMSOL and beam theory comparison.

Figure 3.22: Case 6 - $4 \times 4 \times 20$ cantilever beam with distributed load.

3. CREATING A STRUCTURAL MECHANICS SOLVER

3.10.8 Thermal Expansion of Block Under a Fixed Temperature Change

This case was chosen to demonstrate that the SMS can simulate a linear elastic structure undergoing thermal expansion, as described in section 3.7.

Exploring thermal expansion requires some additional material properties and elements of problem setup to be defined. The coefficient of thermal expansion $\alpha = 32.1 \mu\text{m}/\text{K}$ was used, arbitrarily taking the value for Indium. The reference temperature for this structure was taken to be 300 K, with this case modelling a scenario where the temperature was uniformly raised to 400 K. The data comparisons indicate a close match in accuracy between the SMS and COMSOL for this scenario.

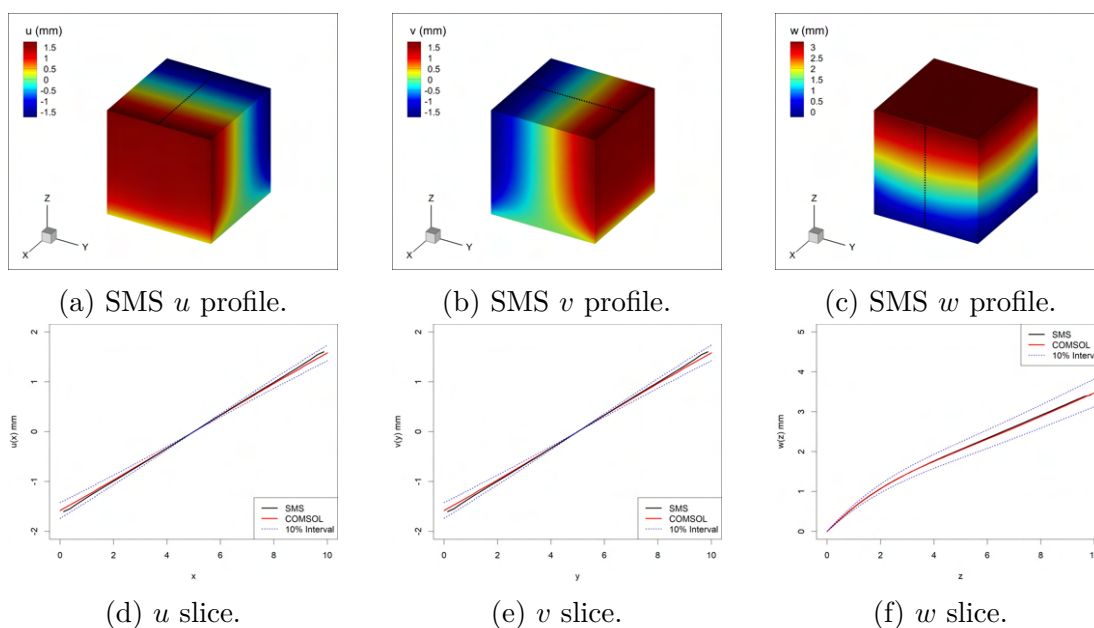


Figure 3.23: Case 7 - Floor fixed block structure experiencing thermoelastic expansion under temperature increase.

3.10.9 Verification Conclusions

Examining the verification cases presented in this section and in Appendix B, the SMS has consistently demonstrated the correct underlying structural mechanical behaviours which match those observed in the corresponding COMSOL simulations which were performed. This indicates that experimental results obtained using the SMS can be taken as indicative of how a linear elastic material would truly act. The actual values obtained were also usually in very close agreement with the COMSOL solutions for a variety of different scenarios, however it was found that having to represent more complex edges, faces and structures in general with the cubic volumes did lower the accuracy of the spot values taken.

Despite this, even in the worst cases the values were of the same order and comparable behaviour to the COMSOL cases, with the implementation of higher order boundary conditions (see section 3.9.3) or increasing the grid density (see section 3.10.1) being possible avenues to explore if the accuracy of the solutions becomes an issue in practice.

For cases modelling the behaviour of beams, the analytic solution provided by the Euler-Bernoulli beam theory was also found to be in good agreement with the modelled 3D beam deflection obtained from the SMS, providing the beam theory assumptions continued to hold true for the case being modelled.

Thermal expansion was also examined, showing a good match with COMSOL for uniform temperature increases and temperature gradients, meaning that thermally driven structural behaviour can also be accurately examined by the SMS.

3.11 Summary

This section outlines the theory of linear elasticity, explaining the inherent assumptions and limitations of this material model. The justification was given for utilising a quasi-stationary approach for the solver when used in the context of coupling with solidification. The approach for obtaining the displacement formulation of the equilibrium equations was described, which were then expanded into a formulation which accepted variable material properties. These equations were then discretised into a staggered grid finite volume method and the boundary conditions for this system were described. The process of including thermal expansion, structure identification within a larger domain, obtaining stress outputs as well as providing a brief overview of the algorithmic implementation. Finally, a selection of verification cases were run to ascertain the accuracy of the SMS, which found it to be in good agreement with both commercial structural mechanic codes and relevant analytic solutions.

Chapter 4

COUPLING STRUCTURAL MECHANICS TO SOLIDIFICATION

4.1 Overview

This chapter contains a selection of smaller, more loosely related sections which were important aspects to the process of coupling structural mechanics and solidification, yet were not significant enough to warrant an entire chapter of their own. First a brief overview of the existing TESA code which the SMS has been designed to integrate with was given, providing a summary of the other solvers it utilises. More detail is then given on the solidification models which have been used during the course of this research. A description is given of how existing deformation is accounted for over time given the quasi-stationary nature of the SMS. Finally, enhancements to improve the performance of the solver are presented in the form of multi-scale modelling and parallel computing.

4.2 TESA Solvers

The **ThermoElectric Solidification Algorithm** (TESA) is a bespoke code which has been in constant developed for nearly a decade by the Computation Science and Engineering Group (CSEG). This code has been designed such that multi-physics problems including solidification, fluid flow and thermoelectric magnetohydrodynamics (TEMHD) can be resolved in a single coupled model where these processes can influence each other. This framework has been used to examine complex multi-physics problems such as TEMHD effects on crystal growth [88, 89] and the formation of freckle defects [90], utilising parallel computing [91] (see section 4.5.2) to run large scale simulations where both micro- and macro- scale phenomena and their interactions can be simultaneously examined. One of the key requirements of the structural mechanics solver described in chapter 3 was that it would be able to coalesce with this prior research so that the SMS can potentially be added as a module included in TESA, able to be turned on and off according to the requirements of the scenario being modelled.

With the SMS completed and integrated into TESA there will be five solvers comprising the code, all weakly coupled so that each aspect is solved separately with relevant quantities being updated and passed between the solvers as required. The relationship between these solvers has been summarised in figure 4.1, where structural mechanics, solidification and diffusive transport are the core solvers which are being run for the research in this thesis. However, future work could explore how fluid flow and magnetic forces interact with these structural behaviours, including potentially providing extra inputs for the forces driving the structural mechanics solutions.

Further information about the solvers and their relationship as depicted in figure 4.1 are summarised below:

4. COUPLING STRUCTURAL MECHANICS TO SOLIDIFICATION

- Solidification - using Cellular Automata (CA) method, see section 4.3.2 for further details.
- Structural Mechanics - using a staggered grid Finite Volume Method to obtain displacements, see Chapter 3 for more details. These displacements can influence solidification by changing the orientation of the dendrite (Chapter 5) and/or physically moving the structure by driving an advection process (Chapter 6).
- External forces - these include any forces driving structural mechanical behaviour, which could be a predefined force such as gravity which is unrelated to any other TESA processes, but could also include dynamically generated forces from the other modules.
- Transport - using the Finite Difference Method to alter the concentration distribution based off of diffusion and any inputted flow velocities, where this change in concentration will impact the solidification behaviour.
- Fluid Flow [91] - using the Lattice Boltzmann method to calculate flow velocities. This could potentially be used to generate forces from the pressure to drive deformation and stress build up in the structural mechanics module.
- Thermoelectrics [88, 89] - using a staggered Finite Difference Method to obtain the current which can be used to calculate a Lorentz force to drive fluid flow. The Lorentz force could also potentially be used to drive deformation and stress build up in the structural mechanics module.

4. COUPLING STRUCTURAL MECHANICS TO SOLIDIFICATION

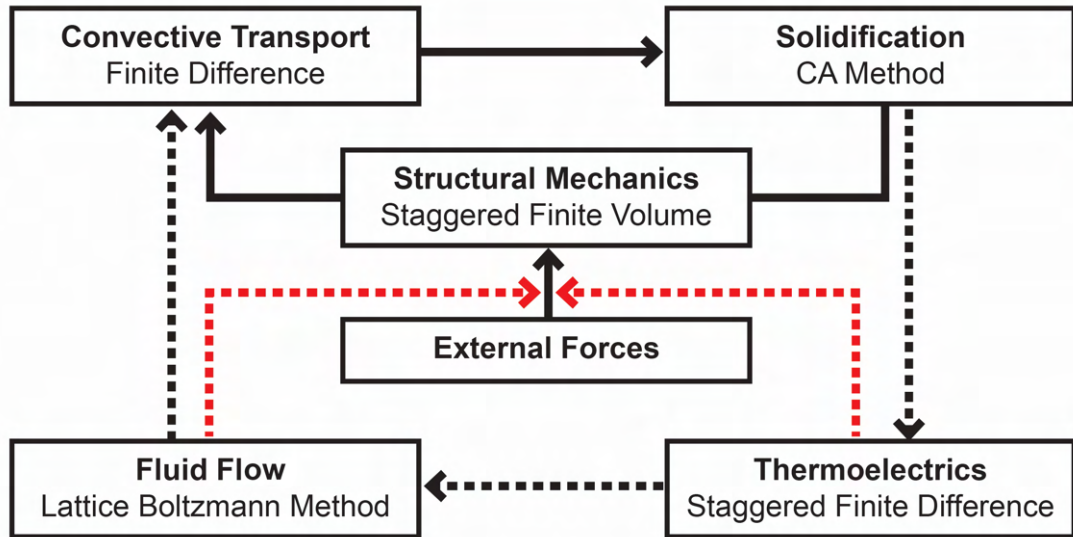


Figure 4.1: Flow chart of relationship between TESA modules

4.3 Solidification Modelling

The solidification behaviour of metal alloys is a complex process where the system is governed by many factors [83] and is undoubtedly an intrinsic aspect of this research. However, the primary focus of the work being presented is on the integration of structural mechanics with existing solidification models which have been essentially fully developed prior to this work being commenced. Consequently, only a brief summary of the theory behind the solidification processes will be provided alongside an explanation of how the solidification models were utilised. It should also be noted that due to the approach used to couple solidification to structural mechanics, while these models are the only models that have been tested, there is potential to couple the SMS to other solidification models if future research required it.

At the most fundamental level, a liquid metal solidifies as it is cooled, preferentially nucleating around any impurities in the mixture or spontaneously

4. COUPLING STRUCTURAL MECHANICS TO SOLIDIFICATION

in the melt should it become sufficiently cooled. Once a nucleation event has occurred, the solidification front progresses as an interface forming crystalline structures known as dendrites. The speed and growth behaviour of this process largely depends on the temperature and composition of the alloy. This can be observed in the phase diagrams describing the relationship between the phases, concentration and temperature for two component alloys.

A further important consideration in these relationships is the temperature where the eutectic phase forms, which is the lowest temperature where melting can occur, hence meaning any part of a dendritic system at this temperature or cooler must be fully solid, while any part above this temperature will still be solidifying. Furthermore, the shape of these dendritic structures relates to an underlying crystallographic lattice, the most fundamental of which being the cubic lattice where if unconstrained the dendrite will grow in 6 orthogonal directions. An unconstrained dendrite growing in this manner is known as an equiaxed dendrite and can be thought of as a dendrite nucleated within the liquid which is free to grow in all directions, leading to a dendrite with 4-fold symmetry in the absence of any other phenomena which could interfere with the growth, such as fluid flow, temperature gradients or contact with a mould wall.

However, for this research equiaxed dendrites are generally not appropriate for structural mechanical consideration as, due to being free floating, external forces impart no stress to the structure. Under a strong fluid flow, an equiaxed dendrite would simply move through the liquid rather than deform, only possibly experiencing deformation if they came into contact with other dendrites or the mould wall. While certainly a related area and a potential avenue of future work, modelling the movement and impact of equiaxed dendrites in this manner is beyond the current scope of this research.

For this reason, this research is more concerned with directional

4. COUPLING STRUCTURAL MECHANICS TO SOLIDIFICATION

solidification leading to the formation of columnar dendrites. This occurs where the solidification starts at one end of the casting, generally with the nucleation happening on the mould wall, the dendritic front then advances towards the other side of the casting mould. This manner of solidification development is more germane to the fundamental questions of the relationship between structural mechanics and microstructure solidification as these columnar dendrites possess an anchor point where they attach to the mould wall due to their nucleation conditions. Consequently, when subjected to external forces columnar dendrites must build up stress and deform, unlike the free to move equiaxed dendrites.

4.3.1 The Enthalpy Method

For the initial tests of coupling structural mechanics with microstructure solidification, an enthalpy based method for undercooled growth as described by Voller [92] was used. This method was attractive for these initial explorations of the topic as it was believed that as a 2D method which generated binary dendrites would be a more straightforward test of the core concepts of the research than a full coupling with the more complicated implementation of CA method being used in the main TESA solver.

The method implemented is essentially identical to the method presented in the paper by Voller, so only the key principles will be reproduced in brief here.

The order parameter f is used to formulate an enthalpy-based method for representing a diffuse interface, where f represents a liquid fraction taking $f = 1$ as fully liquid and $f = 0$ as fully solid.

Governing equations for this approach relate f to the volumetric enthalpy H , defining H as the sum of the sensible heat:

4. COUPLING STRUCTURAL MECHANICS TO SOLIDIFICATION

$$H = c_p T + fL \quad (4.1)$$

where c_p is the specific heat, T is the temperature and L is the latent heat of the volume. With the conservation of enthalpy being given by

$$\frac{\partial H}{\partial t} = \nabla \cdot (K \nabla T) \quad (4.2)$$

At the interface, the temperature is undercooled, defining the interface temperature as:

$$T^i = T_m - \frac{\Gamma(\theta)}{L} T_m \kappa \quad (4.3)$$

where κ is the curvature, T_m is the melting temperature and the surface stiffness is defined via a fourfold symmetry model. Where Voller then takes a numerical approach to convert these equations into a dimensionless system, discretised onto a Cartesian grid.

Examples of a developing equiaxed and columnar dendrite using the Enthalpy method can be observed in figure 4.2 and 4.3 respectively. The homogeneous nature of the dendrites produced by the enthalpy method can be seen here, with values very sharply changing from fully solid to fully liquid, with only the boundary cells containing any intermediate values.

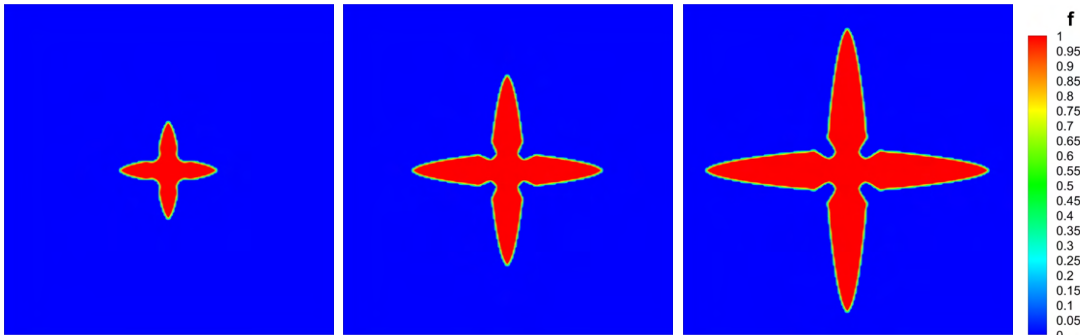


Figure 4.2: Enthalpy method equiaxed dendrite.

4. COUPLING STRUCTURAL MECHANICS TO SOLIDIFICATION

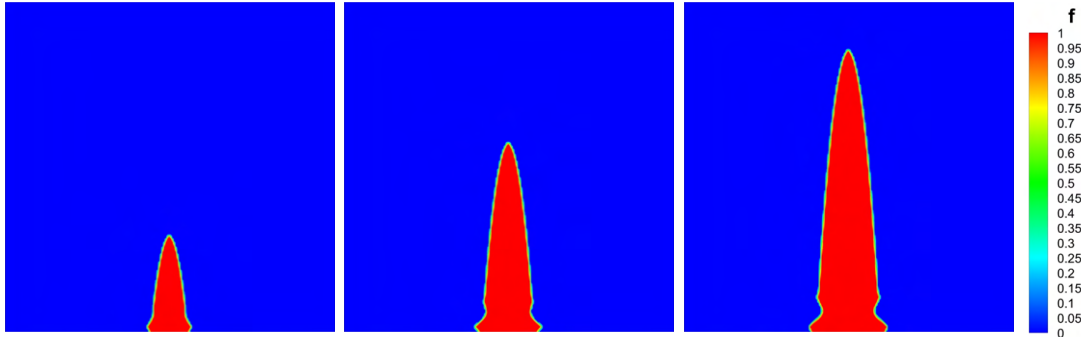


Figure 4.3: Enthalpy method columnar dendrite.

This solidification approach was used for the initial examinations of coupling solidification with structural mechanics, both by means of solid material advection and orientation changes, being the solidification model in use for work presented in a conference paper by Soar *et al.* (2020) [93]. However, while this solidification model possessed attributes allowing it to be relatively effectively coupled with solid advection (see Chapter 6 for more details on the strengths and weaknesses of this model for this approach), examinations of how the model responded to orientation changes (see Chapter 5) highlighted the strong grid anisotropy of the enthalpy method.

This causes the solidification to lock onto discrete orientations with potentially large observable changes in growth behaviour as it switches between these preferential growth angles, which became unacceptable as it became clearer that potentially subtle changes to dendrite orientation can have large potential effects on the development of a dendritic system.

Furthermore, the highly undercooled systems this method was designed to model are not generally applicable to the industrial cases where structural behaviour has most often been observed. These issues, as well as a desire to move the simulations into 3D (where this implementation of the Enthalpy was 2D) and to couple the SMS with the main TESA process halted any further

4. COUPLING STRUCTURAL MECHANICS TO SOLIDIFICATION

work being done with the Enthalpy method.

4.3.2 The Cellular Automata (CA) Method

The finite difference decentred octahedral Cellular Automata (CA) method employed by TESA is based on the open source μ MatIC code developed in Imperial College by Professor Peter Lee and his colleagues [94–97]. The CA method was extracted, refactored and implemented in TESA, a process that was extensively documented and explained in the Thesis of M. Alexandrakis [98], being further explained and summarised in more recent research papers presented by Dr Andrew Kao and his colleagues [90, 91]. Being so widely documented elsewhere and implemented before the commencement of this research, only the core governing equations and principles which underpin the method will be reproduced here.

This method uses a continuous phase variable ϕ to represent the solidification process, where $\phi = 1$ is fully solid, $\phi = 0$ is fully liquid and any intermediate values represent a solidifying cell. When modelling the solidification of a metal alloy, the relationship between the concentration of solute in the solid (C_s) and liquid (C_l) is governed by:

$$C_s = kC_l \quad (4.4)$$

where k is the partitioning coefficient of solute, which can correspondingly be defined as $k = \frac{C_l}{C_s}$. Phase change and the partitioning of solute is then governed by the transient process

$$C_l(1-k)\frac{\partial\phi_s}{\partial t} = -\nabla \cdot (D_e\nabla C_l) + [1 - (1-k)\phi_s]\frac{\partial C_l}{\partial t} \quad (4.5)$$

where t is the time, $D_e = (1 - \phi_s)D_l + \phi_s D_s$ is the equivalent mass diffusivity

4. COUPLING STRUCTURAL MECHANICS TO SOLIDIFICATION

coefficient which defines the linear relationship in ϕ between the diffusion coefficient of the solid (D_s) and liquid (D_l). The equilibrium interface temperature T^i is given by

$$T^i = T_0 + m_l (C_l - C_0) \quad (4.6)$$

where m_l is the liquid slope, C_0 is the initial concentration and T_0 is the liquidus temperature at C_0 .

Finally, the equivalent concentration $C_e = (1 - \phi_s) C_l + \phi_s C_s$ is defined as the linear relationship in ϕ between the solid and liquid concentration, which is the concentration quantity taken by the transport solver to resolve diffusive and/or convective transport within the problem domain, which can be parsed back into the CA method to undergo further solidification.

An equiaxed dendrite simulated using the CA method can be seen in figure 4.4, which by contrasting it with the enthalpy example in figure 4.2 highlights some key differences between the dendrites provided by this approach. The overall morphology of the dendrite interface is different, with the dendrites generated having a more diffuse boundary and clear internal patterns of higher and lower solid fraction, whereas the enthalpy method produces dendrites with a step function interface.

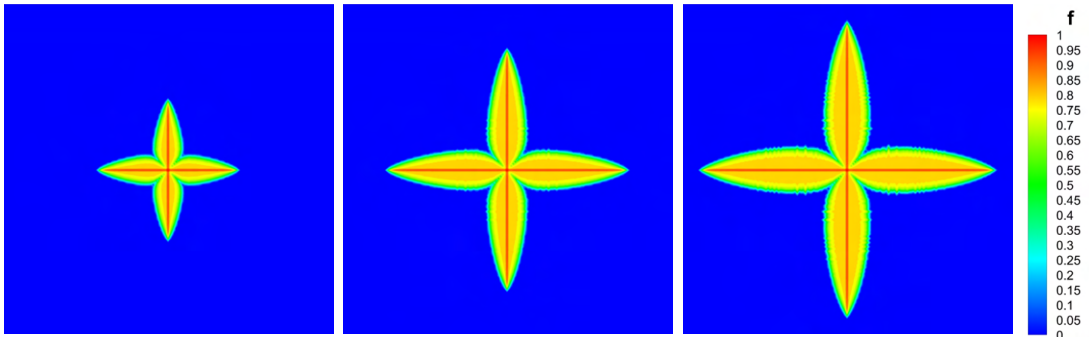


Figure 4.4: CA method equiaxed dendrite.

4. COUPLING STRUCTURAL MECHANICS TO SOLIDIFICATION

It is notable that these dendrites are rather broad and lacking in secondary dendrite arms branching from the main trunk, this is due to the orientation of the dendrites being modelled. The orientation of a dendrite has a large impact on how it develops, with the case where the dendrite is aligned exactly orthogonal to the axis having the particular distinct morphology observed so far.

However, the CA method lacks the rather severe grid anisotropy which the enthalpy method presents, and can be given a pre-defined collection of Euler angles to describe the orientation of the dendrite. The stark difference these changes in orientation can make have been highlighted in figure 4.5, where (a) provides an example of a 0° dendrite and (b) shows a columnar dendrite growing at an angle of 25° .

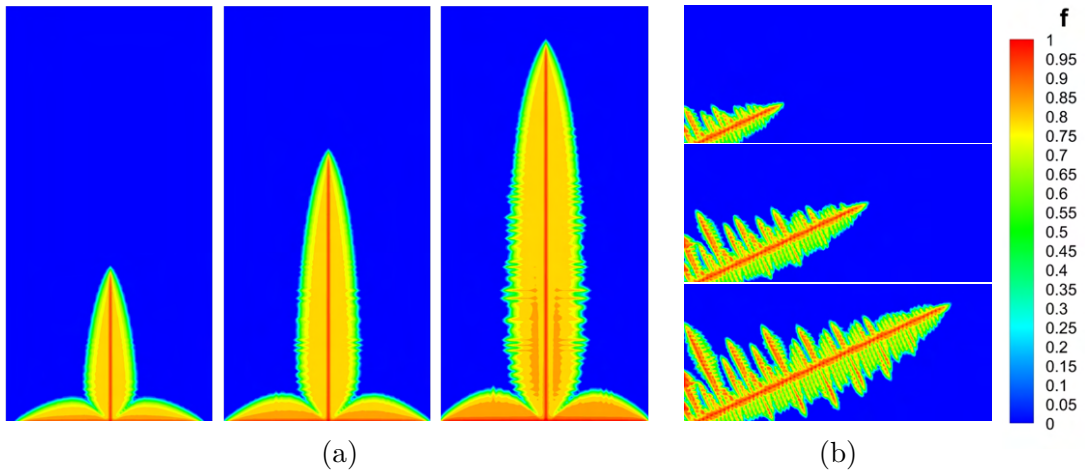


Figure 4.5: CA method Columnar dendrite. (a) 0° dendrite. (b) 25° dendrite.

The 0° dendrite is largely a special case which highlights the grid anisotropy still existing within the CA method, with the dendritic microstructure generally observed in experiments looking more broadly similar to the dendrite in (b) with many secondary arms competing to establish their spacing from the start. Secondary arm growth and competition does occur for 0° dendrites, with the perturbation visible at the dendrite interface in the final image in (a) being the

4. COUPLING STRUCTURAL MECHANICS TO SOLIDIFICATION

start of this process, however due to the grid anisotropy this process takes significantly longer to begin and can lead to a quite distinct microstructure.

These dendrites have been presented as 2D slices to highlight their internal variations in solid fraction, but they have in fact been modelled in 3D. This is another advantage over the enthalpy method which was previously being used, with 3D solutions being better able to represent the true solidification behaviour.

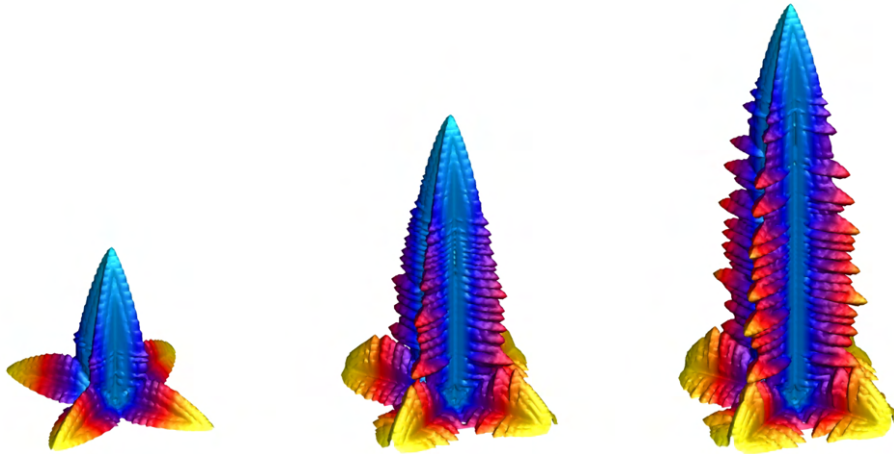


Figure 4.6: CA method 3D Columnar dendrite.

Figure 4.6 provides an example of the 3D structure of a growing columnar 0° dendrite, while figure 4.7 provides a comparison between growing equiaxed dendrites with set crystallographic orientation of (a) 0° and (b) random 3D rotation. Even at the early stages of growth this highlights the vastly different morphology which occurs, with a much less homogeneous structure and secondary arms forming.

For the reasons outlined, the CA method is the solidification model that has been used for much of the later development and to produce the results presented in Chapter 7.

4. COUPLING STRUCTURAL MECHANICS TO SOLIDIFICATION

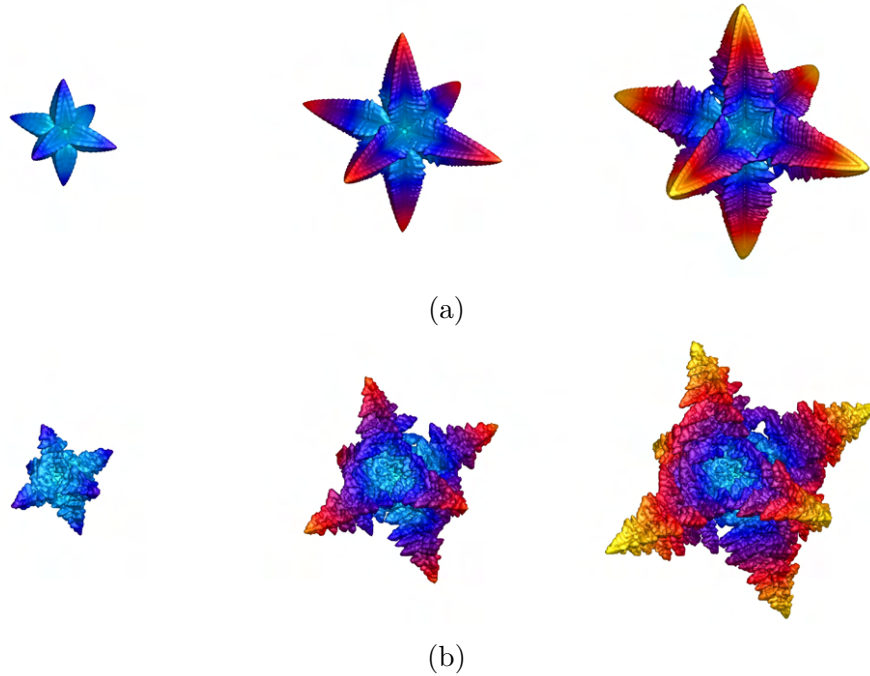


Figure 4.7: CA method 3D equiaxed dendrites. (a) 0° dendrite. (b) Randomly rotated dendrite.

4.4 Accounting for Existing Deformation

When creating the structural mechanics solver, one of the key considerations was how to keep track of how the shape has deformed as it continues to grow. Given the derivation of the linear elasticity equations in Chapter 3, we can see these equations can be solved in a transient and stationary manner, so this choice had to be made on the basis of what would best synergise with the coupling process.

Considering that solidification and the other physical modules act in a transient manner, it would seem intuitive that solid mechanics should be similarly treated as a transient process, updating the solution for the displacement as the shape solidifies and changes. However, a transient approach does offer complications in representing the behaviour of a solidifying structure

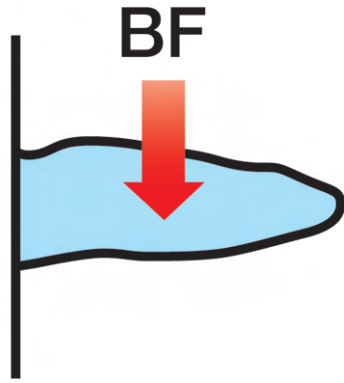
4. COUPLING STRUCTURAL MECHANICS TO SOLIDIFICATION

being resolved on a fixed Cartesian grid. As structural mechanics is solved, it generates a displacement profile which describes how the structure will deform from its original position which can then be used to drive solid advection process to move structures through the grid and/or to change the local growth orientation.

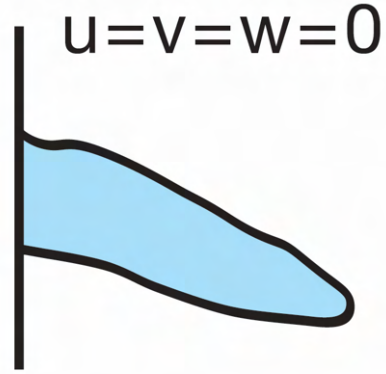
In the case of solid advection, keeping track of existing deformation is not a straightforward process as after the structure has ‘moved’, the deformation at the new position should be 0. Nonetheless, there will still be strains inside the structure which must be accounted for when solving subsequent time steps to limit unrealistic deformation. There is a similar problem with the orientation tracking being derived from the change in deformation at each time step. Given that a transient solution would be providing the absolute deformation of the structure, an older time step would need to be retained in order to obtain the local orientation changes which occur at each step.

For these reasons, it was decided that it would be preferable to solve successive stationary solutions to resolve the deformation at each time step. This is done by keeping track of the forces acting upon each volume of the structure, using the concept that for a structure growing under a constant body force, the force can only affect each cell of the structure once. In figure 4.8 an exaggerated example of this process can be observed where (a) the structure is subjected to a structural force; (b) these deformations are applied to moving the shape through the grid and changing the orientation before being reset; (c) the solidification solver will then run to generate more structure; (d) at the next call of the structural mechanics solver, the force will be calculated for the entire structure, but any force already applied will be removed so that the force will only act on cells which are newly solidified. This will deform the shape more and the process continues.

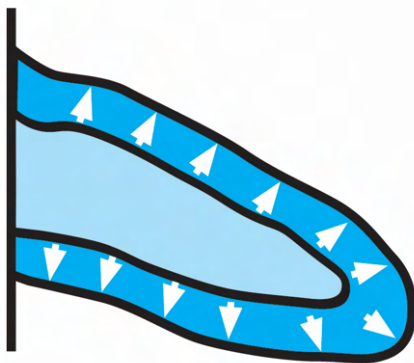
4. COUPLING STRUCTURAL MECHANICS TO SOLIDIFICATION



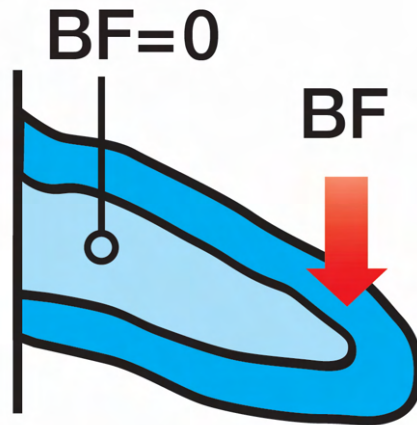
(a) Body force applied.



(b) Reset displacements on structure.



(c) Solidification creates more mass.



(d) Body force applied to new growth only.

Figure 4.8: Procedure for applying force to growing structures.

This approach relies on the force being stored locally for each cell, where the applied body force (ABF) value actually being used by the SMS at a given time step for each cell can be thought of as the following equation:

$$ABF_t(i, j, k) = BF_t(i, j, k) - BF_{t-1}(i, j, k) \quad (4.7)$$

4. COUPLING STRUCTURAL MECHANICS TO SOLIDIFICATION

With this approach, under a constant body force only newly solidified cells would have a force applied to them, but this is equally able to account for situations where the force changes, potentially applying forces in an opposing direction to the previous time step and undoing any deformation that occurred. The structural mechanics equations are still solved for the whole structure, so there will be a displacement profile generated for every solid cell, but the only forces driving these new displacements are found in parts of the structure where the force has changed since the prior time step.

In order to appraise how accurately this quasi-stationary approach can capture the transient accumulation of deformation in a growing structure, a test case tracking the deformation of a growing beam was constructed for comparison with a Beam Theory analytic solution for a cantilever beam under a distributed load (see 3.10.7). For the test, a beam with the following properties was used:

$$\text{Dimensions} = 20 \times 20 \times 120$$

$$E = 10 \text{ GPa}$$

$$\Delta x = 10 \text{ }\mu\text{m}$$

$$\rho = 7020 \text{ kg/m}^3$$

$$\text{Force} = \rho g \text{ N/m}^3$$

To represent a growing structure, a $20 \times 20 \times 20$ block was fixed to a wall in the manner of a cantilevered beam, this was then grown in 5 volume increments until it reached the final length of 120 volumes, applying force to the new growth and solving structural mechanics after each growth event before adding this to the existing deformation to obtain the overall deformation of the beam at that point in time, as can be observed in the selection of time steps shown in figure 4.9.

4. COUPLING STRUCTURAL MECHANICS TO SOLIDIFICATION

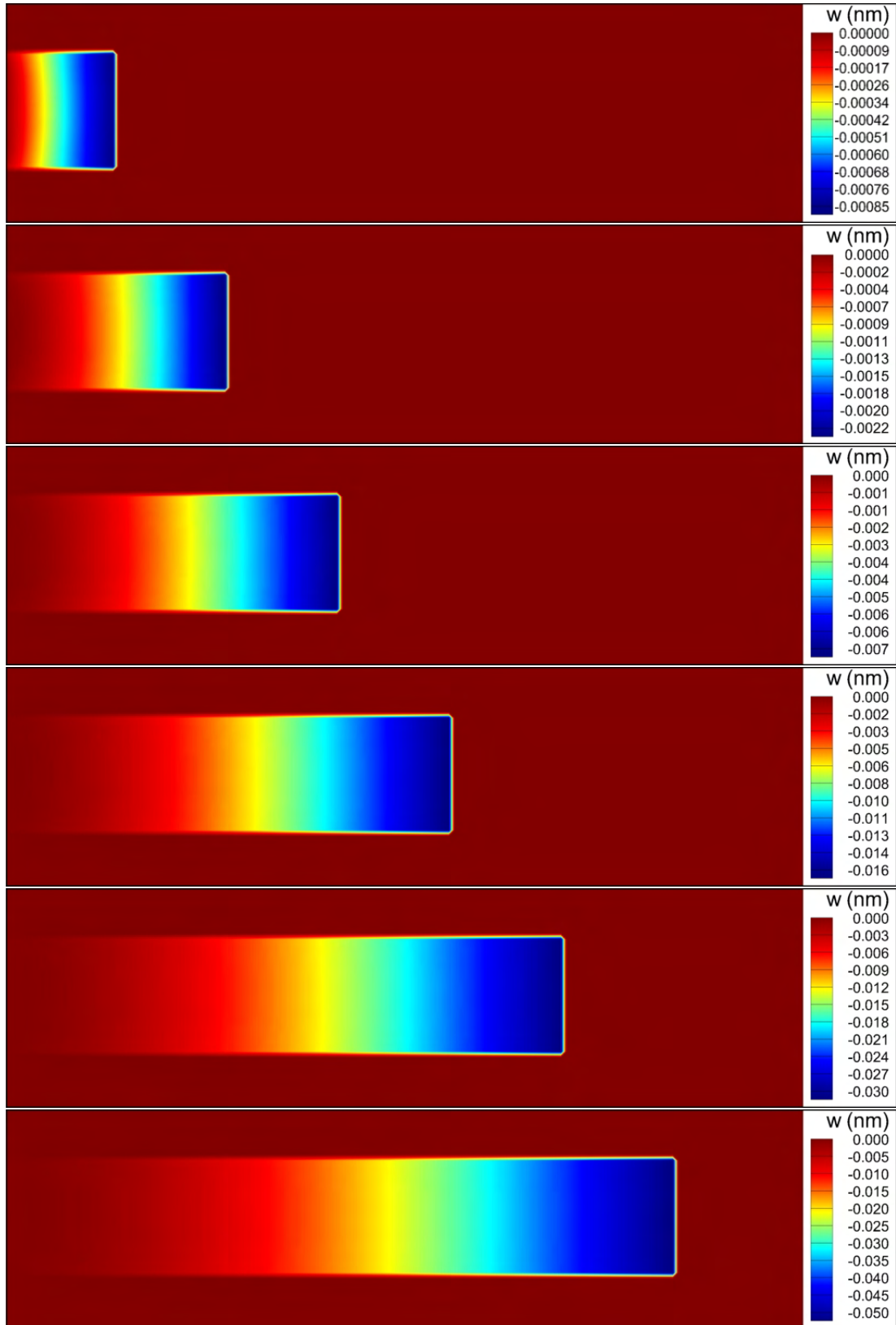


Figure 4.9: Deformation of a growing beam.

4. COUPLING STRUCTURAL MECHANICS TO SOLIDIFICATION

This is an idealised case where the beam simply grows by a fixed amount along the x axis, calculating the change in deformation to allow the beam to reach a stationary solution rather than directional solidification where the growth behaviour of the dendrites can be changed to create a different structure. As such, the final deformation profile obtained from this growing beam should match the case where a beam of length 120 was deformed from an initial state where it experiences no force, thereby matching the beam theory solution for the same beam.

This comparison has been demonstrated in figure 5.10, where the local deformations observed running through the centre of the grown beam at full length have been plotted alongside the predicted deformations from beam theory. While the grown beam does demonstrate a slight under prediction, it has a comparable values and behaviour to the beam theory solution. This would seem to indicate that this approach of applying successive deformations as the structure grows will provide a reasonable approximation to the true deformation behaviour a growing structure would experience.

4. COUPLING STRUCTURAL MECHANICS TO SOLIDIFICATION

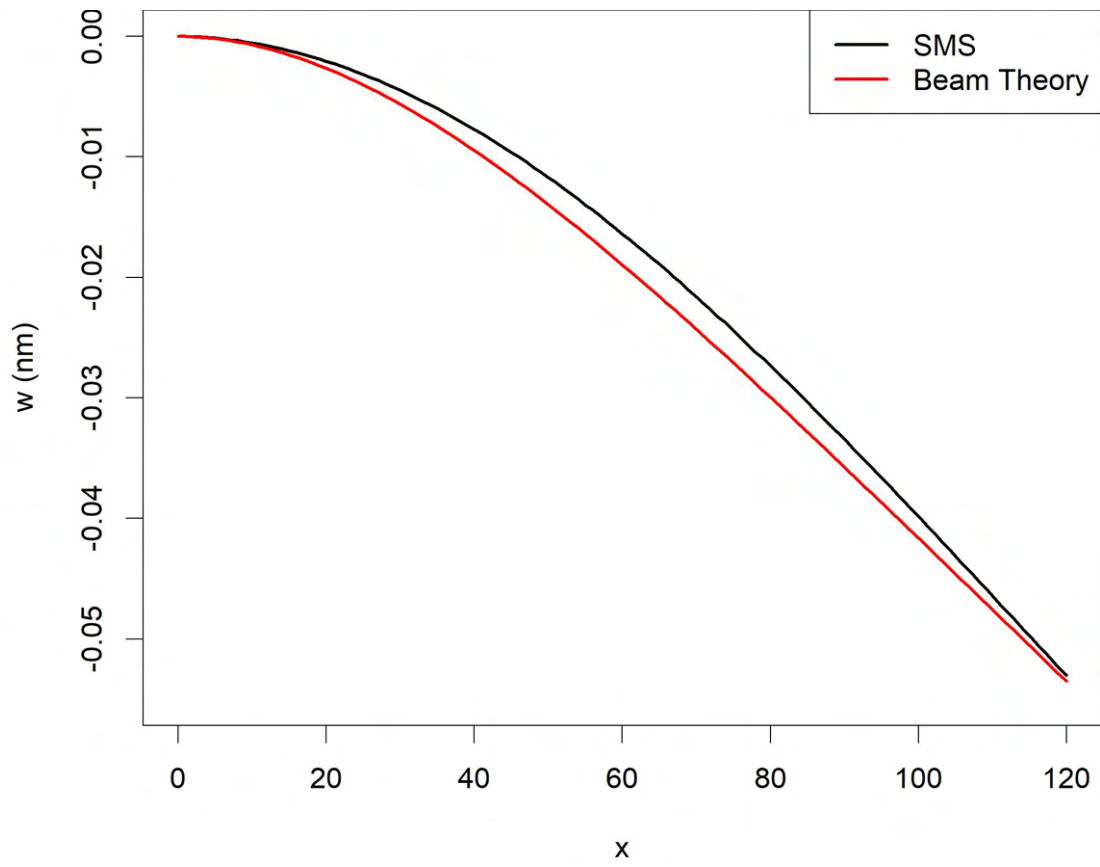


Figure 4.10: Final deformation of a grown beam.

4.5 Solver Performance Enhancements

As the SMS is currently using a point-by-point Gauss Seidel approach, there can be potential issues with the solution speed of large scale problems. This section will address the enhancements which have been implemented in order to reduce both the computational and real world time required to solve these larger problems.

4.5.1 Multi-Scale Modelling with Trilinear Interpolation

As mentioned prior, the problems being solved by TESA can include modelling multiple different numerical processes, structural mechanics and solidification for the simplest cases being examined, but this can be expanded to include other elements such as fluid flow and electromagnetism. One of the advantages of solving all these phenomena on a Cartesian grid means that any information can be easily passed between the solvers.

However, having all these grids linked in this way means that the grid resolution must be as fine as the most sensitive part of the solver requires, which can potentially lead to parts of the solver being solved at a much finer resolution than is required to get an accurate answer, costing computing power and real time unnecessarily. For this reason, grid multi-scaling was introduced for the structural mechanics, allowing structural mechanics to be solved at a coarser scale than the solidification solver.

In the current setup, this takes the solid fraction existing on a fine grid for solidification and aggregates these cells to obtain an average value for a corresponding cell on a coarser grid. This allows a smaller problem to be solved by the SMS, significantly shortening the solution time.

4. COUPLING STRUCTURAL MECHANICS TO SOLIDIFICATION

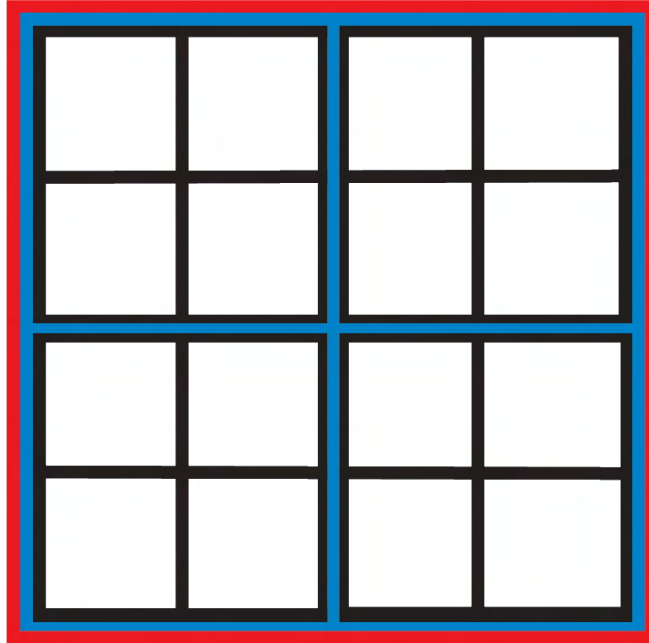


Figure 4.11: Overlaid 4×4 cells showing a multi-scaling of 2 (blue cells) and 4 (red Cell).

Figure 4.11 presents a 2D example of how this multi-scaling process relates different grid sizes, demonstrating how a 4×4 selection of cells on a fine grid be aggregated into 2×2 cells using a 2 cell multi-scaling, or a single cell using a 4 cell multi-scaling. The 2 and 4 cell scaling shown here is only an example, as odd numbered scaling and scaling going to higher numbers could also theoretically be used, providing the domain size was divisible by the scaling value.

This has been presented in 2D for ease of demonstration, but the solver in fact considers the 3D volumes when performing this process, which means the gains in computation time are even greater as by taking a $4 \times 4 \times 4$ group of computational cells on the fine grid, by applying multi-scaling you would reduce the cells from 64 to 8 for a scale factor of 2 and to a single cell for a scale factor

4. COUPLING STRUCTURAL MECHANICS TO SOLIDIFICATION

of 4.

This process of multi-scaling is generalised using the following pseudo-code to obtain a node on the coarse Volume Grid V_c (dimensions $\frac{nx}{s} \times \frac{ny}{s} \times \frac{nz}{s}$) from a fine volume grid V_f (dimensions $nx \times ny \times nz$) using a given scaling value S (where nx , ny and nz must all be divisible by S):

$$\text{for } i = 1 : nx, j = 1 : ny, k = 1 : nz$$

$$V_c(i, j, k) = \frac{1}{S^3} \left(\sum_{ui}^S \sum_{vj}^S \sum_{wk}^S V_f((i-1)*S + ui, (j-1)*S + vj, (k-1)*S + wk) \right)$$

Once the coarse grid is obtained, this can be used as the input for the SMS, which should now solve significantly faster. But once this coarse problem has been resolved, the displacements obtained will also be at a coarse resolution, meaning that they must be converted back to a finer grid so that they can act as inputs to other processes impacting the solidification behaviour.

The most straightforward approach would be to simply take the value of the coarse grid for all of the volumes it covers on the fine grid, as can be seen in figure 4.12, and can be conceptualised by the following pseudo-code describing the propagation of the coarse grid values onto the fine nodes:

$$\text{for } i = 1 : \frac{nx}{S}, j = 1 : \frac{ny}{S}, k = 1 : \frac{nz}{S}$$

$$\text{for } l = 0 : S - 1$$

$$V_s(i+l, j+l, k+l) = V_c(i, j, k)$$

4. COUPLING STRUCTURAL MECHANICS TO SOLIDIFICATION

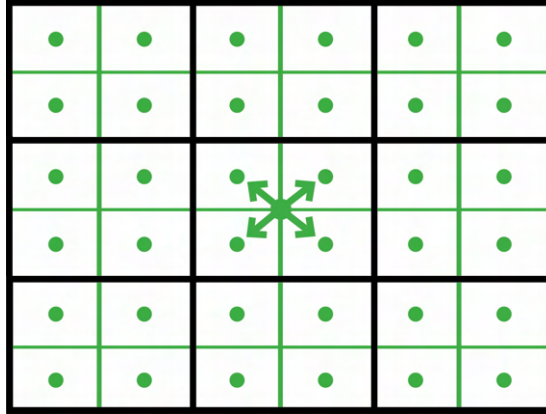
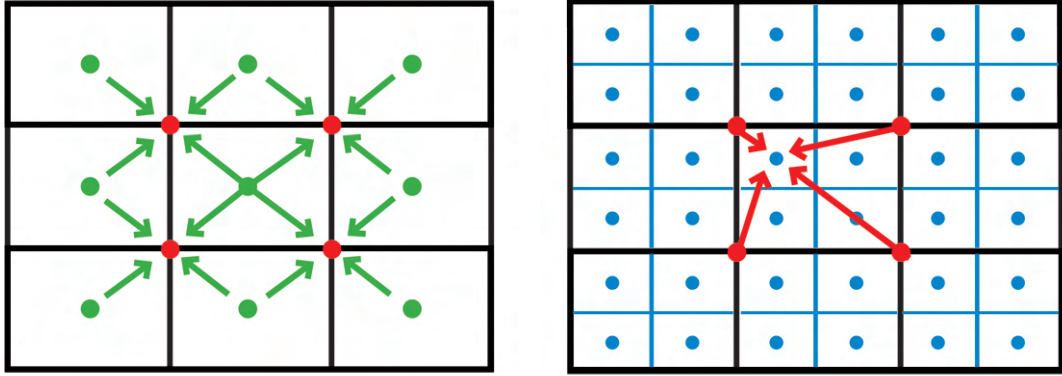


Figure 4.12: Copying coarse cell value into constituent fine cells.

However, this will provide blocky solutions, where the results for the structure will be made by groups of $S \times S \times S$ volumes of the same value. This may be acceptable for some applications, but especially if higher S values are used, this will fail to capture the realistic gradients of change that will be occurring at a finer resolution.

For this reason, it was decided to implement Trilinear Interpolation method, such as the one described by P. Bourke [99]. For the implementation in the case of the displacements, first on the coarse grid the displacements are interpolated to the corners of the volume as demonstrated in figure 4.13a (using a 2D example for visual clarity). Having these values at the corners of the volume allows the Trilinear Interpolation algorithm to obtain a value for any point inside of the volume where the value obtained considers how close the given point inside of the structure is to the corners, weighting the value accordingly, as demonstrated in figure 4.13b (again in 2D for visual clarity).

4. COUPLING STRUCTURAL MECHANICS TO SOLIDIFICATION



(a) Interpolates cell centre values to cell vertices. (b) Cell centre values on fine grid obtained using trilinear interpolation.

Figure 4.13: 2D trilinear interpolation example.

Once these corner values have been found, any point within the volume can be obtained by considering a cubic lattice where values at the vertexes can be used to obtain the target of the trilinear interpolation at the generic point $C(x, y, z)$ inside the volume (see figure 4.14). The distance between this point and the preceding coordinate in that plane can then be derived as follows:

$$x_d = \frac{x - x_0}{x_1 - x_0} \quad (4.8)$$

$$y_d = \frac{y - y_0}{y_1 - y_0} \quad (4.9)$$

$$z_d = \frac{z - z_0}{z_1 - z_0} \quad (4.10)$$

where x_0 is the x -coordinate at the face of the volume below the location of x , with x_1 being the location of the face above. The same principles applying to y_0 , y_1 , z_0 and z_1 ; see figure 4.14d. Initially, locations corresponding to a point along the edges of the volume at x position are interpolated, giving:

4. COUPLING STRUCTURAL MECHANICS TO SOLIDIFICATION

$$C_{(x,y_0,z_0)} = C_{(x_0,y_0,z_0)} * (1 - x_d) + C_{(x_1,y_0,z_0)} * x_d \quad (4.11)$$

$$C_{(x,y_0,z_1)} = C_{(x_0,y_0,z_0)} * (1 - x_d) + C_{(x_1,y_0,z_1)} * x_d \quad (4.12)$$

$$C_{(x,y_1,z_0)} = C_{(x_0,y_1,z_0)} * (1 - x_d) + C_{(x_1,y_1,z_0)} * x_d \quad (4.13)$$

$$C_{(x,y_1,z_1)} = C_{(x_0,y_1,z_1)} * (1 - x_d) + C_{(x_1,y_1,z_1)} * x_d \quad (4.14)$$

which can then be interpolated along the y axis in a similar way to obtain two further points:

$$C_{(x,y,z_0)} = C_{(x,y_0,z_0)} * (1 - y_d) + C_{(x,y_1,z_0)} * y_d \quad (4.15)$$

$$C_{(x,y,z_1)} = C_{(x,y_0,z_1)} * (1 - y_d) + C_{(x,y_1,z_1)} * y_d \quad (4.16)$$

finally allowing these two points to be interpolated along the z axis to obtain the desired point $C_{(x,y,z)}$:

$$C_{(x,y,z)} = C_{(x,y,z_0)} * (1 - z_d) + C_{(x,y,z_1)} * z_d \quad (4.17)$$

This presented approach is a general method for finding any location within the volume, but for this implementation the trilinear interpolation has been used to obtain the value at the cell centres of the volumes on the fine grid to provide a smoother representation of the displacement behaviour.

4. COUPLING STRUCTURAL MECHANICS TO SOLIDIFICATION

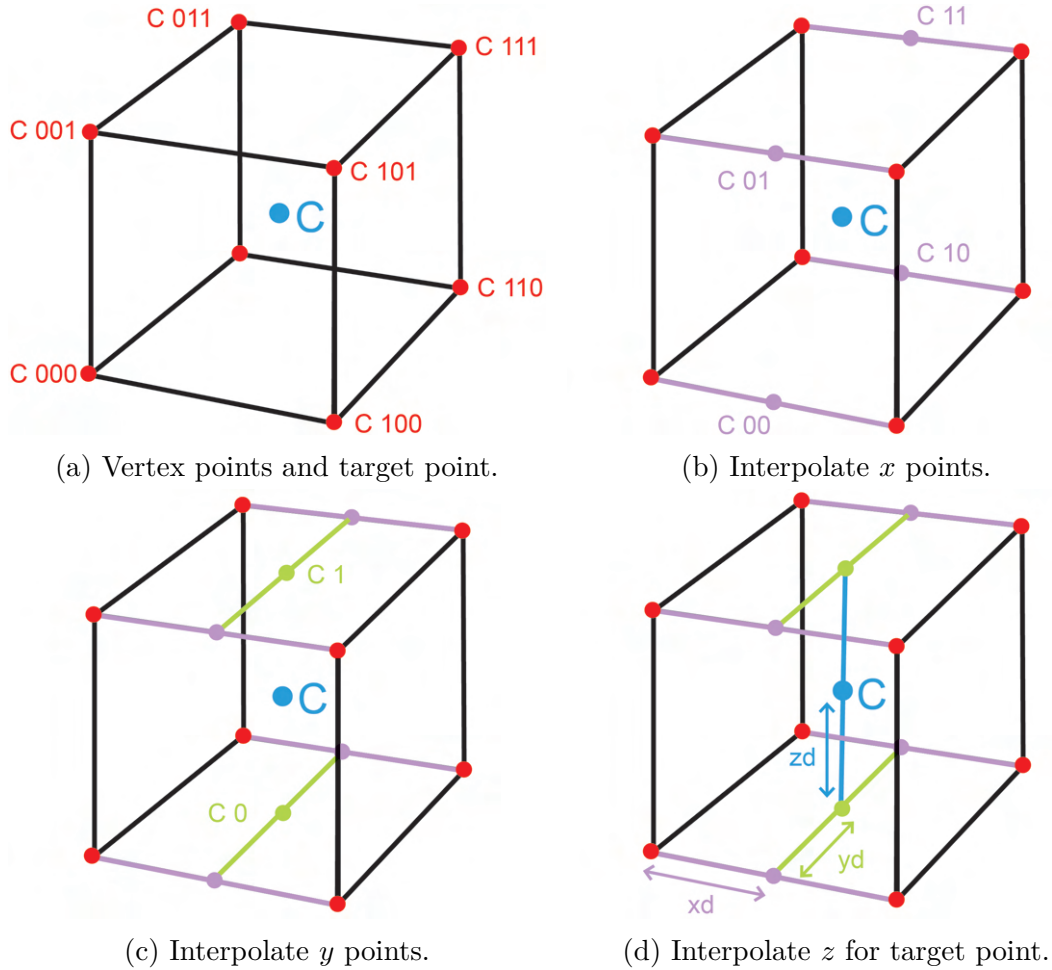


Figure 4.14: 3D trilinear interpolation process.

Using multi-scaling methods such as these will have implication for the accuracy of the displacements obtained, and hence any other metrics being derived from them. This impact is hard to measure in an absolute way however, as the degree to which the accuracy of the solution is reduced will be very problem specific, depending on how much lower than grid independence the fine grid is than the structural mechanics solver needs, as well as considering how much detail in the structure will be lost by aggregating the solid fraction onto a coarser grid and if this will have a significant effect on the mechanical

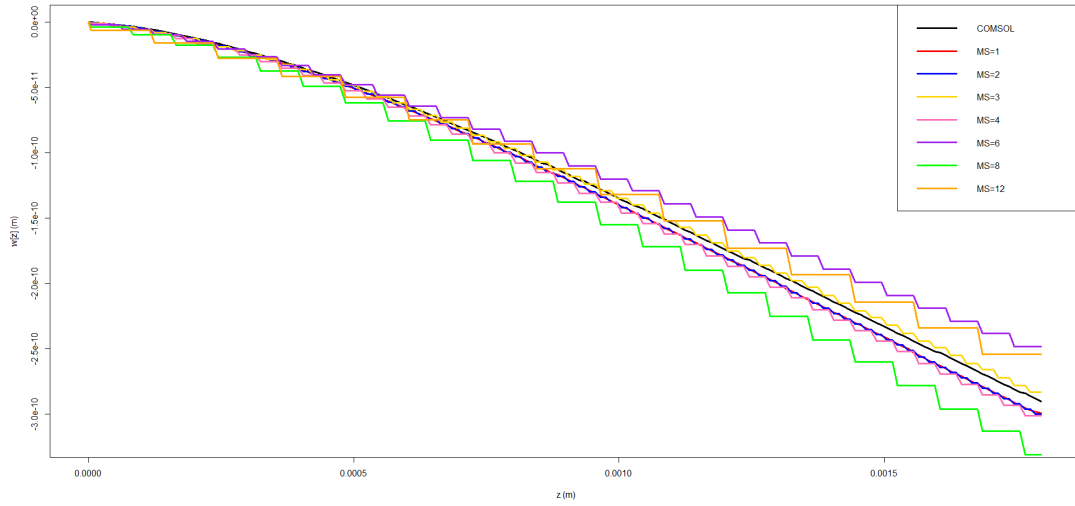
4. COUPLING STRUCTURAL MECHANICS TO SOLIDIFICATION

behaviour.

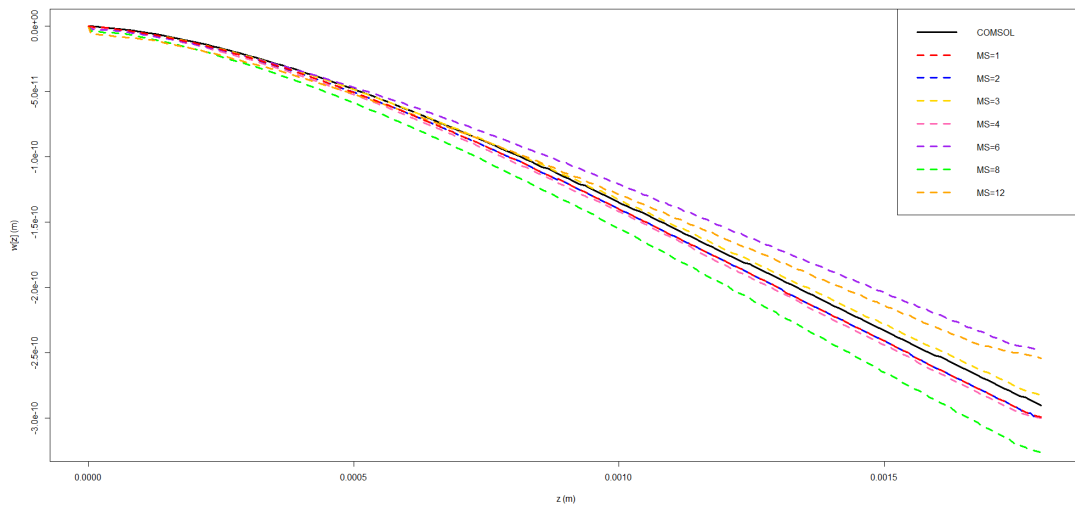
However, to provide a general idea of the impact of this approach for an idealised case, a cantilever beam was modelled using a selection of increasingly coarser multi-scaling grids (all sizes cannot be used as the structure has to be divisible by the coarse grid for an accurate solution for a structure with a sharp interface such as the beam being modelled). The displacement profiles generated by these models are not easy to visually distinguish, so for comparison a line running through the middle of the beam has been plotted in figure 4.15, which demonstrates that even for significantly coarser grids the SMS is still providing results of comparable accuracy and behaviour to both COMSOL and the SMS solution using the fine grid, while being considerably quicker to converge due to the smaller problem size.

To demonstrate the impact of trilinear interpolation, figure 4.15a shows the raw values of the multi-scaled solutions where significant discontinuities are caused due to simply copying the coarse value directly into all constituent cells on the fine grid. The smoother results obtained by applying the previously outlined trilinear interpolation process to these values can be observed in figure 4.15b.

4. COUPLING STRUCTURAL MECHANICS TO SOLIDIFICATION



(a) Raw multi-scaled solutions.



(b) Solutions after trilinear interpolation.

Figure 4.15: Accuracy comparisons for a beam using multi-scaled SMS vs COMSOL.

4.5.2 Parallel Programming

As previously mentioned in Section 4.2, TESA has been designed to utilise parallel computing to solve problems using potentially billions of cells. This allows problems to be examined which would take a prohibitive amount of real time to obtain using a serial computing setup. The parallel libraries have been developed and implemented to the existing elements of TESA prior to the commencement of this research, the details of this process, along with benchmarks for the performance of the parallel libraries can be found in existing published work [91, 98].

However, to ensure that the structural mechanics code does not act as a performance bottleneck when it becomes necessary to run large cases it was considered necessary to apply these principles to the structural mechanics solver. Consequently, this section will briefly outline how the parallel libraries were implemented for the SMS, as while existing parallel libraries were adopted for this task, there were complications unique to the SMS that required addressing.

The parallelisation process utilises a domain decomposition method to split the problem into sub-domains which can be solved by individual processors, only being limited by the number of processor cores available and if the geometry of the problem allows it to be split into equally sized sub-domains. In figure 4.16 an indicative example is shown of a domain being split in four subdomains which can then be solved simultaneously on four processors, where each processor has a domain comprised of computational cells and a one cell border of ‘halo region’ cells surrounding the domain to represent the boundaries where data is passed into the solver, but no computation occurs.

For the domain boundaries, this information will be defined elsewhere based on the boundary conditions used for the problem. For the inter-core boundaries,

4. COUPLING STRUCTURAL MECHANICS TO SOLIDIFICATION

the parallel libraries must be used to pass information between the cores (as highlighted by the coloured cells and arrows) which will be updated with each iteration of the solver, allowing the solution to propagate across all cores being employed so that it can converge to the same solution as would be observed if computed in serial. While the diagram is for a 2D problem, these principles can be scaled up for use with any number of processors potentially dividing the domain in all three dimensions, so long as the size of the domain in each dimension is divisible by the number of processors being used to split up and solve it.

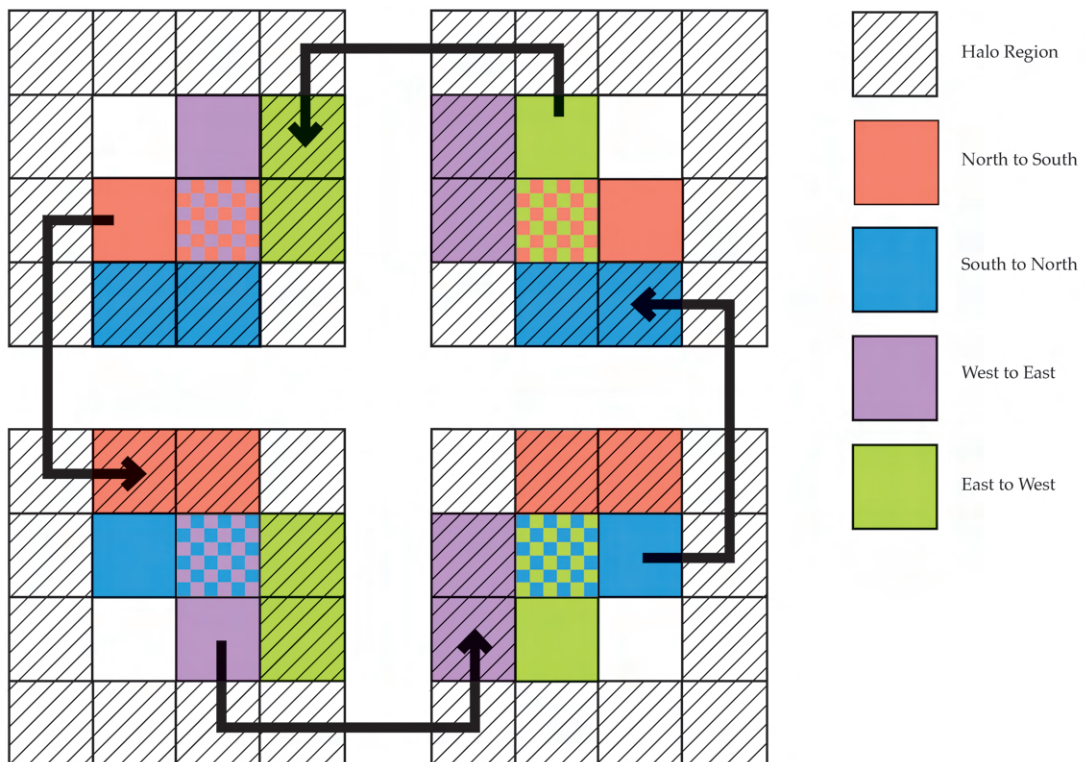


Figure 4.16: Boundary behaviour for a 2D system of four parallel processors.

A zoomed in example of how this works across a single boundary can be seen in figure 4.17a, where the halo-region containing the boundary information for each processor will be populated by the last computational cell in the domain of the other processor.

4. COUPLING STRUCTURAL MECHANICS TO SOLIDIFICATION

However, some slight changes had to be made to this for the SMS as this uses a staggered grid, meaning that while a cell centred domain was being used for most other variables, the displacements have one extra computational cell in the direction of staggering when compared to the cell centred quantities. To account for this, as demonstrated in figure 4.17b, each processor has been given an extra cell in the direction of staggering, these cells are ignored by the parallel libraries and the SMS on every processor except for the furthest processor(s) in the staggered direction, meaning that the number of cells being used to perform calculations matches the amount that would be required in serial.

The implementation of these parallel libraries with the SMS has allowed large scale problems to be run on Greenwich’s HPC using hundreds of processor cores, but even on a single work station using the parallel libraries to split the problem between all processor cores in this manner can obtain solutions in significantly faster times than if run in serial.

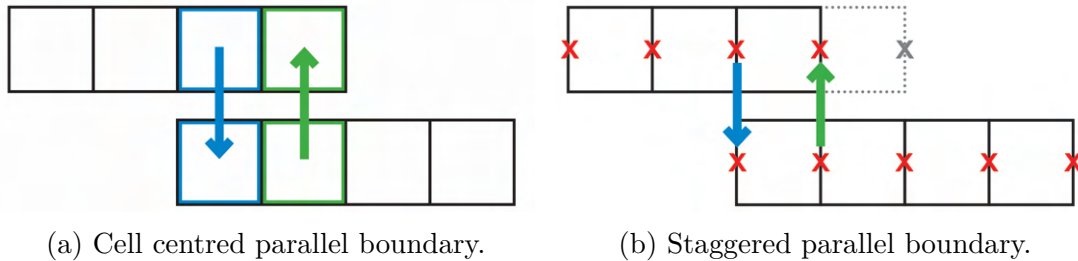


Figure 4.17: Comparison of cell centred and cell staggered parallel boundaries.

4.5.3 Enhancement Speed Impact

Quantifying the improvements in solution speed gained by using the solver enhancements discussed in this section is not a straightforward task for a coupled, multi-physics solver such as TESA. Parallel computing is seldom 100% efficient due to time taken in communication between the nodes and while multi-scale modelling can have a huge impact on reducing the solution time,

4. COUPLING STRUCTURAL MECHANICS TO SOLIDIFICATION

this is often limited by the level of accuracy required by the solutions.

Kao *et al.* [91] provides a summary of the parallel performance of the CA method on domain sizes of up to a billion cells. The parallel efficiency was found to vary between 60 – 70%, where 100% efficiency would mean that in real time the problem ran as many times faster as there are parallel nodes (so for example, a problem using 400 nodes would run 400 times faster than if only 1 node was used at 100% efficiency). It is also mentioned that multi-scale modelling is being employed for modelling the fluid flow, using a grid size four times larger than the one the CA method uses for solidification. This means that even when utilising 64 times fewer cells to model fluid flow than the rest of the solver, fluid flow still takes 1/3 of the total simulation time.

Aside from highlighting the necessity of using variable length scales in a more general sense, this is more directly pertinent to the SMS as a 4-1 grid scaling is also being applied to structural mechanics for the cases presented in Chapter 7 to improve the solution time. Having both structural mechanics and fluid flow solved using the same grid scaling may also prove to be helpful in future work where both processes are run for the same problem, as resolving both at the same length scale which would allow them to interact without having to interpolate solver outputs.

A full performance study to assess the efficiency of the SMS on the parallel libraries would be a very time consuming task to do properly while being of questionable benefit to the research. This is because the libraries had already been created prior to this project, have already been tested for the other models and there are future plans to improve the SMS to use more efficient methods than the currently applied point-by-point Gauss-Seidel method, which would render any insight from the study moot.

However, to provide a indication of the impact these solver enhancements

4. COUPLING STRUCTURAL MECHANICS TO SOLIDIFICATION

have had on the solution speed of the SMS, a speed test was performed on a simple problem where the entire $96 \times 96 \times 96$ (884736) volume domain was a solid fixed at all boundaries and subjected to a constant body force. The converged displacement profiles for this problem can be observed in figure 4.18.

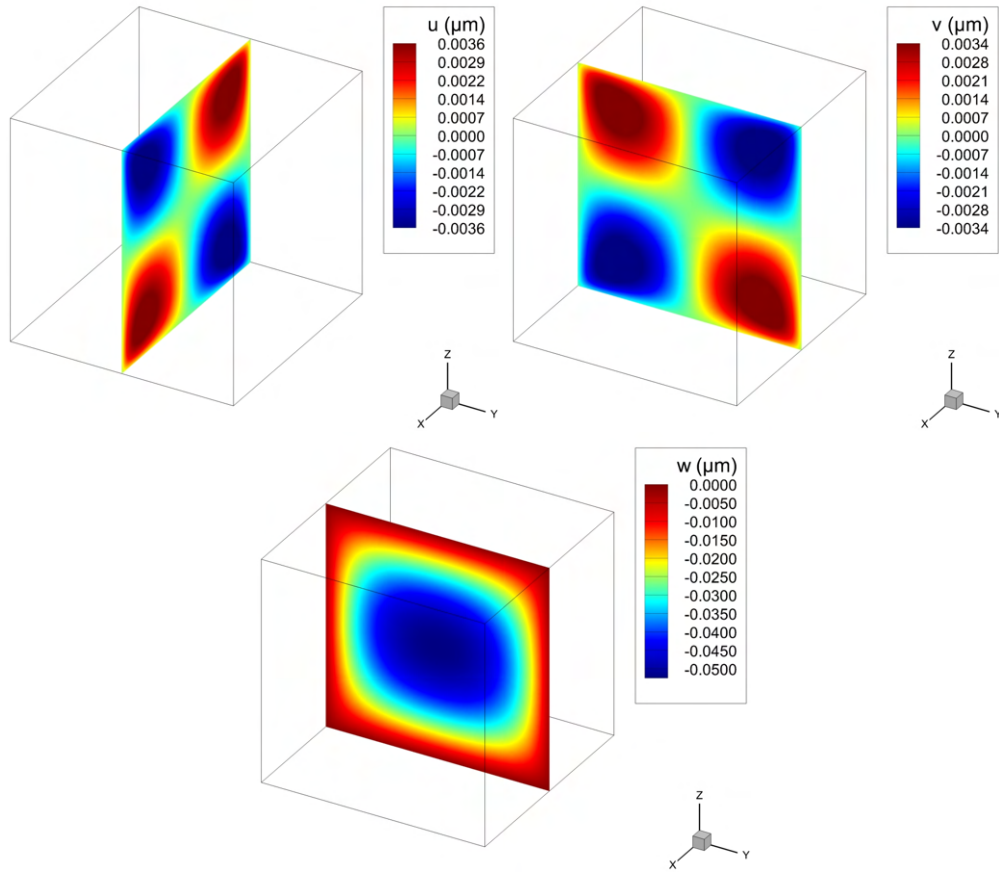


Figure 4.18: Displacement profiles for test case used to test timing.

This problem was solved using an increasing number of processor cores and grid sizes, including the interactions between applying different numbers of cores and grid sizes concurrently. The time in seconds to run the SMS to convergence for this problem under for all these cases have been summarised in table 4.1. This data clearly highlights the massive impact multi-scale modelling can have on solution time, as even on a single processor, the problem is nearly 150 times

4. COUPLING STRUCTURAL MECHANICS TO SOLIDIFICATION

faster using a 4-1 scaling factor (13824 cells) and is still over 25 times faster for a 2-1 scaling (110592 cells).

Multi-scale modelling can clearly be highly impactful in shrinking the problem and thereby lowering the computational complexity to allow for solutions to be obtained faster by potentially orders of magnitude. However, for many more complex problems there is a strict limit to how much the scaling can be increased before the answers obtained are effectively useless due to the behaviour of interest being too precise to capture on coarse grid resolutions. As such, while in theory the grid could be scaled such that any problem could be solved quickly, in reality to actually capture complex phenomena in reasonable times using parallel programming to share the computational load between many computers is a more practical solution. Looking at the parallel timings in table 4.1, it can be seen that even at 1-1 grid scaling, the problem can be solved in significantly less real time when run using multiple cores.

There are clear inefficiencies due to processor communications, with the case with 2 cores not quite being 2 times faster, and so on as the number of cores being applied increases. It is notable that while still significantly faster in real time, the 16 core job is far less efficient than the other cases being only 78% efficient while for the other cases the efficiency was above 90%. This is likely due to the way the domain had to split up to facilitate running on 16 cores leading to domains with surface areas which exacerbate communication inefficiencies, which highlights a common concern of choosing the best dimensions for domain decomposition to maximise efficiency.

For the cases including both multi-scaling and multiple cores the efficiency seems to grow even lower due to the progressively smaller domain sizes where the number of cells at the surface of the domain becomes relatively large compared to the total number of cells, which increases the relative amount of time spent on

4. COUPLING STRUCTURAL MECHANICS TO SOLIDIFICATION

communications between domains. Regardless, by applying 16 cores and a 4-1 scaling to this problem, the initial solution time of nearly 25 minutes can now be reduced to a single second, truly highlighting the power of these enhancements in shortening the real time required to obtain solutions.

Cores	Grid Scaling		
	1	2	4
1	1493	59	10
2	781	41	6
4	379	22	3
8	199	12	2
16	119	7	1

Table 4.1: Timing data in seconds comparing real time improvements from parallel computing and multi-scale modelling.

4.6 Summary

In this chapter a summary was provided for the TESA framework which the SMS was specifically designed for integration with. This gave a brief description of the individual solvers and how they relate to one another, which was expanded in the following section to describe the applied solidification models in greater detail. The novel process of how existing deformation is accounted for by the SMS was described. Finally, the processes of multi-scale modelling and parallel programming were introduced, where it was explained how these solver enhancements were implemented to allow for faster solution times to be attained.

Chapter 5

STRUCTURAL CHANGES TO DENDRITE ORIENTATION

5.1 Overview

This section discusses the dendrite orientation methodology used by the CA method and how local orientations were implemented such that they could be updated by the outputs from the SMS. The requirement for a local definition of dendrite orientation is introduced, explaining the relationship between intrinsic Euler angle orientation and CA method growth. A method is then implemented to allow for the changing of these angles using the displacement outputs from structural mechanics, with the accuracy of this approach assessed theoretically then verified using an idealised test case.

5.2 Local Orientation Tracking

In the Cellular Automata (CA) method (see section [4.3.2](#)), a dendrite has a fourfold symmetry that will cause it to grow into a symmetrical crystal. In

5. STRUCTURAL CHANGES TO DENDRITE ORIENTATION

previous work undertaken with TESA, in order to replicate experimental results dendrite grains would be seeded with a starting orientation¹ estimated from analysing the experimental results and using Euler angle transformations to determine the preferential growth of the solidification.

By pre-seeding an orientation in this manner, dendrites growing at any given orientation can be obtained, with approaches such as this being employed in almost all of the papers discussed in section 2.3 which were concerned with dendritic orientation in numerical modelling. However, dendrites with pre-seeded orientations will remain fixed at this orientation throughout the simulation, so experimental results such as those presented as motivation in section 2.2 demonstrating dendritic growth where the orientation changes as the structure develops cannot be replicated by this modelling.

In order to address this shortcoming, the approach has been expanded so that rather than having a single orientation for each grain, the orientations are instead localised – with each computational volume used by the structure having a unique orientation variable. This allows the orientation of the dendrite to vary as it grows and even allow individual arms growing from a grain to develop and grow in entirely different orientation to the main body of the starting dendrite.

For the CA method, intrinsic Euler angles are required in the form of a ZXZ rotation matrix. Intrinsic rotations are able to describe any given orientation in 3 dimensional space by using a combination of 3 rotations about the axis relative to the moving body, that is to say that the reference axes are moved with each rotation. As implied by the name, a ZXZ Euler Angle matrix rotates around the Z axis, the new X axis then finally the new Z axis to describe a rotation in 3D space. This principle of intrinsic rotations is demonstrated in figure 5.1,

¹In some of the diagrams and examples of behaviour presented in this section, values in degrees (°) may be used to aid clarity when understanding the observed behaviour, but within the code itself radian values are used.

5. STRUCTURAL CHANGES TO DENDRITE ORIENTATION

demonstrating a generic ZXZ rotation on the axis and the corresponding volume, with the arrow at the top of the cube indicating the current orientation of the volume.

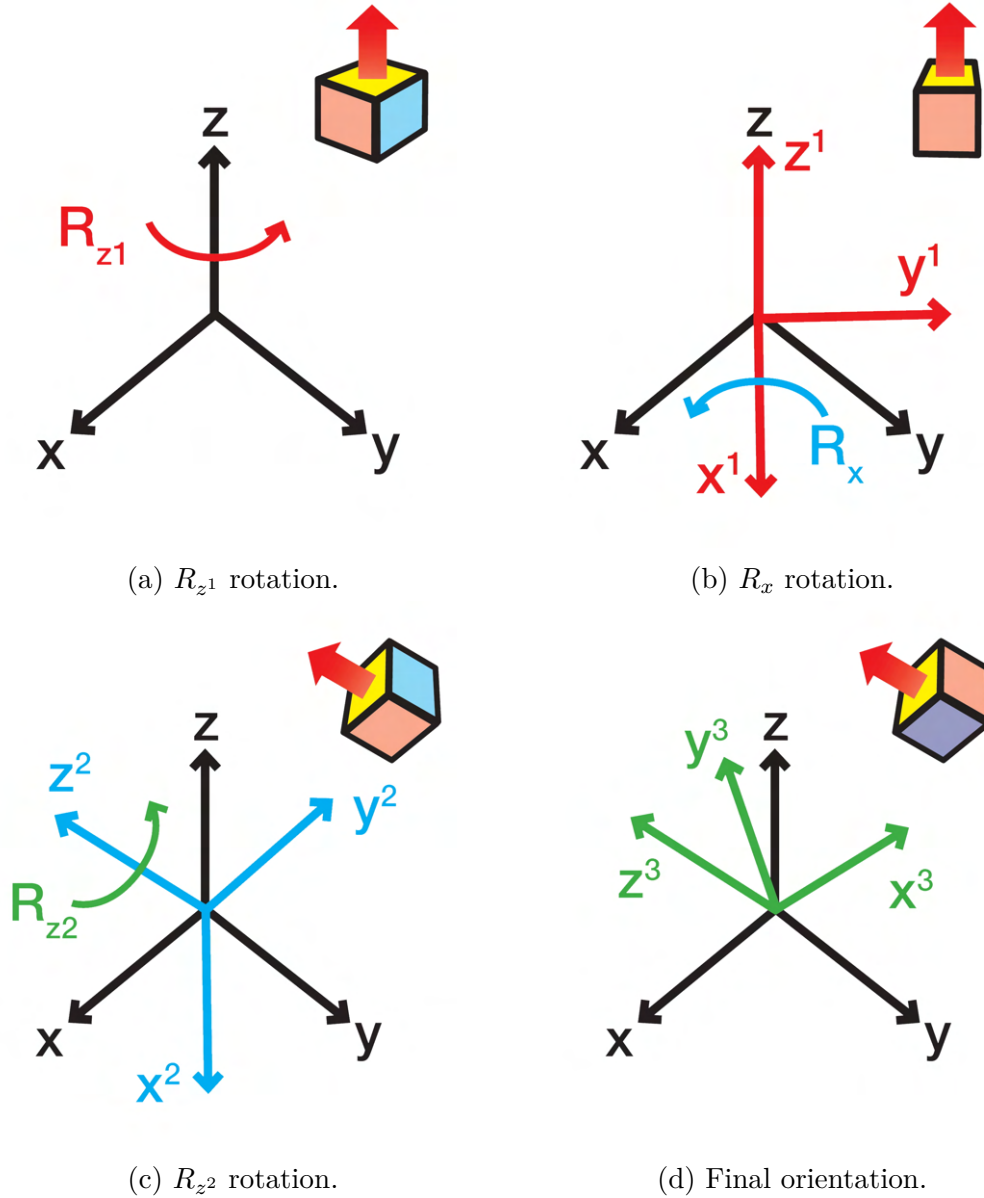


Figure 5.1: Intrinsic rotation example.

Prior to the implementation of the localised orientations, the fixed orientation

5. STRUCTURAL CHANGES TO DENDRITE ORIENTATION

of a dendrite was attached to a given grain number. However, now each volume has its own orientation, this local orientation needs to be tracked and passed on to any new volumes the dendrite seeds as it grows, allowing new growth to continue developing in the correct direction. This behaviour has been integrated into the CA method, so that whenever a new volume is seeded by solidifying material that volume will inherit the orientation of the volume which seeded it.

When considering structural mechanical behaviour in this context, the need for local orientation becomes clear, as if you consider a long dendrite which experiences a significant force at the tip, that may cause a relatively large change in the local orientation at this location while barely changing the orientation further down the arm of the dendrite (or indeed in any secondary arms growing from these regions). Even though no further force may be applied, having localised orientation ensures that any further growth will retain a memory of the previous orientation changes as new volumes are seeded and growth continues.

5.3 Displacement Driven Orientation Change

For the localised orientation approach to work, a framework for using the displacements to change the orientation of a volume needed to be developed. As the objective of this was to make a generic and local process, it was imperative for this approach to be able to function without using only information which could be obtained from the surrounding volumes.

A process was developed to take the input of the u , v and w displacements and from these generate a collection of ZZZ rotation matrices for every volume comprising the structure.

By considering the case of a single volume, due to the nature of the

5. STRUCTURAL CHANGES TO DENDRITE ORIENTATION

staggered grid, there exists a deformation at each face of the volume. However, by considering these displacements in figure 5.2, it can be seen that by applying these deformations to the volume it would only be deformed, not rotated.

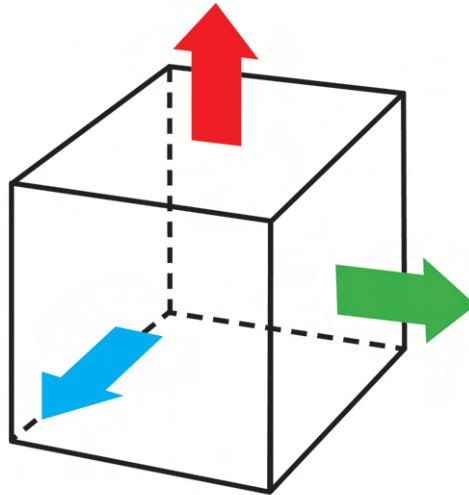


Figure 5.2: Displacements normal to cube faces.

However, by considering the deformations of the surrounding volumes, it is trivial to interpolate the displacements so that there are values for all three displacements located at each face, as shown in figure 5.3 (though this example only shows a 2D example with two displacements for visual clarity). Due to the way the staggered grids line up, the interpolation process finds a point in the middle of four staggered displacement nodes, providing each volume face with tangential displacements as indicated in figure 5.4.

5. STRUCTURAL CHANGES TO DENDRITE ORIENTATION

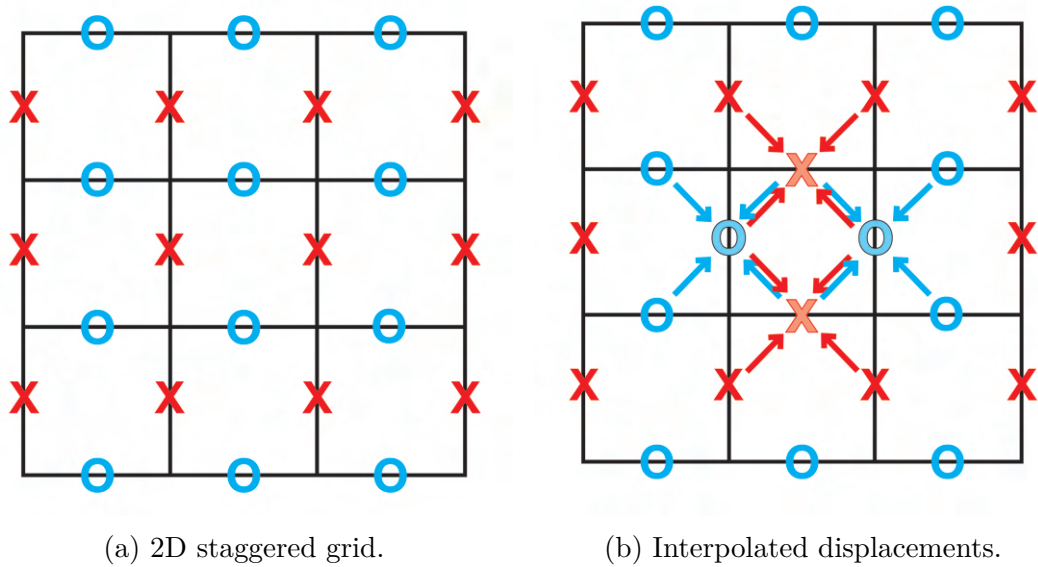


Figure 5.3: Method of interpolating displacements on all faces of a volume.

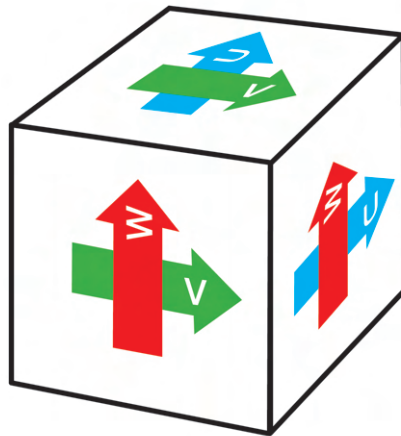


Figure 5.4: Displacements tangential to volume faces.

Now that the displacements along each axis have been obtained at each face, it can be considered how this movement at the face of the volumes will change the overall orientation of the volume. This has been done by treating the cubic volume

5. STRUCTURAL CHANGES TO DENDRITE ORIENTATION

as a sphere with a diameter of Δx , then the three rotations around the fixed x , y and z axis can be established by considering the 2D cases of a Δx diameter circles being rotated around their respective axis as shown for a rotation around the z axis in figure 5.5.

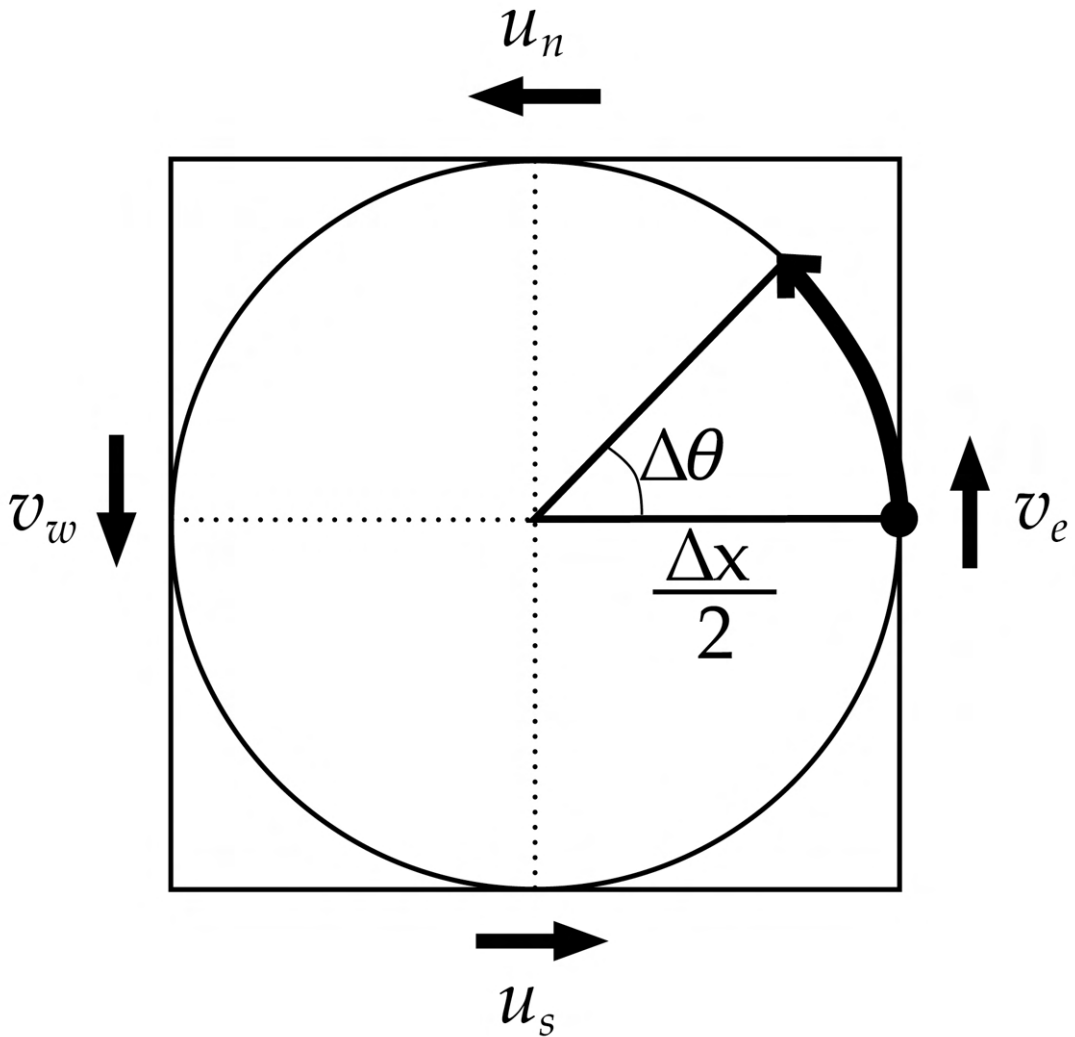


Figure 5.5: Obtaining $\Delta\theta$ from interpolated displacements.

The angle $\Delta\theta$ is obtained by taking the average of the combined displacements to describe the amount this imagined circle has rotated around the axis from its original position, which is here being displayed as a straight line from the central

5. STRUCTURAL CHANGES TO DENDRITE ORIENTATION

point to the East face of the volume. But this is simply a convention, as due to the fourfold symmetry the same behaviour could be demonstrated using a line drawn from the centre to any of the volume faces. Note, the angle here is defined as $\Delta\theta$ as it is a change in orientation from whatever the current orientation may be, with the current value of θ having no impact on the calculation of $\Delta\theta$.

This change in orientation can be obtained using the geometrical formula for the length of a circle arc, again considering figure 5.5, the length of the arc A is described by taking the average of the displacements acting to rotate the volume:

$$A = \frac{1}{4}(v_e - v_w - u_n + u_s) \quad (5.1)$$

$$r\Delta\theta = A \quad (5.2)$$

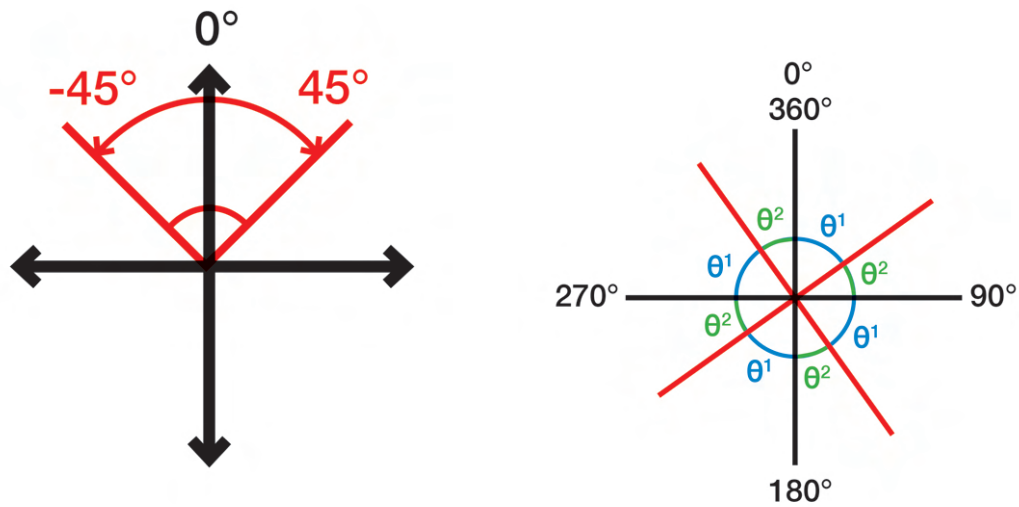
$$\frac{1}{2}\Delta x\Delta\theta = \frac{1}{4}(v_e - v_w - u_n + u_s) \quad (5.3)$$

$$\Delta\theta = \frac{1}{2\Delta x}(v_e - v_w - u_n + u_s) \quad (5.4)$$

Having obtained this angle to describe the change in volume orientation it is useful to make a note of the behaviour of the four-fold symmetry governing dendrite development in the CA method. Within this framework there is only a meaningful range of $90^\circ(\pm 45^\circ)$ around the default orientation corresponding to the fixed axis, as seen in figure 5.6a. This is because the four-fold growth symmetry of the crystals means that for any given orientation there are three complementary orientations (in the range 0-360°) at which the structure will grow identically as indicated in figure 5.6b. For example, a rotation of +50 degrees from the starting orientation is identical to a rotation of -40° or +140°

5. STRUCTURAL CHANGES TO DENDRITE ORIENTATION

(or any other corresponding rotation satisfying the symmetry). This simplifies the problem to an extent, as the solidification method will accept any of these symmetrical rotations as an input and behave correctly.



(a) 90° Region of Orientation Change

(b) Fourfold Symmetry Relations

Figure 5.6: Orientation changes with four-fold symmetry.

This allows orientation change to accumulate to large values without requiring any special treatment, though for the case of bending linear elastic dendrites orientation change of this scale this should not often occur in many of the cases being examined in this research. However, in the case of a twisting dendrite (see case 7.8), where a dendrite arm grows long enough under a torsional force it is not unreasonable that it may accumulate large changes in orientation as it twists across the domain.

Furthermore, this behaviour could prove essential for cases of tumbling dendrites which have been highlighted as a potential area for future work (see the rotating dendrite in figure 6.18 in Chapter 6 for a more limited example of a

5. STRUCTURAL CHANGES TO DENDRITE ORIENTATION

dendrite spinning in place), as these falling dendrites may spin round their axis many times as they move through the domain to accumulate a rotation which may be very large when measured from their initial position. In these scenarios, even if the total orientation change accumulates to hundreds or even thousands of degrees, the solidification process will simply consider this rotation in relation to how much it varies ± 45 from the fixed axis and grow accordingly.

In this manner, by considering the three 2D rotations about each axis the overall rotation of the volume in 3D space can be defined. However, these three rotations are not the intrinsic Euler Angle rotations about relative axes that the CA method requires, these are extrinsic rotations about fixed axes. A demonstration of how extrinsic rotations can be used to rotate a structure in three-dimensional space can be seen in figure 5.7, to be compared with rotations using intrinsic rotations shown earlier in figure 5.1. Nevertheless, any given 3D orientation can be described as a combination of three rotations, whether intrinsic or extrinsic.

5. STRUCTURAL CHANGES TO DENDRITE ORIENTATION

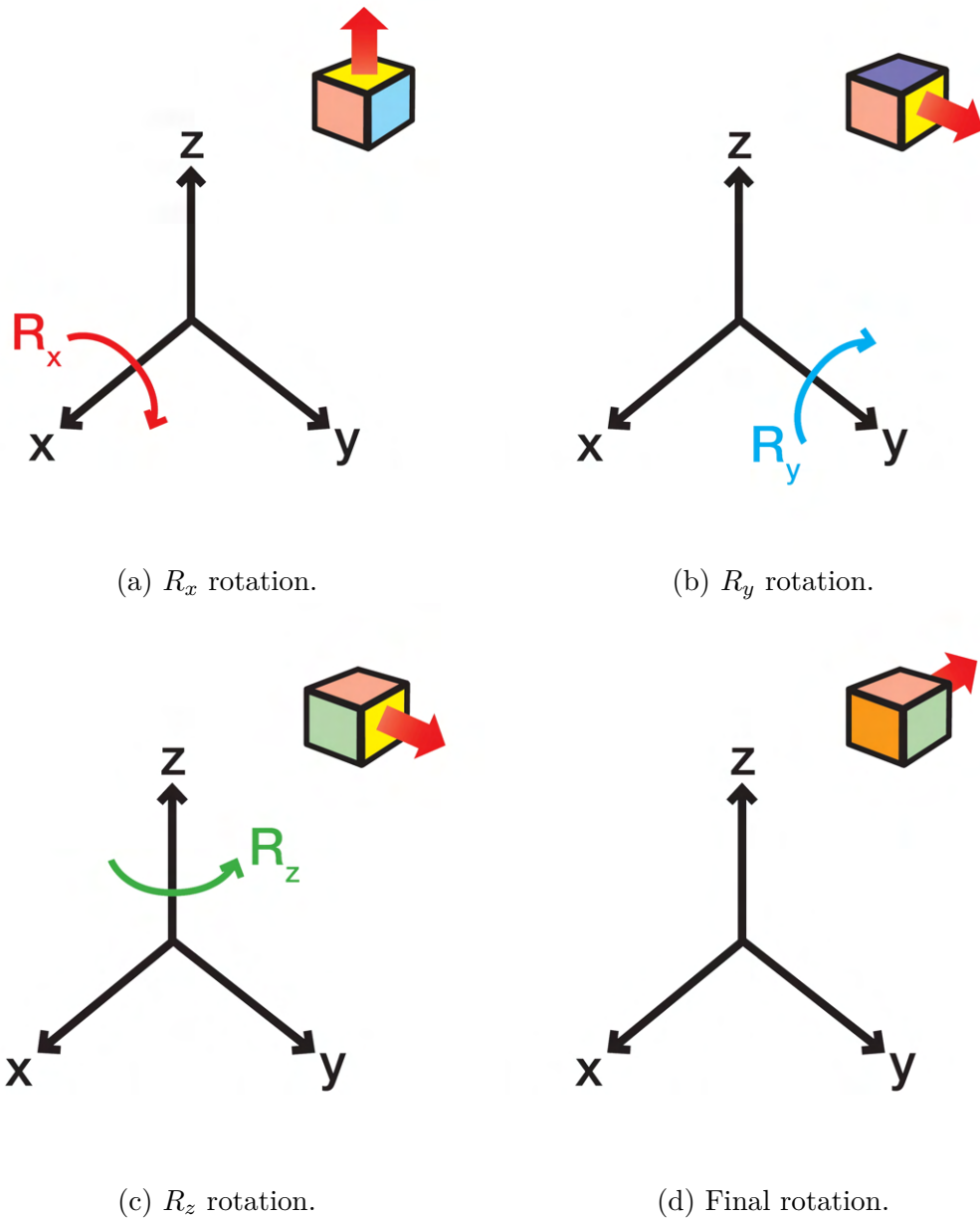


Figure 5.7: Extrinsic rotation example.

A process using the methods outlined by Eberly (2008) [100] was used to construct 3D rotation matrices using these extrinsic rotation angles and then extract intrinsic Euler angles was implemented. For this, the extrinsic rotations

5. STRUCTURAL CHANGES TO DENDRITE ORIENTATION

were combined into a 3D rotation matrix which maps ZYX¹ extrinsic rotations around the fixed axes.

A 3D rotation matrix describing the combination of the three successive ZYX extrinsic rotations $R_z(\theta_z)$, $R_y(\theta_y)$ and $R_x(\theta_x)$ can be obtained as follows:

$$\mathbf{R} = R_z(\theta_z)R_y(\theta_y)R_x(\theta_x) = \begin{bmatrix} r^{11} & r^{12} & r^{13} \\ r^{21} & r^{22} & r^{23} \\ r^{31} & r^{32} & r^{33} \end{bmatrix} = \tag{5.5}$$

$$\begin{bmatrix} \cos(\theta_x) \cos(\theta_z) & \cos(\theta_z) \sin(\theta_x) \sin(\theta_y) - \cos(\theta_x) \sin(\theta_z) & \cos(\theta_x) \cos(\theta_z) \sin(\theta_y) + \sin(\theta_x) \sin(\theta_z) \\ \cos(\theta_y) \sin(\theta_z) & \sin(\theta_x) \sin(\theta_y) \sin(\theta_z) + \cos(\theta_x) \cos(\theta_z) & \cos(\theta_x) \sin(\theta_y) \sin(\theta_z) - \cos(\theta_z) \sin(\theta_x) \\ -\sin(\theta_y) & \cos(\theta_y) \sin(\theta_x) & \cos(\theta_x) \cos(\theta_y) \end{bmatrix}$$

Then from this rotation matrix, the ZXZ Euler angles required by the CA method can be extracted using the following process written in pseudo-code:

¹The choice of ZYX rotation matrix is arbitrary, as the combination of these extrinsic rotations in any order would generate a valid rotation matrix for this process

5. STRUCTURAL CHANGES TO DENDRITE ORIENTATION

$$\begin{aligned}
 & \textit{if} (r_{33} < 1) \\
 & \quad \textit{if} (r_{33} > -1) \\
 & \quad \quad \theta_{z1} = \text{atan2}(r_{13}, -r_{23}) \\
 & \quad \quad \theta_x = \text{acos}(r_{33}) \\
 & \quad \quad \theta_{z2} = \text{atan2}(r_{31}, r_{32}) \\
 & \quad \textit{else if} (r_{33} = -1) \\
 & \quad \quad \theta_{z1} = -\text{atan2}(-r_{12}, r_{11}) \\
 & \quad \quad \theta_x = \pi \\
 & \quad \quad \theta_{z2} = 0 \\
 & \quad \textit{end if} \\
 & \quad \textit{else if} (r_{33} = 1) \\
 & \quad \quad \theta_{z1} = \text{atan2}(-r_{12}, r_{11}) \\
 & \quad \quad \theta_x = 0 \\
 & \quad \quad \theta_{z2} = 0 \\
 & \quad \textit{end if}
 \end{aligned} \tag{5.6}$$

As the shape grows and deforms further the angle of orientation can accumulate and change, consequently it was necessary to store the orientation information for each volume. The most straightforward way found to do this was to store the extrinsic rotations about the ZYX axis, which could be updated by calculated $\Delta\theta$ values to account for changes in rotation angle before being converted at any time to the intrinsic Euler Angle form required by the CA method.

5.4 Displacement Driven Orientation Change Verification

The review of the literature indicates that using the displacements obtained from structural mechanics to drive a change in a structure's orientation is a novel approach, as such it was necessary to confirm that this provides an acceptably accurate approximation of orientation change in a growing structure as caused by the application of concurrent structural mechanics.

This was first done theoretically, by simplifying the problem to consider a cantilevered beam as described by the Euler-Bernoulli beam theory (see section 3.10.6) and considering the relationship between the deformation and orientation change of a beam (see chapter 9 of 'Mechanics of Materials' by J. Geere [101] for more details).

If a beam of length L is subjected to a force causing a deflection w , as can be seen in figure 5.8a this allows the angle of rotation for the entire beam to be described using the tangent trigonometric identity as:

$$\theta = \tan^{-1}\left(\frac{w}{L}\right) \quad (5.7)$$

To relate this back to solidification this means that if a beam grew to length L at the angle θ , the tip of that beam would be in the same location as if the beam grew at angle $\theta = 0$ to length L and was deformed by w . However, while we are able to assume that both the grown and deformed beam are essentially identical in length due to the infinitesimal deformations implied by beam theory, in the exaggerated example in the figure the morphological differences between the straight grown beam and bent deformed beam are obvious. The problem this causes has been highlighted in figure 5.8b where the obtained angle θ is not the

5. STRUCTURAL CHANGES TO DENDRITE ORIENTATION

angle of orientation at the tip of the deformed dendrite. Meaning that while the deformation can be accounted for by growth at a given angle, any further growth will be incorrectly aligned.

Behaviour such as this highlights why it is important for the orientation of the dendrites to be stored locally for each volume rather than having a fixed orientation for the entire structure. Considering the bent beam in figure 5.8c, much as the local deformation $w(x)$ varies depending upon location along the beam, there is a varying local orientation $\theta(x)$ along the length of the beam that can be conceptualised as the angle between the x axis and the tangent of the deflection curve at that point. Here the beam has only been split at $x = L$ and $x = L + \Delta x$, where the distance between L and $L + \Delta x$ has been made significant for clarity.

In reality the beam can be subdivided into any number of points with corresponding orientations, where as the subdivision causes Δx to shrink, the difference between successive orientations $\Delta\theta$ will correspondingly also shrink. These local orientations can be obtained using the slope of the deformation curve, which is by definition the first derivative $\frac{d}{dx}w(x)$ of the deformation w , and as shown in figure 5.8d where for a section of the deformation curve the angle of rotation can be defined as:

$$\frac{d}{dx}w(x) = \frac{w(L + \Delta x) - w(L)}{(L + \Delta x) - L} = \frac{\Delta w}{\Delta x} = \tan(\theta(x)) \quad (5.8)$$

where due to the small deformation assumptions being used by linear elasticity, the angle of rotation will be correspondingly small. This means that $\tan(\theta) \approx \theta$, allowing the equation to be further simplified to:

$$\theta(x) = \frac{\Delta w}{\Delta x} \quad (5.9)$$

5. STRUCTURAL CHANGES TO DENDRITE ORIENTATION

which is in fact a 1D version of the equation 5.4 formulated earlier to describe the orientation change from displacements.

Using this approach, the local orientation along the length of a deformed beam can be calculated from the local displacements, allowing the physical deformation to be accounted for by a change in orientation as demonstrated in figure 5.8a, but by subdividing the beam into increments of Δx any growth using the approximation of $\theta(x)$ will match the true behaviour of the deformed beam increasingly closely as Δx grows smaller, with it having an approximately correct tip orientation for any future growth.

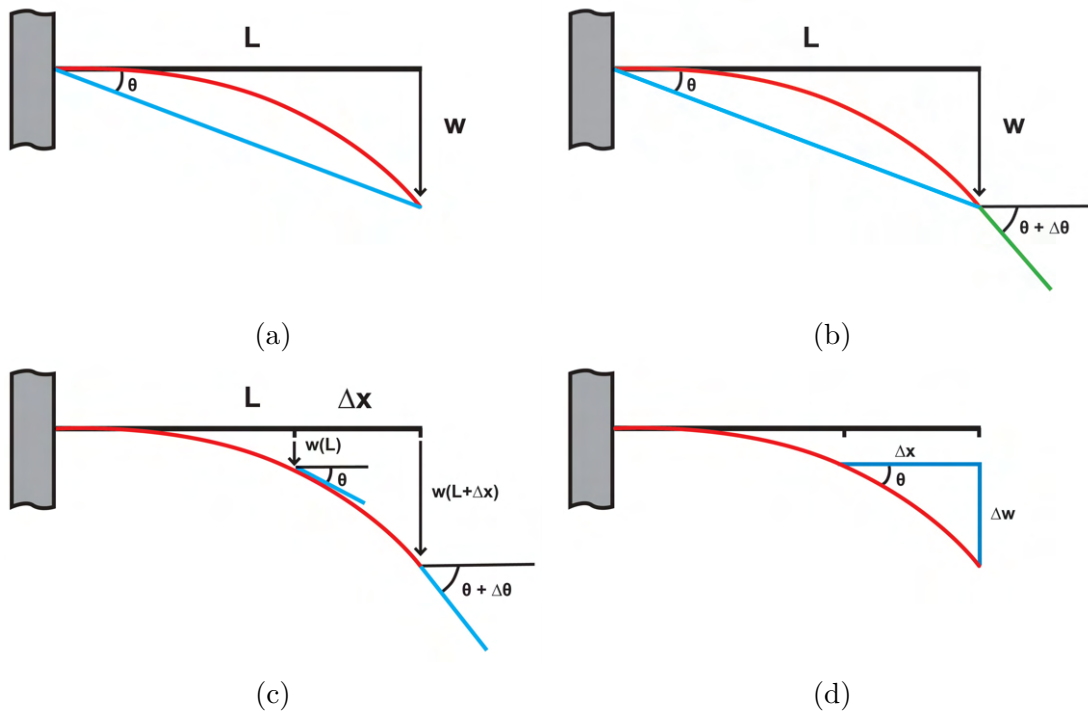


Figure 5.8: Obtaining the local angle of a deformed beam.

However, while in theory this approach should be able to account for all deformation from changes in orientation (providing the deformations obtained satisfy linear elasticity), in practice it will always under predict the change in orientation to some degree. One reason for this is that there will always be

5. STRUCTURAL CHANGES TO DENDRITE ORIENTATION

some loss when reconstructing the tangent for a local orientation as in figure 5.8d, where the deflection curve will not quite match the hypotenuse of the right angled triangle formed by Δx and Δw .

Nevertheless, any loss in accuracy from this effect should be miniscule as for any reasonable value of Δx the small deformations and small values of $\theta(x)$ cause this hypotenuse to be practically the same as Δx . A potentially more significant factor causing under prediction is the manner in which these orientation changes are applied to the structure.

In the theoretical model, the observed deformations $w(x)$ can be accounted for by growth at the varying orientation $\theta(x)$. However, in the way they are being applied in the SMS, the orientation change for a deformation step is calculated then added to the existing orientation of the structure, only influencing future growth, meaning that while the structure is now correctly orientated, the physical movement of the structure has not been accounted for.

Any impact from this can be mitigated by having an appropriately small time step between solving structural mechanics so that any deformation being neglected this way is insignificant. A further justification for overlooking this physical movement can be found in definitions of ‘small’ deformations described earlier in section 3.2.2, where the deformation is assumed to be so small that the structure is physically in the same location, essentially meaning that any deformations obtained whose physical movement cannot be safely overlooked would mean that the solution is in violation of linear elasticity.

In order to appraise how these issues may effect accuracy in practice, the test case which was used to assess the accuracy of the method used to account for existing deformation given the quasi-stationary approach as described in section 4.4 was again used (everything stated about the problem setup in this section holds true for this example, though some information will be repeated for clarity).

5. STRUCTURAL CHANGES TO DENDRITE ORIENTATION

These results can easily be repurposed to compare how the orientation of a growing beam changes based on the methods described in this chapter, comparing these values against the expected orientation given by a beam theory analytic solution. For this test, both the SMS and beam theory are used to calculate the orientation change of a deforming beam with the following properties:

$$\text{Dimensions} = 20 \times 20 \times 120$$

$$E = 10 \text{ GPa}$$

$$\Delta x = 10 \text{ } \mu\text{m}$$

$$\rho = 7020 \text{ kg/m}^3$$

$$\text{Force} = \rho g \text{ N/m}^3$$

The beam theory approximations for a beam with distributed load (see [3.10.7](#)) were used to obtain the displacements along the length of the beam, from which the local orientations were calculated using the approximation in equation [5.9](#).

To validate this approach of using successive deformations as a structure grows to update the change in orientation, a $20 \times 20 \times 20$ block was fixed to a wall in the manner of a cantilevered beam which was then grown in 5 volume increments until it reached the final length of 120 volumes, solving structural mechanics after each growth event and updating the orientation of the beam correspondingly, as can be observed in the selection of time steps shown in figure [5.9](#).

5. STRUCTURAL CHANGES TO DENDRITE ORIENTATION

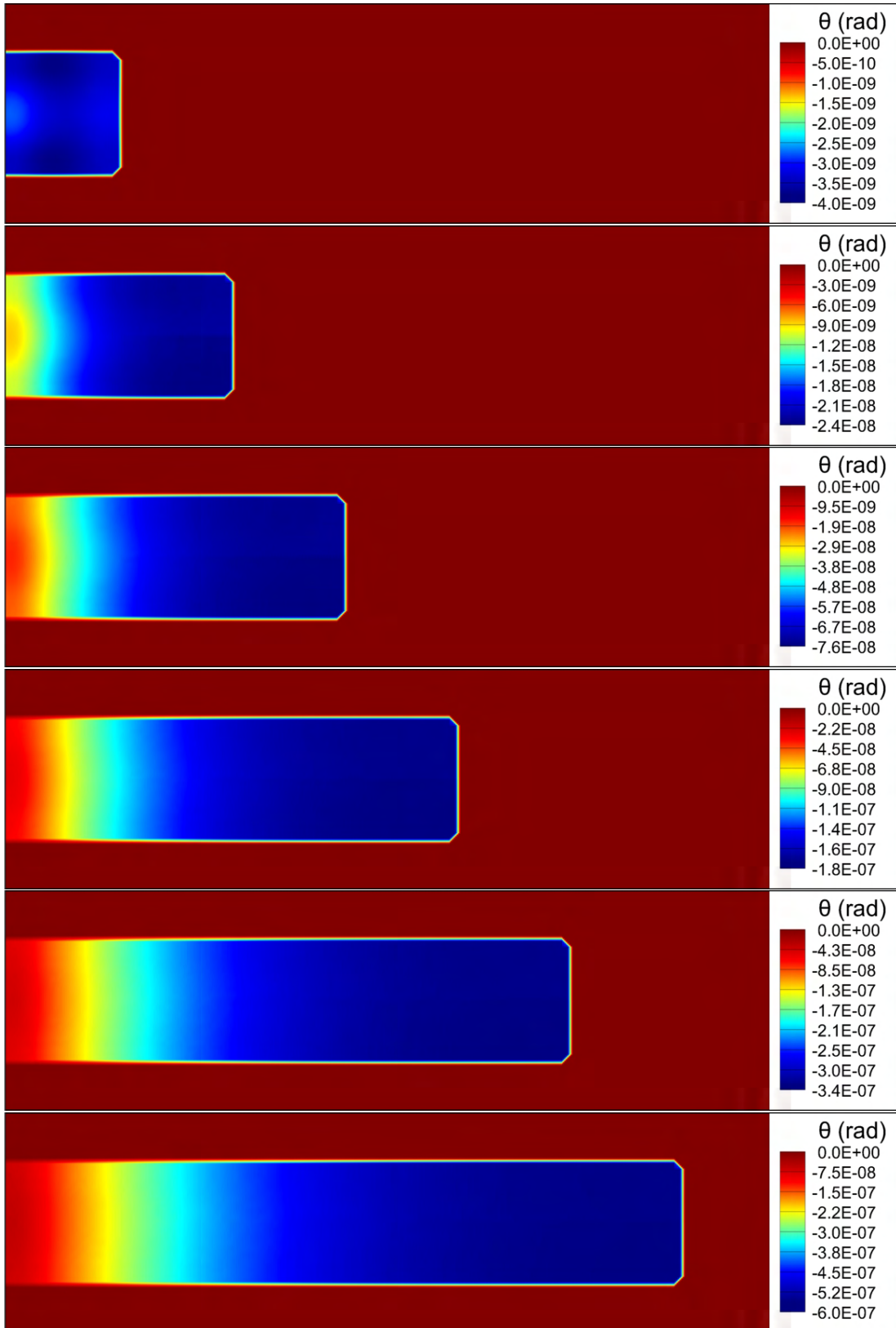


Figure 5.9: Changing orientation of a growing beam.

5. STRUCTURAL CHANGES TO DENDRITE ORIENTATION

This is an idealised case where the beam simply grows by a fixed amount along the x axis, calculating the change in deformation to allow the beam to reach a stationary solution rather than directional solidification where the growth behaviour of the dendrites can be changed to create a different structure. As such, the final deformations (and hence orientation change) obtained from this growing beam should match the case where a beam of length 120 was deformed from a starting state experiencing no forces, thereby matching the beam theory solution for the same beam.

Section 4.4 found a good agreement between the observed deformation of the fully grown beam for both the SMS and beam theory, where the same would be expected for the derived orientation values. A comparison of these aggregated final orientation values can be seen in figure 5.10, where the local orientations observed running through the centre of the grown beam at full length have been plotted alongside the predicted orientation from beam theory. While the grown beam does demonstrate a clear under prediction, it has a comparable values and behaviour to the beam theory solution, seemingly indicating this approach provides a realistic approximation of the true orientation change occurring in a growing structure. In addition, as the fivefold volume increment being used here represents a much larger structural mechanics time step than would generally be considered desirable for a microstructure solidification problem, these larger intervals between solutions potentially exacerbate the previously outlined issues which can lead to an under prediction of the orientation.

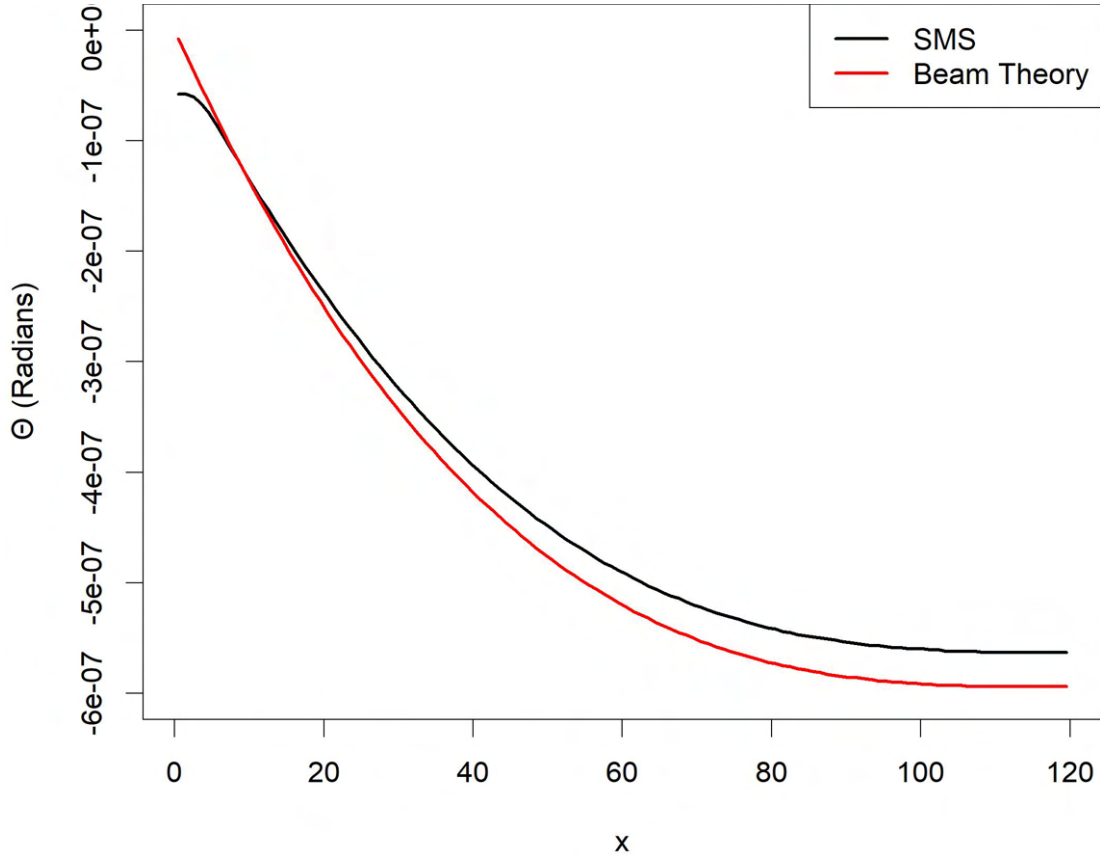


Figure 5.10: Final orientation along a grown beam.

5.5 Summary

A novel approach to obtaining local orientation changes throughout a structure was developed, where the displacements obtained from the structural mechanics code are used to continuously update the orientation of each volume as the structure grows and changes in shape. This represents a two-way coupled process, as the orientation of a volume will influence the preferential growth direction of a dendrite, where any new mass from this growth will cause displacements that will further change the orientation. The theoretical validity of this approach was explored as well as performing verification of an idealised

5. STRUCTURAL CHANGES TO DENDRITE ORIENTATION

modelling case against an analytic solution obtained using the Euler Bernoulli beam theory, finding the accuracy of this approach to be comparable to the predictions of the analytic solution.

Chapter 6

DENDRITE ADVECTION

6.1 Overview

This section discusses the implementation of advection processes to move dendrites through the problem domain. The utility of transporting dendrites through the domain is introduced both within the context of structural mechanics and more widely in the context of microstructure solidification. The process of modelling advection is described and implemented for a homogeneous structure using different approaches, with the most effectual implemented to work concurrently with a solidification model. How these principles can be applied to the advection of a heterogeneous structure is then discussed, in particular highlighting the difficulties of modelling significant advection concurrently with solidification using the CA method. Finally, the current level of implementation of dendrite advection within the wider context of the research will be summarised.

6.2 Transporting Dendrite Structures

The ability to move a dendritic structure through the problem domain has a direct application in modelling structural mechanical effects. The most obvious utility of this will be to account for the impact of deformation, where a deformed structure will be physically moving through the problem domain. This is easily expanded to related phenomena that could be potentially modelled in the wider scope of TESA but cannot currently be considered, such as fractures causing dendrite arms to break off and fall/float away, modelling the columnar to equiaxed transition and dendrites demonstrating significant transient movement.

Free moving dendrites can settle during solidification to cause macrosegregation, which can cause many defects in the material such as non-uniform material properties, impacting, material size and production rates [102] and as such this is an area of great interest to people modelling the solidification process [103]. It was initially conceived that accounting for dendrite deformation as an transport process would be the main driver of structural mechanical influence on the dendritic structure, however changes to dendrite orientation (Chapter 5) proved to be sufficient to account for the structural impact in cases where linear elasticity assumptions hold true.

Regardless, as an argument can be made that even for these small deformations the inclusion of advection would lead to a more physically accurate representation of the deformation process than orientation on it's own (see section 6.6) and that the implementation of a robust solid transport method will be a requirement for many expansions of the research, the work done on the topic will be presented in the rest of this chapter.

When representing the interface, either between two liquids or a solid-liquid interface, two broad families of methods can be classified: surface methods and volume methods [104]. The surface methods explicitly describe the location of a

sharp interface either with particles, functions acting over the entire domain or by attaching a body fitted mesh to the separate phases. Conversely, volume methods mark within each volume how much of each phase is present in each cell, meaning that the exact location of the interface is not known and has to be interpreted from these markers in each volume. While there are many examples of solidification problems utilising surface methods such as the phase field method [105, 106], level-set method [107] and sharp interface methods [108, 109]. Yamaguchi and Beckerman (2013) [65] went further than this, and in fact implemented a phase field advection process, allowing the compressed dendrites to move through the computational domain.

Given the solidification models being employed in this research represent structures as a collection of solid fraction values for each volume, while it would be theoretically possible to interpret this information in a manner compatible with surface methods, it would seem more natural to embrace the volumetric interface definition intrinsic to the solidification processes and apply volume methods to the goal of transporting growing dendrites through the domain.

Furthermore, aside from the complication of converting between a solid fraction and a sharp interface method, issues encountered later (see section 6.5) would potentially make these approaches less viable due to the important internal morphologies of alloy dendrites generated using the CA method, which would present problems if implementing surface methods that are generally used only for homogeneous dendrites.

6.3 Advection of a Homogeneous Structure

When first investigating methods to transport a solidifying structure, the solidification model being used was that of the enthalpy method (see 4.3.1),

where the dendrites generally only have a single cell interface and hence form a homogeneous structure. As such, this was the framework where the solid transport of a dendrite was first considered.

Before considering coupling transport to solidification, it was important to test the functionality of the transport process in isolation so that the behaviour and accuracy could be appraised without the confounding factor of the solidification. The method of transporting the solid material first conceived of was an advection process which could be driven by displacement or velocity fields as the problem required. Relating this process back to a finite volume formulation, this can be thought of the flux into and out of a volume such that for a 3D problem the transient change in solid fraction for a given volume is:

$$\frac{\partial f}{\partial t} = \frac{\Delta t}{\Delta x} (Fl_w - Fl_e + Fl_s - Fl_n + Fl_l - Fl_h) \quad (6.1)$$

Where the Fl is the flux out of the indicated face of the volume (with the underscored standing for the following in the order presented: west, east, south, north, low and high). This will be the fundamental form of all the advection processes examined, though the definitions of the flux values will change depending on the method. In figure 6.1, for added clarity a grid has been provided showing a volume f at a generic point P indicating which displacements and volumes are used to calculate the flux for this volume.

However, it should be noted that the advection processes can also work in three dimensions, so there are also potentially faces and volumes going into and out of the page in the high and low directions that may be referenced in the given formulas.

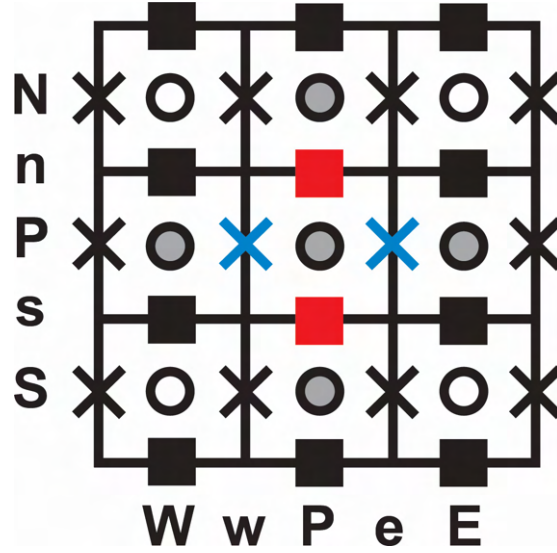


Figure 6.1: Grid used for solid advection process.

6.3.1 Basic Advection

Where the advection equation for the Solid Fraction (f) under a constant velocity \mathbf{u} can be defined for a multi dimensional problem as follows:

$$\frac{\partial f}{\partial t} + \mathbf{u} \cdot \Delta f = 0 \quad (6.2)$$

Which for the 2D cases under initial consideration simplifies to the following:

$$\frac{\partial f}{\partial t} + u \frac{\partial f}{\partial x} + v \frac{\partial f}{\partial y} = 0 \quad (6.3)$$

This process could then intuitively be discretised is by using a forwards difference in time and central differences in space to obtain the equation:

$$\frac{f_P^{t+1} - f_P^t}{\Delta t} + O(\Delta t) = -u \frac{f_E^t - f_W^t}{2\Delta x} - v \frac{f_N^t - f_S^t}{2\Delta y} + O(\Delta t, \Delta x^2, \Delta y^2) \quad (6.4)$$

6. DENDRITE ADVECTION

Which, using the fact that for a uniform Cartesian grid $\Delta x = \Delta y$ can be rearranged to obtain the following scheme describing a change in Solid Fraction for a given volume:

$$f_P^{t+1} = f_P^t - \frac{\Delta t}{2\Delta x} (u(f_E^t - f_W^t) + v(f_N^t - f_S^t)) + O(\Delta t, \Delta x^2) \quad (6.5)$$

However, stability analysis shows that the error continuously grows, making the scheme *unconditionally unstable*. With an obvious solution to this instability being to make it upwind in space like so (assuming both u and v are positive):

$$f_P^{t+1} = f_P^t - \frac{\Delta t}{\Delta x} (u(f_E^t - f_P^t) + v(f_N^t - f_P^t)) + O(\Delta t, \Delta x) \quad (6.6)$$

However, upwinding in this fashion carries complications, as the direction of flow must first be identified to establish what the appropriate direction for upwinding is at a given location (hence why the above only holds for positive u and v).

As such for a generalised 3D upwind scheme, the differencing scheme can still be defined as a collection of the fluxes:

$$f_P^{t+1} = f_P^t + \frac{\Delta t}{\Delta x} (Fl_w - Fl_e + Fl_s - Fl_n + Fl_l - Fl_h) \quad (6.7)$$

but the fluxes will have to check the flow direction by appraising displacements/velocities at the faces (V) the like so:

$$\begin{array}{rcc}
 & V > 0 & V < 0 \\
 Fl_w & : u_w f_W^t & \text{or } u_w f_P^t \\
 Fl_e & : u_e f_P^t & \text{or } u_e f_E^t \\
 Fl_s & : v_s f_S^t & \text{or } v_s f_P^t \\
 Fl_n & : v_n f_P^t & \text{or } v_n f_N^t \\
 Fl_l & : w_l f_L^t & \text{or } w_l f_P^t \\
 Fl_h & : w_h f_P^t & \text{or } w_h f_H^t
 \end{array} \tag{6.8}$$

Once implemented, another shortcoming of a basic advection algorithm using upwinding is that the shape of of structure is lost over time due to diffusion. The reason that this occurs can be easily understood by considering the example of 1D flow in shown in figure 6.2, where the amount of solid fraction being moved by the velocity field becomes progressively thinner at the front and back of the structure being advected. This is because the solid fraction is only a marker value which does not intrinsically inform the advection process there is a structure to be maintained, so without updating the flux definitions to preserve the structure in some manner this value of f will continue to diffuse.

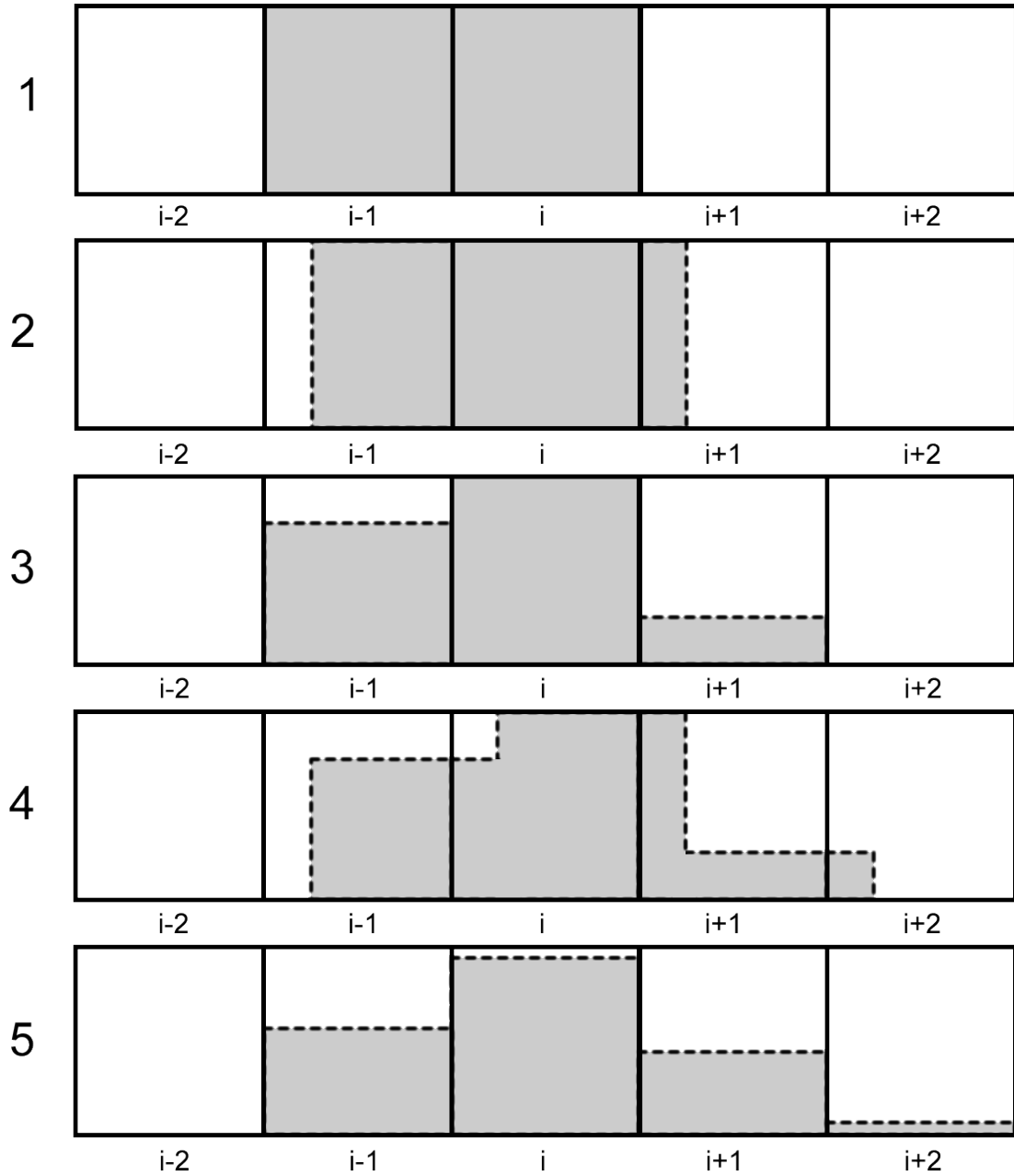


Figure 6.2: Standard 1D advection.

A 2D example of this diffusive behaviour can be observed in figure 6.3, where a homogeneous square has been advected from the bottom left to top right corner of a domain using upwinded advection. This diffusion will clearly be unacceptable

for retaining a dendritic structure moving through a domain, especially one that has a clear discontinuous boundary such as generated by the Enthalpy Method.

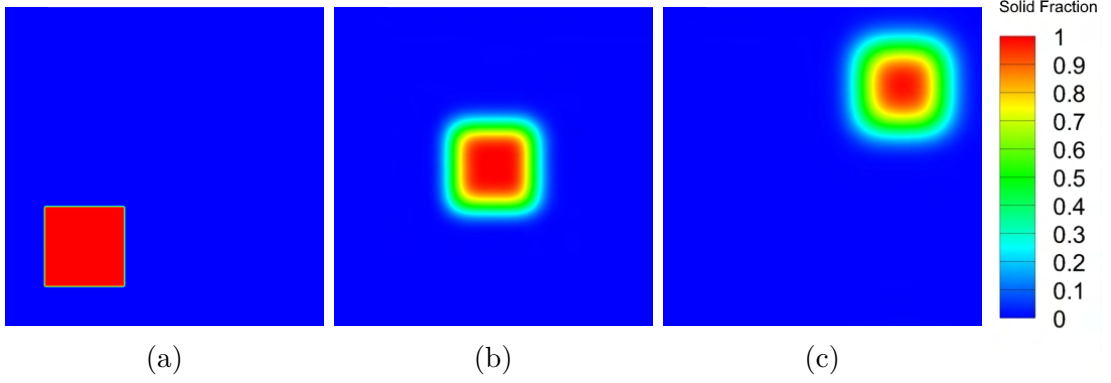


Figure 6.3: Homogeneous square advected using upwind method.

6.3.2 Flux Limited Advection

Flux Limited Advection [110] is an expansion of the advection equation which alters the flux terms to limit diffusion by attempting to maintain any significant discontinuities. This is done by updating the generic advection equation 6.7 to use the following expanded flux terms:

$$\begin{aligned}
 Fl_w &= \frac{1}{2}u_w [(1 + \theta_w)f_W^t + (1 - \theta_w)f_P^t] + \frac{1}{2}abs(u_w) \left(1 - \frac{abs(u_w)\Delta t}{\Delta x}\right) \Phi(r_w) (f_P^t - f_W^t) \\
 Fl_e &= \frac{1}{2}u_e [(1 + \theta_e)f_P^t + (1 - \theta_e)f_E^t] + \frac{1}{2}abs(u_e) \left(1 - \frac{abs(u_e)\Delta t}{\Delta x}\right) \Phi(r_e) (f_E^t - f_P^t) \\
 Fl_s &= \frac{1}{2}u_s [(1 + \theta_s)f_S^t + (1 - \theta_s)f_P^t] + \frac{1}{2}abs(u_s) \left(1 - \frac{abs(u_s)\Delta t}{\Delta x}\right) \Phi(r_s) (f_P^t - f_S^t) \\
 Fl_n &= \frac{1}{2}u_n [(1 + \theta_n)f_P^t + (1 - \theta_n)f_N^t] + \frac{1}{2}abs(u_n) \left(1 - \frac{abs(u_n)\Delta t}{\Delta x}\right) \Phi(r_n) (f_N^t - f_P^t) \\
 Fl_l &= \frac{1}{2}u_l [(1 + \theta_l)f_L^t + (1 - \theta_l)f_P^t] + \frac{1}{2}abs(u_l) \left(1 - \frac{abs(u_l)\Delta t}{\Delta x}\right) \Phi(r_l) (f_P^t - f_L^t) \\
 Fl_h &= \frac{1}{2}u_h [(1 + \theta_h)f_P^t + (1 - \theta_h)f_H^t] + \frac{1}{2}abs(u_h) \left(1 - \frac{abs(u_h)\Delta t}{\Delta x}\right) \Phi(r_h) (f_H^t - f_P^t)
 \end{aligned}$$

(6.9)

where the flux terms now have three new terms requiring consideration: the flip flop parameter θ_p , a measure of the smoothness of the solutions at that location r and the flux limiter function Φ .

The flip flop parameter is a function that allows for the direction of the velocity to be accounted for in a single expression, which is required due to the flux limited advection varying depending on the direction of the flow, as discussed for basic upwinding. The flip flop parameter at generic facial point p with the velocity V_p at that face can be defined as:

$$\theta_p = \theta(V_p) = \begin{cases} +1, & \text{for } V_p > 0 \\ -1, & \text{for } V_p < 0 \end{cases} \quad (6.10)$$

The smoothness of the solution is then defined as r , which in this case is being taken as a ratio of consecutive gradients and has been defined as follows (though other definitions exist):

$$\begin{aligned} r_w &= \frac{f_P - f_E}{f_W - f_P} \\ r_e &= \frac{f_P - f_W}{f_E - f_P} \\ r_s &= \frac{f_P - f_N}{f_S - f_P} \\ r_n &= \frac{f_P - f_S}{f_N - f_P} \\ r_l &= \frac{f_P - f_H}{f_L - f_P} \\ r_h &= \frac{f_P - f_L}{f_H - f_P} \end{aligned} \quad (6.11)$$

The flux limiter function Φ then uses r in the chosen flux limiter scheme, which essentially uses this smoothness function to ascertain if the location is at a discontinuity that should be preserved. There are many different flux limiter functions that can be used in this scheme, easily switched between thanks to the

way the flux is now defined. A selection of popular limiters have the following definitions:

$$\begin{aligned}
 \textit{Upwind} : \phi(r) &= 0 \\
 \textit{Lax - Wendroff} : \phi(r) &= 1 \\
 \textit{Beam - Warming} : \phi(r) &= r \\
 \textit{Minmod} : \phi(r) &= \max(0, \min(1, r)) \\
 \textit{Van - Leer} : \phi(r) &= \frac{r + |r|}{1 + |r|} \\
 \textit{MUSCL} : \phi(r) &= \max(0, \min(2r, 0.5 * (r + 1), 2)) \\
 \textit{Superbee} : \phi(r) &= \max(0, \min(1, 2r), \min(2, r))
 \end{aligned} \tag{6.12}$$

Where it can be observed that if ϕ is set to 0 the flux terms in equation 6.9 simplify back to the upwind equations. Having tested all of these flux limiters and researched their theoretical accuracy, the Superbee limiter was selected as the most appropriate to be used for advecting dendrites. This is because the Superbee is a high resolution non-linear scheme that is the least diffusive of the popular limiters (and hence the most likely to preserve discontinuities). The Superbee can be seen working in figure 6.4, where a square structure has been advected from the bottom left to the top right corner of a domain. When contrasted with the upwind solution in figure 6.3, the Superbee has clearly preserved the structures shape and edges with far greater clarity.

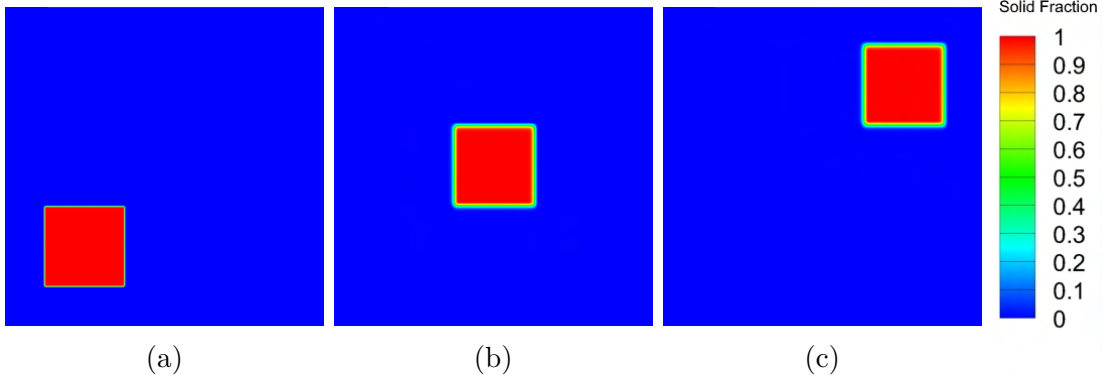


Figure 6.4: Homogeneous square advected using Superbee method.

A consideration when implementing an advection process with more than one dimension is whether unsplit advection should be implemented. The processes described so far using the generic flux formulation in equation 6.7 is a case of unsplit advection, meaning that the the fluxes in x , y and z are all resolved simultaneously. This can cause a bias in the advected solution as the fluxes ignore the influence of each other for that given time step, essentially meaning that material will only be fluxed into cells parallel to each axis, though in reality there would be an influence from the cells at the corners as both contributors and recipients of fluxed material (see figure 6.5 for a collection of examples demonstrating this). As such, split methods are generally preferred, where the fluxes in each direction are resolved separately, updating a temporary value of f until the flux in all directions is accounted for. A flux split form of equation 6.7 can be defined as follows:

$$\begin{aligned}
 f_P^{u*} &= f_P^t + \frac{\Delta t}{\Delta x} (Fl_w - Fl_e) \\
 f_P^{v*} &= f_P^{u*} + \frac{\Delta t}{\Delta x} (Fl_s - Fl_n) \\
 f_P^{t+1} &= f_P^{v*} + \frac{\Delta t}{\Delta x} (Fl_l - Fl_h)
 \end{aligned} \tag{6.13}$$

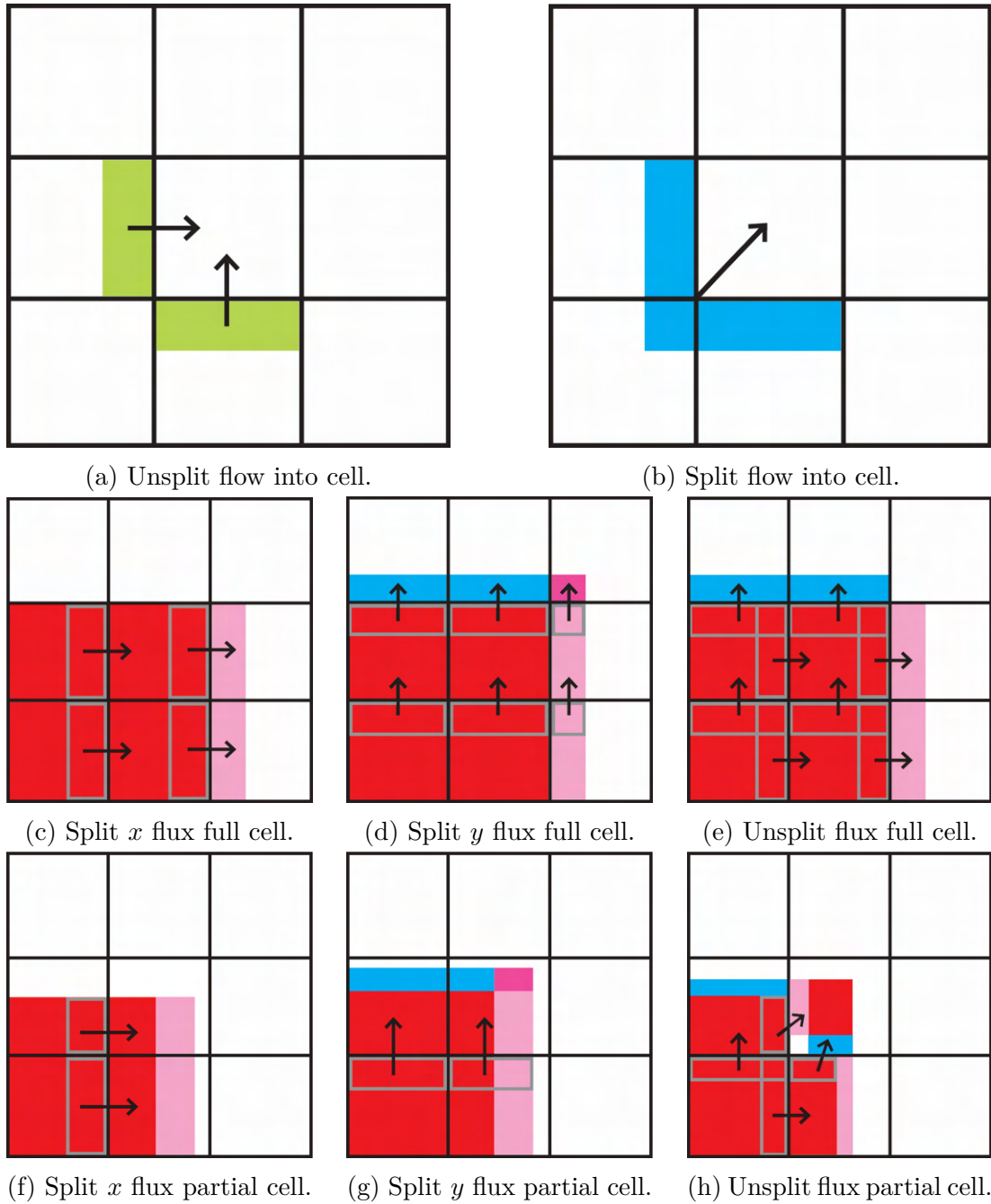


Figure 6.5: Split vs unsplit advection examples.

An example of split vs unsplit advection of an equiaxed dendrite can be seen in figure 6.6, where the split advection maintains the symmetry of the dendrite when

compared the unsplit case which demonstrates a clear bias in the morphology. As such, split advection methods will be utilised going forward.

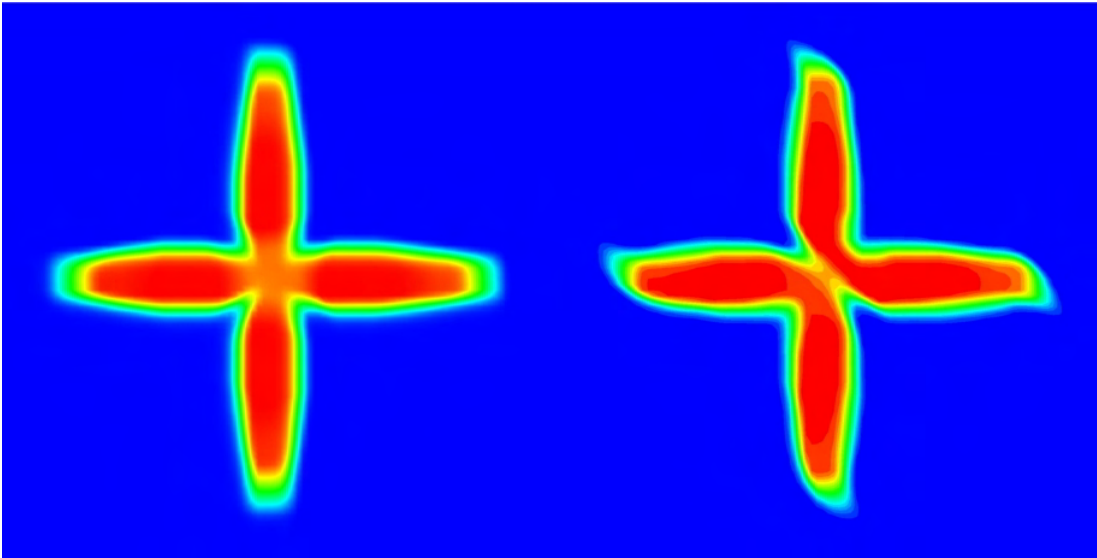


Figure 6.6: Split (left) vs unsplit (right) advection.

While these flux limited advection methods do perform well at transporting a structure across the domain while maintaining the fundamental shape of the structure, even for the Superbee there is some clear blurring at the boundary which could lead to issues for solidification methods such as the enthalpy method which require a 1 cell boundary for the solid fraction.

6.3.3 Volume of Fluid Methods

In order to have access to an advection method other than flux limiters which would be capable of maintaining a sharp boundary, another family of methods know as the Volume of Fluid (VoF) methods [111] were examined. These follow a donor-acceptor approach which preserves hard discontinuities by treating the quantity being advected as a marker function that can only take values of 0 or 1. For a homogeneous structure such as those examined so far, the fractional cell can

be conceptualised in two ways: first as a semi solid cell that is undertaking phase change or second as a measure of how much of the cell contains fully solidified material, with this second case being the way in which the solid fraction is treated for VoF methods.

Interface reconstruction then becomes an important consideration for how to interpret the collection of solid fraction values as a single solid shape, as this reconstructed shape is used by the VoF methods to update the flux terms so that material only moves between cells when it is appropriate for the reconstructed interface to do so. This is easily conceptualised in 1D, as can be seen in figure 6.7 (which should be contrasted with the behaviour observed in the upwind advection example in figure 6.2) where the f value is reconstructed into a single solid structure before advection, where the maintenance of this sharp boundary will prevent unwanted diffusion as a cell must be entirely filled before advection can move material into the neighbouring cell.

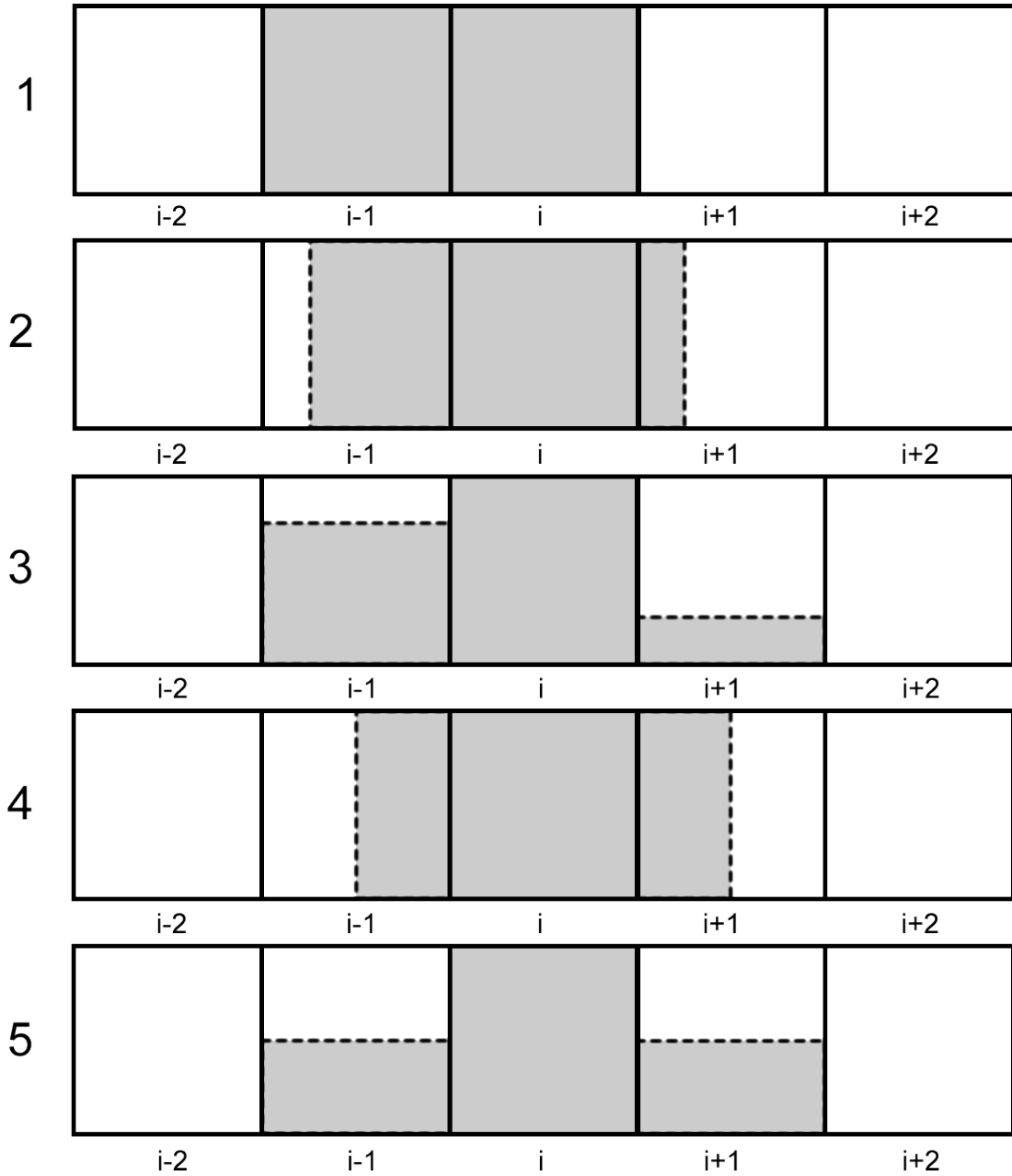


Figure 6.7: VOF 1D advection.

While straightforward in principle, the implementation of the interface reconstruction can become increasingly complicated depending on the accuracy of the reconstruction required. Possibly the most fundamental interface

restoration approaches is the Simple Line Interface Calculation (SLIC) [112], which reconstructs the interface so that it is always parallel to one of the axes. The axis that it is parallel to is chosen based on the solid fraction of the surrounding cells such that new cells should not have any new material advected until it is appropriate. Operating as a split advection method as previously described, the structure will be preferentially reconstructed differently for each flux direction to minimise any flux which would lead to diffusion. This can be seen in figure 6.9, where a SLIC reconstruction has been performed for an x sweep and a y sweep for different interfaces. In all of these cases it can be seen how when a cell is surrounded by solid material on two or less sides, it will reconstruct to be perpendicular to the sweep direction to prevent advection into new cells.

However, for a cell bordered on three sides it will reconstruct so that the interface always points towards the empty cell. In the case where a cell is surrounded on all sides, the cell will again always reconstruct in the sweep direction, selecting whichever neighbouring cell that has the highest solid fraction to be the side of the cell the solid material will occupy.

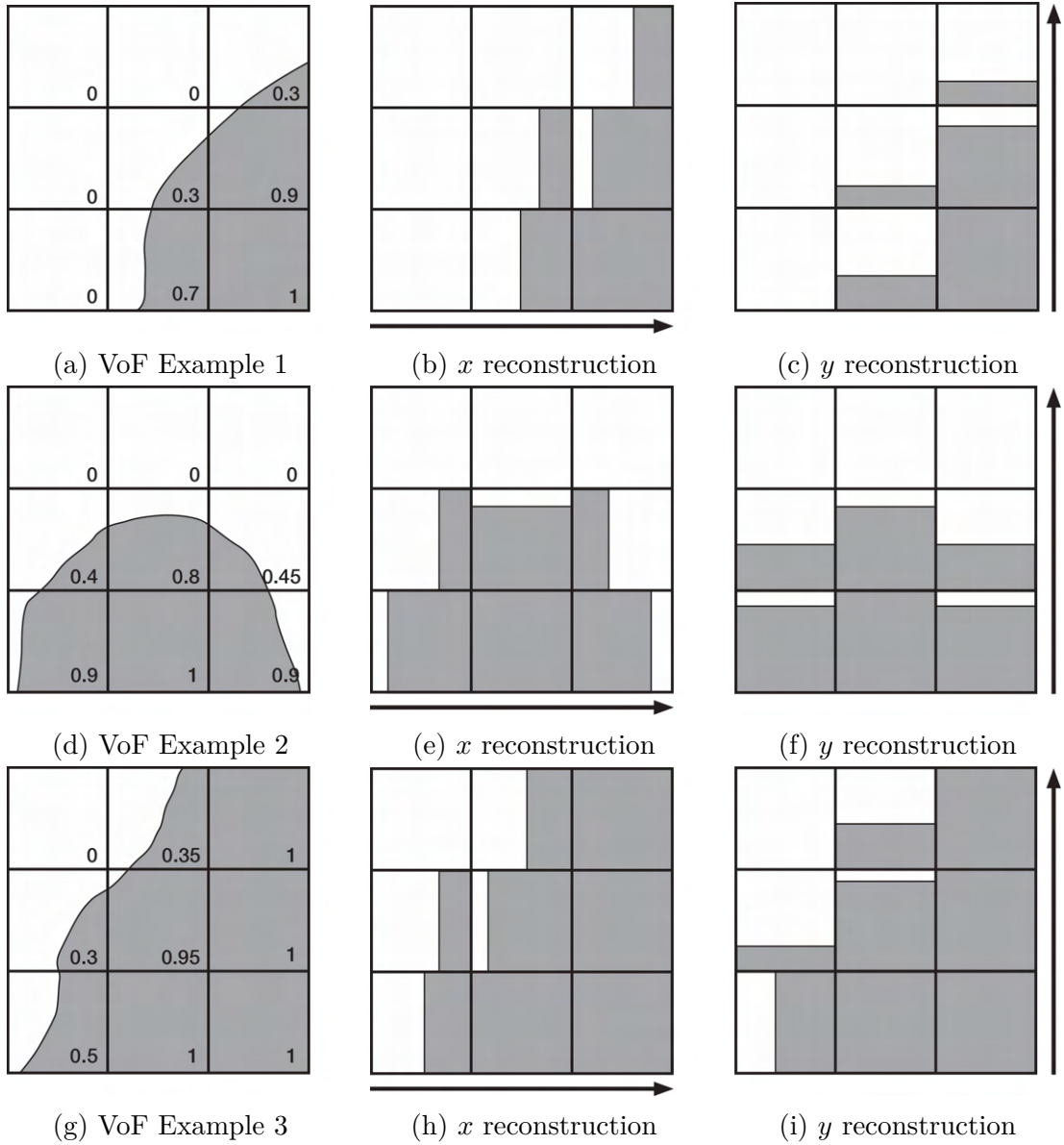


Figure 6.8: SLIC reconstruction examples.

To describe advection using a SLIC reconstruction, the equation 6.7 has to be changed to the following form:

$$\begin{aligned}
 f_P^{u*} &= f_P^t + (Fl_w - Fl_e) \\
 f_P^{v*} &= f_P^{u*} + (Fl_s - Fl_n) \\
 f_P^{t+1} &= f_P^{v*} + (Fl_l - Fl_h)
 \end{aligned}
 \tag{6.14}$$

Where the flux terms now include the time and space steps due to VOF advection potentially describing a flux that includes neither of these terms under some conditions where the cells either overflow or empty. The logic to describe these flux terms, while simple in concept, is quite lengthy. Consequently only the definitions for the fluxes F_e and F_w in the x direction have been provided in the following equation 6.15. The definitions in the y and z directions use identical in logic, but with the East-West references being replaced with North-South or High-Low to match the flux terms being calculated. To aid comprehension, figure 6.9 has been provided to show the 6 different flux conditions (note, a full cell where $f = 1$ is always identified as a ‘parallel’ reconstruction) that may arise from a SLIC reconstruction used by F_w .

$$\begin{aligned}
 Fl_w = & \begin{cases} \min\left(\frac{\Delta t}{\Delta x}u_w, f_W\right), & \text{for } u_w > 0 \text{ and East Reconstruction for } f_W \\ \max\left(\frac{\Delta t}{\Delta x}u_w - (1 - f_W), 0\right), & \text{for } u_w > 0 \text{ and West Reconstruction for } f_W \\ \frac{\Delta t}{\Delta x}u_w f_W, & \text{for } u_w > 0 \text{ and Parallel Reconstruction for } f_W \\ \min\left(\frac{\Delta t}{\Delta x}u_w, f_P\right), & \text{for } u_w < 0 \text{ and West Reconstruction for } f_P \\ \max\left(\frac{\Delta t}{\Delta x}u_w - (1 - f_P), 0\right), & \text{for } u_w < 0 \text{ and East Reconstruction for } f_P \\ \frac{\Delta t}{\Delta x}u_w f_P, & \text{for } u_w < 0 \text{ and Parallel Reconstruction for } f_P \end{cases} \\
 Fl_e = & \begin{cases} \min\left(\frac{\Delta t}{\Delta x}u_e, f_P\right), & \text{for } u_e > 0 \text{ and East Reconstruction for } f_P \\ \max\left(\frac{\Delta t}{\Delta x}u_e - (1 - f_P), 0\right), & \text{for } u_e > 0 \text{ and West Reconstruction for } f_P \\ \frac{\Delta t}{\Delta x}u_e f_P, & \text{for } u_e > 0 \text{ and Parallel Reconstruction for } f_P \\ \min\left(\frac{\Delta t}{\Delta x}u_e, f_E\right), & \text{for } u_e < 0 \text{ and West Reconstruction for } f_E \\ \max\left(\frac{\Delta t}{\Delta x}u_e - (1 - f_E), 0\right), & \text{for } u_e < 0 \text{ and East Reconstruction for } f_E \\ \frac{\Delta t}{\Delta x}u_e f_E, & \text{for } u_e < 0 \text{ and Parallel Reconstruction for } f_E \end{cases}
 \end{aligned} \tag{6.15}$$

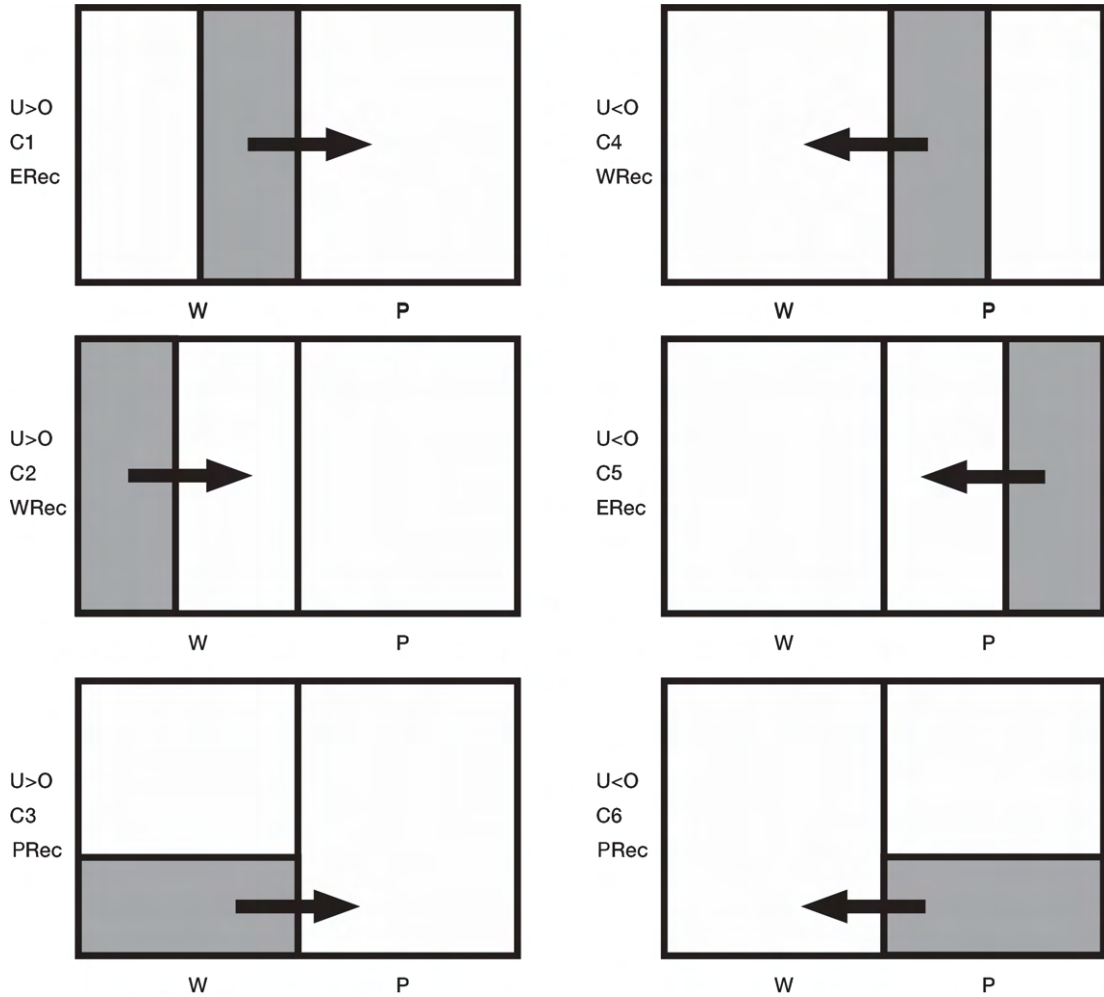


Figure 6.9: Six SLIC reconstruction cases used by F_w in equation 6.15.

A VoF method using a SLIC reconstruction was applied to advecting a grown dendrite from the bottom left to the top right of a 2D domain, as can be seen in figure 6.10. Here it is obvious that the VoF method has done a good job of maintaining a sharp interface all around the structure, however the SLIC reconstruction has quite quickly flattened all of the edges, leaving a structure that is shaped more like a cross than a dendrite with flat faces at the end of the dendrite arms rather than tapering to a point.

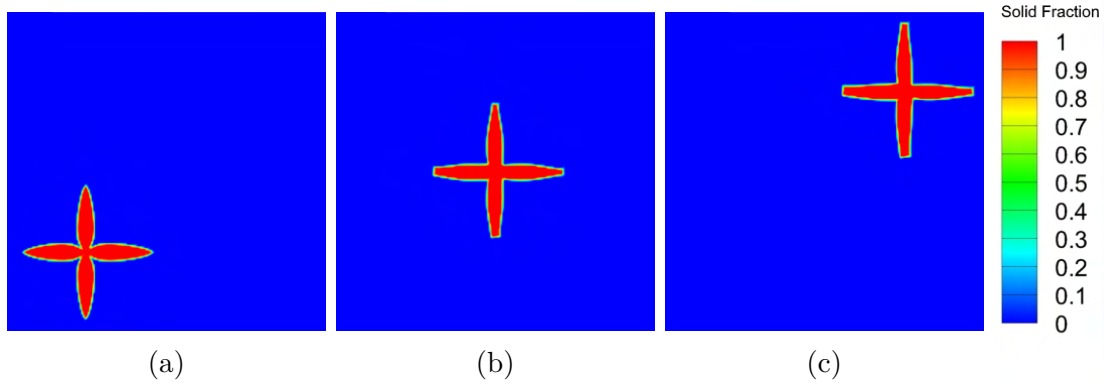


Figure 6.10: Homogeneous dendrite advected using VOF with a SLIC reconstruction.

Due to the importance of the arm and tip morphology in solidification, for a VoF method to be appropriate it would require a more accurate interface reconstruction than the SLIC approach can offer. To this end, the Weighted Linear Interface Calculation (WLIC) [113], also known as the Simplified Volume of Fluid (SVOF) [114], is a method which accounts for the interface by calculating the surface normal based on the 3×3 cells surrounding the cell being reconstructed. These surface normals are then used as an input into a weighting function which is used in new flux terms so that both the x and y reconstructions can contribute to a more accurate flux.

While not a substitute in accuracy for the higher order interface reconstructions that exist, it nevertheless allows for representation of far more complex boundaries than the SLIC reconstruction while being comparatively easy to implement.

Young's method was used to construct the surface normal as in the implementation by Marek et al [114], though there are other definitions that could be used. The calculated the x and y normal components for a 2D problem are as follows:

$$\begin{aligned}
 N_x &= -(f_{NE} + f_{SE} - f_{NW} - f_{SW} + 2(f_E - f_W)) \\
 N_y &= -(f_{NW} + f_{NE} - f_{SW} - f_{SE} + 2(f_N - f_S))
 \end{aligned}
 \tag{6.16}$$

These surface normals can then be used to calculate the weighting function at that location, there are several options for this weighting function mentioned in the literature [113–115], but the one seeming to produce the best results was the following:

$$\begin{aligned}
 \Omega_x^P &= 1 - \frac{2}{\pi} \operatorname{acos} \left(\frac{\operatorname{abs}(N_x)}{N_x^2 + N_y^2} \right) \\
 \Omega_y^P &= 1 - \frac{2}{\pi} \operatorname{acos} \left(\frac{\operatorname{abs}(N_y)}{N_x^2 + N_y^2} \right)
 \end{aligned}
 \tag{6.17}$$

Which can then be used to define the flux, again for brevity only the F_w and F_e terms have been provided due to the identical logic applying for the other flux terms, simply replacing the Ω_x^P with Ω_y^P , N_x with N_y , and the East-West references with North-South. And likewise with z terms is expanding the scheme into 3D. The logic defining the flux in a WLIC scheme is as follows:

$$\begin{aligned}
 Fl_w = & \begin{cases} \Omega_x^W \min \left(u_w \frac{\Delta t}{\Delta x}, f_W \right) + (1 - \Omega_x^W) u_w f_W \frac{\Delta t}{\Delta x}, & \text{for } u_w > 0 \text{ and } N_x^W < 0 \\ \Omega_x^W \max \left(u_w \frac{\Delta t}{\Delta x} - (1 - f_W), 0 \right) + (1 - \Omega_x^W) u_w f_W \frac{\Delta t}{\Delta x}, & \text{for } u_w > 0 \text{ and } N_x^W > 0 \\ u_w f_W \frac{\Delta t}{\Delta x}, & \text{for } u_w > 0 \text{ and } N_x^W = 0 \\ \Omega_x^P \min \left(u_w \frac{\Delta t}{\Delta x}, f_P \right) + (1 - \Omega_x^P) u_w f_P \frac{\Delta t}{\Delta x}, & \text{for } u_w < 0 \text{ and } N_x^P < 0 \\ \Omega_x^P \max \left(u_w \frac{\Delta t}{\Delta x} - (1 - f_P), 0 \right) + (1 - \Omega_x^P) u_w f_P \frac{\Delta t}{\Delta x}, & \text{for } u_w < 0 \text{ and } N_x^P > 0 \\ u_w f_P \frac{\Delta t}{\Delta x}, & \text{for } u_w < 0 \text{ and } N_x^P = 0 \end{cases} \\
 Fl_e = & \begin{cases} \Omega_x^P \min \left(u_e \frac{\Delta t}{\Delta x}, f_P \right) + (1 - \Omega_x^P) u_e f_P \frac{\Delta t}{\Delta x}, & \text{for } u_e > 0 \text{ and } N_x^P < 0 \\ \Omega_x^P \max \left(u_e \frac{\Delta t}{\Delta x} - (1 - f_P), 0 \right) + (1 - \Omega_x^P) u_e f_P \frac{\Delta t}{\Delta x}, & \text{for } u_e > 0 \text{ and } N_x^P > 0 \\ u_e f_P \frac{\Delta t}{\Delta x}, & \text{for } u_e > 0 \text{ and } N_x^P = 0 \\ \Omega_x^E \min \left(u_e \frac{\Delta t}{\Delta x}, f_E \right) + (1 - \Omega_x^E) u_e f_E \frac{\Delta t}{\Delta x}, & \text{for } u_e < 0 \text{ and } N_x^E < 0 \\ \Omega_x^E \max \left(u_e \frac{\Delta t}{\Delta x} - (1 - f_E), 0 \right) + (1 - \Omega_x^E) u_e f_E \frac{\Delta t}{\Delta x}, & \text{for } u_e < 0 \text{ and } N_x^E > 0 \\ u_e f_E \frac{\Delta t}{\Delta x}, & \text{for } u_e < 0 \text{ and } N_x^E = 0 \end{cases} \tag{6.18}
 \end{aligned}$$

An example of a dendrite advected across a domain using WLIC advection can be seen in figure 6.11, which demonstrates smoother surfaces than the SLIC reconstruction, with the dendrite tips becoming rounder rather than flattened. While certainly an improvement over the SLIC reconstruction for maintaining a realistic dendrite structure, this WLIC reconstruction still seems to lose some key definition of the structure when advected over long distances.

If examining homogeneous dendrites transported over large distances with complicated movement, such as is the case for tumbling dendrites, then a more accurate interface reconstruction scheme may be required for the VoF advection. Some noted higher order interface reconstruction methods are the

Piecewise-Linear Interface Calculation (PLIC) [116], FLAIR [117] and methods of reconstruction using a least-squares fit [118] to name but a few. However, to test advection coupled to concurrent solidification, the WLIC reconstruction was deemed sufficiently effective for advecting a dendrite over short distances, allowing the validity of the approach to be appraised before implementing these more complex methods.

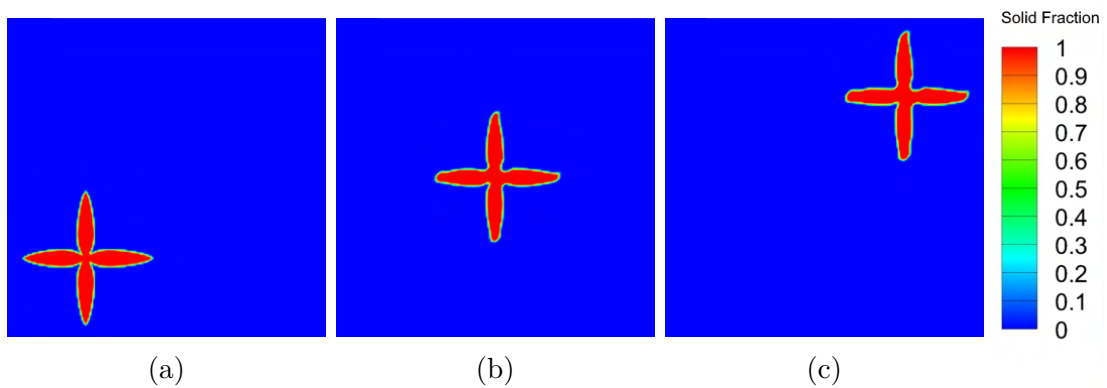


Figure 6.11: Homogeneous dendrite advected using VOF with a WLIC reconstruction.

6.3.4 Concurrent Advection with Solidification

Solidification using the Enthalpy method was tested to run concurrently with displacement driven advection of the solid fraction. This was linked with structural mechanical deformation driven by gravity and presented in a conference paper for MCWASP in 2020 [93], with figure 6.12 replicated from this paper, showing the compression and stretching of dendrites growing with the opposition and support of a body force.

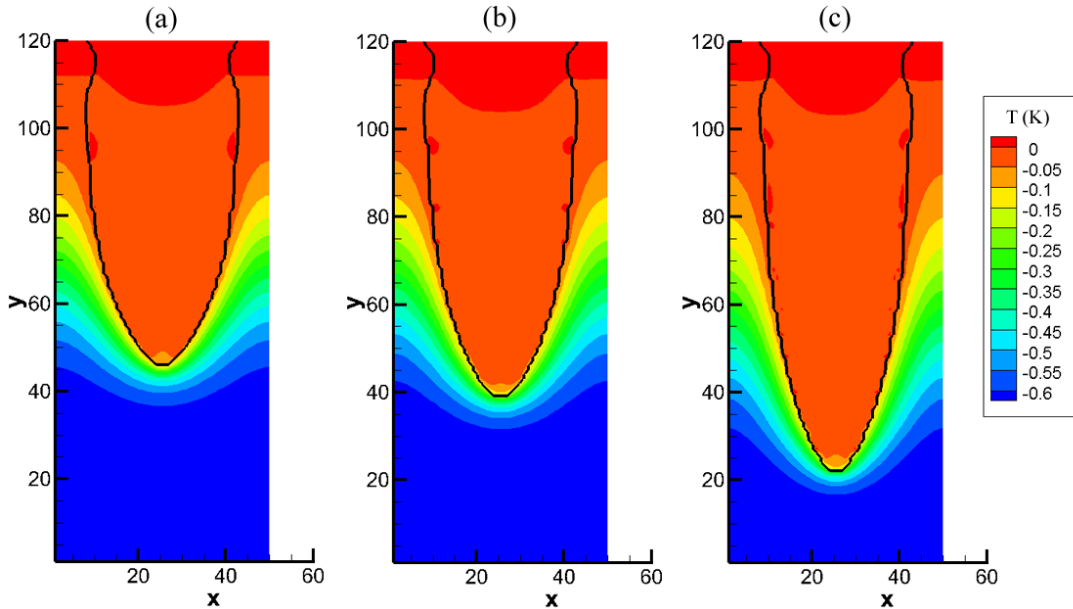


Figure 6.12: Dendrite growth behaviour under external forces showing thermal field T from Soar *et al.* [93]. (a) positive force opposing growth direction (b) no force (c) negative force in growth direction.

While this was a promising combination of structural mechanics, solidification and advection, it remained the case that the deformations were very small comparative to the growth rate and it was unknown how forces perpendicular to the growth would impact the growth behaviour after advection had been undertaken. To test the impact of the advection and orientation changes separately, a growing dendrite moving under a fixed velocity was considered, as this uniform advection should not lead to any changes in dendrite orientation as it grows. An extreme example of these tests can be seen in figure 6.13, where a columnar dendrite is being advected at rates of approximately double the growth velocity to see if sensible growth behaviour can be maintained.

Despite physically moving, if the reconstruction and advection work perfectly then the dendrite growth should behave as if it is not being advected

at all with only the position changing, meaning that (g) and (h) in figure 6.13 should have dendrites with identical morphologies. While clearly not identical, with the advected dendrite in (h) having a slight lean into the direction of advection and altered base morphology, it has still developed into a similarly shaped dendrite of comparable length and width. Considering the extreme advection and fairly fundamental VoF interface reconstruction approach used, results such as these indicate the feasibility of modelling a homogeneous dendrite growing while undergoing significant advection using an approach such as this.

However, at this stage in the research the issues caused by the grid anisotropy of the Enthalpy method as discussed in section 4.3.1 became apparent. Consequently, it became clear that in order to model the desired deformation behaviour in a manner which accurately accounts for the orientation another solidification model would have to be used, which proved to have numerous implications for the advection modelling going forward.

6. DENDRITE ADVECTION

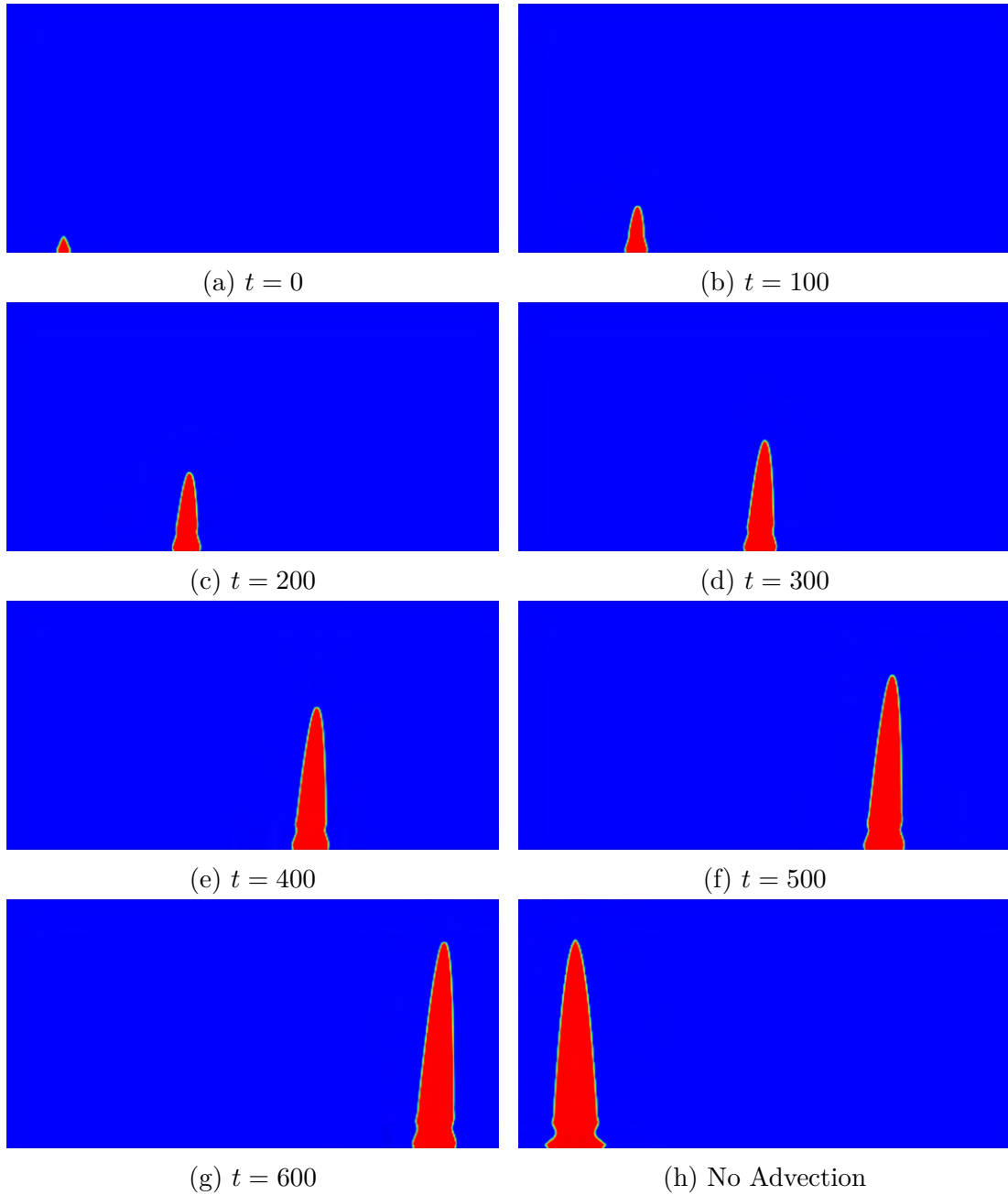


Figure 6.13: Columnar dendrite under constant advection growing using enthalpy method.

6.4 Advection of a Heterogeneous Structure

With the adoption of the CA Method (see section 4.3.2) as the solidification model, the methodology behind the growth of the dendrites offers new complications when coupling it to an advection process, with the most obvious being the change in morphology. While the dendrites grown using the Enthalpy method are homogeneous, with a sharp interface between the solid and liquid material, the CA method produces dendrites with varying solid fraction based on the concentration.

This variable solid fraction meant that VoF methods would no longer be an appropriate approach for the advection of the dendrites, as they would quickly aggregate the diffuse solid fraction structure into a structure with a hard boundary and $f = 1$ at all points, which would not be compatible with further growth using the CA method. For this reason flux limited methods were examined again to see how well they could behave for an already slightly diffuse structure, as the slightly blurred boundary that led to flux limiters being abandoned for use with the Enthalpy method will no longer necessarily be a problem with a CA method implementation.

This line of enquiry started by using the CA method to grow a 3D equiaxed dendrite to a meaningful size and advecting it from the low bottom left to the high top right corner of the domain using advection with a Superbee flux limiter, as can be observed in figure 6.14. While the fine definition on the outside of the dendrite is clearly lost through this process, the structure remains unmistakably an equiaxed dendrite in form, demonstrating potential for concurrent coupling of these processes.

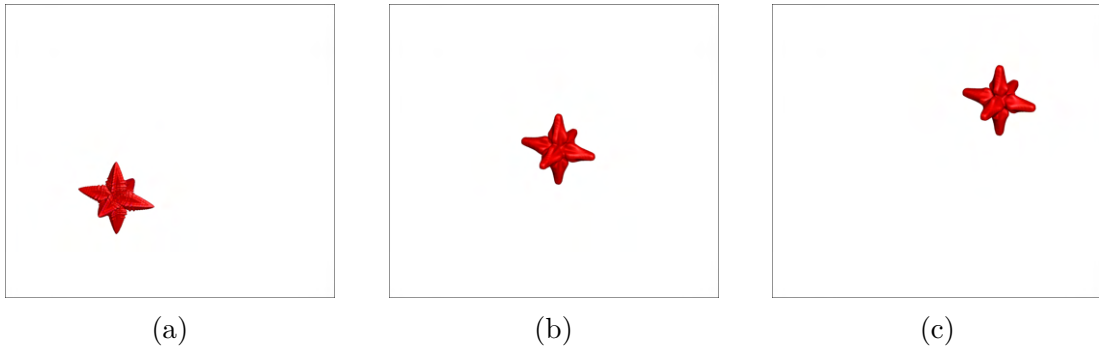


Figure 6.14: Advection of a 3D dendrite using the Superbee flux limiter.

6.5 Complications of Coupling Significant Advection with Solidification

A major complication of combining significant advection with the CA method is the number of variables used by the solidification process which also need to be kept lined up with the solid fraction. Other than the solid fraction, the equivalent concentration and liquidus concentration (see section 4.3.2 for details of how these concentration variables are defined and used by the CA method) also require advection to keep them in the correct position relative to the solid fraction and each other, as can be seen in figure 6.15. Under the same velocity fields these different variables remain well aligned, however each variable advected in this manner adds to the computation time for the coupled process. Furthermore, in examining the solid fraction and equivalent concentration it becomes clear that even the Superbee method is not preserving internal structures and dendrite tips to the sharpness which would be required for solidification to continue seamlessly after advection.

6. DENDRITE ADVECTION

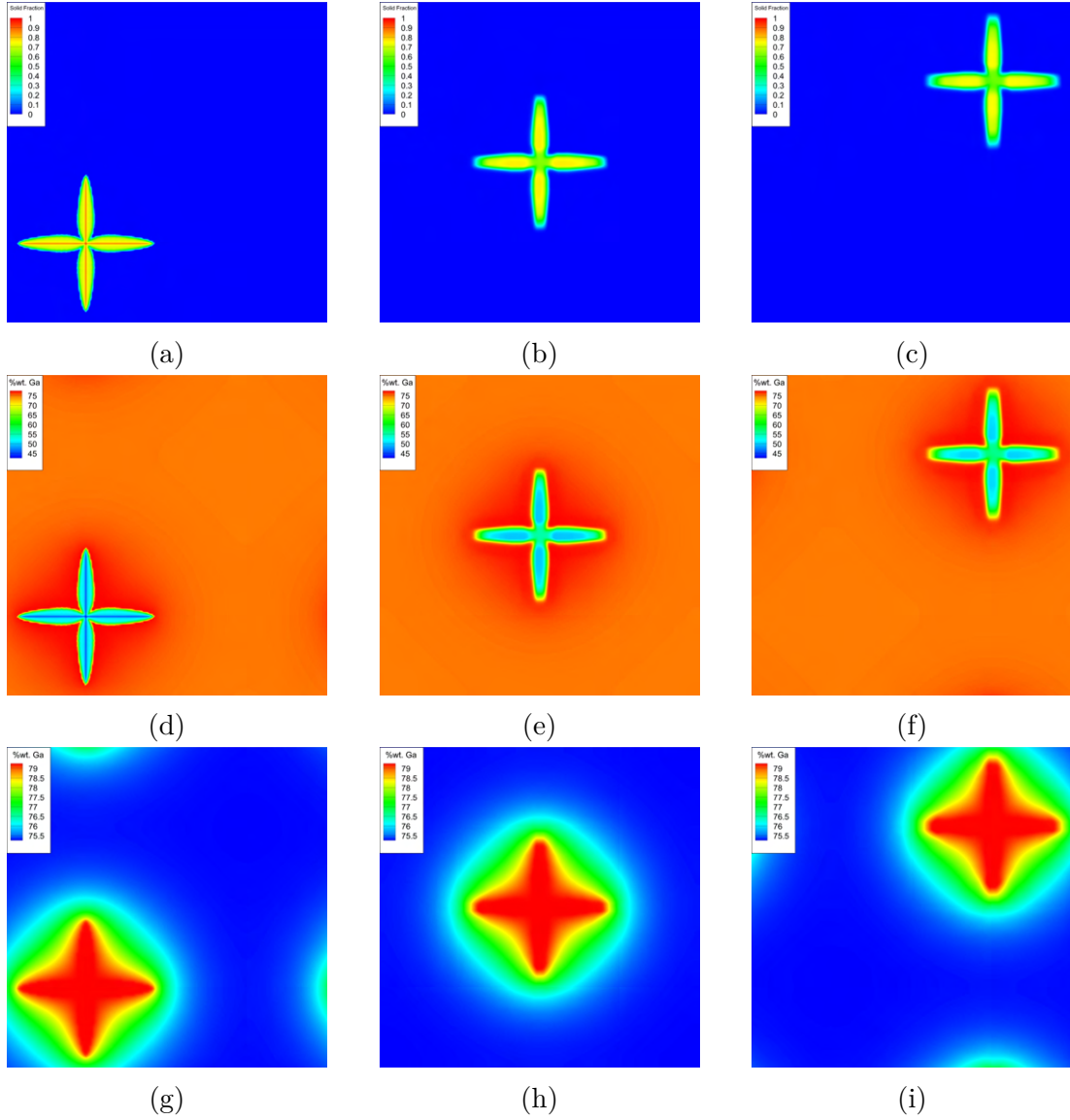


Figure 6.15: Variables needing advection for CA method. (a)-(c) solid fraction, (d)-(f) equivalent concentration, (g)-(i) liquidus concentration.

For this reason, a sub-grid method was investigated for the advection process, allowing it to be resolved on a denser grid than the one solidification was occurring on by using the interpolation methods described in section 4.5.1 to populate the denser sub-grid. The solid fraction of a grown dendrite advected using this method can be seen in figure 6.16. While still not perfectly matching

the dendrite before advection in morphology, this example does provide a vastly superior match for the arm tips, edges and interior concentration structures. These results certainly show a greater promise for allowing solidification to continue smoothly after advection.

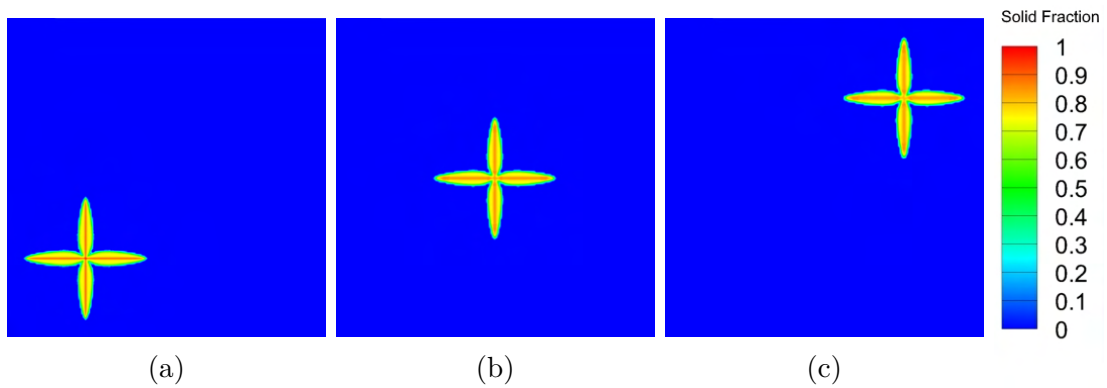


Figure 6.16: Advection using higher grid density.

To enable solidification to continue after advection has occurred, information about the dendrite orientation also needs to be advected to stay in the correct relative position. To judge how well this process worked tests were undertaken where the dendrite was allowed to grow, was advected a significant distance, then solidification was allowed to resume, with three cases of this process presented in figure 6.17.

For the first case (images (a) - (c)), a dendrite fixed at an orientation with the arms growing perpendicular to the axis shows some clear artefacts where it tries to regrow, seeming to almost re-nucleate at the tip of the arms before continuing. However, 0° dendrites generated by the CA method have a rather unique morphology, taking longer to grow secondary arms than at other orientations, so it seems possible that this sensitive system could not directly continue due to the slight changes to the dendrite morphology that unavoidably occur even with the sub-grid method. Consequently, for the second case (images

(*d*) - (*f*)), a dendrite at 45° was used for the experiment, which develops dense secondary dendrite arms along the length of the primary arms.

Evidence of the process restarting can certainly be observed in some unusual secondary arm growth, however it is certainly far less noticeable to the degree it may not even be noteworthy at all in a system with an element of randomness/noise in the cell seeding process. The final case (images (*g*) - (*i*)) is most relevant to the wider research as a columnar dendrite has been subjected to a large body force, which has generated displacement value resulting in significant deformation. Note that the deformations used in this case (and any further cases in this chapter using calculated deformations) use the linear elasticity model described elsewhere for the SMS development, as such any deformations relatively large enough to be of use for tests such as this cannot be considered physically accurate as the ‘small’ deformation condition of linear elasticity has been violated.

However, as these cases are merely proof of concepts for the advection process, the values generated by the deformation process are largely irrelevant, simply demonstrating that the SMS and the advection solver can communicate to allow for large physical deformation of structures. Looking at the regrowth in this case there is again some slightly odd behaviour in the secondary arms around where the growth continues, but this remains relatively minor.

Another possibility as to the source of this instability upon the resumption of solidification could be the grid anisotropy still present within the CA method, as the tip of the dendrite along with some of the internal structure try to only occupy a single cell. This means that if the advection does not leave the structure perfectly lined up within new grid locations, instabilities may be caused by this grid anisotropy forcing the newly seeded cells back to being perfectly lined up to the grid.

6. DENDRITE ADVECTION

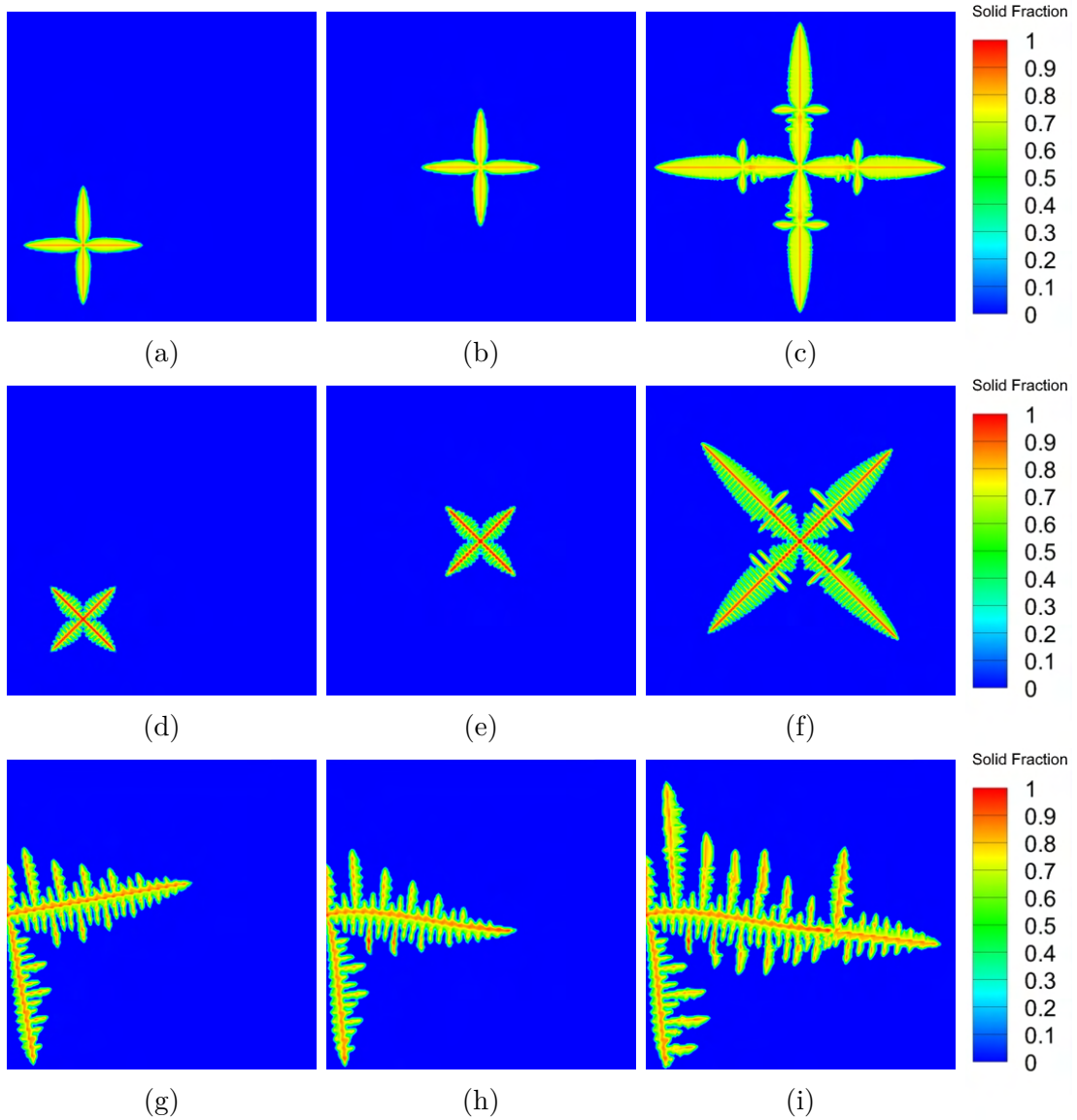


Figure 6.17: Regrowth after significant advection for a 0° equiaxed dendrite ($a - c$), a 45° equiaxed dendrite ($d - f$) and a columnar dendrite starting at 10° ($g - i$).

Trying to implement cases closely coupling solidification with structural mechanics and deformation driven advection highlighted a major complication in the sub-grid approach being adopted. The sub-grid approach requires significant advection to occur on the sub-grid before going back to the main grid, with the benefit of going to the sub-grid lessening with every movement

between the grids as the discontinuities being preserved on the fine grid become amalgamated and blurred. This means that while a structure can be advected a large distance on the sub-grid and retain a very close approximation to the initial structure on the main grid, if the advected quantity has to be regularly returned to the main grid while advecting the same distance, this will effectively leave the solution no more well defined than a regular Superbee advection process working on the main grid.

An example of this effect can be seen in figure 6.18, where a dendrite has been rotated 360° by a fixed rotational velocity field, where the fundamental morphological characteristics have been maintained throughout the rotation. However, this is because the structure could remain on the sub-grid for the entirety of this rotation.

In a case where the solid fraction was returned to the main grid after every iteration as can be seen in (f), the lack of definition is comparable to the Superbee solution operating on the main grid in figure 6.15. This makes the implementation of large advections using this sub-grid method quite sensitive and problem dependent, as to preserve structure integrity the sub-grid advection should be called as little as possible to provide the cleanest structure. If taken to extremes this could lead to unrealistic, dislocated changes in the dendrites position which would not be a realistic representation of what would be physically occurring when growth and movement should be occurring simultaneously.

6. DENDRITE ADVECTION

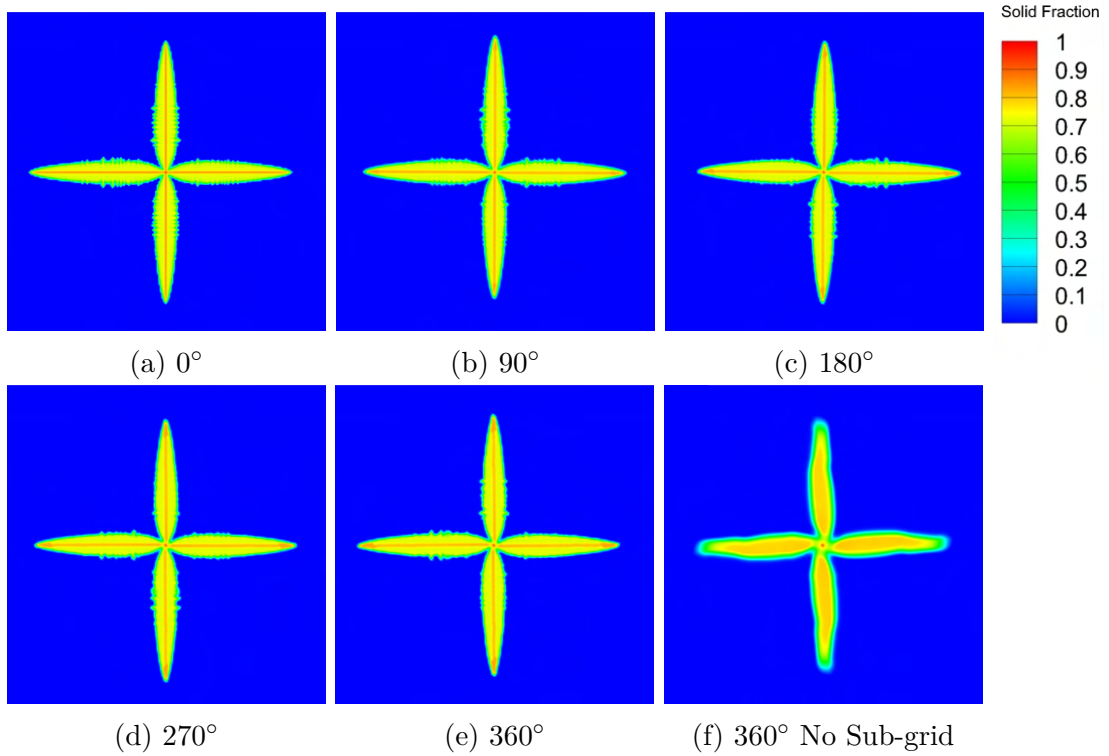


Figure 6.18: Rotating dendrite.

To demonstrate this further, figure 6.19 presents an equiaxed dendrite constantly growing as it advects through the domain with the same time steps for both processes. While it does manage to continue growing in a somewhat sensible way for an equiaxed dendrite, it becomes clear that the advection is not able to maintain the resolution to keep all of the secondary arms separate as it advects and grows, leading to a fairly continuous region of an intermediate solid fraction where there should be separate arms.

6. DENDRITE ADVECTION

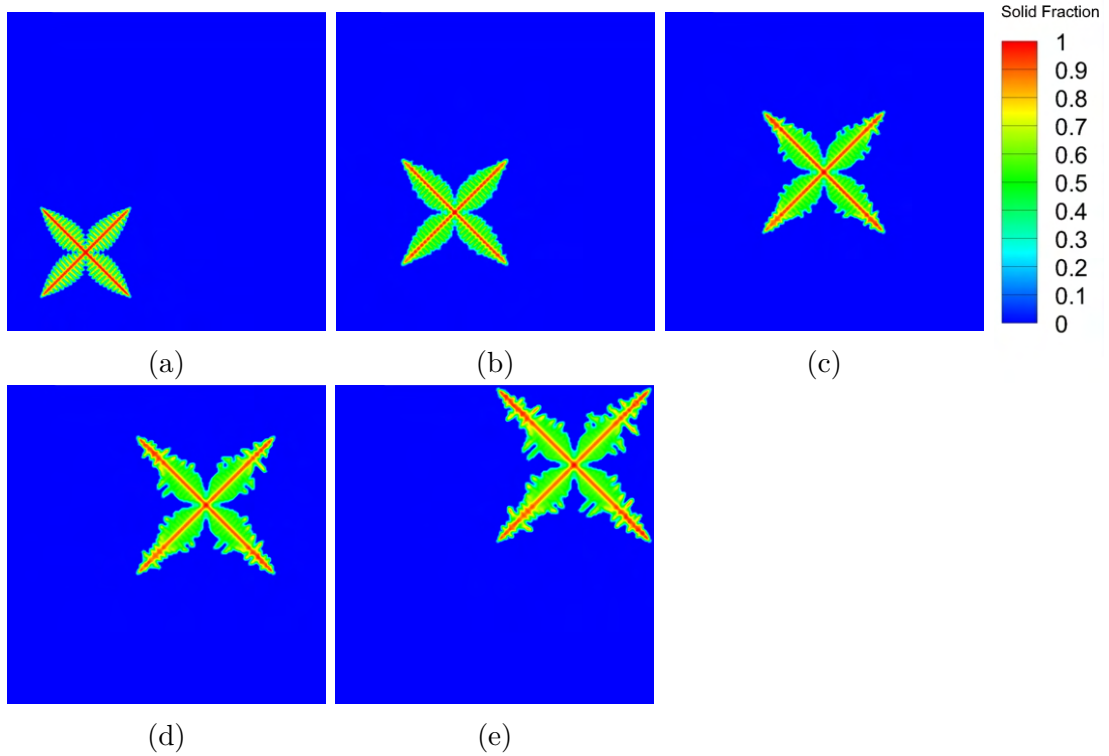


Figure 6.19: Growing equiaxed dendrite advecting using Superbee.

A case more indicative of how these large deformation driven advections could be coupled with solidification can be seen in figure 6.20, which presents a somewhat extreme situation where structural mechanics and advection are only applied once for every 1000 solidification steps. This demonstrates that the dendrite can deform significantly and change orientation yet still continue growing in a sensible manner. However, this also highlights the aforementioned weakness of the sub-grid approach as to ensure the morphological integrity of the dendrite is maintained during advection, step sizes causing notable discontinuities have had to be used. For situations such as a dendrite arm breaking off and falling, where the movement is so fast compared to the solidification rate that no meaningful solidification can occur, the sub-gridded flux limiter approach could account for these large and relatively instantaneous

movements well.

While this method shows promise as a means to combine large deformation driven advection with solidification, this has proven to not be a straightforward process as this implementation of the CA method was never designed to account for physically moving dendrites, leading to the many complications discussed in this chapter. Possibly increasing the grid density of the solidification process would create dendrites with enough detail to be preserved using Superbee advection, but utilising grid sizes of greater density than the ones used for these tests would greatly limit the size of the problems which could be modelled.

For some use cases the examples of growth with advection demonstrated here may prove to be sufficiently accurate, even when the advected solutions are not preserving the symmetry and the expected secondary arm behaviour which can be observed in dendrites modelled without advection. In reality, dendrites are never perfectly symmetrical and the growth of secondary arms can often be a more stochastic process than is generally indicated in these modelling results (as for repeatability of results any stochastic behaviour is being neglected).

Considering this, while there are clear changes to the structure and solidification development due to the impact of the advection, it may be the case that in some modelling situations the inaccuracy introduced by advection may in fact be at a comparable level to that of intrinsic factors being overlooked elsewhere in the modelling.

Furthermore, outside of the specific application of dendrite advection driven by displacement or velocity, the sub-grid approach and the advection software in general has a wider potential for application to simulating other physical processes germane to this field where many of the complications highlighted in this specific use case would not apply.

Nevertheless, an improved advection process remains a potential avenue of

future work, as solutions could only be enhanced by using an advection process capable of being called more regularly at the same grid size used for solidification without the blurring and lack of internal definition observed in the flux limited Superbee method occurring.

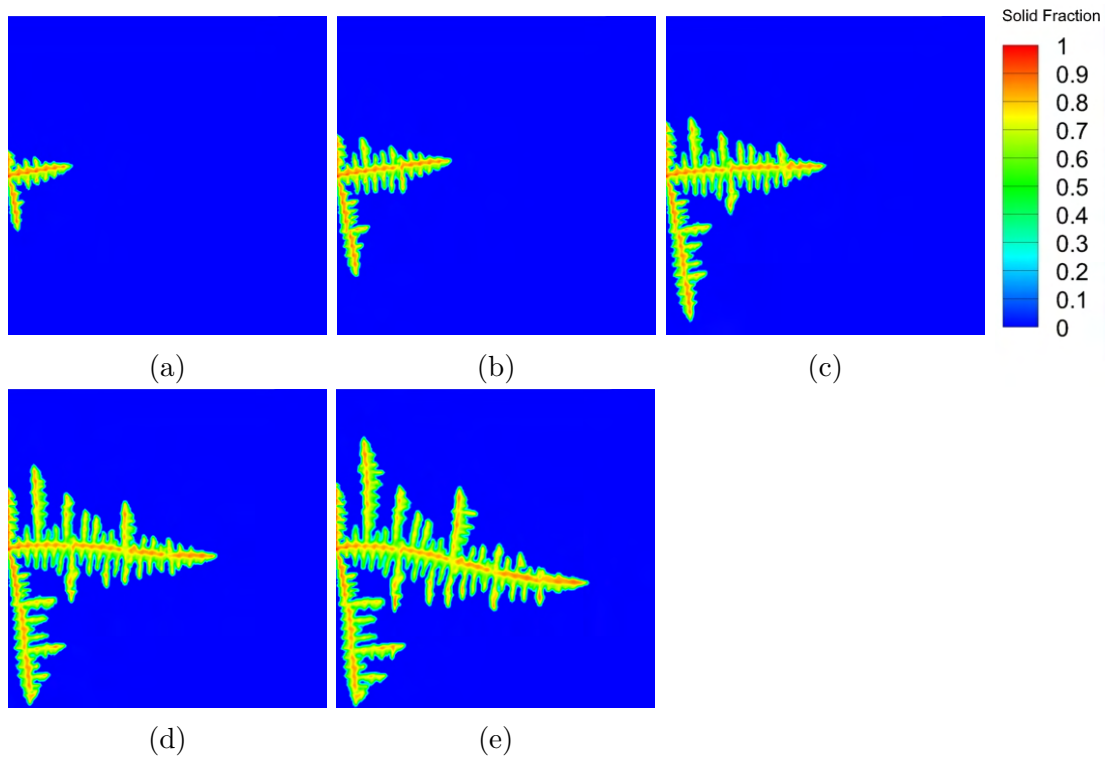


Figure 6.20: Concurrent solidification with significant deformation.

6.6 Currently Implemented Advection

Further work on advection driven processes ultimately stalled due to the discoveries outlined in Chapter 5 of how small deformations can theoretically be accounted for entirely by the change in orientation. Due to the assumptions of ‘small’ deformations constraining Linear Elasticity, large deformation driven advection such as the cases presented in this chapter should never occur, as if they did these results could not be considered reliably accurate due to violating

the assumptions of a linear elastic material. In order to obtain a large advection such as those investigated, either a new material model capable of large deformation would have to be implemented or large velocities would have to be obtained from one of the other physical processes modelled in TESA.

While both of these are potential expansions being considered to expand the research (see section 8.2 for future work), they remain secondary to the primary goal of exploring the impact of small deformations on the dendrite growth, though this does not necessarily mean that solid advection has no place within this framework. Whilst in theory for small deformations the orientation change can account for the movement, in practice the orientations calculated and applied to cells actually lag a time step behind where they should be to fully account for the deformation. That is to say, the calculated orientation would only account for the *deformation that has already taken place*, but not necessarily going forward.

To theoretically account for all deformation using orientation changes, the dendrite would have to be growing at an orientation which could only be calculated after growth had occurred, while for obvious reasons in reality the calculated orientations can only apply to subsequent growth. If the structural mechanics and solidification are closely coupled, this distinction should be largely insignificant, but it remains the case there is movement within the structure not being accounted for.

One possible answer to this would be an advection process which could use these deformations to move small quantities of the solute between the cells, allowing the influence of these overlooked deformations to be accounted for in the microstructure. As it currently works the advection process is more than capable of accounting for this, with the concerns about interface reconstruction maintaining internal morphology not being applicable for such relatively small

advections and the flux limited Superbee advection being sufficient to prevent the dendrite from diffusing into the surrounding environs and unrealistically seeding cells. On the other hand, the inclusion of these small advections would not be computationally insignificant, while generally not having a meaningful impact on the development of the microstructure if the orientations are updated with sufficient regularity. Furthermore, the assumption of ‘small’ strains/deformations dictate that the structure should be treated as occupying the same position in space after the deformation has occurred, meaning that accounting for these small deformations in this manner is arguably violating these linear elasticity assumptions.

Considering these factors, at present the described small advection behaviour has been implemented such that it can be turned off, or on, as the problem requires, but is currently often neglected for large scale cases due to the minor impact it has on the solutions when compared to the computational time added to obtain said solutions.

6.7 Summary

The theory behind and current implementation of advection driven by either displacements generated by the SMS or velocity field generated elsewhere in TESA are discussed in this chapter. Flux limited advection and Volume of Fluid methods are introduced and discussed in the context of advecting structures of different consistencies and morphologies. These advection techniques were then applied to solidification problems, demonstrating the difficulties but also the potential viability of these methods for large advection concurrent with solidification. Finally, it was described how advection was being applied in the context of the small deformations which are the primary focus of this research.

Chapter 7

MODELLING CASES

7.1 Overview

This chapter will present a selection of modelling cases which have been chosen to highlight behaviours and mechanisms which can only be captured by modelling concurrent structural mechanics and microstructure solidification. Starting by explaining the context of these cases as well as the standard problem setup, the initial cases presented are all using a thin sample setup with the first showing orientation change of a single columnar dendrite under a gravity like body force. The subsequent case demonstrates the potential influence of thermal strains on a growing dendrite. The ability to account for transient forces is shown by a sinusoidally changing force before presenting some large scale solutions obtained using parallel computing. The remaining cases show truly 3D dendrites, where all dimensions are significant, demonstrating how a single dendrite can be bent out of plane as well as showcasing how the model handles a rotational force. Finally, a small parametric study is performed to examine the impact of forces of increasing magnitudes on a single growing dendrite to demonstrate the non-linear nature of this process and emphasise the importance of this field of research.

7.2 Context and Problem Setup

The cases being presented in this section have been primarily selected to highlight the unique behaviours which can only be modelled using coupled microstructure solidification and structural mechanics rather than trying to obtain a realistic match to experimental test cases (though some realistic cases will be shown). While there are numerous examples of dendrites bending and becoming misorientated as outlined in chapter 2, many involve deformation outside of the linear elasticity assumptions, lack experimental details the modelling would require or would require other physics to be modelled for a realistic chance of a close match. In particular, due to fluid flow not being implemented at this stage, for many cases there are a number of missing factors which would influence the solidification and complement the structural effects such as remelting, changed solute transport and additional pressure forces from the flow. While the force could be increased to represent the pressure and weakened base of the structure caused by remelting (though quantifying the increase in force that would account for these factors, even loosely, would be a difficult task), this would still be entirely neglecting the changing solidification behaviour.

While there are differences in the problem setup that will be highlighted for each case, there are many aspects which they share and will be outlined here. The cases in section 7.3 - 7.6 are all modelling ‘thin sample’ cases as can be seen in figure 7.1. This means that one of the dimensions has far fewer computational cells in one of the axis directions than in the other two (for all of these cases this is in the x axis using only 20 cells). This means that while the structure is truly three-dimensional, and is being solved as such, the behaviour will be similar to a two dimensional case under plane stress, with the displacements in u and rotations calculated around the y or z axis generally being insignificant. Many practical

7. MODELLING CASES

experiments use a thin sample to facilitate easier visual observation, and similarly the thin sample cases have been chosen for these cases as they make it easier to observe the modelled behaviours. The other cases in sections 7.7 - 7.9 are ‘fully 3D’ in the sense that they have a significant number of computational cells in all directions, allowing complex phenomena to arise which could not be captured in 2D simulations. The boundary conditions (see section 3.6) are generally the same across comparable cases, where any exceptions will be noted. For thin sample cases, the East and West faces are slip conditions where $u = 0$, the South face has all displacements fixed, the North face is free and the High and Low faces are periodic. For the fully 3D cases the Low face is fixed, the High face is free and all other faces are periodic.

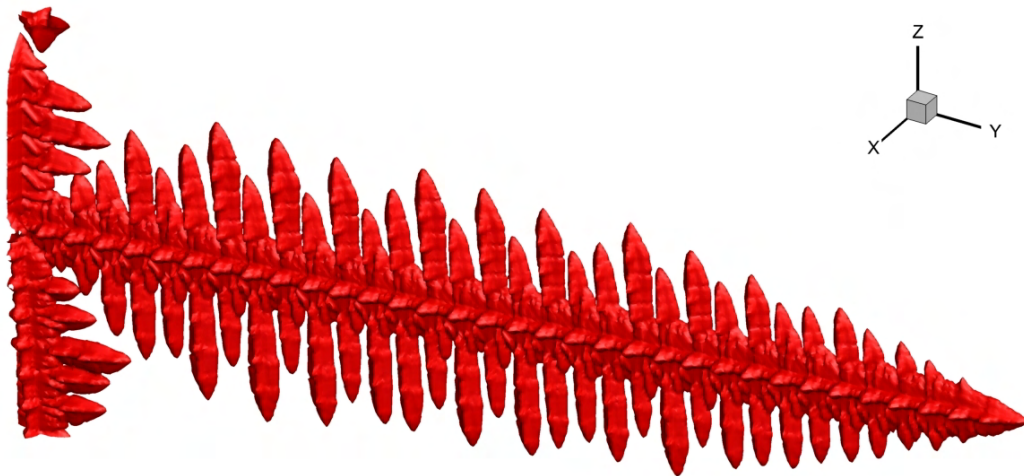


Figure 7.1: Thin sample 3D view.

Outside of the problem domain, all relevant variables related to the material

7. MODELLING CASES

properties and problem setup have been summarised in table 7.1, as representative of experiments to solidify Ga – 25wt%In alloys, this being a material used in previous work published using this model [45]. The only pertinent information which has not been included in the table is the Young’s Modulus and force definitions being used, as these related quantities (increasing the force or decreasing the Young’s Modulus by the same factor leads to identical deformations being obtained) are defined differently for many cases presented, generally to exaggerate and highlight the structural effects so they can be easily observed and discussed even when solidification is only occurring over a relatively a small domain. Thermal expansion has been neglected for all cases except for those which explore this behaviour. This has been done as for most cases the temperature variations at the micro-scale are small, so if realistically modelled would often have little to no impact on the structural development. However, if the relevant variables were increased for the sake of demonstrating their impact, this would cause results to develop in a way which would distract from any behaviour being driven by external forces.

Finally, it must be reiterated that these results are being modelled under the assumptions laid out in this section as well as the earlier defined linear elastic assumptions, with the primary aim being to highlight the functionality of the model and consequently should generally not be taken as indicative of the actual behaviour of deforming dendrites from a Ga – 25wt%In alloy. The linear elastic assumptions mean that the presented stress profiles are particularly questionable, as it is very likely that there is a significant degree of plasticity within the semi-solid dendrites being considered which would likely significantly lower the internal stresses of the structure.

7.3 Thin Sample Fixed Force

The case presented in figure 7.2 shows a single seed growing into a columnar dendrite in a $400 \times 160 \times 20$ cell domain, where the orientation significantly changes as a constant body force is applied in the z direction at each structural mechanics time step. This is defined as $F_z = -\Delta\rho g$ N/m³, where $\Delta\rho$ is the density difference within a cell and g is the gravitational acceleration. In order to obtain a notable orientation change over such a small domain a rather low Young's Modulus of $E = 10000$ Pa was used. The seed had an initial orientation of $\theta_x = 5^\circ$, so that secondary arms should start growing early on in the simulation.

Looking at the results in figure 7.2 showing the changing solid fraction over time, it can be seen that by (a) there was no visible evidence of orientation change, which by (b) had been changed to almost negate the starting seed orientation, while by (c) the orientation is now growing at a visibly negative inclination. This is highlighted further in (d) which shows how there is wide local variation in the orientations of the structure from the initial orientation it was seeded with. For the final state of the dendrite this shows the misorientation growing along

Property	Variable	Value	Unit
Density Ga	ρ_{Ga}	6095	kgm ⁻³
Density In	ρ_{In}	7020	kgm ⁻³
Poisson's Ratio	ν	0.3	—
Liquidus Slope	m_l	-2.9375	K%wt. ⁻¹
Partition Coefficient	k	0.5	—
Liquid Mass Diffusivity	D_l	2×10^{-9}	m ² s ⁻¹
Solid Mass Diffusivity	D_s	1×10^{-12}	m ² s ⁻¹
Cooling Rate	Q	0.01	Ks ⁻¹
Thermal Gradient	G	1	Kmm ⁻¹
Cell Size	Δx	10	μm
Time step	Δt	5	ms

Table 7.1: Properties used for problem setup.

7. MODELLING CASES

the length of the dendrite, having the largest change at the tip in a manner somewhat analogous with the claims that a columnar dendrite will behave like a cantilever beam. Some small positive changes in orientation can be seen in the secondary arms growing off of the wall, caused by the elastic nature of the material causing these arms to bend upwards to balance the deformation of the main arm. The image in (e) shows the Von Mises Stress which had accumulated within the dendrite, highlighting that the highest regions of stress are generally where secondary arms attach to the main arm or interact with each other. Finally, in (f) a result showing the state of a dendrite grown without a force acting upon it is shown for the sake of comparison.

This case was chosen to demonstrate that the key mechanism of a dendrite becoming misoriented over time due to external forces can be captured, where significant changes in microstructure development can be observed.

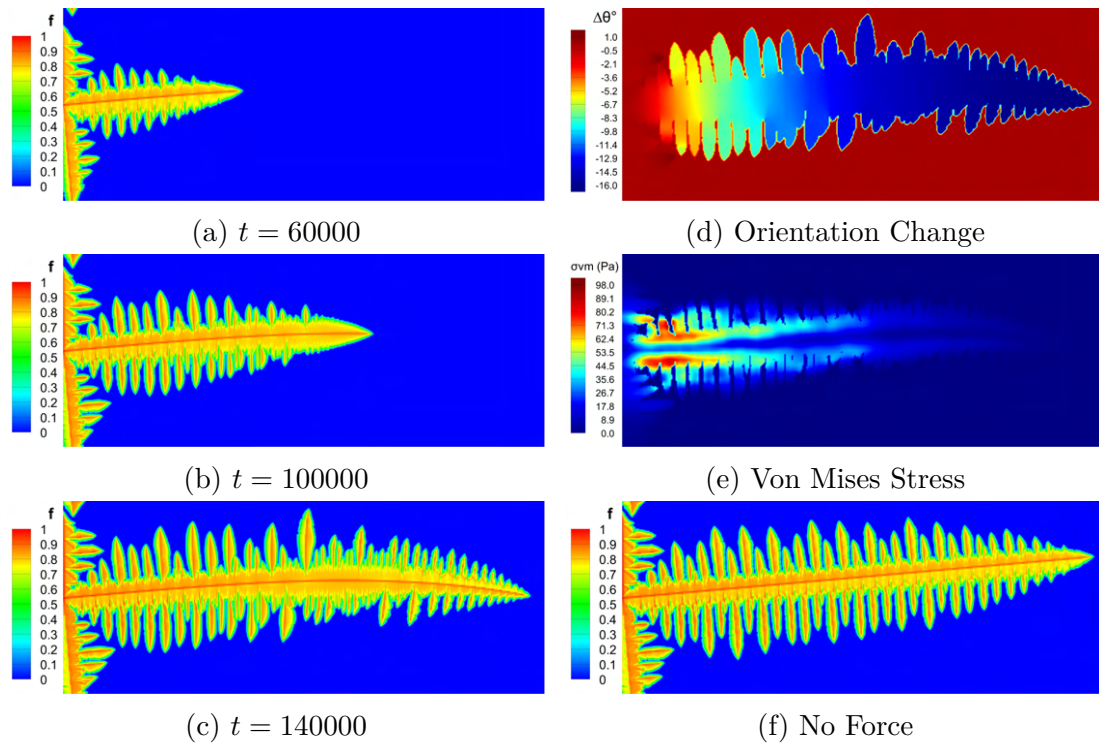


Figure 7.2: Thin sample dendrite growing under a constant body force.

7.4 Growth Under Thermal Strain

The case presented in figure 7.3 shows a single seed growing into a columnar dendrite in a $400 \times 320 \times 20$ cell domain, where the orientation is significantly changed by thermal expansion occurring as the dendrite solidifies. In order to present a clear case where thermal stress is the only driver of deformation, a slightly different problem setup was chosen where the thermal gradient was fixed (so cooling rate $Q = 0 \text{ Ks}^{-1}$) and to account for thermal expansion a coefficient of thermal expansion $\alpha = 3.1 \times 10^{-4} \text{ K}^{-1}$ was used, where the reference temperature for expansion was taken to be $T_{ref} = 295.1675 \text{ K}$, which is the constant temperature running north to south through the centre of the domain. Again a Young's Modulus of $E = 10000 \text{ Pa}$ was used to exaggerate the orientation change over such a short distance. The seed had an initial orientation of $\theta_x = 0^\circ$, so that the columnar dendrite would grow straight along this centre line absent of any structural mechanical intervention.

Looking at the results, in (a) the final state of the simulation can be seen, where the structure has deformed into the cool region below the reference temperature, with the fixed temperature gradient being found in plot (b). The orientation of the dendrite can be observed in plot (c), again showing the largest misorientation at the tip of the dendrite. Finally, in plot (d) the Von Mises Stress driven by the thermal expansion can be observed, which as would be expected is most significant in the regions where the expansion or compression of the dendrite would be most constrained.

This behaviour corresponds with what would intuitively be expected, where the thermal gradient around the reference temperature means that anything growing in the upper half of the domain wants to expand, while any material in the lower half wishes to contract. The combination of these influences is consistent with the bend into the cold region being observed. This case was

7. MODELLING CASES

chosen to demonstrate that the thermal expansion structural mechanics behaviour described in section 3.7 functions correctly when fully coupled with microstructure solidification and can have a notable impact on the development of the microstructure under the correct conditions.

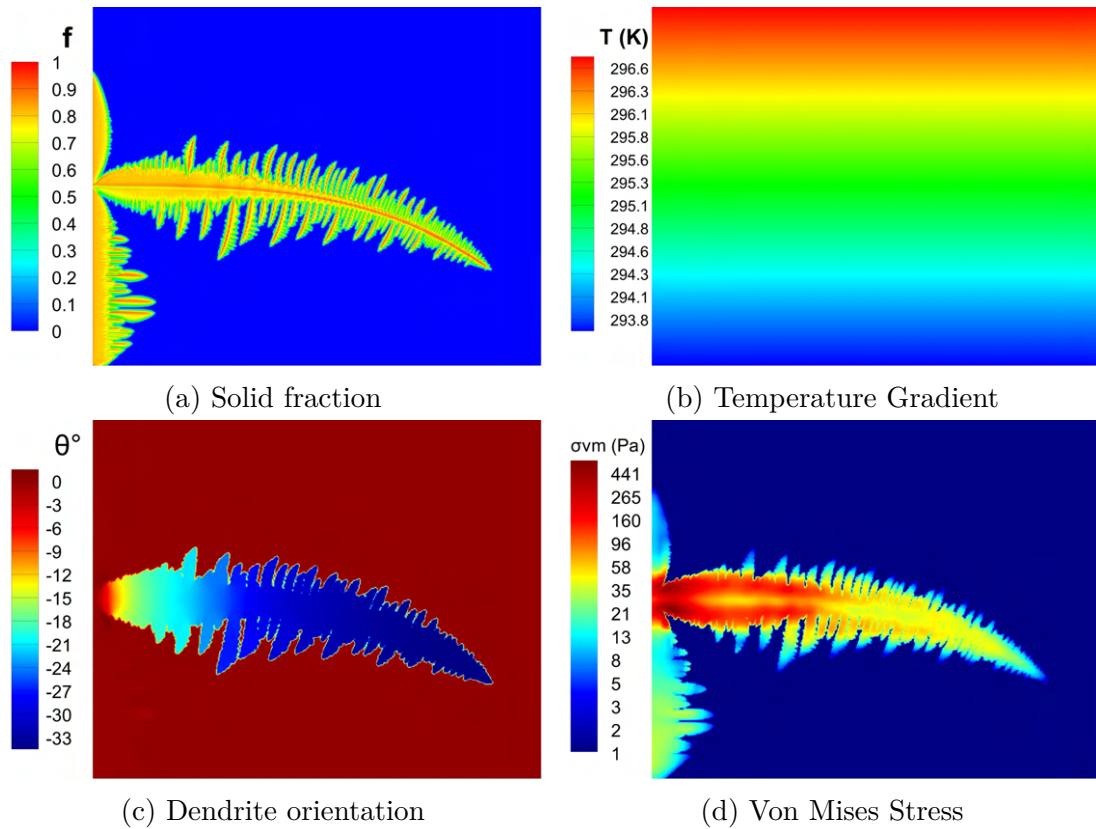


Figure 7.3: Dendrite growing under thermal strain.

7.5 Sinusoidally Changing Force

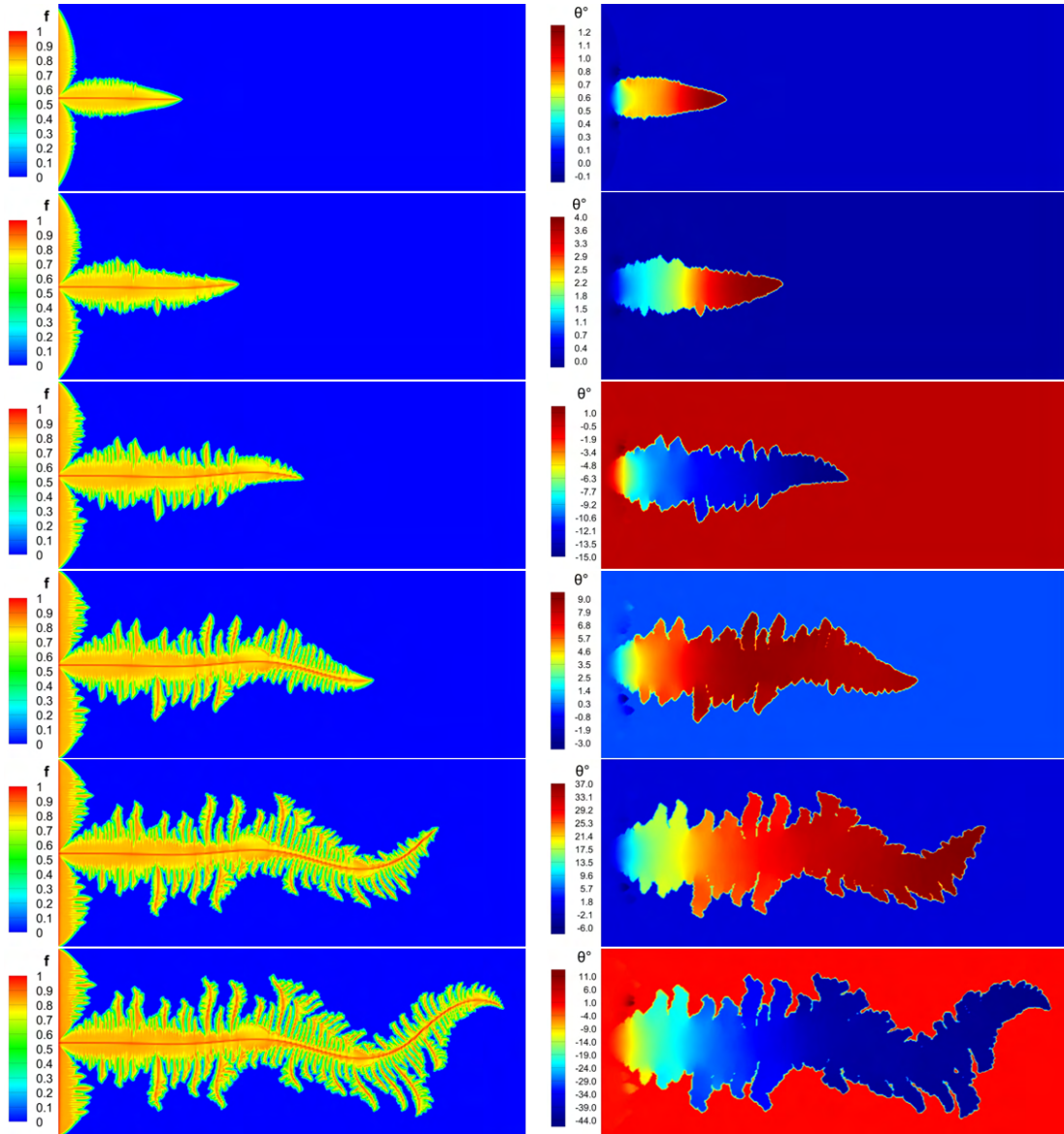
The case presented in figure 7.4 shows a single seed growing into a columnar dendrite in a $400 \times 160 \times 20$ cell domain, where the orientation of the dendrite changes significantly over time due to a body force which changes sinusoidally over time. This time dependent force was defined as $F_z(t) = -\sin(\beta t) \times \Delta\rho g \text{ N/m}^3$, where $\beta = 5 \times 10^{-3}$ is a variable to change the frequency of the sine wave, chosen somewhat arbitrarily to allow multiple distinct waves to be visible, g is three times the usual value of Earth's gravitational constant and a Young's Modulus of $E = 10000 \text{ Pa}$ was used to allow significant orientation changes to happen over the relatively short domain. The seed had an initial orientation of $\theta_x = 0^\circ$, so that there is no existing bias in the preferred growth direction before the force is applied.

The results show the development of the (a) solid fraction and (b) orientation, where the sinusoidal nature of the force becomes more obvious as the solution develops, with the 'amplitude' increasing due to the deformations growing larger as the dendrite increases in length. Graphs extracting information at the tip of the dendrite showing how the force, tip location along the y axis, total orientation and observed deformation for the time step change throughout the simulation can be observed in figure 7.5. In particular, figure 7.5e scales all of these variables so they can be compared on a single plot. This demonstrates that while the displacement largely matches movements in the force as would be expected, the orientation change lags behind so that it has a turning point when the force is close to zero. The tip location then itself lags behind the orientation, this time having a turning point when the orientation approaches zero, which actually causes it to move in opposition to the force. However, when considering the process of coupled solidification, these lagged behaviours make intuitive sense. If it is not altered by further deformation the

dendrite orientation will maintain its value in perpetuity, so even after the force has reached its peak amplitude and begun to decrease in size, these will still result in correspondingly signed deformations which will continue to increase the magnitude of the orientation, albeit at a decreasing rate. Only after the force approaches zero will the increase in orientation stop, and correspondingly only when the force begins acting in a direction opposing the current growth orientation will the orientation finally begin to diminish in magnitude. A similar relationship exists between the orientation and the tip location, where the tip location of the dendrite will continue to increase in magnitude due to the dendrite continuing to grow away from the starting location even if the orientation stops changing. Consequently the same relationship can be observed where the tip location only stops changing when the orientation approaches zero, and the tip will only be moving counter to its current bearing when the orientation has changed sign. These plots seem to indicate that once the lag is accounted for, the tip location, orientation and deformation all demonstrate a similar increase in peak amplitude with each wave period. However, the increase in amplitude does not seem to be consistent with each cycle, which is likely a consequence of the changing morphology of the dendrite giving it significantly different deformation behaviour over time, which is passed on to the deformation dependant orientation and tip location quantities.

This case was chosen to demonstrate that the method of accounting for existing deformation outlined in section 4.4 is also capable of accounting for transient forces which may negate or even reverse previous deformation.

7. MODELLING CASES

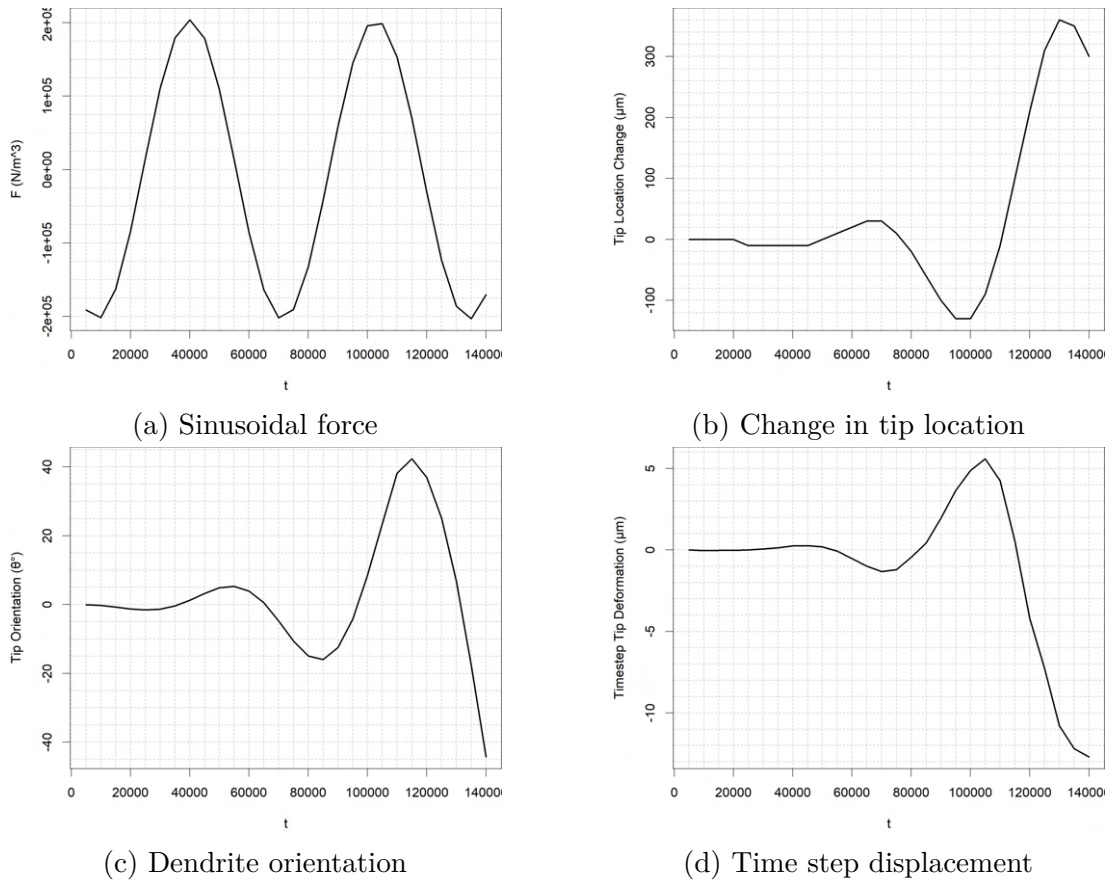


(a) Solid Fraction

(b) Dendrite Orientation

Figure 7.4: Dendrite growing under sinusoidal force.

7. MODELLING CASES



(c) Dendrite orientation (d) Time step displacement

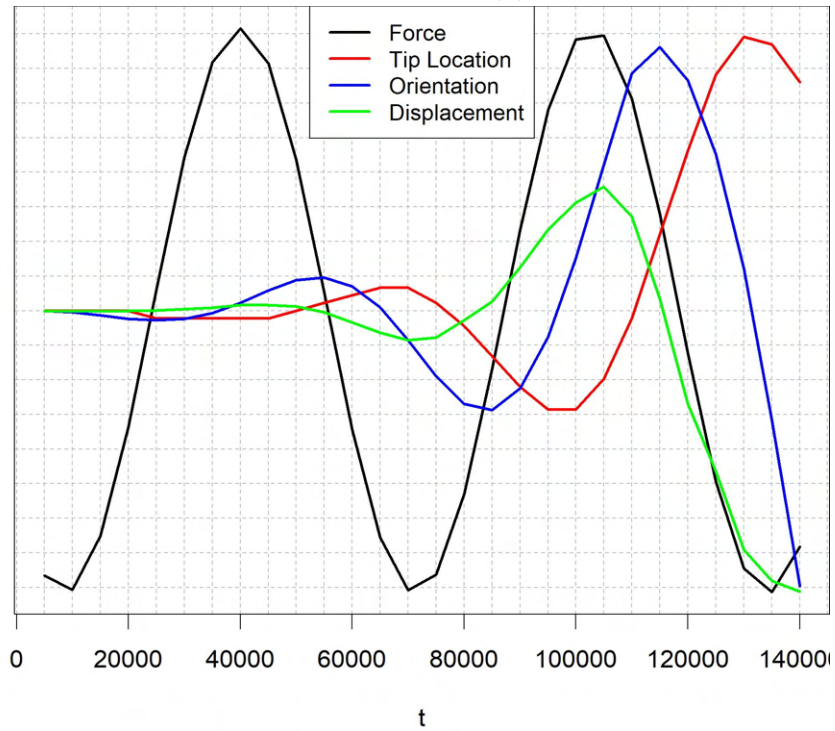


Figure 7.5: Variable comparisons over time for dendrite under sinusoidal force.

7.6 HPC Thin Sample Cases

This section will showcase some examples of large scale thin sample modelling run on the HPC facility at Greenwich University, allowing much larger problem sizes to be solved thanks to the use of parallel programming.

The work in figure 7.6 was presented in the paper “Predicting Concurrent Structural Mechanical Mechanisms During Microstructure Evolution” by Soar *et al.* (2021) [45]. This took a $6400 \times 1600 \times 1$ cell domain, with $F_z = -\Delta\rho g$ where g is 3 times terrestrial gravity and a Young’s Modulus of $E = 30MPa$ was used. This Young’s Modulus is taken as the lower bound for a semi solid alloy within the Eutectic region, as determined from the compressibility of constrained liquid Indium and Gallium [119]. This is in fact a 2D problem, obtained before 3D was fully implemented, however the behaviour should be similar to a thin sample 3D case. The grains were seeded with an initial orientation of $\theta_x = 20^\circ$, so that they would grow at a noticeable orientation before structural mechanics grows large enough to noticeably counteract it.

In part (a) of the image the deformations are too small to cause any notable orientation change, becoming small but visible in (b), by (c) the starting orientation of 20° is almost entirely counteracted and by the final step taken in (d) the orientation changes have accumulated to such a degree that the starting positive orientation is entirely counteracted and the orientation at the tip is now clearly negative. Part (e) of the image shows the orientation changes throughout the sample, with the misorientation growing larger towards the tip, though areas where secondary arms interact also demonstrate local misorientation. Part (f) shows accumulated v displacement within the dendritic structure, where the highest deformation can generally be found somewhere in the centre of the dendrites, fading out towards the tip and root. While these deformations may at first appear counter intuitive, attaining the largest

7. MODELLING CASES

accumulated deformation within a structure requires balancing the magnitude of individual deformations against the total accumulated deformation. The region satisfying this is usually at the centre as the tip of the dendrite has only experienced a few deformation events, even if their magnitude is relatively large, while conversely the root of the dendrite has been experiencing deformation events for the entire simulation, but these are of a consistently small magnitude compared to the constantly increasing deformations occurring at the tip. Part (g) shows the Von Mises stress within the microstructure, demonstrating that the main regions of stress are pivot points where primary arms or stable parts of the microstructure are fixed or where secondary arms impinge upon each other. Finally, part (h) shows the contrasting case where the solidification occurred without any force being applied, allowing it to grow along the starting orientation unimpeded. This case was chosen to demonstrate that significant structural mechanical effects can be captured by this model using realistic conditions in a domain size comparable to those used in practical experiments.

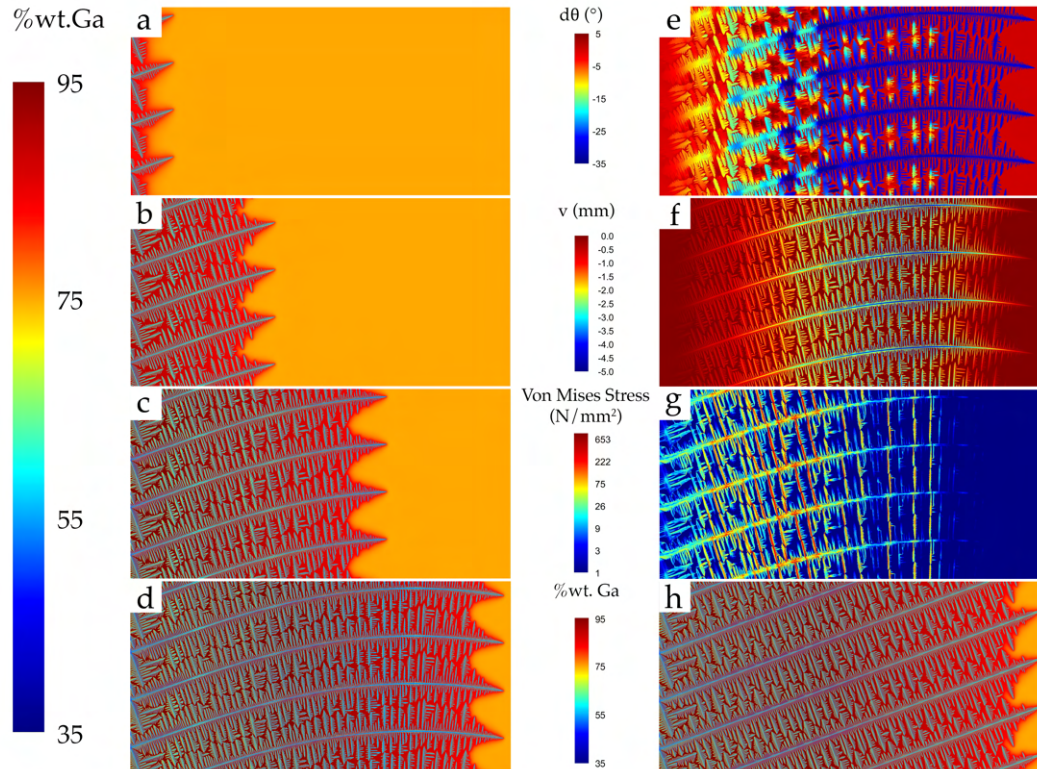


Figure 7.6: Large scale thin sample solutions from *Soar et al.* [45].

A further, preliminary case from this paper can be seen in figure 7.7, which has the same setup except for some grains having their deformation and hence orientation fixed, while other grains are free to deform. This is analogous to the situation where a dendrite may have fused to or otherwise be somehow constrained by some imperfection on the thin sample wall. This leads to examples of converging/diverging grains due to the continuous nature of the modelling, where in this case the deforming grain was ultimately trapped by the fixed grain. However, grain competition being a complicated phenomenon, under slightly different conditions the deforming grain could have out competed the fixed one, leading to the formation of a stray grain.



Figure 7.7: Converging grain example from *Soar et al.* [45].

Similar cases were later modelled in 3D (though still thin sample), one of which has been presented in figure 7.8. This case was chosen as it demonstrates some interesting behaviour which differentiates it from the 2D case, despite having smaller deformations. Part (a) shows the concentration within the structure rather than solid fraction, for easier comparison with the prior HPC case. Part (b) shows the same behaviour with the deformations, having a maximum in the centre of the dendrite. The orientations which can be seen in (c) highlight the interesting behaviour due to secondary arms interacting with one another, the tips of two primary dendrites have been bent away from each other, which if the simulation could continue, would eventually lead to the formation of a new primary arm between them. The Von Mises Stress in (d) shows stress accumulating throughout the dendritic structure except for the tips which are still relatively free to move, with there being a high region of stress which quickly diminishes at the point where the arms start to noticeably diverge.

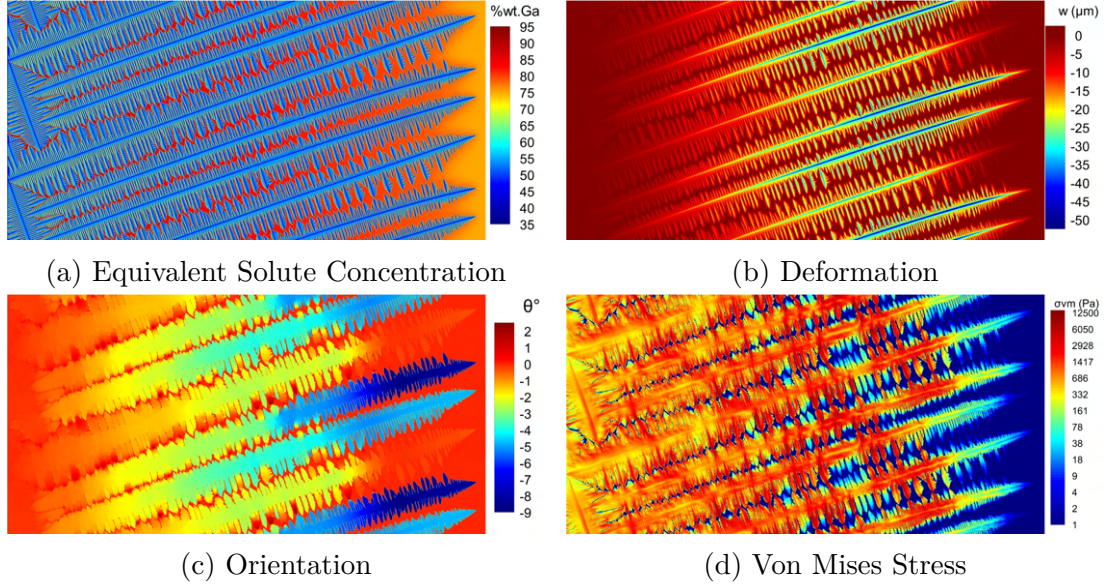


Figure 7.8: Large thin sample dendritic system.

7.7 3D Dendrites

The cases in this section were chosen to highlight some behaviours only observable in fully 3D environments, without the constraint of the thin length in one direction as in the prior thin sample cases.

The first case in figure 7.9 takes a single dendrite growing from the floor of a sample and applies two body forces simultaneously to cause it to deform out of plane. For this the forces were taken as $F_x = F_y = -\Delta\rho g \text{ N/m}^3$, where g is equivalent to terrestrial gravity and a Young's Modulus of $E = 10000 \text{ Pa}$ was used. From applying two forces in this way, significant orientation change around both the x and y axis can be observed, causing the dendrite to grow into one of the corners of the domain.

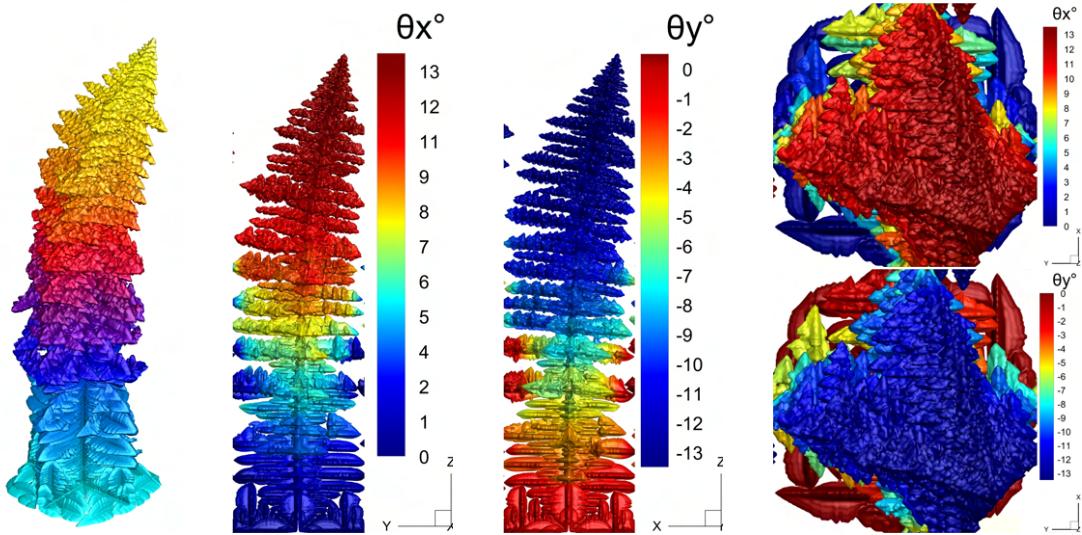


Figure 7.9: Dendrite bending out of plane.

The case in figure 7.10 takes a domain where 50 dendrites were seeded in random locations and with random orientations between $\pm 20^\circ$, to highlight that within this complex framework of competing dendrites, the SMS is able to correctly identify and obtain displacements for the structures, which each have their own distinct orientations which still can change within a single dendrite. For this a force of $F_z = -\Delta\rho g \text{ N/m}^3$, where g is equivalent to five times terrestrial gravity and a Young's Modulus of $E = 10000 \text{ Pa}$ was used. While, ultimately, the same two dendrites managed to outcompete the others in both cases, clear differences in dendrite orientation can be observed throughout the sample. In larger samples, or even just a different random distribution, the impact from the structural mechanical changes could easily influence which dendrites will out compete one another.

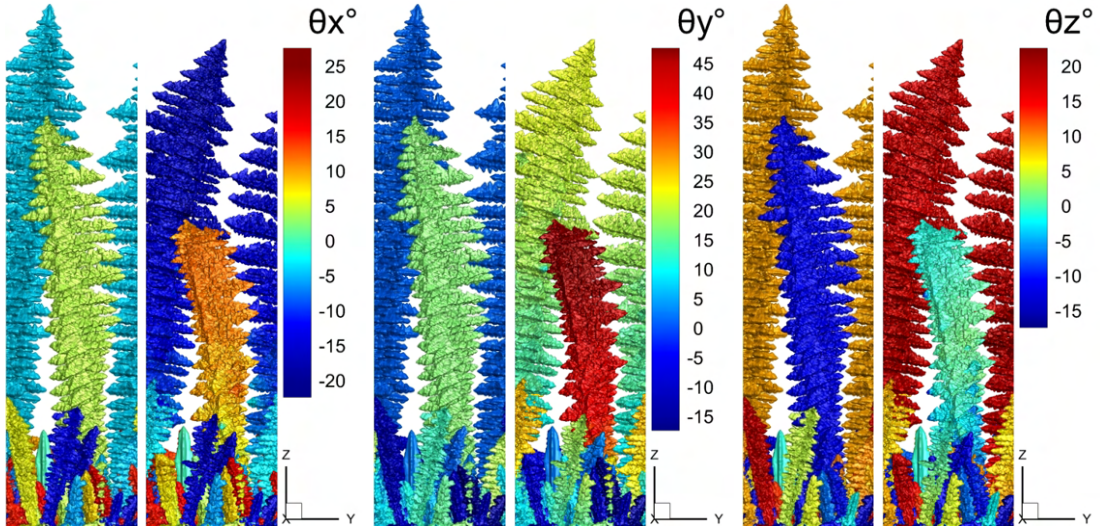


Figure 7.10: Forest of dendrites showing orientation components in pairs to compare behaviour without (left) and with (right) force applied.

7.8 Rotational Force

This case presents a single dendrite growing upwards through a rotational force. To represent this, at the centre of the dendrite the force acting upon the structure is zero, but the forces F_x and F_y increase in magnitude as they approach the domain boundaries to $\pm\Delta\rho g$ N/m³, where g is five times terrestrial gravity and a Young's Modulus of $E = 10000$ Pa is used. This imparts a counter clockwise rotational force upon the structure as it grows. Under these conditions this dendrite can be observed in (a)-(c) to form a clear spiral, with the secondary arms preferentially growing counter clockwise as they grow. Part (d) shows how the rotation around the y axis varies along the length of the dendrite, with the tip of the dendrite having experienced approximately an entire 360° rotation in the course of the simulation.

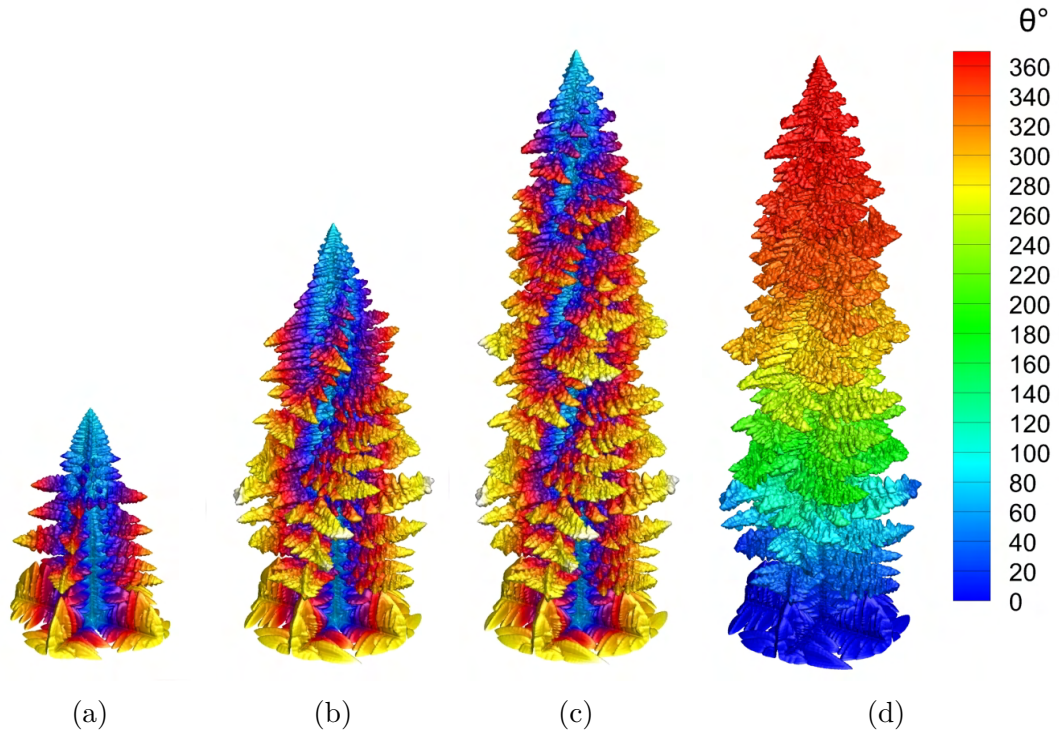


Figure 7.11: Rotational force acting upon a dendrite.

7.9 Parametric Study

The final case chosen to be presented in this section is a parametric study examining the changing behaviour of a single dendrite growing under increasing body forces. For this study a seed with an initial orientation of $\theta = 20^\circ$ was placed on the east wall of a $200 \times 200 \times 1200$ cell domain with a thermal gradient across the 1200 cells which cools after the simulation starts. Periodic boundaries were used so that rather than modelling a single dendrite growing in a solid ‘box’, the modelling instead represents a three-dimensional region being taken out of an infinite field of identically seeded dendrites. While this certainly still presents an idealised scenario, it should serve to highlight the impact of interaction on deformation and orientation which would occur in situations

7. MODELLING CASES

where multiple dendrites are growing. This periodic approach also allows the mass and secondary arm length of the different cases to remain comparable between the cases, where a bending dendrite in a solid ‘box’ could become top or bottom heavy as it develops and is limited in growth by interaction with the wall.

Five cases will be taken for this parametric study where for a structure with a Young’s modulus of $E = 10000$ Pa when fully solidified the only variable changed is the body force, with body forces of 100 N/m^3 , 1000 N/m^3 , 2500 N/m^3 , 5000 N/m^3 and 10000 N/m^3 being examined. Going forward, the cases using these forces will be identified by the multiple of force used relative to the initial case, making the cases examined in the study 1, 10, 25, 50 and 100 respectively. Each case has been run for 250000 time steps where $\Delta t = 0.005$ seconds, so that the final state presented is at a point 1250 seconds after initial seeding.

The final state after 250000 steps can be seen for all cases in figure 7.12. This shows that for cases 1 and 10 little to no visible orientation change has occurred, though for case 10 the orientation change has accumulated to cause a notably different location and orientation for the tip of the dendrite, along with various small changes in the secondary arm development. Case 25 now clearly shows the changed orientation, with the dendrite tip almost flattening off so that the total orientation is approaching 0° . Case 50 exaggerates the orientation change further, with the initial orientation not just being matched but almost entirely reversed. Case 100 has become difficult to directly compare to the other cases as it demonstrates misorientation so great that the tip of the main dendrite arm was approaching an orientation parallel with the force direction, seemingly only being stopped due to being outcompeted by a secondary arm. If the simulation continued one of these now competing secondary arms would

7. MODELLING CASES

become the new primary dendrite, leading to a vastly different overall microstructure. One observation about the different microstructures is that as larger forces are used, the length of the dendrite from base to tip becomes smaller. While the difference between cases 50 and 100 from the prior three cases is the most obvious, on close inspection this holds true for the first three cases also. It is not entirely clear why this is the case, with more research into the growth of curving dendrites under different conditions being required to establish if this is realistic. If the curving dendrites were to be somehow straightened then the distance covered would be more comparable, but would still be lagging behind the tip distance attained by case 1.

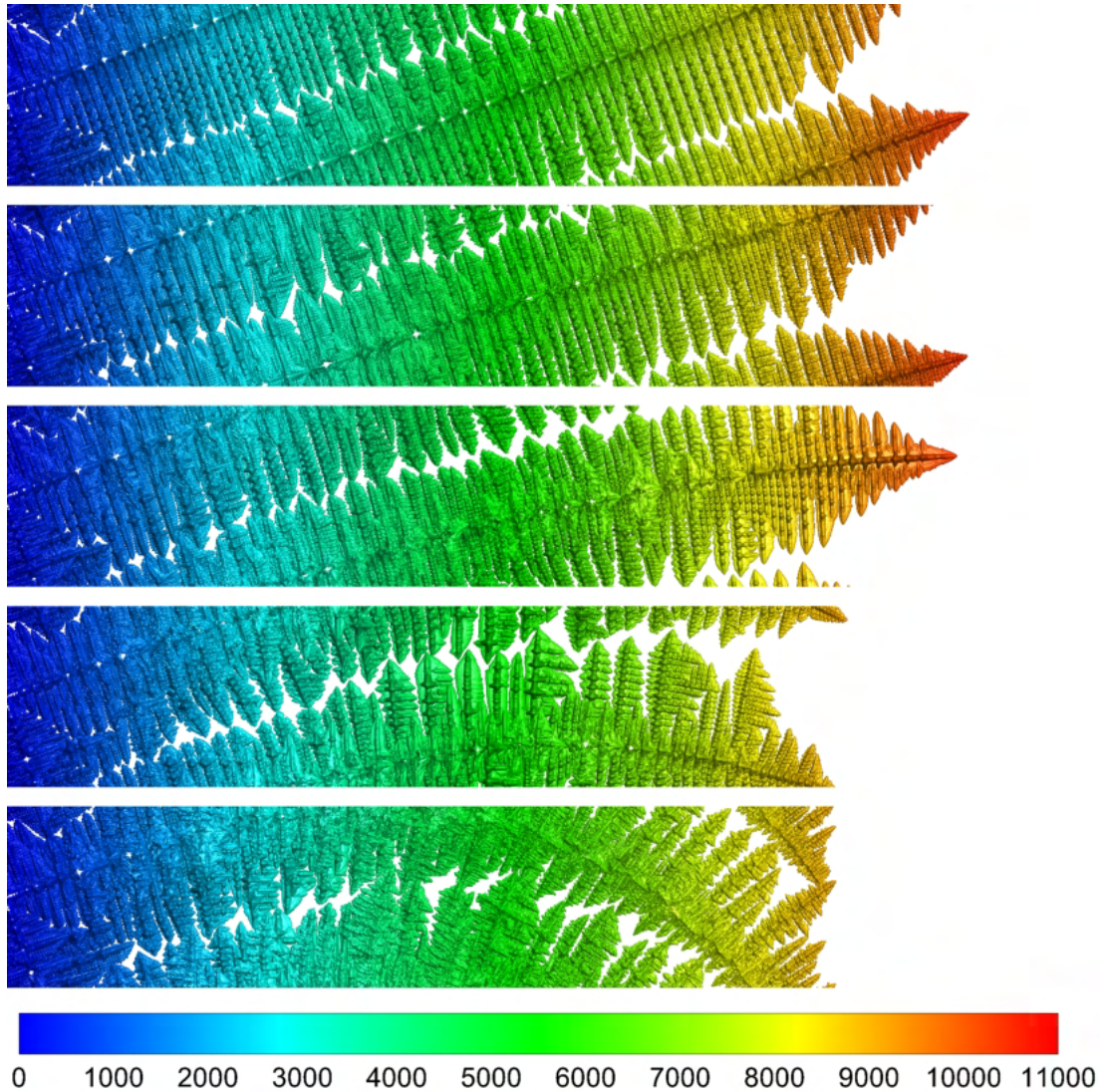


Figure 7.12: Dendrite structures for cases 1, 10, 25, 50 and 100 in descending order at final time step $t = 250000$, colour indicating length of microstructure in μm .

However, it is not just the final state of the microstructure that is of interest, but rather how the microstructure, orientation change and deformation develops over time to reach this final state and if there are any patterns to be observed. To this end, the microstructure and orientation change over time can be observed in figures 7.13 - 7.17, which will be referenced later to provide possible context

and explanations for observed behaviour differences between the cases.

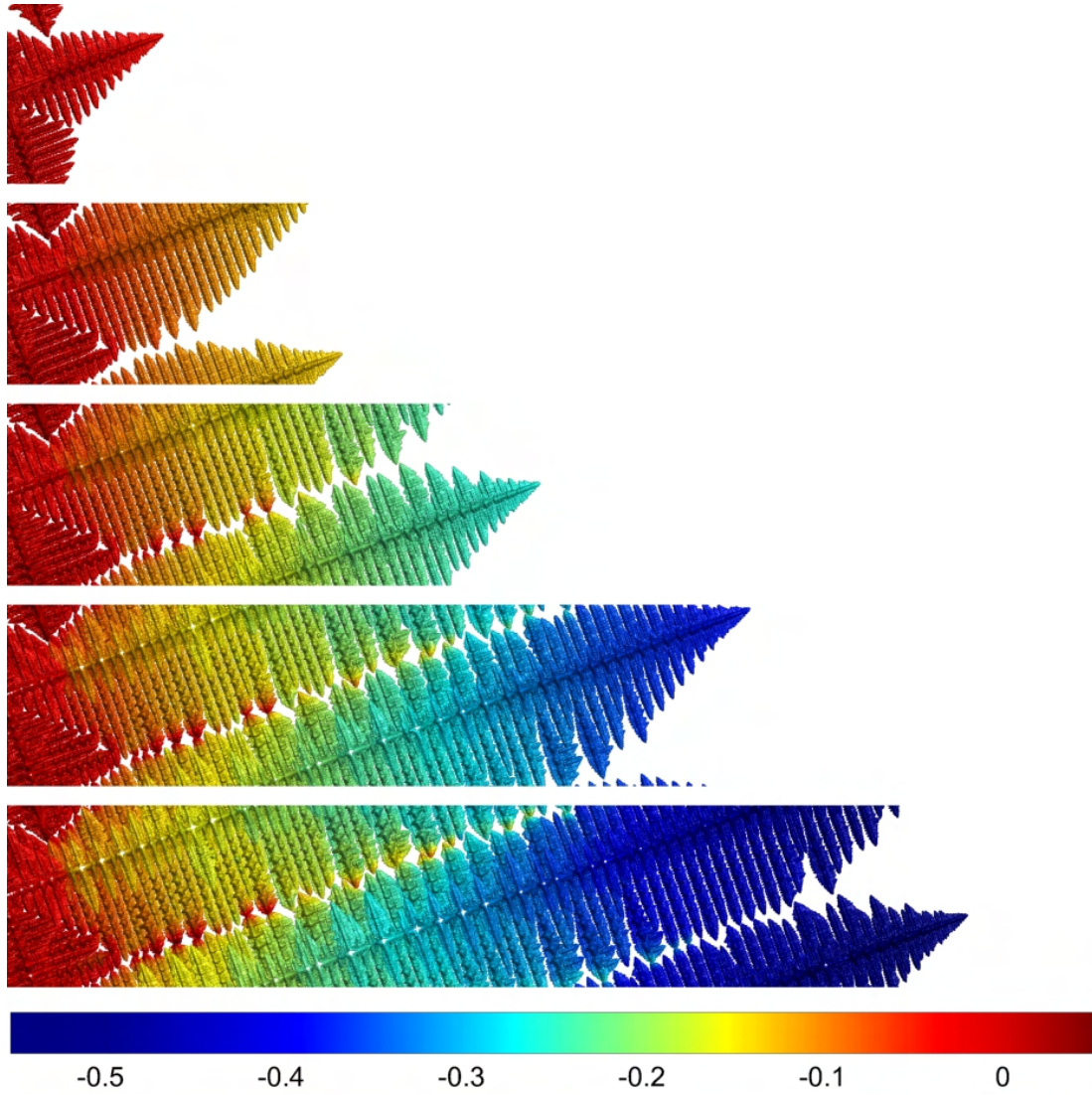


Figure 7.13: Case 1 microstructure and orientation change (θ°) development at $t = 50000, 100000, 150000, 200000, 250000$.

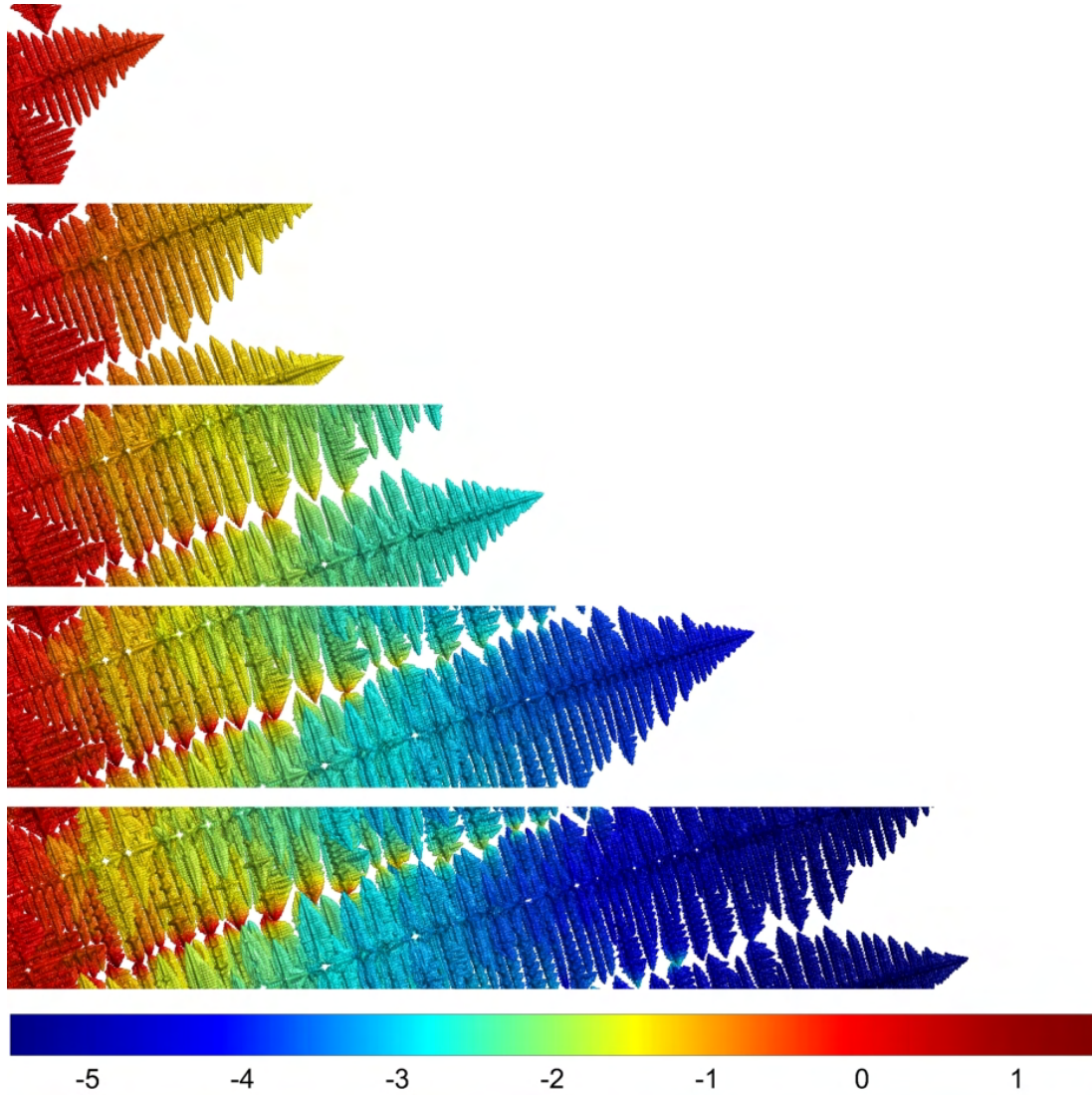


Figure 7.14: Case 10 microstructure and orientation change (θ°) development at $t = 50000, 100000, 150000, 200000, 250000$.

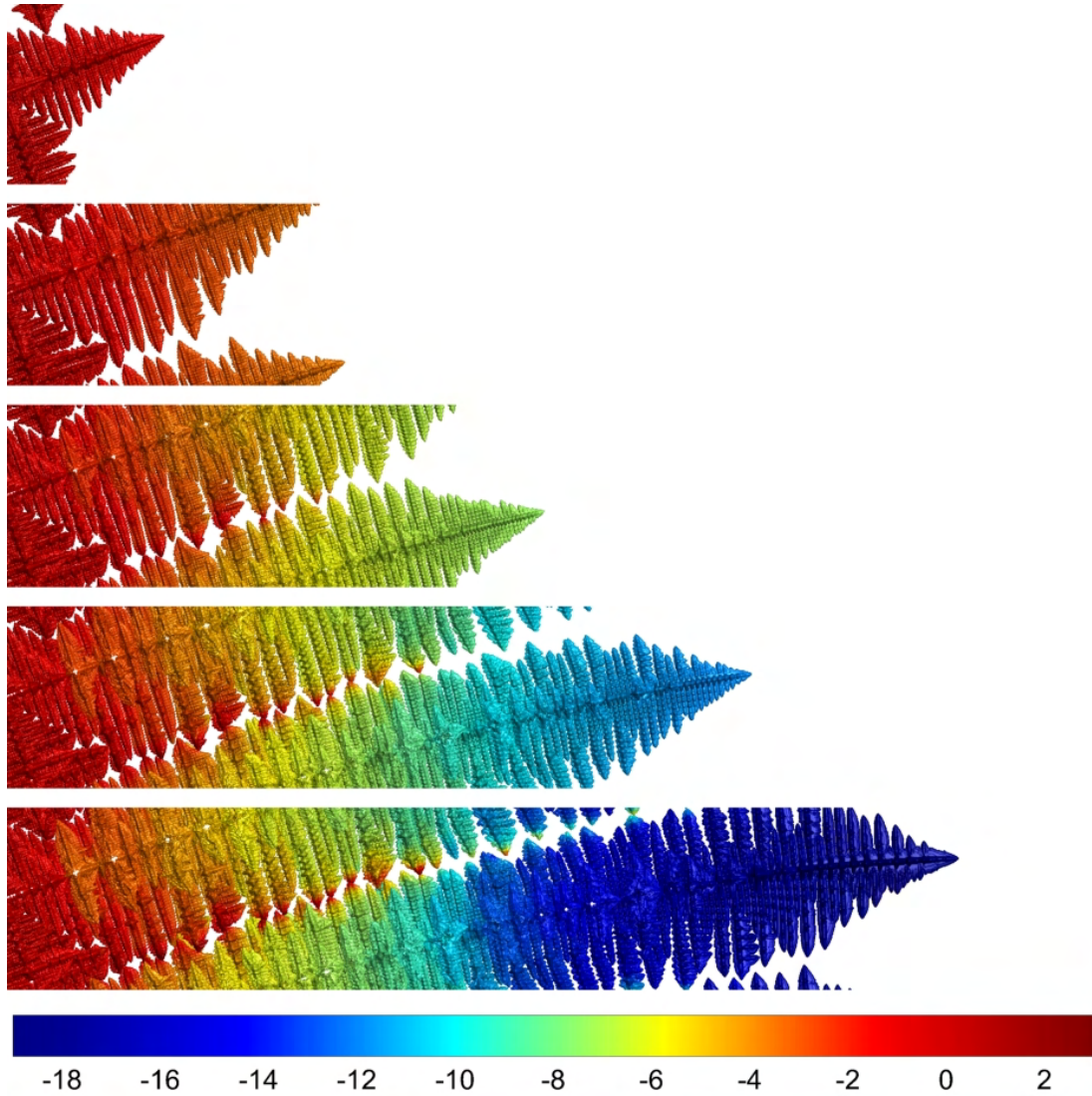


Figure 7.15: Case 25 microstructure and orientation change (θ°) development at $t = 50000, 100000, 150000, 200000, 250000$.

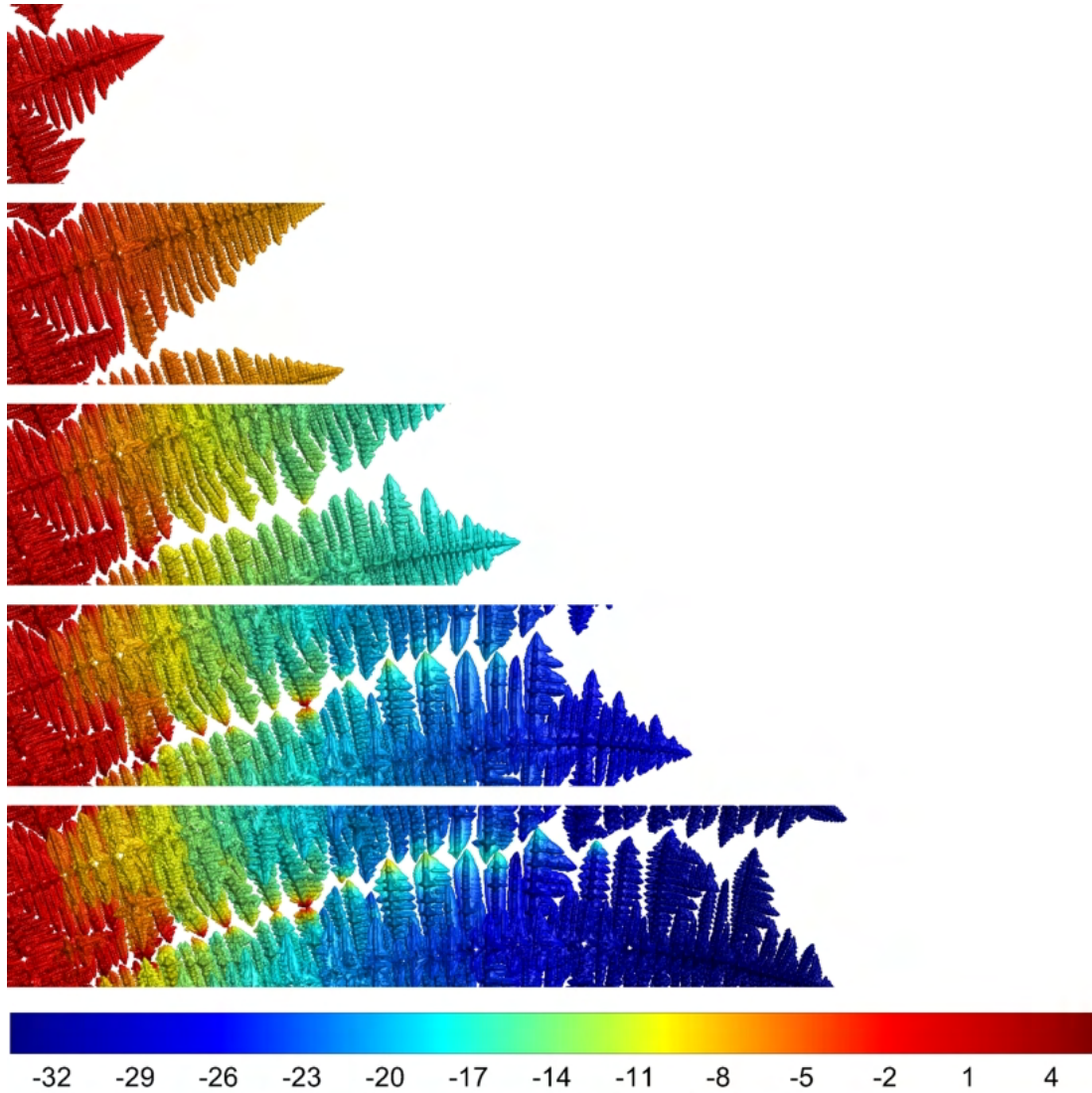


Figure 7.16: Case 50 microstructure and orientation change (θ°) development at $t = 50000, 100000, 150000, 200000, 250000$.

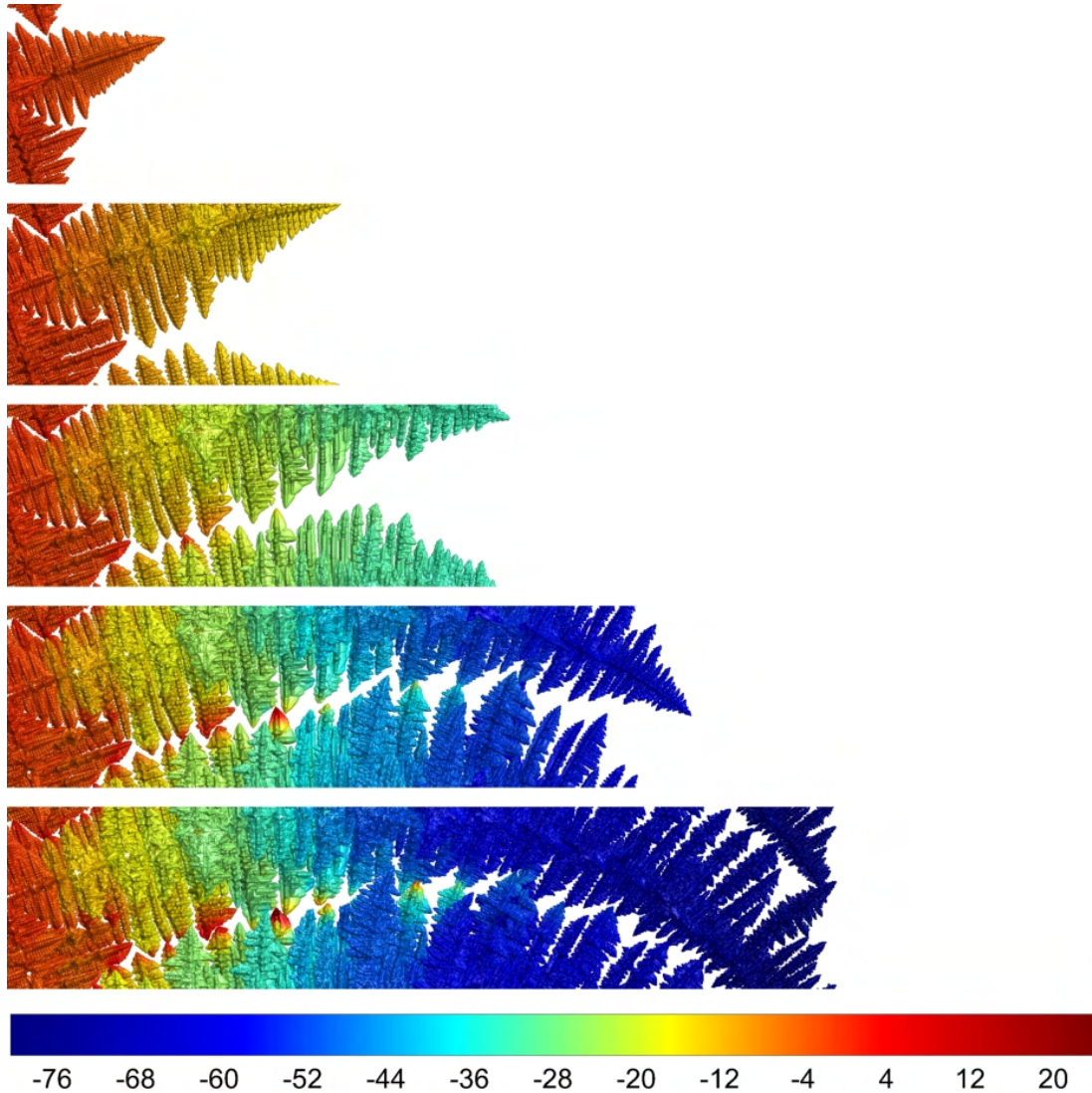


Figure 7.17: Case 100 microstructure and orientation change (θ°) development at $t = 50000, 100000, 150000, 200000, 250000$.

The first structural behaviour to assess is the change in orientation (all of the values specify how much the dendrites' orientation has been altered from the initial orientation it was seeded with, rather than the overall orientation of the dendrite). Looking at these figures, it can be seen that at the most basic level, for all cases the orientation profiles develop in a similar manner to earlier cases presented in this chapter, with the tip being the point of highest

orientation change, which increases in magnitude as the dendrite grows longer. Furthermore, the secondary arms show some relatively large local misorientation due to interaction with other secondary arms, though as by the point of contact the arms are generally constrained and unable to grow further this rarely has a meaningful effect on further microstructural development.

To aid in the interpretation of the orientation behaviour, a table of the maximum orientation change values found in figures 7.13 - 7.17 can be found in table 7.2. For easier visual interpretation of the orientation change behaviour, graphs showing more granular maximum orientation change values throughout the simulation have been plotted in figure 7.18. This includes the raw values to show the absolute difference in values in 7.18a; these values have been normalised to all run from 0 to -1 in 7.18b to allow the relative rates of change to be compared; finally in 7.18c the ‘scaled’ orientation change values have been presented as an alternative method of comparing the relative rates of orientation change. ‘Scaled’ in this context means that the final orientation value has been divided by the force multiplier being used for that case, which will bring the values to the same order as in case 1 and if the relationship between body force increase and orientation change was linear should lead to all of the lines behaving identically.

7. MODELLING CASES

t	Case				
	1	10	25	50	100
50000	-0.0364	-0.367	-0.905	-1.85	-3.64
100000	-0.132	-1.39	-3.54	-7.38	-14.4
150000	-0.256	-2.79	-7.33	-17.6	-32.3
200000	-0.383	-4.14	-12.0	-26.9	-60.1
250000	-0.507	-5.49	-18.5	-34.0	-78.1

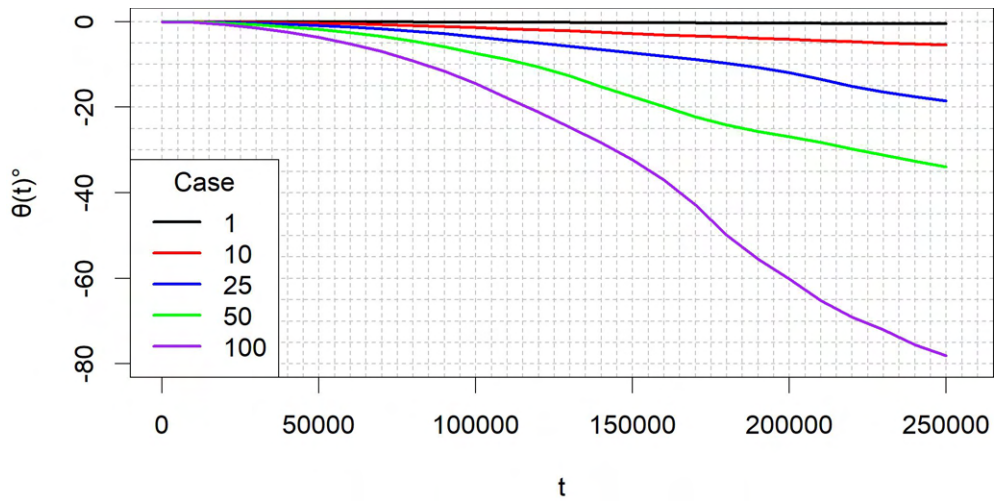
Table 7.2: Comparison of orientation change (θ°) values.

Using a combination of these outputs some patterns in the development of the orientation change become clear. Up until step $t = 100000$ the relationship between force and orientation change appears to be essentially linear, with the observed orientation change for case 100 being approximately 100 times larger than the orientation observed for case 1, likewise with the intermediate cases. This almost linear relationship remains until the final step for cases 1 and 10, with almost identical behaviour and values (when adjusted for the force multiplier), however for the other three cases both the behaviour and values begin diverging quite significantly from what would be expected if there was a linear relationship between the force and orientation change. The likely cause for this disparity is the impact of the orientation on the growth behaviour of the microstructures, where the dendrites up to step 100000 are all relatively similar across the five cases due to the relatively small orientation changes (likewise this is why cases 1 and 10 are similar throughout the simulation), but after this point the cases experiencing large forces begin to have radically different microstructural development and hence structural behaviour.

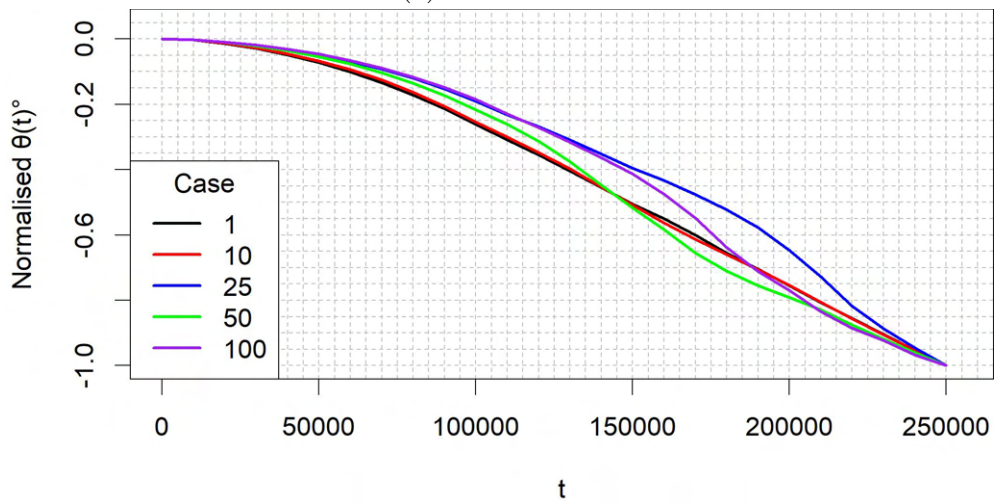
Looking at the plots in figure 7.18 in more detail also serves to highlight interesting relationships between the force and orientation change over time. The

change in orientation for all five cases seem to approximately follow a power law of $\theta(t) = -4 \times 10^{-11}t^{1.91}$ for the first 100000 steps (see figure 7.19a), but after this point the behaviour stops following this power law distribution and begin to vary drastically between cases. For cases 1 and 10 after this point orientation change becomes essentially linear, the likely cause of this change being the transition from a largely freely deforming dendrite (loosely analogous to a freely deforming cantilever beam) to having any movement limited by interaction with surrounding dendrites. This means that a relatively consistent section near the tip of the dendrite before the secondary arms are able to interact remains free to deform throughout the rest of the simulation. The behaviour observed in cases 25, 50 and 100 after step 100000 is more complicated, with significant behavioural differences between the cases. There is no fixed pattern shown in the behaviour of the cases from this point onwards, with the rate of orientation change both increasing and decreasing at seemingly unrelated time steps. While in absolute terms the orientation change is always larger for cases with larger forces being applied, by considering the normalised and scaled solutions it can be observed that in relative terms the largest force does not always have the largest (scaled) orientation change. In particular, when considering the scaled solutions case 50 has the largest relative orientation change between $t = 125000$ to 175000 , yet by the end of the solution it has a relative orientation change lower than case 25. This all seems to further highlight the fact that predicting orientation change for a structure becomes increasingly difficult once structural mechanics starts to influence the growth behaviour and interaction with other dendrites begins.

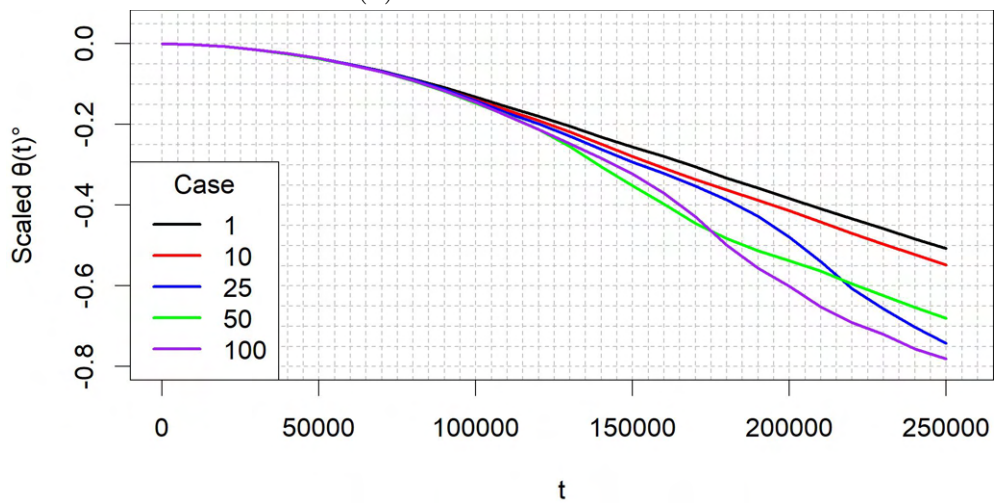
7. MODELLING CASES



(a) Real values.

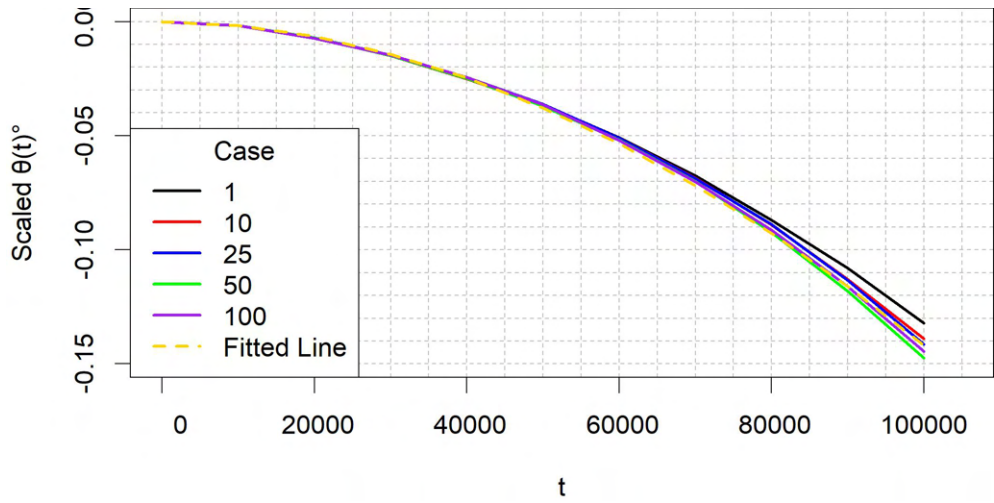


(b) Normalised values.

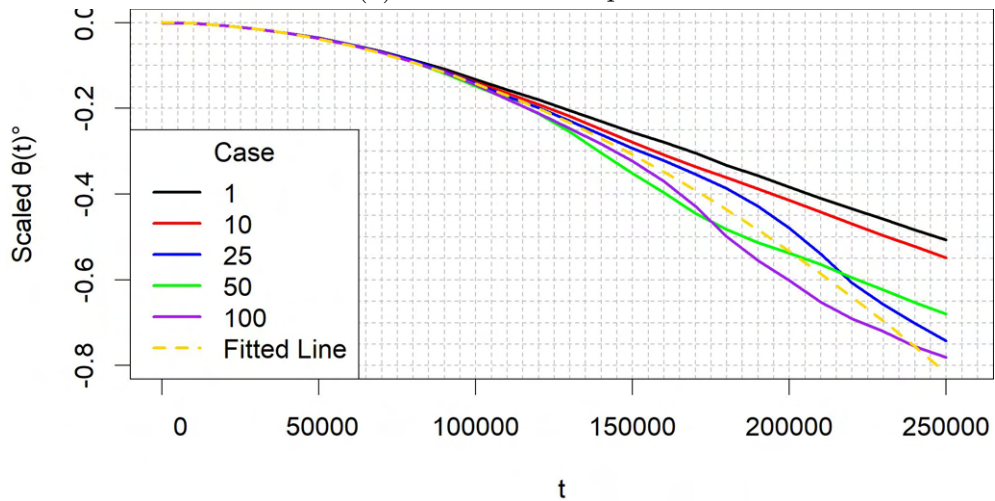


(c) Scaled values.

Figure 7.18: Case comparison plots for largest observed orientation change θ at time step.



(a) First 100000 steps.



(b) Full simulation.

Figure 7.19: Scaled orientation change θ comparing all cases and showing fitted power law of $\theta(t) = -4 \times 10^{-11}t^{1.91}$.

Similar conclusions can be drawn when examining the accumulated displacements w being observed between the different cases (the u and v displacements have been neglected due to being significantly smaller in magnitude and hence far less impactful on the microstructural development). The profile of these displacements at the final time step can be observed in figure 7.20, where the phenomenon of the largest deformation region occurring

7. MODELLING CASES

in the centre of the dendrite as was described in section 7.6 can again be observed. As with the orientation, table 7.3 contains the largest accumulated orientation value for every case at 50000 time step intervals and plots of more frequent data observations giving the raw, normalised and scaled relationships can be found in figure 7.21.

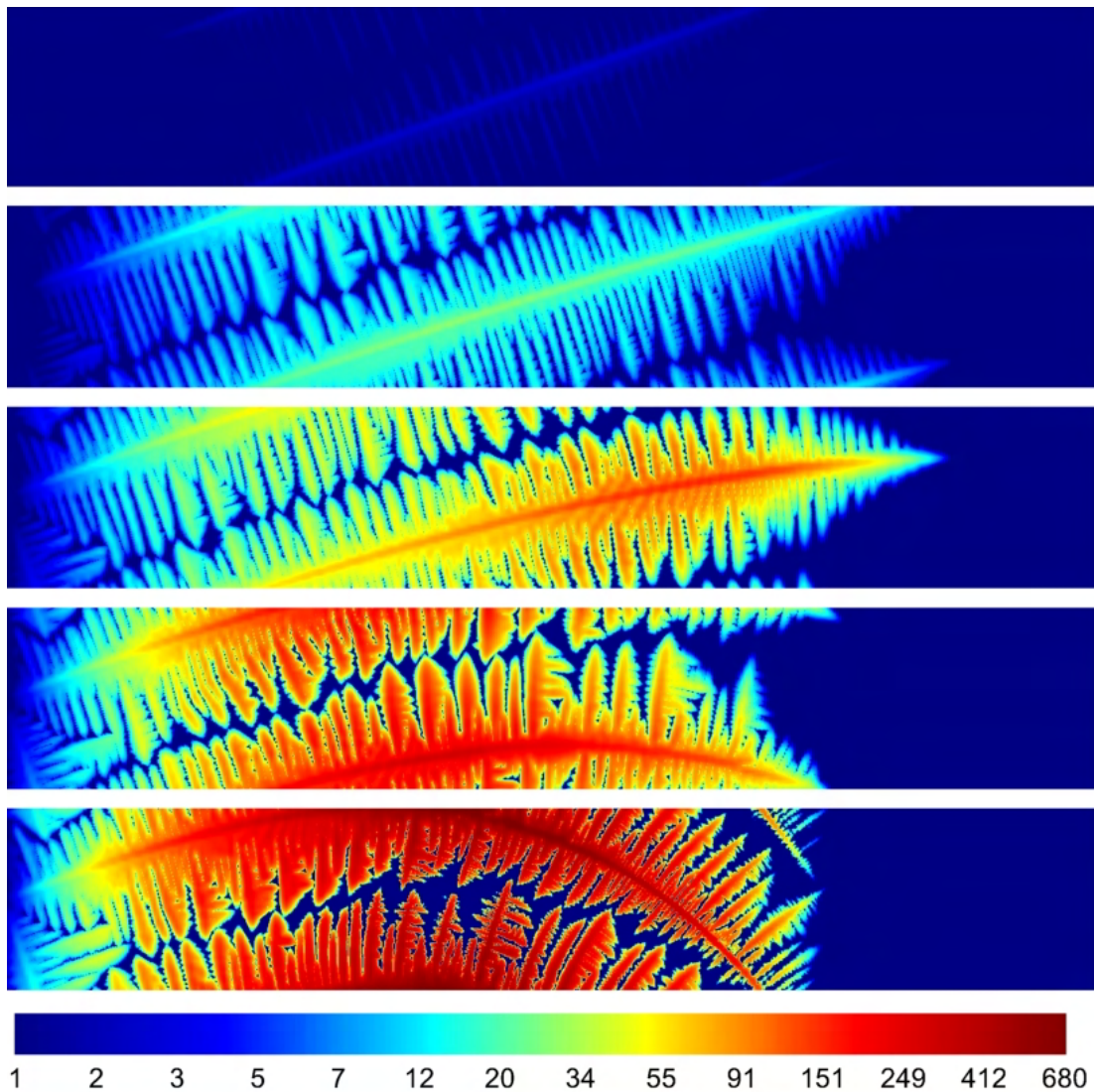


Figure 7.20: Accumulated w displacements (μm) for all cases at final time step $t = 250000$.

7. MODELLING CASES

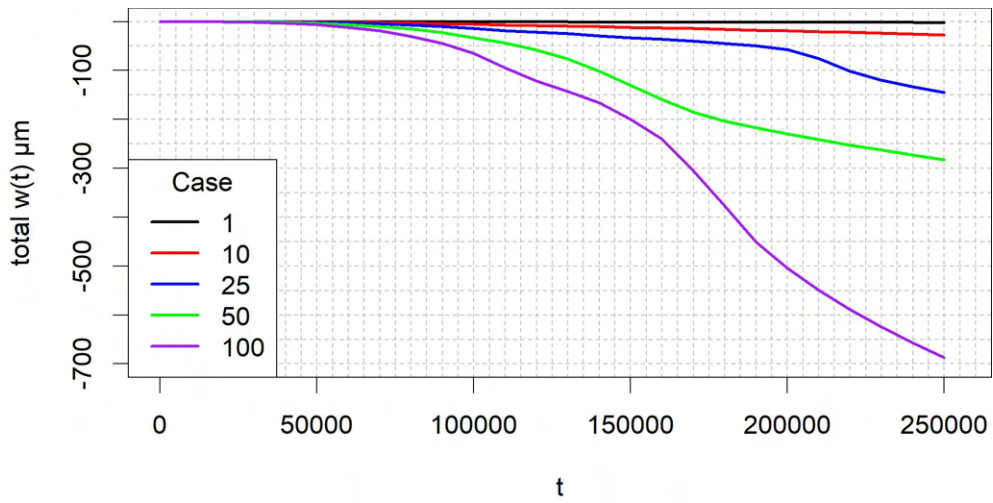
For these displacements it can be observed that, much like with the orientations, the relative values for all cases up to 100000 are similar, and cases 1 and 10 are quite similar throughout. However, there is an unmistakable divergence in the values as the forces and time steps increase that was far less apparent in the orientation data. This divergence in the relative displacements can be highlighted by considering the final time step for case 1 and 100, where the accumulated displacements for case 100 are in fact nearly 350 times larger than the displacements observed for case 1, where a linear relationship would anticipate them to be only 100 times larger.

t	Case				
	1	10	25	50	100
50000	-0.0612	-0.604	-1.50	-3.17	-6.66
100000	-0.503	-5.49	-13.8	-32.7	-65.1
150000	-0.998	-11.6	-32.9	-130	-200
200000	-1.39	-18.9	-57.6	-230	-504
250000	-2.00	-27.0	-144.467	-282	-687

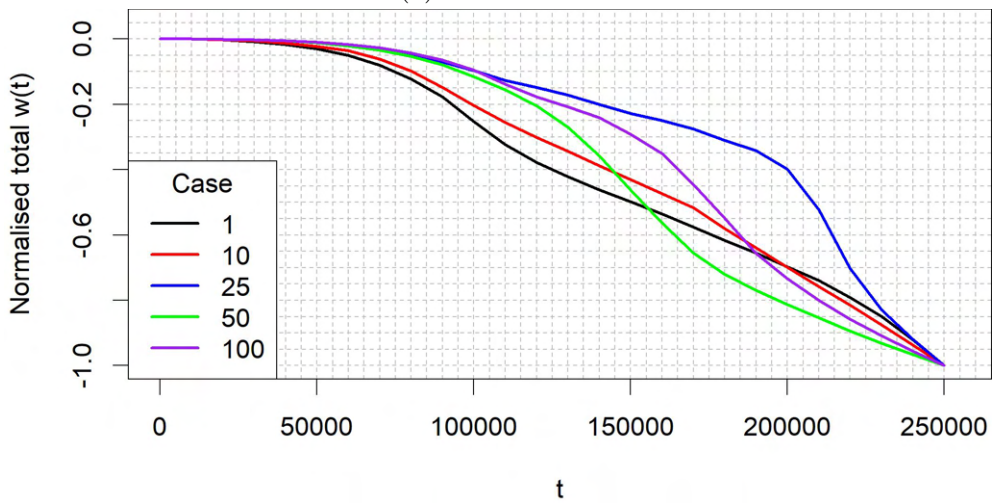
Table 7.3: Comparison of maximum accumulated deformation (μm) values.

Despite these changes in magnitude, when considering the normalised and scaled values in figure 7.21, the behaviour of the deformations over time does match that of those previously described for the orientations for each case, with the behaviour simply being exaggerated due to the larger relative values. This serves to highlight that the displacements are also affected by the changes in growth behaviour and structure interaction, with a clear relationship between the displacements and orientations in behaviour.

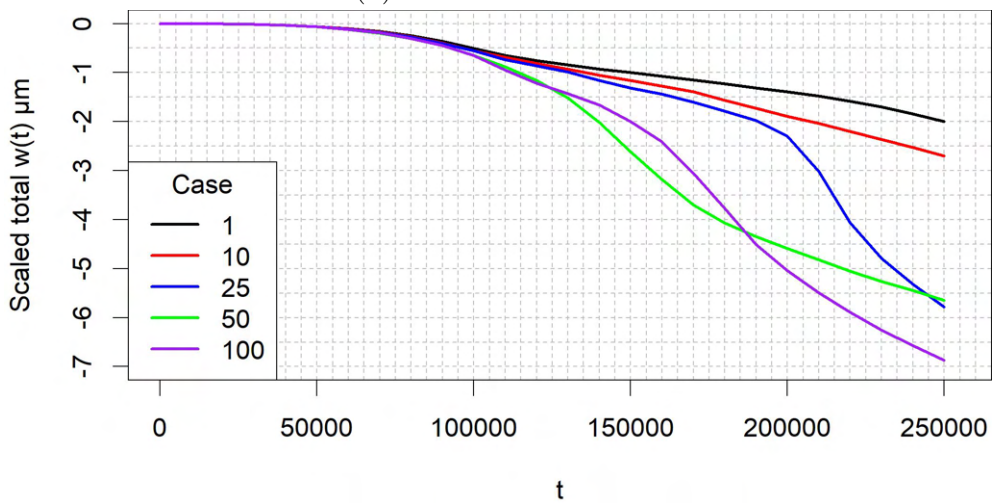
7. MODELLING CASES



(a) Real values.



(b) Normalised values.



(c) Scaled values.

Figure 7.21: Case comparison plots for largest observed cumulative w displacement at time step.

The time step displacements are the displacements calculated by the SMS for a single time step (to be contrasted with the cumulative displacements previously examined, which combine all extant time step displacements) have been plotted in figure 7.22. The time step displacement profiles and a table of values has not been provided for the parameter due to it having high variability depending on the state of the system at a given time step, so only by considering the overall evolution of a large number of time step displacements occurring throughout the simulation can anything useful be inferred. Considering cases 1 and 10, these time step displacements appear to support the earlier observations by demonstrating some similar behaviours to the other parameters throughout the simulation, starting with the displacements increasing geometrically until around step $t = 100000$ to correspond with the power law behaviour observed in the orientation changes in figure 7.19, after which both level off to a very gradual, approximately linear increase. For case 25, after a steady increase broadly corresponding to that observed in cases 1 and 10, there is then a very sharp increase in time step displacements between approximately $t = 175000$ and 210000 (attaining the highest observed scaled displacement), at which point it then begins sharply decreasing again until the end of the simulation. It seems probable that this was caused by a period of growth where the tip was able to attain a relatively long length and weight without being constrained by the interaction of secondary arms, however this clearly became constrained again around step 210000, causing the large curtailment in the magnitude of the observed displacements. For case 50, this further highlights that there was a sharp increase in displacements between $t = 100000$ and 140000 , at which point it sharply fell again until 190000 , where the displacements then levelled off. This would seem to be a similar case of the altered growth behaviour allowing a relatively large length near the tip to

remain free for a short period, before the secondary arm interaction begins curtailing this effect to reach a relative equilibrium where even as the microstructure keeps growing, the displacements remain relatively constant due to the ‘free’ length of dendrite near the tip remaining broadly the same. For case 100 the time step displacements seem to increase until step $t = 180000$, at which point they decrease by a comparable rate until the simulation ends. This decrease in displacements is so precipitous that even in absolute values it is approaching the values observed in cases 25 and 50. The reason for this notable decline in displacements becomes clear when considering the final two time steps presented in figure 7.17, where the tip goes from having relative freedom to deform to experiencing secondary arm interaction along the dendrite’s entire length, eventually becoming trapped by the end of the simulation. At this stage, rather than being a dendrite with a free tip which can deform, the microstructure has instead become essentially a continuous block, with a consequently significantly smaller capability for deformation. This would again seem to highlight the complex nature of microstructural development where structural mechanics is being considered.

7. MODELLING CASES

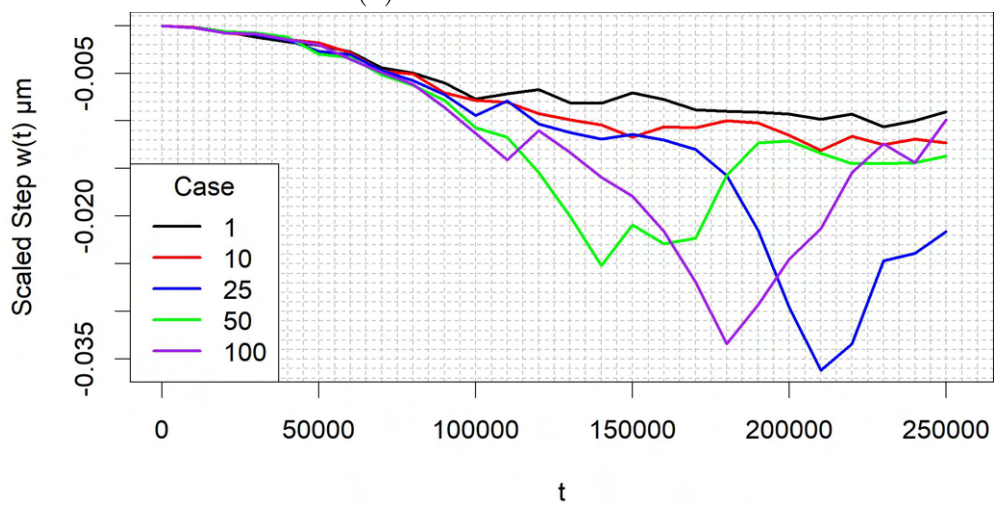
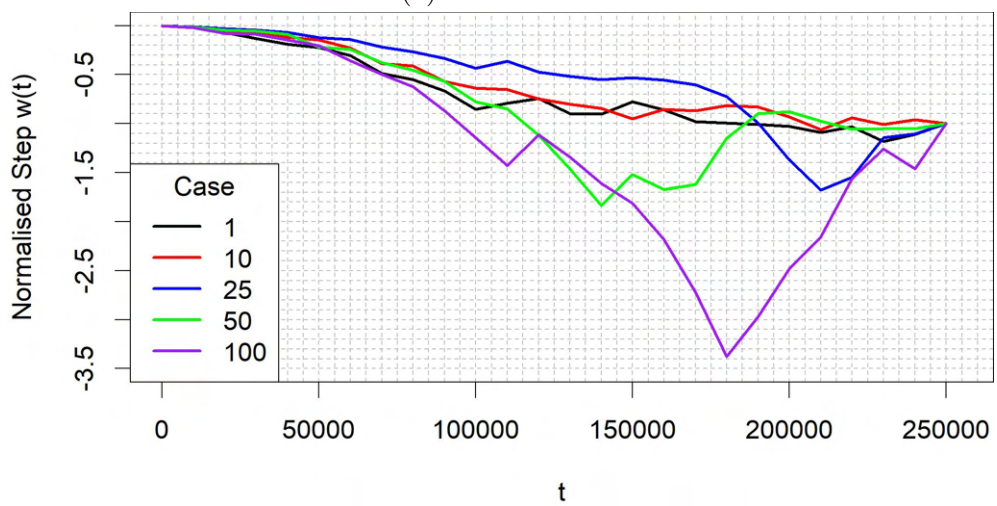
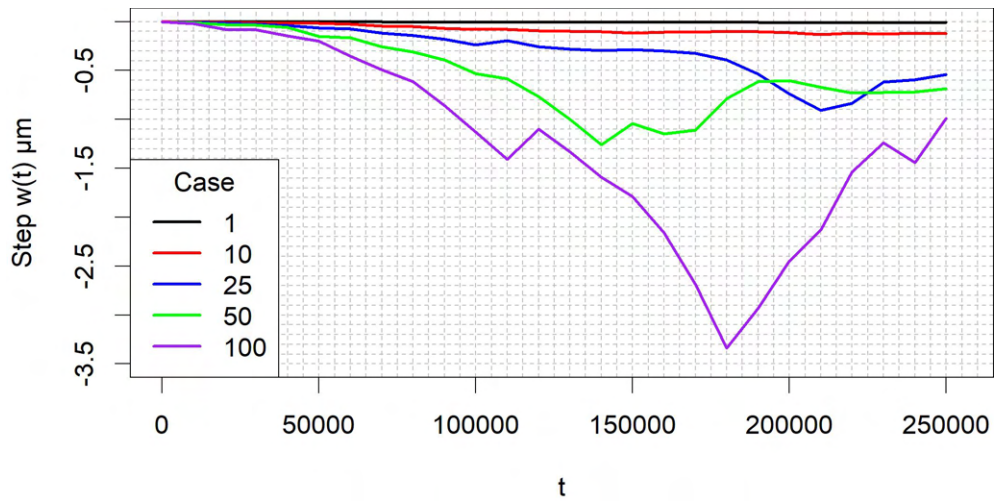


Figure 7.22: Case comparison plots for largest observed single time step w displacement.

Finally, the Von Mises stress for the final time step can be viewed in figure 7.23 where the exponentially distributed key values indicate the relationship between force and stress is not linear, however the general stress accumulation behaviour appears to be consistent throughout the cases. For all cases, the centre of the main trunk of the dendrite is largely a low stress region, with the regions of highest stress always being observed in interacting arms, in particular where the tips come into contact. Overall, this shows that while the internal stress of a dendrite will increase as it experiences larger forces, the precise regions of the relative high and low stresses are largely dependent on precise mechanical interactions.

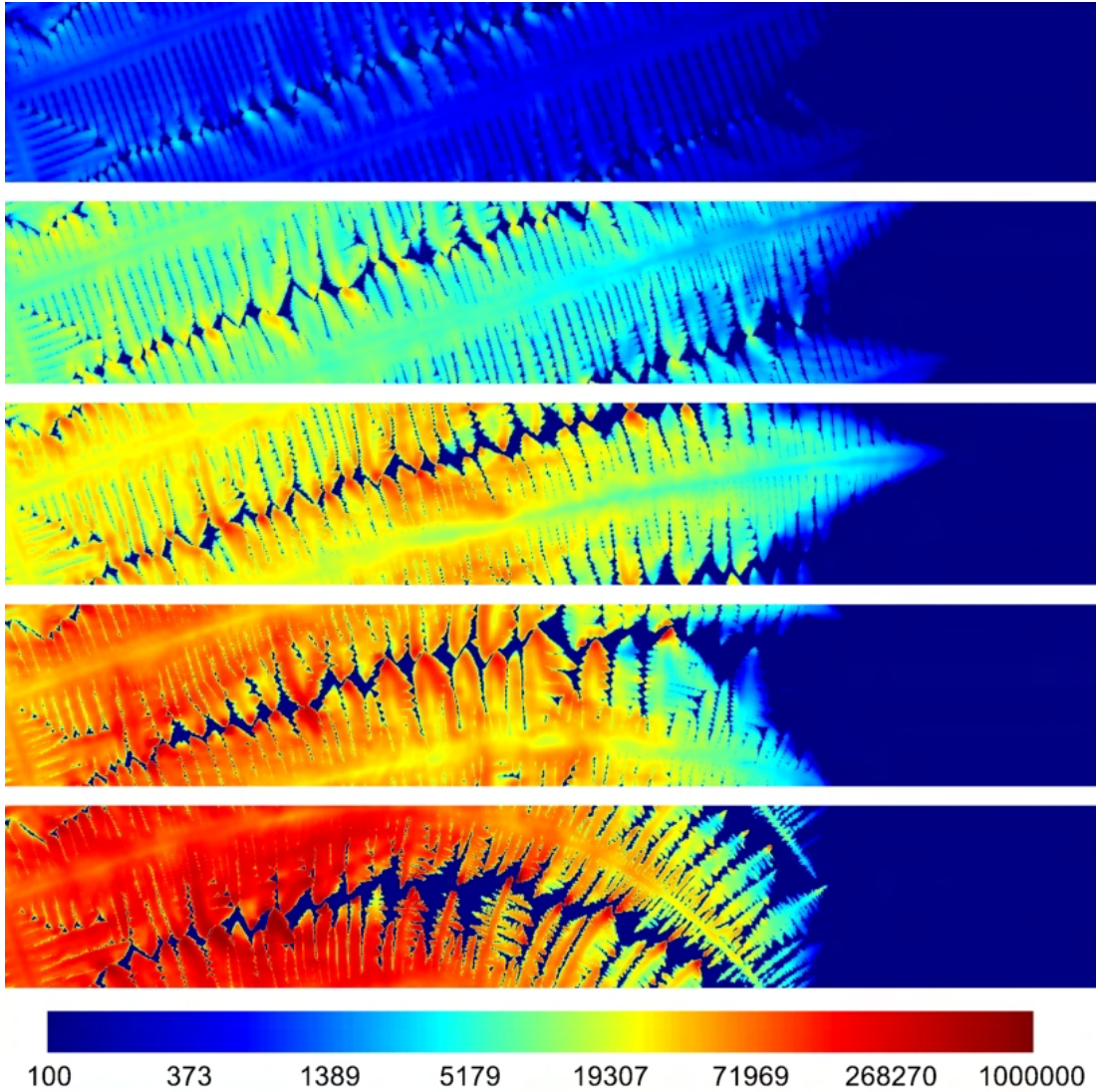


Figure 7.23: Von Mises stress σ_{vm} (Pa) for all cases at final time step $t = 250000$.

Many papers in the literature treat a columnar dendrite as a structure analogous to a cantilever beam when trying to estimate the deformation or stress accumulation within the dendrite, which is often a reasonable assumption for post processing a single dendrite. However, this study highlights that this assumption quickly falls down in more realistic scenarios where structural mechanics is being concurrently solved such that it influences the growth

behaviour of the microstructure. Even in cases where any changes in orientation are fairly small (as in cases 1 and 10), the approximate behaviour of a deforming cantilever beam will not hold true if there is interaction with the secondary arms limiting the freedom of the dendrite to deform like a beam. For the cases experiencing larger forces (cases 25, 50 and 100), aside from sharing this issue with secondary dendrite interaction, it will ultimately grow into a structure with a curved morphology so distinct from a beam that any attempt to compare it with a cantilever beam becomes increasingly dubious.

For the initial stages of the simulation there seems to be an approximately linear relationship between the increase in force and the increase in observed displacement and orientation changes, which would be the expected behaviour for identical beams of any length experiencing increasing forces. While this seems to hold mostly true for the entirety of cases 1 and 10, for the other cases this relationship fails at some point during the simulation, again due to the morphology becoming increasingly less beam like and due to the secondary arm interaction.

Overall, this parametric study highlights the importance of this research, as simply by increasing the force on otherwise identical modelling cases, significantly different microstructural development can be observed which could not be predicted using previously existing methods.

7.10 Summary

This chapter began by providing the modelling context and basic setup of the cases being presented. Thin sample cases were presented to demonstrate that the coupled SMS with microstructure solidification can model a single dendrite changing orientation over time. This further explored thin sample cases where

7. MODELLING CASES

thermal strains change the growth orientation, transient forces were applied which counteracts itself over time and large scale cases were run using parallel computing which are representative of realistic cases. Fully three-dimensional cases were then presented, showing how multiple orientations can be changed to cause the dendrite to bend out of plane, how a forest of dendrites can be modelled using the SMS and how the application of a constant rotational force can generate a dendrite which grows in a spiral. Finally, a parametric study was undertaken which highlights how significantly different microstructures can be attained simply by increasing the body force the system is grown under. This has overall demonstrated a wide variety of modelling cases, mechanisms and behaviours which can only be modelled using the current coupled modelling setup developed by this research.

Chapter 8

CONCLUSION & FUTURE WORK

8.1 Conclusions

The aim of this research was to develop a structural mechanics model which could be coupled to an existing microstructure solidification code, allowing mechanisms caused by these concurrent physical processes to be captured by numerical modelling for the first time. Two key research questions were defined at the start of this thesis, the first being:

What is the most effective way to couple the separate structural mechanics and microstructure solidification models within a single interdependent process?

In order to answer this, the solidification and structural mechanics models to be used had to be defined. For solidification modelling, the existing CA method solidification code in use by TESA was chosen, being a proven framework for

8. CONCLUSION & FUTURE WORK

generating accurate solutions for large problems thanks to the parallel computing framework it utilises. For the structural mechanical behaviour, a linear elastic material model was chosen as a fundamental model which would be relatively straightforward implement. While the material model comes with assumptions limiting the mechanical behaviour it can represent, it nevertheless allows for the exploration of a wide variety of new modelling scenarios considering the nascent stage of any current research to examine the influence of structural mechanics on solidifying dendritic microstructures. The numerical method chosen to solve the linear elasticity equations was a staggered grid Finite Volume method, which was chosen over the more commonly applied Finite Element methods due to the greater suitability of Finite Volume approaches for coupling to an evolving microstructure.

With the SMS developed and verified for accuracy for purely structural mechanics problems as shown in Chapter 3, the main topic of coupling with a solidification process could finally be approached. Given the quasi-stationary nature of the SMS, an approach had to be developed which would account for any existing deformation when solving structural mechanics at a new time step. This was done by keeping track of how the forces acting on the structure change over time as it solidifies, so that only ‘new’ forces acting upon the structure were accounted for at any given time step. With this complication resolved, the main thrust of this research question could finally be addressed in the examination of the most effective approach for allowing structural mechanics to influence the behaviour of the microstructure solidification. The key influences identified in the literature where structural mechanics alters the solidification process was crystallographic orientation change, changes in the structures position caused by deformation and the accumulation of stress causing parts of the structure to fragment. Fragmentation, or any other mechanism causing parts of the dendrite

8. CONCLUSION & FUTURE WORK

to become unattached were deemed outside of the scope of the research at this point, requiring significant additional work to model the movement of any unattached parts of the structure as well as being unlikely to occur within modelling scenarios which satisfy the linear elasticity assumptions. Nevertheless, this model is capable of predicting the regions of the microstructure where the maximum stress arises, which could be used to identify the locations and mechanisms which could cause such fragmentation events.

Using the deformations obtained from structural mechanics to change the position of structures is undoubtedly an important interaction between structural mechanics and solidification, being examined in depth during Chapter 6 of this thesis by using the obtained deformations to drive an advection process which moves the solidifying structure through the fixed grid. While the work done in this area shows great promise, incorporating it within a solidification process proved more complicated than expected, with the CA method being very sensitive to the internal structures or edges of the dendrite being blurred to any degree, which could make the resumption of solidification after the solid advection behave in an undesirable manner. Furthermore, it became apparent that due to the linear elastic material model, expanding these modelling assumptions to the rest of the system means that the small deformations being modelled could be justifiably overlooked with regards to physically changing the location of the structure. Even if solid advection was implemented for these small deformations, only small amounts of material should pass between the volumes each time structural mechanics is resolved.

For these reasons, while the work undertaken on representing the movement and deformation of solid structures as an advection process is fundamental for many of the proposed expansions of this research, given the assumptions underpinning the current modelling the impact of structural mechanics could be

8. CONCLUSION & FUTURE WORK

entirely represented by changes to the crystallographic orientation as demonstrated in Chapter 5. To do this, the local orientation of each volume comprising the structure was altered by allowing the deformations at each face to compete and ultimately calculate how much each volume will ‘rotate’ around the x , y and z axis, in an approach justified both theoretically and verified against analytic solutions. As the CA method being used to describe the solidification already describes the growth orientation of the dendrites as three Euler angle rotations, it was relatively straightforward to update these Euler angles locally with the rotations caused by structural mechanics. With the growth orientation changed the dendrite will grow at an altered angle, changing the distribution of new growth across the structure and thereby where new force will be applied the next time structural mechanics is solved. In this manner the structural mechanics and solidification are interdependent, with structural mechanics changing the growth behaviour of the solidification process and the solidification process dictating where new force is applied in structural mechanics.

Can numerical modelling of concurrent microstructure solidification and structural mechanics predict the fundamental behaviours observed in practical experiments?

To highlight the novel functionality of coupling structural mechanics with microstructure solidification, a selection of cases were presented in Chapter 7 to explore distinct modelling scenarios. It was demonstrated that a single dendrite arm growing under a constant body force analogous to gravity would slowly accumulate orientation changes, a situation observed numerous times in literature where a long dendrite arms slowly becomes misoriented across the

8. CONCLUSION & FUTURE WORK

domain but has no visually identifiable point where a large deformation has occurred [29–31]. It was also demonstrated that the solver could account for deformation caused by thermal expansion, as this was widely identified as a potential cause for dendrite deformation and misorientation within the literature [18, 26–31]. A case was presented where the force changes in both magnitude and sign over time, demonstrating the solver could account for situations with a non constant force which could allow for the modelling of more complex cases where an observed change in orientation shrinks or even reverses along the length of a dendrite at least once [26, 29].

Large scale cases using a HPC were shown, demonstrating that system of dendrites can demonstrate these misorientation behaviours under realistic conditions and at sizes comparable to real life experiments. The large and complex dendritic systems on display in these HPC cases also demonstrate the ability of the SMS to identify and resolve the displacements for complex collections of structures. However, these cases described so far all were set up as thin sample cases such that one of the dimensions could almost be ignored, so a fully 3D case where all dimensions are significantly thick was shown, where a large number of randomly placed and oriented dendrites could still be identified and have their displacements calculated by the SMS. Subsequently, the capability for modelling cases where significant forces act in multiple directions was shown, where more complex bending leads to growth at an orientation which does not line up directly with any of the axis. In particular a single columnar dendrite bending out of plane was shown along with a further case where a rotational force leads to a dendrite growing in a spiral. Finally, a small parametric study was performed which highlighted the significant morphological change a dendritic system could undergo simply by increasing the force it grows under.

8. CONCLUSION & FUTURE WORK

While exaggerated to allow for easy visual examination, these cases demonstrate the ability to account for complex three-dimensional orientation changes which is crucial for capturing the mechanisms which lead to defects such as stray grains and slivers. Considering these cases presented, the fully coupled model demonstrates the ability to simulate a wide variety of behaviours observed in existing practical experiments which could not be captured using any currently existing microstructure solidification modelling.

8.2 Future Work

This work has demonstrated the fundamental mechanism that small deformations can change the orientation of growing dendrites in such a manner that the microstructural development changes significantly, this has been demonstrated in a manner consistent with experimental observations. However, many of the experimental results where structural mechanical effects have been observed are either post processed examples of fully solidified structures or otherwise lack many details which would be required for accurate recreation using the coupled code. For this reason, it would be desirable to arrange practical experiments specifically designed to examine the mechanically driven misorientation of dendrites, this would allow modelling to be performed where the setup can fully match that of the experiment, allowing the accuracy of the modelled behaviour to be truly validated against experimental results.

However, before this would likely be possible there are desirable expansions to the model which would ideally be implemented. Fully coupling the SMS with the fluid flow and/or TEMHD modules would likely be necessary to accurately match the experimental results as both processes have been observed to have a significant impact on microstructure development. The inclusion of fluid flow

8. CONCLUSION & FUTURE WORK

can greatly alter the distribution of solute within an experiments, changing the solidification behaviour, possibly causing remelting as well as potentially imparting significant force from the flow velocities. TEMHD is less ubiquitous as a factor in solidification experiments, but including magnetic forces in the experiment can induce changes to the fluid flow, with the changes that entails to the development, as well as potentially directly applying a Lorentz force which may contribute to the deformation of the solidifying structure. A related, but as yet unexplored aspect of coupled structural mechanics with microstructure solidification would be the field of contact problems where dendrites grow into one another in a manner which will directly exert force between the interacting dendrite. Due to the manner in which the SMS has been created, special considerations would have to be made in how best to prevent dendrites from fusing together when interpreting the structure solved by the SMS, and instead allow dendrites which are brought into contact to impart appropriate forces upon one another.

The inclusion of fluid flow behaviour would lead to systems where significant remelting of dendrites becomes possible, which leaves a potential for dendrite arms to become detached from the rest of the structure. In this scenario, it would be imperative that the SMS is able to identify any unattached structure and ignore this for the purpose of solving structural mechanics. How the detached solid material behaves may change depending on the problem, in some cases it may be sufficient to leave it in the detached location and allow growth to continue and possibly reattach the structure. But in order to model more complex phenomena such as detached structures floating away to trigger the columnar to equiaxed transition or falling and interacting with other parts of the microstructure, a solid body mechanics solver would be required to calculate how the structure will be moved through the domain by the fluid flow. This would also likely require

8. CONCLUSION & FUTURE WORK

further development of the advection processes outlined in Chapter 6 to be better able to handle the transport of dendrites over potentially large regions of the domain without the observed loss of definition for the internal concentration and tip sharpness.

Other methods of detachment than remelting could also be examined, such as can be observed in the experiment by Reinhart et al (2014) [20] where an arm bends and fragments under gravity. However, there is some debate over the mechanism which causes the arms to detach in this manner, with some observed fracturing events being attributed to mechanical brittle fracturing whilst others claim the stress build-up causes rapid remelting to occur, with a combination of both of these mechanisms also being a possibility.

While there are a large number of scenarios which are yet to be explored where the deformations are ‘small’ and the structural mechanical changes can be accounted for entirely by orientation change, expanding the material model from linear elasticity to a model which allows for large deformations and plastic behaviour would greatly expand the structural mechanics scenarios which could be modelled. In any case, this would again likely require an improved advection process to allow the underlying morphology of the dendrite to be maintained as it is deformed over a significant distance.

Finally, an obvious algorithmic improvement would be to replace the point-by-point method currently in use, as this makes structural mechanics an obvious bottleneck in the solution speed for larger problems. Re-writing the algorithm to use a more efficient method such as a Tri-Diagonal Matrix Solver (TDMA) approach would greatly improve the solution speed of the SMS, saving computational time and making the modelling of larger cases a more realistic possibility.

REFERENCES

- [1] J. Strickland, B. Nenchev, and H. Dong, “On directional dendritic growth and primary spacing—a review,” *Crystals*, vol. 10, no. 7, pp. 1–30, 2020.
- [2] O. Sanchez-Mata, X. Wang, J. A. Muñiz-Lerma, S. E. Atabay, M. Attarian Shandiz, and M. Brochu, “Dependence of mechanical properties on crystallographic orientation in nickel-based superalloy Hastelloy X fabricated by laser powder bed fusion,” *Journal of Alloys and Compounds*, vol. 865, p. 158868, 2021.
- [3] F. Pöhl, C. Hardes, F. Scholz, and J. Frenzel, “Orientation-dependent deformation behavior of 316L steel manufactured by laser metal deposition and casting under local scratch and indentation load,” *Materials*, vol. 13, no. 7, 2020.
- [4] T. He, L. Min, Y. ming Huo, H. J. Liu, and X. jie Yi, “Effect of temperatures and pulling rates on microstructure and mechanical properties of 6061 aluminium alloy in directional solidification,” *Mechanika*, vol. 24, pp. 149–154, feb 2017.
- [5] R. D. Doherty, H. I. Lee, and E. A. Feest, “Microstructure of stir-cast metals,” *Materials Science and Engineering*, vol. 65, no. 1, pp. 181–189, 1984.

REFERENCES

- [6] J. R. P. Rodrigues, J. L. Peralta, J. L. d. M. Barros, M. d. L. N. M. Melo, J. R. P. Rodrigues, and K. C. R. Martins, “Analysis of the influence of deformation in microstructure formation during solidification of Pb-2.5% Sb alloy,” *Acta Scientiarum - Technology*, vol. 41, no. 1, 2019.
- [7] S. Wang, J. Kang, X. Zhang, and Z. Guo, “Dendrites fragmentation induced by oscillating cavitation bubbles in ultrasound field,” *Ultrasonics*, vol. 83, pp. 26–32, 2018.
- [8] H. Westengen and K. Nes, “Twin roll casting of aluminium: the occurrence of structure Inhomogeneities and defects in as cast strip,” in *Essential Readings in Light Metals*, pp. 972–980, Springer, 2016.
- [9] Y. Zhou, “Formation of stray grains during directional solidification of a nickel-based superalloy,” *Scripta Materialia*, vol. 65, no. 4, pp. 281–284, 2011.
- [10] C. Yang, L. Liu, X. Zhao, J. Zhang, D. Sun, and H. Fu, “Formation of stray grains during directional solidification of a superalloy AM3,” *Applied Physics A: Materials Science and Processing*, vol. 114, no. 3, pp. 979–983, 2014.
- [11] W. Xu, F. Wang, D. Ma, X. Zhu, D. Li, and A. Bührig-Polaczek, “Sliver defect formation in single crystal Ni-based superalloy castings,” *Materials and Design*, vol. 196, p. 109138, 2020.
- [12] Y. Huang, J. Shen, D. Wang, G. Xie, Y. Lu, L. Lou, and J. Zhang, “Formation of Sliver Defect in Ni-Based Single Crystal Superalloy,” *Metallurgical and Materials Transactions A: Physical Metallurgy and Materials Science*, vol. 51, no. 1, pp. 99–103, 2020.

-
- [13] D. Han, W. Jiang, J. Xiao, K. Li, Y. Lu, and L. Lou, “Investigating the evolution of freckles into sliver defects in Ni-based single-crystal superalloy castings,” *Materials Today Communications*, vol. 27, no. April, p. 102350, 2021.
- [14] W. Bogdanowicz, J. Krawczyk, R. Paszkowski, and J. Sieniawski, “Primary crystal orientation of the thin-walled area of single-crystalline turbine blade airfoils,” *Materials*, vol. 12, no. 7, 2019.
- [15] W. Bogdanowicz, J. Krawczyk, R. Paszkowski, and J. Sieniawski, “Variation of Crystal Orientation and Dendrite Array Generated in the Root of SX Turbine Blades,” *Materials*, vol. 12, no. 24, pp. 1–13, 2019.
- [16] J. Krawczyk, W. Bogdanowicz, and J. Sieniawski, “The number of subgrain boundaries in the airfoils of heat-treated single-crystalline turbine blades,” *Materials*, vol. 14, no. 1, pp. 1–16, 2021.
- [17] Y. Li, D. Qian, J. Xue, J. Wan, A. Zhang, N. Tamura, Z. Song, and K. Chen, “A synchrotron study of defect and strain inhomogeneity in laser-assisted three-dimensionally-printed Ni-based superalloy,” *Applied Physics Letters*, vol. 107, no. 18, 2015.
- [18] R. D. Doherty, “Comments on ”Mechanical deformation of dendrites by fluid flow during the solidification of undercooled melts”,” *Scripta Materialia*, vol. 49, no. 12, pp. 1219–1222, 2003.
- [19] G. Reinhart, A. Buffet, H. Nguyen-Thi, B. Billia, H. Jung, N. Mangelinck-Noël, N. Bergeon, T. Schenk, J. Härtwig, and J. Baruchel, “In-situ and real-time analysis of the formation of strains and microstructure defects during solidification of Al-3.5 Wt Pct Ni alloys,” *Metallurgical and Materials*

REFERENCES

- Transactions A: Physical Metallurgy and Materials Science*, vol. 39 A, pp. 865–874, apr 2008.
- [20] G. Reinhart, H. Nguyen-Thi, N. Mangelinck-Noël, J. Baruchel, and B. Billia, “In situ investigation of dendrite deformation during upward solidification of Al-7wt.%Si,” *Jom*, vol. 66, no. 8, pp. 1408–1414, 2014.
- [21] J. Lee, M. Ohno, Y. Shibuta, and T. Takaki, “Uniquely selected primary dendrite arm spacing during competitive growth of columnar grains in Al–Cu alloy,” *Journal of Crystal Growth*, vol. 558, no. January, p. 126014, 2021.
- [22] H. Xing, X. Dong, J. Wang, and K. Jin, “Orientation Dependence of Columnar Dendritic Growth with Sidebranching Behaviors in Directional Solidification: Insights from Phase-Field Simulations,” *Metallurgical and Materials Transactions B: Process Metallurgy and Materials Processing Science*, vol. 49, no. 4, pp. 1547–1559, 2018.
- [23] Z. Liu, M. Lin, D. Yu, X. Zhou, Y. Gu, and H. Fu, “Dependence of competitive grain growth on secondary dendrite orientation during directional solidification of a Ni-based superalloy,” *Metallurgical and Materials Transactions A: Physical Metallurgy and Materials Science*, vol. 44, no. 11, pp. 5113–5121, 2013.
- [24] S. Hu, W. Yang, Q. Cui, T. Huang, J. Zhang, and L. Liu, “Effect of secondary dendrite orientations on competitive growth of converging dendrites of Ni-based bi-crystal superalloys,” *Materials Characterization*, vol. 125, pp. 152–159, 2017.
- [25] J. W. Aveson, G. Reinhart, H. Nguyen-Thi, N. Mangelinck-Noël, A. Tandjaoui, B. Billia, K. Goodwin, T. A. Lafford, J. Baruchel, H. J.

REFERENCES

- Stone, and N. D'Souza, "Dendrite bending during directional solidification," *Proceedings of the International Symposium on Superalloys*, pp. 615–624, 2012.
- [26] J. W. Aveson, G. Reinhart, H. Nguyen-Thi, N. Mangelinck-Noël, N. D'Souza, and H. J. Stone, "Origins of misorientation defects in single crystal castings: A time resolved in situ synchrotron X-ray radiography study," *MATEC Web of Conferences*, vol. 14, p. 05003, 2014.
- [27] J. W. Aveson, G. Reinhart, C. J. Goddard, H. Nguyen-Thi, N. Mangelinck-Noël, A. Tandjaoui, J. R. Davenport, N. Warnken, F. di Gioacchino, T. A. Lafford, N. D'Souza, B. Billia, and H. J. Stone, "On the Deformation of Dendrites During Directional Solidification of a Nickel-Based Superalloy," *Metallurgical and Materials Transactions A: Physical Metallurgy and Materials Science*, vol. 50, no. 11, pp. 5234–5241, 2019.
- [28] D. Sun, L. Liu, W. Yang, T. Huang, M. Huo, S. Hu, J. Zhang, and H. Fu, "Influence of Secondary Dendrite Orientation on the Evolution of Misorientation in the Platform Region of Single Crystal Superalloy Turbine Blades," *Advanced Engineering Materials*, vol. 21, no. 2, pp. 1–8, 2019.
- [29] P. Hallensleben, F. Scholz, P. Thome, H. Schaar, I. Steinbach, G. Eggeler, and J. Frenzel, "On crystal mosaicity in single crystal Ni-based superalloys," *Crystals*, vol. 9, no. 3, pp. 15–20, 2019.
- [30] D. Sun, L. Liu, T. Huang, W. Yang, Y. Li, Q. Yue, J. Zhang, and H. Fu, "Insight of the dendrite deformation in Ni-based superalloys for increased misorientation along convergent boundaries," *Progress in Natural Science: Materials International*, vol. 28, no. 4, pp. 489–495, 2018.

REFERENCES

- [31] S. Hu, L. Liu, W. Yang, D. Sun, M. Huo, T. Huang, J. Zhang, H. Su, and H. Fu, “Formation of Accumulated Misorientation During Directional Solidification of Ni-Based Single-Crystal Superalloys,” *Metallurgical and Materials Transactions A: Physical Metallurgy and Materials Science*, vol. 50, no. 4, pp. 1607–1610, 2019.
- [32] J. W. Gibbs, D. Tournet, P. J. Gibbs, S. D. Imhoff, M. J. Gibbs, B. A. Walker, K. Fezzaa, and A. J. Clarke, “In Situ X-Ray Observations of Dendritic Fragmentation During Directional Solidification of a Sn-Bi Alloy,” *Jom*, vol. 68, no. 1, pp. 170–177, 2016.
- [33] S. Zhou, R. Hu, J. Li, H. Chang, H. Kou, and L. Zhou, “Stress induced deformation in the solidification of undercooled Co80Pd20 alloys,” *Materials Science and Engineering A*, vol. 528, no. 3, pp. 973–977, 2011.
- [34] S. Ananiev, P. Nikrityuk, and K. Eckert, “Dendrite fragmentation by catastrophic elastic remelting,” *Acta Materialia*, vol. 57, no. 3, pp. 657–665, 2009.
- [35] R. H. Mathiesen, L. Arnberg, P. Bleuet, and A. Somogyi, “Crystal fragmentation and columnar-to-equiaxed transitions in Al-Cu studied by Synchrotron x-ray video microscopy,” *Metallurgical and Materials Transactions A: Physical Metallurgy and Materials Science*, vol. 37, no. 8, pp. 2515–2524, 2006.
- [36] X. Li, A. Gagnoud, Y. Fautrelle, Z. Ren, R. Moreau, Y. Zhang, and C. Esling, “Dendrite fragmentation and columnar-to-equiaxed transition during directional solidification at lower growth speed under a strong magnetic field,” *Acta Materialia*, vol. 60, no. 8, pp. 3321–3332, 2012.

REFERENCES

- [37] E. Liotti, A. Lui, R. Vincent, S. Kumar, Z. Guo, T. Connolley, I. P. Dolbnya, M. Hart, L. Arnberg, R. H. Mathiesen, and P. S. Grant, “A synchrotron X-ray radiography study of dendrite fragmentation induced by a pulsed electromagnetic field in an Al-15Cu alloy,” *Acta Materialia*, vol. 70, pp. 228–239, 2014.
- [38] J. Pilling and A. Hellawell, “Mechanical deformation of dendrites by fluid flow,” *Metallurgical and Materials Transactions A: Physical Metallurgy and Materials Science*, vol. 27 A, no. 1, pp. 229–232, 1996.
- [39] A. K. Dahle, H. J. Thevik, L. Arnberg, and D. H. St. John, “Modeling the fluid-flow-induced stress and collapse in a dendritic network,” *Metallurgical and Materials Transactions B: Process Metallurgy and Materials Processing Science*, vol. 30, no. 2, pp. 287–293, 1999.
- [40] K. Dragnevski, A. M. Mullis, D. J. Walker, and R. F. Cochrane, “Mechanical deformation of dendrites by fluid flow during the solidification of undercooled melts,” *Acta Materialia*, vol. 50, no. 14, pp. 3743–3755, 2002.
- [41] A. B. Hanlon, D. M. Matson, and R. W. Hyers, “Microgravity experiments on the effect of internal flow on solidification of Fe-Cr-Ni stainless steels,” *Annals of the New York Academy of Sciences*, vol. 1077, pp. 33–48, 2006.
- [42] H. Kashima, T. Takaki, T. Fukui, and K. Morinishi, “Numerical investigations of mechanical stress caused in dendrite by melt convection and gravity,” *Computational Plasticity XI - Fundamentals and Applications*, pp. 642–651, 2011.
- [43] X. Xu, Y. Zhao, H. Hou, and F. Liu, “Concentration and fluid flow effects on kinetics, dendrite remelting and stress accumulation upon

REFERENCES

- rapid solidification of deeply undercooled alloys,” *Journal of Alloys and Compounds*, vol. 744, pp. 740–749, 2018.
- [44] G. Wang, J. Liang, Y. Zhou, L. Zhao, T. Jin, and X. Sun, “Variation of crystal orientation during epitaxial growth of dendrites by laser deposition,” *Journal of Materials Science and Technology*, vol. 34, no. 4, pp. 732–735, 2018.
- [45] P. Soar, A. Kao, N. Shevchenko, S. Eckert, G. Djambazov, and K. Pericleous, “Predicting Concurrent Structural Mechanical Mechanisms During Microstructure Evolution,” *Philosophical Transactions of the Royal Society A: Mathematical, Physical and Engineering Sciences*, vol. 380, no. 2217, p. 20210149, 2021.
- [46] B. Billia, N. Bergeon, H. N. Thi, H. Jamgotchian, J. Gastaldi, and G. Grange, “Cumulative mechanical moments and microstructure deformation induced by growth shape in columnar solidification,” *Physical Review Letters*, vol. 93, no. 12, pp. 1–4, 2004.
- [47] J. Strickland, B. Nanchev, K. Tassenberg, S. Perry, G. Sheppard, H. Dong, R. Zhang, G. Burca, and N. D’Souza, “On the origin of mosaicity in directionally solidified Ni-base superalloys,” *Acta Materialia*, vol. 217, pp. 1–34, 2021.
- [48] H. J. Dai, J. C. Gebelin, N. D’Souza, P. D. Brown, and H. B. Dong, “Effect of spiral shape on grain selection during casting of single crystal turbine blades,” *International Journal of Cast Metals Research*, vol. 22, no. 1-4, pp. 54–57, 2009.
- [49] X. Yang, D. Ness, P. D. Lee, and N. D’Souza, “Simulation of stray grain formation during single crystal seed melt-back and initial withdrawal in the

REFERENCES

- Ni-base superalloy CMSX4,” *Materials Science and Engineering A*, vol. 413-414, pp. 571–577, 2005.
- [50] M. Newell, N. D’Souza, and N. R. Green, “Formation of low angle boundaries in Ni-based superalloys,” *International Journal of Cast Metals Research*, vol. 22, no. 1-4, pp. 66–69, 2009.
- [51] X. L. Yang, P. D. Lee, and N. D’Souza, “Stray grain formation in the seed region of single-crystal turbine blades,” *Jom*, vol. 57, no. 5, pp. 40–44, 2005.
- [52] Y. Lee, M. Nordin, S. S. Babu, and D. F. Farson, “Effect of fluid convection on dendrite arm spacing in laser deposition,” *Metallurgical and Materials Transactions B: Process Metallurgy and Materials Processing Science*, vol. 45, no. 4, pp. 1520–1529, 2014.
- [53] D. Fuloria, P. D. Lee, and D. Bernard, “Microtomographic characterization of columnar Al-Cu dendrites for fluid flow and flow stress determination,” *Materials Science and Engineering A*, vol. 494, no. 1-2, pp. 3–9, 2008.
- [54] M. Asta, C. Beckermann, A. Karma, W. Kurz, R. Napolitano, M. Plapp, G. Purdy, M. Rappaz, and R. Trivedi, “Solidification microstructures and solid-state parallels: Recent developments, future directions,” *Acta Materialia*, vol. 57, pp. 941–971, feb 2009.
- [55] J. Thorborg, J. Klinkhammer, and M. Heitzer, “Transient and residual stresses in large castings, taking time effects into account,” *IOP Conference Series: Materials Science and Engineering*, vol. 33, p. 012050, jul 2012.
- [56] G. Palumbo, A. Piccininni, V. Piglionico, P. Guglielmi, D. Sorgente, and L. Tricarico, “Modelling residual stresses in sand-cast superduplex stainless steel,” *Journal of Materials Processing Technology*, vol. 217, pp. 253–261, mar 2015.

- [57] Z. Sun, M. Bernacki, R. Logé, and G. Gu, “Numerical simulation of mechanical deformation of semi-solid material using a level-set based finite element method,” *Modelling and Simulation in Materials Science and Engineering*, vol. 25, no. 6, pp. 0–31, 2017.
- [58] K. N. Seetharamu, R. Paragasam, G. A. Quadir, Z. A. Zainal, B. S. Prasad, and T. Sundararajan, “Finite element modelling of solidification phenomena,” *Sadhana - Academy Proceedings in Engineering Sciences*, vol. 26, pp. 103–120, feb 2001.
- [59] M. Srinivasan, P. Karuppasamy, P. Ramasamy, and A. K. Barua, “Numerical modelling on stress and dislocation generation in multi-crystalline silicon during directional solidification for PV applications,” *Electronic Materials Letters*, vol. 12, pp. 431–438, jul 2016.
- [60] L. Moj, M. Foppe, R. Deike, and T. Ricken, “Micro-macro modelling of steel solidification: A continuum mechanical, bi-phasic, two-scale model including thermal driven phase transition,” *GAMM Mitteilungen*, vol. 40, pp. 125–137, dec 2017.
- [61] M. Fackeldey, A. Ludwig, and P. Sahn, “Coupled modelling of the solidification process predicting temperatures, stresses and microstructures,” *Computational Materials Science*, vol. 7, pp. 194–199, dec 2002.
- [62] T. Uehara, M. Fukui, and N. Ohno, “Phase field simulations of stress distributions in solidification structures,” *Journal of Crystal Growth*, vol. 310, no. 7-9, pp. 1331–1336, 2008.
- [63] T. Takaki and H. Kashima, “Numerical investigations of stress in dendrites

REFERENCES

- caused by gravity,” *Journal of Crystal Growth*, vol. 337, no. 1, pp. 97–101, 2011.
- [64] M. Yamaguchi and C. Beckermann, “Simulation of solid deformation during solidification: Shearing and compression of polycrystalline structures,” *Acta Materialia*, vol. 61, no. 6, pp. 2268–2280, 2013.
- [65] M. Yamaguchi and C. Beckermann, “Simulation of solid deformation during solidification: Compression of a single dendrite,” *Acta Materialia*, vol. 61, no. 11, pp. 4053–4065, 2013.
- [66] M. Yamaguchi and C. Beckermann, “Direct numerical simulation of solid deformation during dendritic solidification,” *Jom*, vol. 66, no. 8, pp. 1431–1438, 2014.
- [67] J. Viktor, “Phase-field simulation of microstructure evolution coupled to plastic deformation : Application to Ni-base superalloys and low carbon steel,” 2018.
- [68] T. Tang and D. Openfoam, “Implementation of solid body stress analysis in OpenFOAM,” *Report*, pp. 1–2012, 2012.
- [69] P. Cardiff and I. Demirdžić, “Thirty Years of the Finite Volume Method for Solid Mechanics,” *Archives of Computational Methods in Engineering*, vol. 28, no. 5, pp. 3721–3780, 2021.
- [70] E. Oñate, M. Cervera, and O. C. Zienkiewicz, “A finite volume format for structural mechanics,” *International Journal for Numerical Methods in Engineering*, vol. 37, pp. 181–201, jan 1994.
- [71] G. A. Taylor, C. Bailey, and M. Cross, “Solution of the elastic/visco-plastic

-
- constitutive equations: A finite volume approach,” *Applied Mathematical Modelling*, vol. 19, no. 12, pp. 746–760, 1995.
- [72] G. A. Taylor, C. Bailey, and M. Cross, “Computational solid mechanics using a vertex-based finite volume method,” *Finite Volumes for Complex Applications II: Problems and Perspectives*, vol. m, no. January, pp. 507–515, 1999.
- [73] G. A. Taylor, M. Hughes, N. Strusevich, and K. Pericleous, “Finite volume methods applied to the computational modelling of welding phenomena,” *Applied Mathematical Modelling*, vol. 26, no. 2, pp. 311–322, 2002.
- [74] A. K. Slone, C. Bailey, and M. Cross, “Dynamic solid mechanics using finite volume methods,” *Applied Mathematical Modelling*, vol. 27, no. 2, pp. 69–87, 2003.
- [75] A. K. Slone, K. Pericleous, C. Bailey, M. Cross, and C. Bennett, “A finite volume unstructured mesh approach to dynamic fluid-structure interaction: An assessment of the challenge of predicting the onset of flutter,” *Applied Mathematical Modelling*, vol. 28, no. 2, pp. 211–239, 2004.
- [76] P. J. Oliveira and C. J. Rente, “Development and Application of a Finite Volume Method for Static and Transient Stress Analysis,” *Proc. NAFEMS World Congr. Effect. Eng. Anal*, vol. 1, pp. 297–309, 1999.
- [77] M. A. A. Cavalcante and M.-J. Pindera, “Generalized Finite-Volume Theory for Elastic Stress Analysis in Solid Mechanics—Part I: Framework,” *Journal of Applied Mechanics*, vol. 79, no. 5, p. 051007, 2012.
- [78] M. A. A. Cavalcante and M.-J. Pindera, “Generalized Finite-Volume Theory for Elastic Stress Analysis in Solid Mechanics—Part II: Results,” *Journal of Applied Mechanics*, vol. 79, no. 5, p. 051007, 2012.

REFERENCES

- [79] H. S. Udaykumar, R. Mittal, and P. Rampungoon, “Interface tracking finite volume method for complex solid-fluid interactions on fixed meshes,” *Communications in Numerical Methods in Engineering*, vol. 18, no. 2, pp. 89–97, 2002.
- [80] M. Yates, “Finite-Volume Method To Fluid-Structure Interaction Analysis,” vol. M, 2011.
- [81] G. Xia and C. L. Lin, “An unstructured finite volume approach for structural dynamics in response to fluid motions,” *Computers and Structures*, vol. 86, pp. 684–701, apr 2008.
- [82] P. Timoshenko and J. Goodier, “Theory of Elasticity,” 1951.
- [83] J. A. Dantzig and M. Rappaz, *Solidification: -Revised & Expanded*. EPFL press, 2016.
- [84] F. H. Harlow and J. E. Welch, “Numerical calculation of time-dependent viscous incompressible flow of fluid with free surface,” *Physics of Fluids*, vol. 8, pp. 2182–2189, dec 1965.
- [85] J. H. Hattel and P. N. Hansen, “A control volume-based finite difference method for solving the equilibrium equations in terms of displacements,” *Applied Mathematical Modelling*, vol. 19, no. 4, pp. 210–243, 1995.
- [86] R. v. Mises, “Mechanik der festen körper im plastisch-deformablen zustand,” *Nachrichten von der Gesellschaft der Wissenschaften zu Göttingen, Mathematisch-Physikalische Klasse*, vol. 1913, no. 4, pp. 582–592, 1913.
- [87] O. A. Bauchau and J. I. Craig, eds., *Structural Analysis*, vol. 163 of *Solid Mechanics and Its Applications*. Dordrecht: Springer Netherlands, 2009.

REFERENCES

- [88] A. Kao and K. Pericleous, “A Numerical Model Coupling Thermoelectricity, Magnetohydrodynamics and Dendritic Growth,” *Journal of Algorithms & Computational Technology*, vol. 6, pp. 173–201, mar 2012.
- [89] A. Kao, B. Cai, P. D. Lee, and K. Pericleous, “The effects of Thermoelectric Magnetohydrodynamics in directional solidification under a transverse magnetic field,” *Journal of Crystal Growth*, vol. 457, pp. 270–274, 2017.
- [90] A. Kao, N. Shevchenko, M. Alexandrakis, I. Krastins, S. Eckert, and K. Pericleous, “Thermal dependence of large-scale freckle defect formation,” *Philosophical Transactions of the Royal Society A: Mathematical, Physical and Engineering Sciences*, vol. 377, p. 20180206, apr 2019.
- [91] A. Kao, I. Krastins, M. Alexandrakis, N. Shevchenko, S. Eckert, and K. Pericleous, “A Parallel Cellular Automata Lattice Boltzmann Method for Convection-Driven Solidification,” *Jom*, vol. 71, pp. 48–58, jan 2019.
- [92] V. R. Voller, “An enthalpy method for modeling dendritic growth in a binary alloy,” *International Journal of Heat and Mass Transfer*, vol. 51, no. 3-4, pp. 823–834, 2008.
- [93] P. Soar, A. Kao, G. Djambazov, N. Shevchenko, S. Eckert, and K. Pericleous, “The integration of structural mechanics into microstructure solidification modelling,” *IOP Conference Series: Materials Science and Engineering*, vol. 861, no. 1, p. 012054, 2020.
- [94] P. D. Lee, R. C. Atwood, R. J. Dashwood, and H. Nagaumi, “Modeling of porosity formation in direct chill cast aluminum-magnesium alloys,” *Materials Science and Engineering A*, vol. 328, no. 1, pp. 213–222, 2002.
- [95] W. Wang, P. D. Lee, and M. McLean, “A model of solidification

REFERENCES

- microstructures in nickel-based superalloys: Predicting primary dendrite spacing selection,” *Acta Materialia*, vol. 51, no. 10, pp. 2971–2987, 2003.
- [96] P. D. Lee, A. Chirazi, R. C. Atwood, and W. Wang, “Multiscale modelling of solidification microstructures, including microsegregation and microporosity, in an Al-Si-Cu alloy,” *Materials Science and Engineering A*, vol. 365, no. 1-2, pp. 57–65, 2004.
- [97] H. B. Dong and P. D. Lee, “Simulation of the columnar-to-equiaxed transition in directionally solidified Al-Cu alloys,” *Acta Materialia*, vol. 53, no. 3, pp. 659–668, 2005.
- [98] M. Alexandrakis, “Parallelised Micro-Macroscale Modelling of Convection Driven Freckles in Binary Alloys,” no. October, 2017.
- [99] P. Bourke, “Trilinear interpolation,” 2020.
- [100] D. Eberly, “Euler angle formulas,” *Geometric Tools, LLC, Technical Report*, pp. 1–21, 2008.
- [101] J. M. Gere, “Mechanics of Materials,” *Mechanics of Materials*, p. 913, 2008.
- [102] C. J. Vreeman, M. J. M. Krane, and F. P. Incropera, “The effect of free-floating dendrites and convection on macrosegregation in direct chill cast aluminum alloys Part I: Model development,” *International Journal of Heat and Mass Transfer*, vol. 43, pp. 677–686, mar 2000.
- [103] Q. Dong, H. Nagaumi, H. Zhang, T. Qu, and J. Wang, “Numerical investigation on the motion of free-floating crystals during dc casting of aluminum alloys,” in *Minerals, Metals and Materials Series*, pp. 295–303, Springer, Cham, 2019.

REFERENCES

- [104] O. Ubbink, “Numerical Prediction of two fluid systems with sharp interfaces,” no. January 1997, p. 158, 2010.
- [105] R. S. Qin and H. K. Bhadeshia, “Phase field method,” *Materials Science and Technology*, vol. 26, no. 7, pp. 803–811, 2010.
- [106] S. Sakane, T. Takaki, M. Ohno, and Y. Shibuta, “Simulation method based on phase-field lattice Boltzmann model for long-distance sedimentation of single equiaxed dendrite,” *Computational Materials Science*, vol. 164, no. January, pp. 39–45, 2019.
- [107] L. Tan and N. Zabaras, “Modeling the growth and interaction of multiple dendrites in solidification using a level set method,” *Journal of Computational Physics*, vol. 226, no. 1, pp. 131–155, 2007.
- [108] H. S. Udaykumar, R. Mittal, P. Rampunggoon, and A. Khanna, “A sharp interface Cartesian grid method for simulating flows with complex moving boundaries,” *Journal of Computational Physics*, vol. 174, no. 1, pp. 345–380, 2001.
- [109] S. Pan and M. Zhu, “A three-dimensional sharp interface model for the quantitative simulation of solutal dendritic growth,” *Acta Materialia*, vol. 58, no. 1, pp. 340–352, 2010.
- [110] P. Colella and E. G. Puckett, “Modern numerical methods for fluid flow,” no. July 2015, p. 148, 1998.
- [111] C. W. Hirt and B. D. Nichols, “Volume of fluid (VOF) method for the dynamics of free boundaries,” *Journal of Computational Physics*, vol. 39, pp. 201–225, jan 1981.

REFERENCES

- [112] W. F. Noh and P. Woodward, “SLIC (SIMPLE LINE INTERFACE CALCULATION),” tech. rep., Lawrence Livermore Laboratory, 1976.
- [113] K. Yokoi, “Efficient implementation of THINC scheme: A simple and practical smoothed VOF algorithm,” *Journal of Computational Physics*, vol. 226, pp. 1985–2002, oct 2007.
- [114] M. Marek, W. Aniszewski, and A. Boguslawski, “Simplified volume of fluid method (SVOF) for two-phase flows,” *TASK Quarterly. v12*, no. 3, pp. 255–265, 2008.
- [115] W. Aniszewski, T. Ménard, and M. Marek, “Volume of Fluid (VOF) type advection methods in two-phase flow: A comparative study,” *Computers & Fluids*, vol. 97, pp. 52–73, jun 2014.
- [116] S. H. Garrioch and B. R. Baliga, “A PLIC volume tracking method for the simulation of two-fluid flows,” *International Journal for Numerical Methods in Fluids*, vol. 52, pp. 1093–1134, dec 2006.
- [117] N. Ashgriz and J. Y. Poo, “FLAIR: Flux line-segment model for advection and interface reconstruction,” *Journal of Computational Physics*, vol. 93, no. 2, pp. 449–468, 1991.
- [118] R. Scardovelli and S. Zaleski, “Interface reconstruction with least-square fit and split Eulerian-Lagrangian advection,” *International Journal for Numerical Methods in Fluids*, vol. 41, pp. 251–274, jan 2003.
- [119] Y. Marcus, “On the compressibility of liquid metals,” *Journal of Chemical Thermodynamics*, vol. 109, pp. 11–15, 2017.

Appendix A

Staggered Grid Solver

Discretisation

This appendix will cover demonstrate the steps required to discretise the equilibrium equations [3.24](#) - [3.26](#) to obtain the staggered grid finite volume method presented in equations [3.27](#) - [3.29](#) for a structure with variable material properties.

This process will only be shown for the u displacements acting along the x axis for the sake of brevity, as an identical process is used to discretise the v and w equations. Grids showing the locations of the displacements and material properties being used in this discretisation can be seen in figure [A.1](#) to aid understanding of the process. It should be noted that this diagram is a 2D slice of the 3D structure in the x - y plane, so there are also displacement and material property nodes in the z plane which cannot be seen in the diagrams but are utilised in the equations.

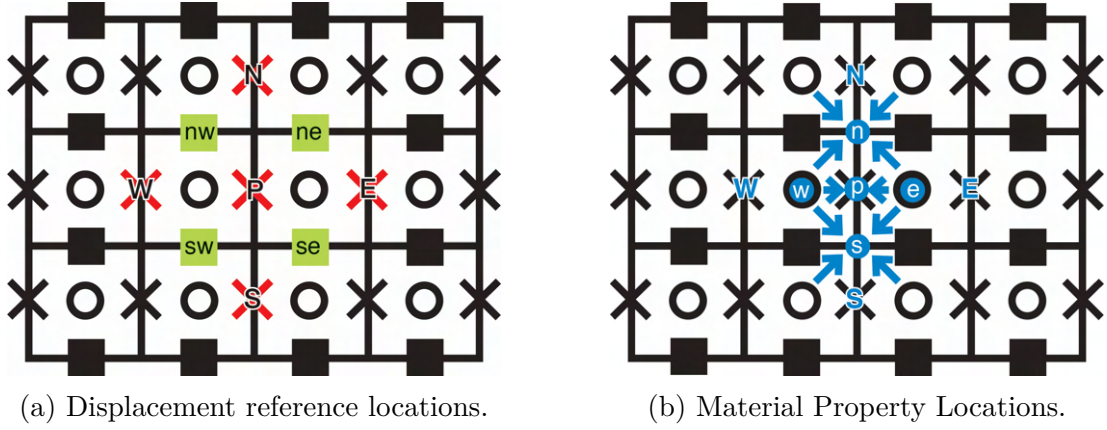


Figure A.1: 2D slice showing information used to obtain u displacement.

Starting with the equilibrium equation for u :

$$2 \frac{\partial}{\partial x} \mu \frac{\partial u}{\partial x} + \frac{\partial}{\partial x} \lambda \frac{\partial u}{\partial x} + \frac{\partial}{\partial y} \mu \frac{\partial u}{\partial y} + \frac{\partial}{\partial z} \mu \frac{\partial u}{\partial z} + \frac{\partial}{\partial x} \lambda \frac{\partial v}{\partial y} + \frac{\partial}{\partial y} \mu \frac{\partial v}{\partial x} + \frac{\partial}{\partial x} \lambda \frac{\partial w}{\partial z} + \frac{\partial}{\partial z} \mu \frac{\partial w}{\partial x} + F_x = 0 \quad (\text{A.1})$$

Due to the variable material properties, none of these terms can be helpfully collected together before discretisation, so have been labelled 1 - 8 and will be discretised individually for clarity before being replaced back into this main equation. Central differences are used for all differencing in the scheme, which leads to the overall scheme for a central node being $O(\Delta x^2)$ accurate for the case being examined using a Cartesian grid where $\Delta x = \Delta y = \Delta z$. Sections 1 - 4 are the terms relating to the primary u deformations, which can be discretised like so:

$$\begin{aligned}
 1 : 2 \frac{\partial}{\partial x} \boldsymbol{\mu} \frac{\partial u}{\partial x} &= 2 \frac{1}{\Delta x} \left(\frac{1}{\Delta x} (\mu_E u_e - \mu_p u_p) - \frac{1}{\Delta x} (\mu_p u_p - \mu_W u_w) \right) \\
 &= \frac{2}{\Delta x^2} (\mu_E u_e - 2\mu_p u_p + \mu_W u_w) \\
 \frac{4\mu_p}{\Delta x^2} u_p &= \frac{2\mu_E}{\Delta x^2} u_e + \frac{2\mu_W}{\Delta x^2} u_w + O(\Delta x^2) \\
 2 : \frac{\partial}{\partial x} \boldsymbol{\lambda} \frac{\partial u}{\partial x} &= \frac{1}{\Delta x} \left(\frac{1}{\Delta x} (\lambda_E u_e - \lambda_p u_p) - \frac{1}{\Delta x} (\lambda_p u_p - \lambda_E u_w) \right) \\
 &= \frac{1}{\Delta x^2} (\lambda_E u_e - 2\lambda_p u_p + \lambda_W u_w) \\
 \frac{2\lambda_p}{\Delta x^2} u_p &= \frac{\lambda_E}{\Delta x^2} u_e + \frac{\lambda_W}{\Delta x^2} u_w + O(\Delta x^2) \\
 3 : \frac{\partial}{\partial y} \boldsymbol{\mu} \frac{\partial u}{\partial y} &= \frac{1}{\Delta y} \left(\frac{1}{\Delta y} (\mu_N u_n - \mu_p u_p) - \frac{1}{\Delta y} (\mu_p u_p - \mu_N u_s) \right) \\
 &= \frac{1}{\Delta y^2} (\mu_N u_n - 2\mu_p u_p + \mu_S u_s) \\
 \frac{2\mu_p}{\Delta y^2} u_p &= \frac{\mu_N}{\Delta y^2} u_n + \frac{\mu_S}{\Delta y^2} u_s + O(\Delta x^2) \\
 4 : \frac{\partial}{\partial z} \boldsymbol{\mu} \frac{\partial u}{\partial z} &= \frac{1}{\Delta z} \left(\frac{1}{\Delta z} (\mu_H u_h - \mu_p u_p) - \frac{1}{\Delta z} (\mu_p u_p - \mu_L u_l) \right) \\
 &= \frac{1}{\Delta z^2} (\mu_H u_h - 2\mu_p u_p + \mu_L u_l) \\
 \frac{2\mu_p}{\Delta z^2} u_p &= \frac{\mu_H}{\Delta z^2} u_h + \frac{\mu_L}{\Delta z^2} u_l + O(\Delta x^2)
 \end{aligned} \tag{A.2}$$

While the sections 5 - 8 are the from the cross terms accounting for the impact of the v and w displacements, which can be discretised like so:

$$\begin{aligned}
 5: \quad \frac{\partial}{\partial x} \lambda \frac{\partial v}{\partial y} &= \frac{\lambda_E \frac{\partial}{\partial y} v_e - \lambda_W \frac{\partial}{\partial y} v_w}{2 * 0.5 * \Delta x} = \frac{\frac{\lambda_E v_{ne} - \lambda_E v_{se}}{2 * 0.5 * \Delta y} - \frac{\lambda_W v_{nw} - \lambda_W v_{sw}}{2 * 0.5 * \Delta y}}{\Delta x} \\
 &= \frac{\lambda_E v_{ne} - \lambda_E v_{se} - \lambda_W v_{nw} + \lambda_W v_{sw}}{\Delta y \Delta x} + O(\Delta x^2) \\
 6: \quad \frac{\partial}{\partial y} \mu \frac{\partial v}{\partial x} &= \frac{\mu_N \frac{\partial}{\partial \Delta x} v_n - \mu_S \frac{\partial}{\partial x} v_s}{2 * 0.5 * \Delta y} = \frac{\frac{\mu_N v_{ne} - \mu_N v_{nw}}{2 * 0.5 * \Delta x} - \frac{\mu_S v_{se} - \mu_S v_{sw}}{2 * 0.5 * \Delta x}}{\Delta x} + O(\Delta x^2) \\
 &= \frac{\mu_N v_{ne} - \mu_N v_{nw} - \mu_S v_{se} + \mu_S v_{sw}}{\Delta x \Delta y} \\
 7: \quad \frac{\partial}{\partial x} \lambda \frac{\partial w}{\partial z} &= \frac{\lambda_E \frac{\partial}{\partial z} w_e - \lambda_W \frac{\partial}{\partial \Delta z} w_w}{2 * 0.5 * \Delta x} = \frac{\frac{\lambda_E w_{he} - \lambda_E w_{le}}{2 * 0.5 * \Delta z} - \frac{\lambda_W w_{hw} - \lambda_W w_{lw}}{2 * 0.5 * \Delta z}}{\Delta x} \\
 &= \frac{\lambda_E w_{he} - \lambda_E w_{le} - \lambda_W w_{hw} + \lambda_W w_{lw}}{\Delta z \Delta x} + O(\Delta x^2) \\
 8: \quad \frac{\partial}{\partial z} \mu \frac{\partial w}{\partial x} &= \frac{\mu_H \frac{\partial}{\partial x} w_h - \mu_L \frac{\partial}{\partial x} w_l}{2 * 0.5 * \Delta z} = \frac{\frac{\mu_H w_{he} - \mu_H w_{hw}}{2 * 0.5 * \Delta x} - \frac{\mu_L w_{le} - \mu_L w_{lw}}{2 * 0.5 * \Delta x}}{\Delta z} \\
 &= \frac{\mu_H w_{he} - \mu_H w_{hw} - \mu_L w_{le} + \mu_L w_{lw}}{\Delta x \Delta z} + O(\Delta x^2)
 \end{aligned} \tag{A.3}$$

Taking these 8 sections, substituting them back into equation A.1 and multiplying through with Δx^2 (where $\Delta x = \Delta y = \Delta z$ due to the Cartesian grid being used), allows a discretised version of the full equation to be collected together in the form:

$$\begin{aligned}
 -4\mu_p u_p - 2\lambda_p u_p - 2\mu_p u_p - 2\mu_p u_p = \\
 2\mu_E u_e + 2\mu_W u_w + \lambda_E u_e + \lambda_W u_w + \mu_N u_n + \mu_S u_s + \mu_H u_h + \mu_L u_l + S_x
 \end{aligned} \tag{A.4}$$

$$\begin{aligned}
 -(2\lambda_p + 8\mu_p) u_p = \\
 (2\mu_E + \lambda_E) u_e + (2\mu_W + \lambda_W) u_w + \mu_N u_n + \mu_S u_s + \mu_H u_h + \mu_L u_l + S_x
 \end{aligned} \tag{A.5}$$

$$-A_p u_p = A_N u_n + A_S u_s + A_E u_e + A_W u_w + A_H u_h + A_L u_l + S_x \tag{A.6}$$

Where S_x is the source term from the influence of the v and w grids and the

body force being defined as:

$$S_x = \mu_N(v_{ne} - v_{nw}) - \mu_S(v_{se} - v_{sw}) + \mu_H(w_{he} - w_{hw}) - \mu_L(w_{le} - w_{lw}) + \lambda_E(v_{ne} - v_{se} + w_{he} - w_{le}) + \lambda_W(v_{nw} - v_{sw} + w_{hw} - w_{lw}) + \Delta x^2 F_x \quad (\text{A.7})$$

Which can then be rearranged into the the final form presented in section 3.4 to calculate the displacement u_p :

$$\begin{aligned} -A_P u_p &= A_N u_n + A_S u_s + A_E u_e + A_W u_w + A_H u_h + A_L u_l + S_x \\ u_p &= \frac{1}{-A_P} (A_N u_n + A_S u_s + A_E u_e + A_W u_w + A_H u_h + A_L u_l + S_x) \end{aligned} \quad (\text{A.8})$$

Appendix B

Structural Mechanics Solver

Validation

This appendix acts as a supplement to the model verification presented in section 3.10, presenting the full 30 verification cases which were examined (including the 7 cases already presented in that section to allow for easier comparison with the other cases). All of the information provided Section 3.10 about problem setup, the presentation of results and numerical grid independence applies to all the cases being presented here. Cases 1-14, 27-30 use a $\Delta x = 0.25$ grid and cases 15-26 use a $\Delta x = 0.125$ grid.

Case 1 - Floor fixed block under negative body force in z (figure B.1).

This case was chosen to demonstrate that the SMS can accurately model the behaviour of regular 3D structure under a body force load. The body force applied was negative in the z direction, representing a case where the block is fixed to the floor and compressed. The data comparisons indicate a close match in accuracy between the SMS and COMSOL for this scenario.

Case 2 - Floor fixed block under positive body force in z (figure B.2).

This case was chosen to demonstrate that reversing the sign of the force would create a reflected solution and have no impact on the accuracy. The body force applied was positive in the z direction, representing a case where the block is fixed to the floor and uniformly stretched. The data comparisons indicate a close match in accuracy between the SMS and COMSOL for this scenario and are indeed the exact reverse of Case 1. As such, there will be no repeat any further cases where the only difference is the sign of the force.

Case 3 - Floor fixed block under positive body force in y (figure B.3).

This case was chosen to demonstrate that the SMS could accurately capture the behaviour of a shear body force running parallel to the fixed face. The body force applied was positive in the y direction, representing a case where the block is fixed to the floor and uniformly pushed throughout the structure going South-North. The data comparisons indicate a close match in accuracy between the SMS and COMSOL for this scenario.

Case 4 - Floor fixed block under positive body force in x (figure B.4).

This case was chosen to round out the prior tests and confirm that the SMS could also correctly model a shearing force in the x direction. The body force applied was positive in the x direction, representing a case where the block is fixed to the floor and uniformly pushed throughout the structure going West-East. The data comparisons indicate a close match in accuracy between the SMS and COMSOL for this scenario.

Case 5 - Floor fixed block under positive body force in x and y (figure B.5).

This case was chosen to demonstrate if the SMS is cable of resolving problems including multiple body forces. The body forces applied was positive in the x and y directions, representing a case where the block is fixed to the floor and uniformly pushed throughout the structure going West-East and South-North. Whilst clearly capturing the general structural behaviour well, these represent the poorest match in value with the COMSOL solutions so far, with the w value in particular being nearly 10% off of the COMSOL values. This may indicate that for a case with complex force conditions like this, a greater grid density or higher order boundaries may be required if a very close value match is desired.

Case 6 - Floor fixed block under positive body force in x and negative force in y (figure B.6).

This case was chosen to demonstrate that when having multiple body forces, the sign of the forces changing will no effect the accuracy of the solution. The body forces applied was positive in x and negative in y , representing a case where the block is fixed to the floor and uniformly pushed throughout the structure going West-East and North-South. As expected, this is just a mirror of the previous case for some displacements, with the accuracy and behaviour matching that which was observed in case 5.

Case 7 - Floor fixed block under positive body force in x , y and z (figure B.7).

This case was chosen to demonstrate that the SMS was capable of resolving problems with body forces acting in all three directions. The body forces applied was positive in x , y and z , representing a case where the block is fixed to the floor and uniformly pushed throughout the structure going West-East, South-North and Low-High. The data comparisons indicate a close match in

accuracy between the SMS and COMSOL for this scenario.

Case 8 - Floor fixed block under positive facial force in w on High face (figure B.8).

This case was chosen to demonstrate that the SMS can accurately model the behaviour of regular 3D structure under a facial force load. The facial force applied was positive in the z direction, representing a case where the block is fixed to the floor and stretched by the top face. The data comparisons indicate a close match in accuracy between the SMS and COMSOL for this scenario.

Case 9 - Floor fixed block under positive facial force in y on High face (figure B.9).

This case was chosen to demonstrate that the SMS could accurately capture the behaviour of a shear facial body force running parallel to the fixed face. The body force applied was positive in the y direction, representing a case where the block is fixed to the floor and is pushed by a uniform force in South-North applied to the high face. The data comparisons indicate a close match in accuracy between the SMS and COMSOL for this scenario, however the u displacements (which for this case are relatively small compared to the v and w displacements) do seem to deviate slightly as their magnitude increases, though still by less than 10% from of the COMSOL values.

Case 10 - Floor fixed block under rotational facial forces (figure B.10).

This case was chosen to demonstrate how well the SMS would model some of the more complex scenarios that could be achieved with facially applied forces, such as apply forces that will attempt to rotate the structure around the z

axis. This was done by applying a positive force in u on the North face, negative in u on the South face, positive in v on the East face and negative in v on the West face. This would represent a situation where a block is fixed to the ground and rotated anticlockwise by applying uniform forces to the faces of the structure. The data comparisons indicate a close match in accuracy between the SMS and COMSOL for this scenario, however the w displacements (which for this case are relatively small compared to the v and w displacements), while clearly following the correct behaviour, do deviate quite significantly from the COMSOL values, going outside of the 10% intervals plotted. This may indicate that for a case with complex force conditions like this, a greater grid density or higher order boundaries may be required if a very close value match is desired for all displacements.

Case 11 - Floor fixed block under opposing facial forces (figure B.11).

This case was chosen as another example to demonstrate how well the SMS would model some of the more complex scenarios that could be achieved with facially applied forces, in this case compressing the block between opposing facial forces. This was done by applying a positive force in u on the West face and negative in u on the East face. This would represent a situation where a block is fixed to the ground and compressed between two equal but opposite uniform forces applied to opposite faces on the side of the structure. The behaviour is well matched to what would be expected, with the compression in u causing the structure to deform outwards in y and w due to the Poisson effect, with the data comparisons indicating a close match in accuracy between the SMS and COMSOL for this scenario.

Case 12 - Floor fixed block under body force in x and facial force in w

on side face (figure B.12).

This case was chosen to demonstrate that the SMS was capable of accurately resolving problem including both body forces and facial forces. The body force applied was positive in the x direction and the facial force was positive in the z plane and applied to the West face, representing a case where the block is fixed to the floor uniformly pushed throughout the structure in one direction while one of the faces is uniformly pulled upwards. The data comparisons indicate a close match in accuracy between the SMS and COMSOL for this scenario.

Case 13 - Floor & wall fixed block under body force in z (figure B.13).

This case was chosen to demonstrate that the SMS can accurately model scenarios where more than one face of the structure is fixed. Here the West, South and Low faces are fixed while a positive body force in z is applied to the structure, representing a case where a block fixed at three faces is uniformly pulled upwards. Aside from a discontinuity near the wall where the displacements approach zero, data comparisons indicate a close match in accuracy between the SMS and COMSOL for this scenario.

Case 14 - Floor block with fixed displacement (figure B.14).

This case was chosen to demonstrate that the SMS can accurately model scenarios where one of the faces is moved by a fixed displacement. While not currently being used in experiments, the ability to set a fixed displacement is still key functionality for a structural mechanics solver, and it is certainly possible in future research that it may be required to parse fixed displacements when trying to model the behaviour of a multi-physics system. Here the top face of the fixed cube was moved downwards by 1 cm. The data comparisons

indicate a close match in accuracy between the SMS and COMSOL for this scenario.

Case 15 - $4 \times 4 \times 10$ cantilever beam with point load (figure B.15).

This case was chosen to demonstrate that the SMS can accurately model the behaviour of a structure where some sides are longer than others, modelling a cantilever beams also allows for comparisons to be made with the analytic solution given by Euler-Bernoulli beam theory (see section 3.10.6 for more details on the beam theory model being used). To test this verification case, a cantilever beam with the dimensions $4\text{m} \times 4\text{m} \times 10\text{m}$ was fixed to the wall at one end and had a negative facial (or ‘point’ for the 1D beam theory model) force in z , representing a case where a fixed cantilever beam has a weight applied at it’s free end. As beam theory is a 1D approximation, only the deflection w is provided, so while the SMS and COMSOL solutions did provide u and v displacement profiles, these have been omitted to focus on the beam theory comparison. The data comparisons confirm that for this case there is also a very close match in values between the SMS and COMSOL, however the beam theory, while still quite close in behaviour, is noticeably lower than the other models. This is because the beam structure being modelled does not actually satisfy the assumptions of beam theory, as for such a squat ‘beam’ the Poisson effect will still have a significant effect on limiting the w displacement.

Case 16 - $4 \times 4 \times 20$ cantilever beam with point load (figure B.16).

This case was chosen to demonstrate that the SMS can accurately model the behaviour of longer cantilever beam under a point load which will satisfy the beam theory assumptions, allowing for comparisons to be made with the analytic solution given by Euler-Bernoulli beam theory (see section 3.10.6 for

more details on the beam theory model being used). To test this verification case, a cantilever beam with the dimensions $4\text{m} \times 4\text{m} \times 20\text{m}$ was fixed to the wall at one end and had a negative facial (or ‘point’ for the 1D beam theory model) force in z , representing a case where a fixed cantilever beam has a weight applied at the free end. As beam theory is a 1D approximation, only the deflection w is provided, so while the SMS and COMSOL solutions did provide u and v displacement profiles, these have been omitted to focus on the beam theory comparison. The data comparisons confirm that for this case there is also a very close match in values between all three models - beam theory, SMS and COMSOL.

Case 17 - $4 \times 4 \times 40$ cantilever beam with point load (figure B.17).

This case was chosen to demonstrate that the SMS can accurately model the behaviour of a significantly longer cantilever beam under a point load where the length is ten times the size of the cross section, allowing for comparisons to be made with the analytic solution given by Euler-Bernoulli beam theory (see section 3.10.6 for more details on the beam theory model being used). To test this verification case, a cantilever beam with the dimensions $4\text{m} \times 4\text{m} \times 40\text{m}$ was fixed to the wall at one end and had a negative facial (or ‘point’ for the 1D beam theory model) force in z , representing a case where a fixed cantilever beam has a weight applied at the free end. As beam theory is a 1D approximation, only the deflection w is provided, so while the SMS and COMSOL solutions did provide u and v displacement profiles, these have been omitted to focus on the beam theory comparison. The data comparisons confirm that for this case there is also a good match between all three models, with COMSOL and beam theory being almost identical, however the SMS solution does seem to under predict slightly by comparison, though still well

within the margin of error.

Case 18 - $4 \times 4 \times 10$ cantilever beam with distributed load (figure B.18).

This case was chosen to demonstrate that the SMS is also capable of modelling a cantilever beam under a uniform body force (or ‘distributed load’), modelling a cantilever beams also allows for comparisons to be made with the analytic solution given by Euler-Bernoulli beam theory (see section 3.10.7 for more details on the beam theory model being used). To test this verification case, a cantilever beam with the dimensions $4\text{m} \times 4\text{m} \times 10\text{m}$ was fixed to the wall at one end and had a negative body force (or ‘distributed load’ for the 1D beam theory model) force in z applied, representing a case where a cantilever beam fixed at one end and free at the other has a weight uniformly applied across its length. As beam theory is a 1D approximation, only the deflection w is provided, so while the SMS and COMSOL solutions did provide u and v displacement profiles, these have been omitted to focus on the beam theory comparison. The data comparisons confirm that for this case there is also a very close match in values between the SMS and COMSOL, however the beam theory, while still quite close in behaviour, is noticeably lower than the other models. This is because the beam structure being modelled does not actually satisfy the assumptions of beam theory, as for such a squat ‘beam’ the Poisson effect will still have a significant effect on limiting the w displacement.

Case 19 - $4 \times 4 \times 20$ cantilever beam With distributed load (figure B.19).

This case was chosen to demonstrate that the SMS can accurately model the behaviour of longer cantilever beam under a distributed load which will satisfy

the beam theory assumptions, allowing for comparisons to be made with the analytic solution given by Euler-Bernoulli beam theory (see section 3.10.7 for more details on the beam theory model being used). To test this verification case, a cantilever beam with the dimensions $4\text{m} \times 4\text{m} \times 20\text{m}$ was fixed to the wall at one end and had a negative body force (or ‘distributed load’ for the 1D beam theory model) force in z applied, representing a case where a cantilever beam fixed at one end and free at the other has a weight uniformly applied across its length. As beam theory is a 1D approximation, only the deflection w is provided, so while the SMS and COMSOL solutions did provide u and v displacement profiles, these have been omitted to focus on the beam theory comparison. The data comparisons confirm that for this case there is also a very close match in values between all three models - beam theory, SMS and COMSOL.

Case 20 - $4 \times 4 \times 40$ cantilever beam with distributed load (figure B.20).

This case was chosen to demonstrate that the SMS can accurately model the behaviour of a significantly longer cantilever beam under a distributed load where the length is ten times the size of the cross section, allowing for comparisons to be made with the analytic solution given by Euler-Bernoulli beam theory (see section 3.10.7 for more details on the beam theory model being used). To test this verification case, a cantilever beam with the dimensions $4\text{m} \times 4\text{m} \times 40\text{m}$ was fixed to the wall at one end and had a negative facial (or ‘point’ for the 1D beam theory model) force in z , representing a case where a fixed cantilever beam has a weight applied at its free end. As beam theory is a 1D approximation, only the deflection w is provided, so while the SMS and COMSOL solutions did provide u and v displacement profiles, these

have been omitted to focus on the beam theory comparison. The data comparisons confirm that for this case there is also a good match between all three models, with COMSOL and beam theory being almost identical, however the SMS solution does seem to under predict slightly by comparison, though still well within the margin of error.

Case 21 - Floor fixed block with diagonal edge under negative body force in z (figure B.21).

This case was chosen to demonstrate that the SMS can simulate the behaviour of structures with diagonal edges being subjected to body forces, as due to the nature of the SMS any parts which are not perfectly aligned with the axis will be approximated by cubic volumes. For this case, the South and Low faces of the structure were fixed and a body force negative in the z direction was applied to the structure, representing a case where a cube with a diagonal face added at one edge is fixed at two faces and uniformly compressed. The data comparisons indicate that this case does still match the general behaviour observed in COMSOL, however the SMS data is outside of the 10% interval for the u and v displacements. While this result does demonstrate that the fundamental behaviour is being captured by the SMS for diagonal faces/edges, these results seem to demonstrate significantly lower accuracy when compared to COMSOL with the current modelling setup.

Case 22 - Floor fixed block with diagonal edge with facial force applied to diagonal edge (figure B.22).

This case was chosen to examine what would happen when the force on a structure was applied only to the diagonal face being approximated by cubic volumes. For this case, the South and Low faces of the structure were fixed and

a facial force negative in y and z was applied to the diagonal face at the edge, representing a case where a cube with a diagonal face added at one edge is fixed at two faces and compressed by force exerted onto this edge. The data comparisons indicate that this case does still match the general behaviour observed in COMSOL, however the SMS data is all outside of the 10% interval for the majority of the data for all displacements. While this result does demonstrate that the fundamental behaviour is being captured by the SMS for diagonal faces/edges, these results seem to demonstrate significantly lower accuracy when compared to COMSOL with the current modelling setup.

Case 23 - Floor & wall fixed block with triangular corner under negative body force in z (figure B.23).

This case was chosen to demonstrate what happens with a more complex diagonal edge. For this case, the West, South and Low faces of the structure were fixed and a body force negative in the z direction was applied to the structure, representing a case where a cube presenting a triangular face at one corner is fixed at three faces and uniformly compressed. The data comparisons indicate that this case does still match the general behaviour observed in COMSOL, in fact seeming to match the COMSOL values better than the prior two diagonal test cases (possibly as the diagonal face comprises less of the surface area in this case). The values are still within a 10% interval for u and w but the v profile offers a less accurate match.

Case 24 - Floor fixed block with curved edge under negative body force in z (figure B.24).

This case was chosen to demonstrate that the SMS can simulate the behaviour of structures with rounded edges being subjected to body forces, as due to the

nature of the SMS any parts which are not perfectly aligned with the axis will be approximated by cubic volumes, making curved edges and surfaces a potential cause of inaccuracy. For this case, the South and Low faces of the structure were fixed and a body force negative in the z direction was applied to the structure, representing a case where a cube with a curved face added at one edge is fixed at two faces and uniformly compressed. The data comparisons indicate that this case does still match the general behaviour observed in COMSOL, however the SMS data is outside of the 10% interval for the u and v displacements.

Case 25 - Floor fixed block with concave round corner under negative body force in z (figure B.25).

This case was chosen to demonstrate that the SMS can simulate the behaviour of structures with a concave rounded face. For this case, the west, south and low faces of the structure were fixed and a body force negative in the z direction was applied to the structure, representing a case where a cube presenting a concave round face at one corner is fixed at three faces and uniformly compressed. The data comparisons indicate that this case does still match the general behaviour observed in COMSOL, in fact seeming to match the COMSOL values better than the prior curved test case (possibly as the curved face comprises less of the surface area in this case). The values are still within a 10% interval for u and w but the v profile offers a less accurate match.

Case 26 - Floor fixed hemispherical structure under negative body force in z (figure B.26).

This case was chosen to demonstrate that the SMS is capable of resolving displacements on more complex structures which have curved faces and/or

edges. As indicated in the prior cases, any parts of the structure not in line with the axis will require approximation using cubic volumes, which means for an entirely rounded structure like this the entire surface is being approximated in this manner. The solution of an extreme case such as this should indicate if the approach being used to approximate the structure is appropriate for more complex geometries. For this case a hemispherical structure was fixed at the flat face and subjected to a negative body force in the z direction, representing a case where a half sphere is subjected to uniform compression. The data comparisons indicate another good match with COMSOL for the general behaviour of the structure, with the values for u and v matching very closely. However, while still within the 10% interval, the w displacement is clearly under predicted.

Case 27 - Floor fixed block structure under uniform temperature increase causing thermoelastic expansion (figure B.27).

This case was chosen to demonstrate that the SMS can simulate linear elastic structural undergoing thermal expansion under a uniform temperature increase. Exploring thermal expansion requires some additional material properties and elements of problem setup to be defined. The coefficient of thermal expansion $\alpha = 32.1 \mu\text{m}/\text{K}$ was used for the material, arbitrarily taking the value for Indium. The reference temperature for this structure was taken to be 300 K, with this case modelling a situation where the temperature was uniformly raised to 400 K. The data comparisons indicate a close match in accuracy between the SMS and COMSOL for this scenario.

Case 28 - Floor fixed block structure under increasing temperature gradient causing thermoelastic expansion (figure B.28).

This case was chosen to demonstrate that the SMS can simulate linear elastic structural undergoing thermal expansion under an increasing temperature

gradient. The same material properties and reference temperature were used as in case 27, with a temperature gradient uniformly rising from 300 K at the low face of the domain to 400 K at the high face. The data comparisons indicate another good match with COMSOL for the general behaviour of the structure, with the values for u and v matching quite closely, with some slight deviation at the tips, though still within the 10% interval, the w displacement matches less well, with sections outside of the interval. This may be due to a minor mismatch in representing the thermal gradient between the COMSOL and the SMS.

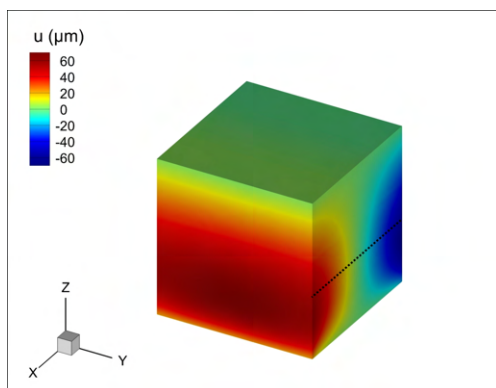
Case 29 - Floor fixed block structure under decreasing temperature gradient causing thermoelastic contraction (figure B.29).

This case was chosen to demonstrate that the SMS can simulate linear elastic structural undergoing thermal contraction under an decreasing temperature gradient. The same material properties and reference temperature were used as in case 27, with a temperature gradient uniformly rising from 200 K at the low face of the domain to 300 K at the high face. The data comparisons indicate a close match in accuracy between the SMS and COMSOL for this scenario.

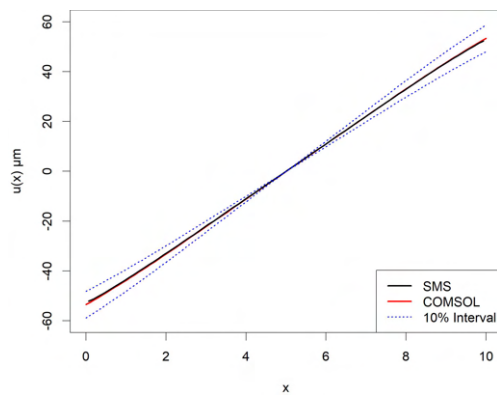
Case 30 - Floor fixed block structure under temperature gradient causing thermoelastic expansion & contraction (figure B.30).

This case was chosen to demonstrate that the SMS can simulate linear elastic structural undergoing thermal expansion and contraction at the same time due to a temperature gradient which crosses the reference temperature. The same material properties and reference temperature were used as in case 27, with a temperature gradient uniformly rising from 250 K at the south face of the domain to 350 K at the north face. The data comparisons indicate another good match with COMSOL for the general behaviour of the structure, however the values obtained can approach and occasionally cross the 10% intervals plotted. This accuracy loss may be exacerbated due to a minor mismatch

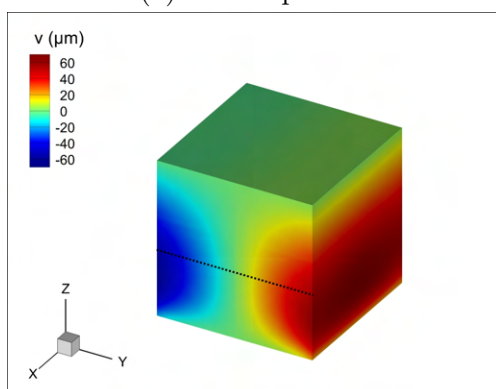
between the thermal gradient used in COMSOL and the SMS.



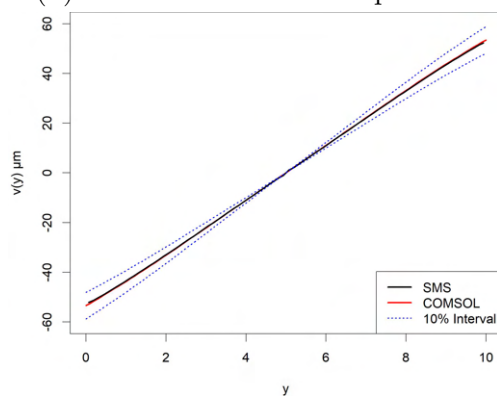
(a) SMS u profile.



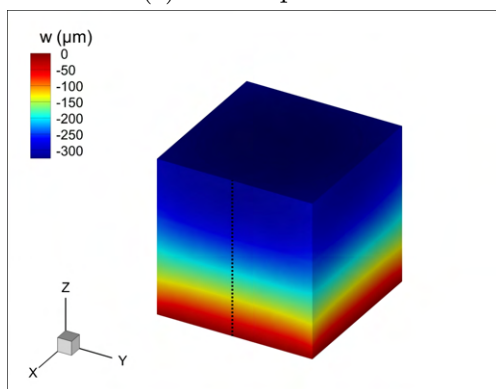
(b) u value COMSOL comparison.



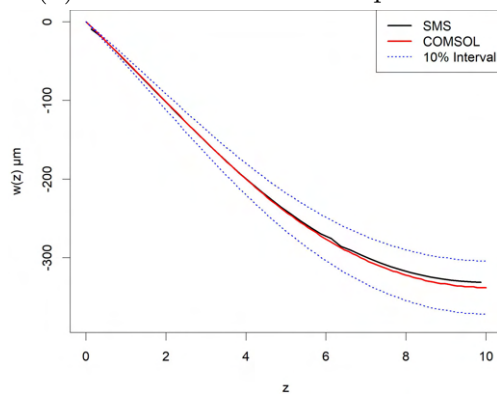
(c) SMS v profile.



(d) v value COMSOL comparison.

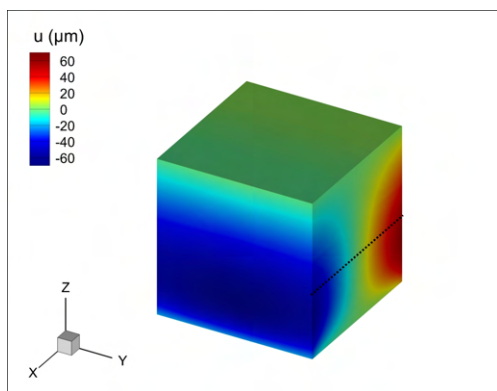


(e) SMS w profile.

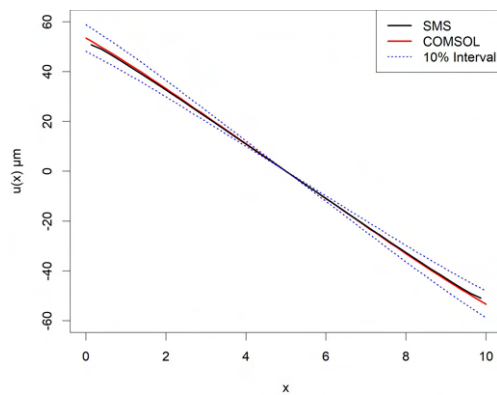


(f) w value COMSOL comparison.

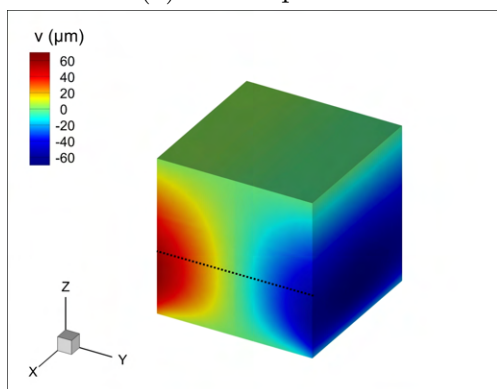
Figure B.1: Case 1 - Floor fixed block under negative body force in z .



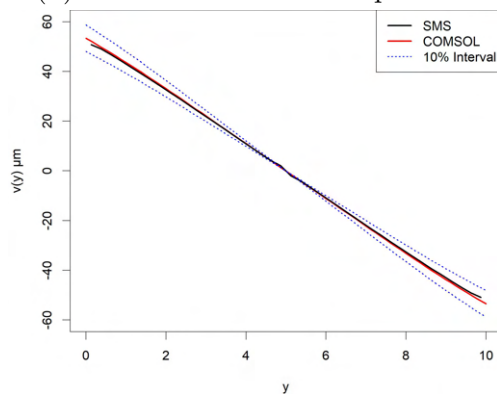
(a) SMS u profile.



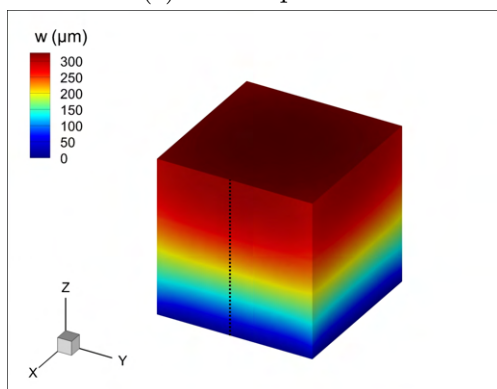
(b) u value COMSOL comparison.



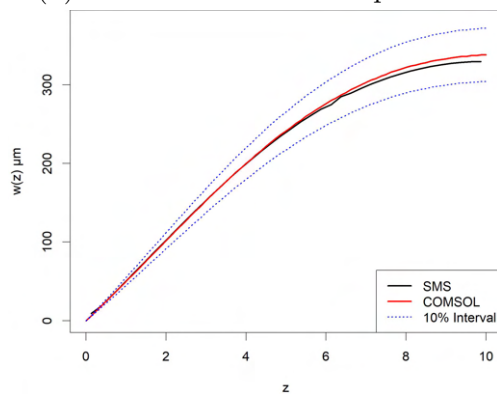
(c) SMS v profile.



(d) v value COMSOL comparison.

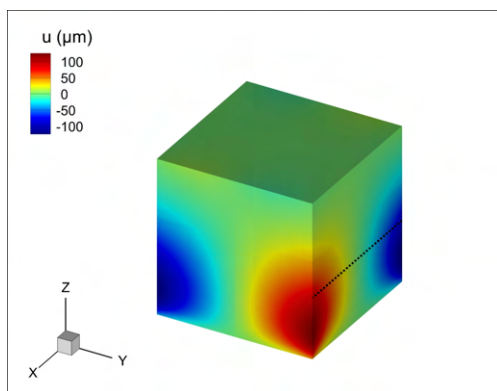


(e) SMS w profile.

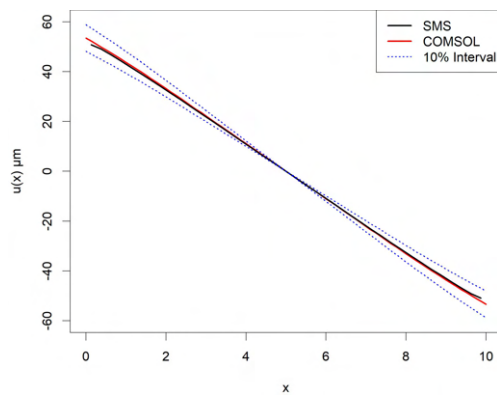


(f) w value COMSOL comparison.

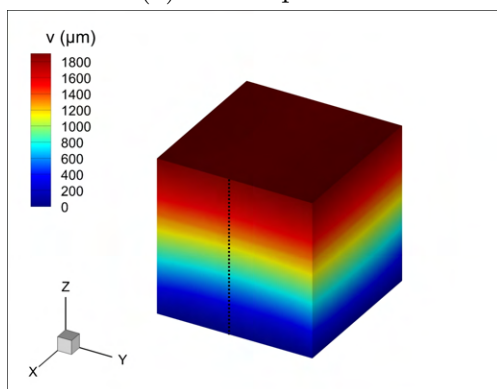
Figure B.2: Case 2 - Floor fixed block under positive body force in z .



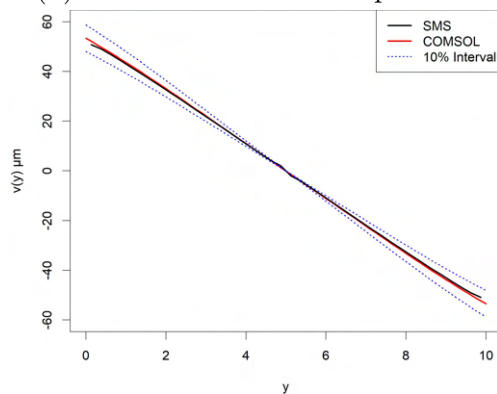
(a) SMS u profile.



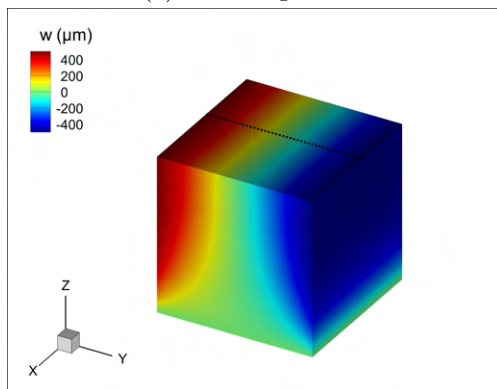
(b) u value COMSOL comparison.



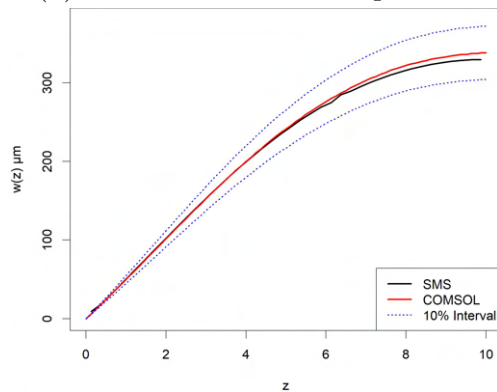
(c) SMS v profile.



(d) v value COMSOL comparison.

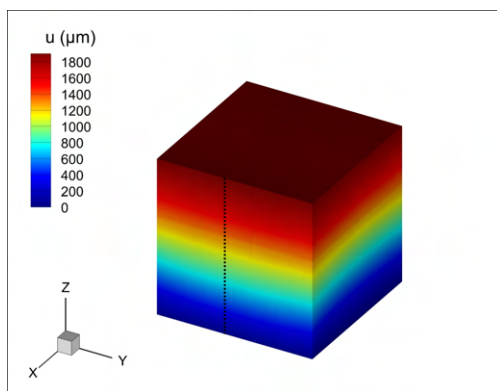


(e) SMS w profile.

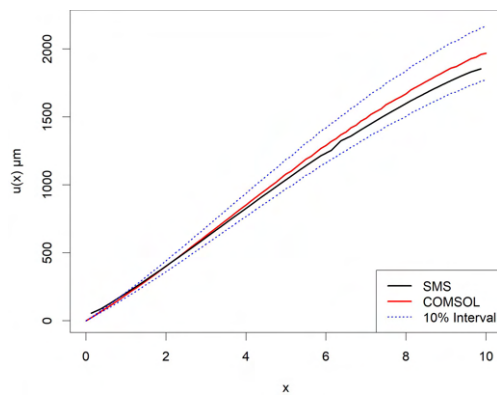


(f) w value COMSOL comparison.

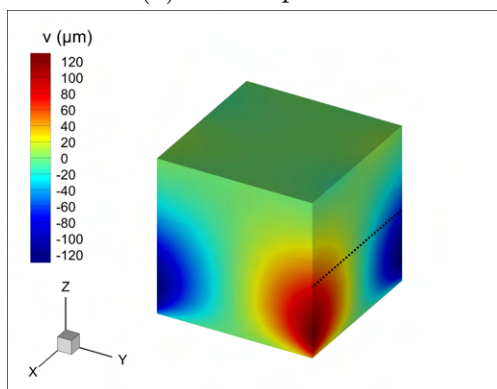
Figure B.3: Case 3 - Floor fixed block under positive body force in y .



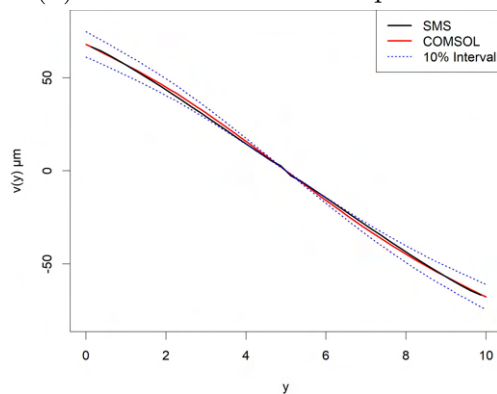
(a) SMS u profile.



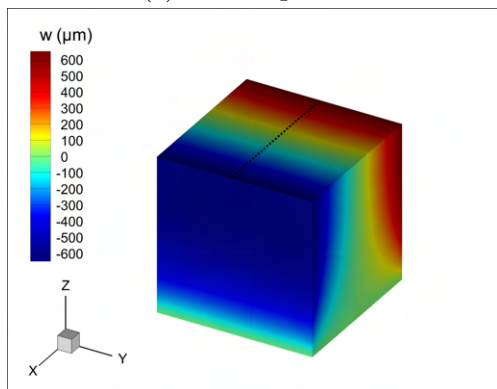
(b) u value COMSOL comparison.



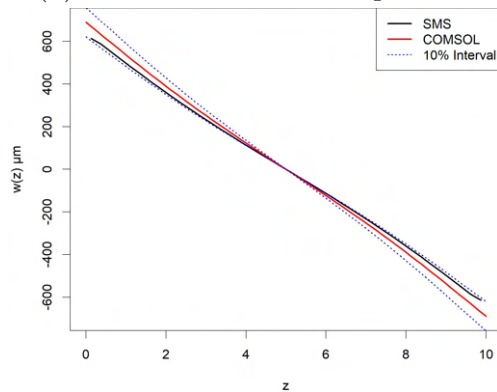
(c) SMS v profile.



(d) v value COMSOL comparison.

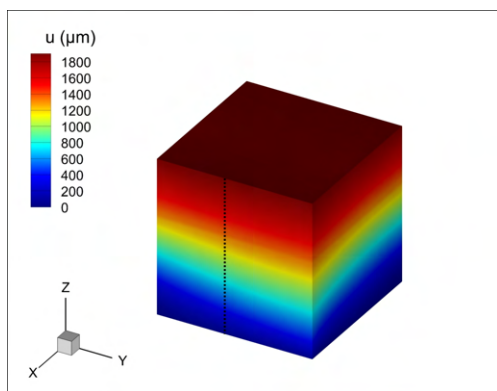


(e) SMS w profile.

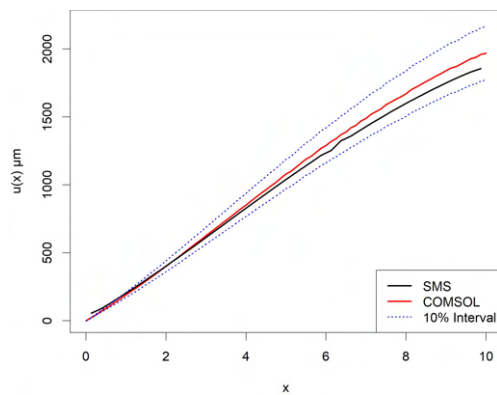


(f) w value COMSOL comparison.

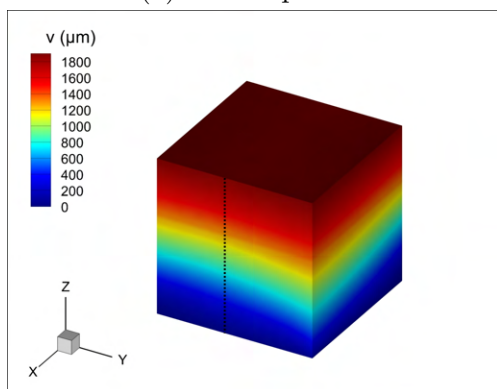
Figure B.4: Case 4 - Floor fixed block under positive body force in x .



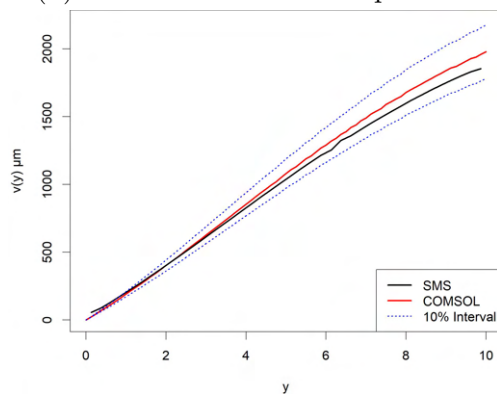
(a) SMS u profile.



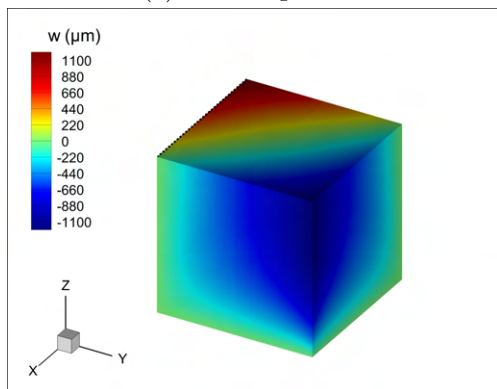
(b) u value COMSOL comparison.



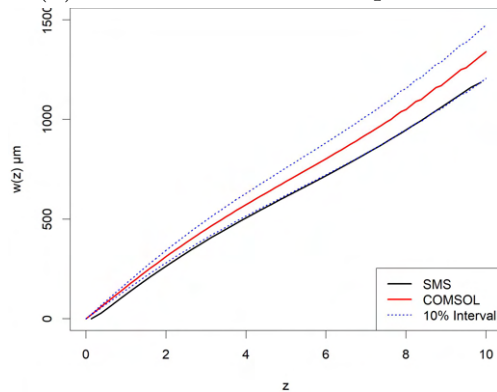
(c) SMS v profile.



(d) v value COMSOL comparison.

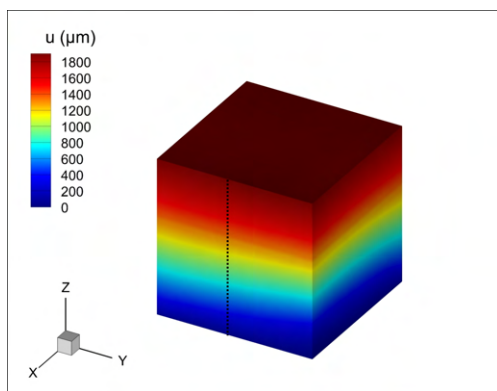


(e) SMS w profile.

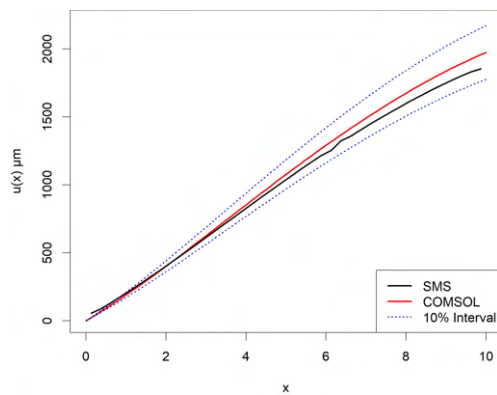


(f) w value COMSOL comparison.

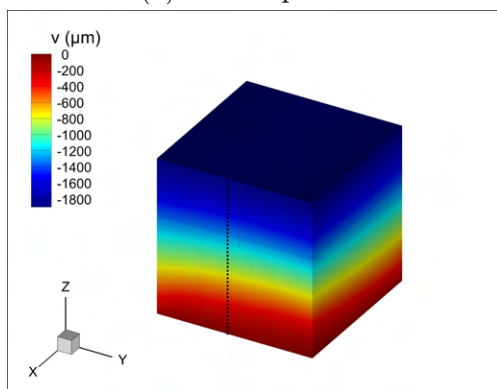
Figure B.5: Case 5 - Floor fixed block under positive body force in x and y .



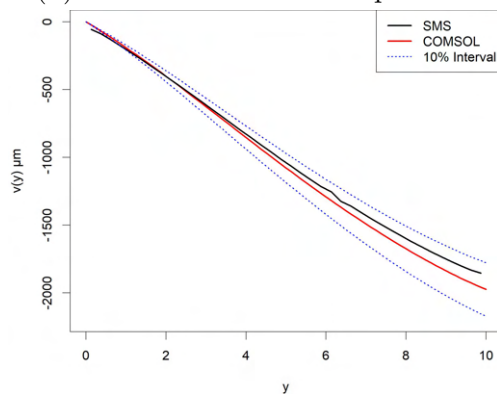
(a) SMS u profile.



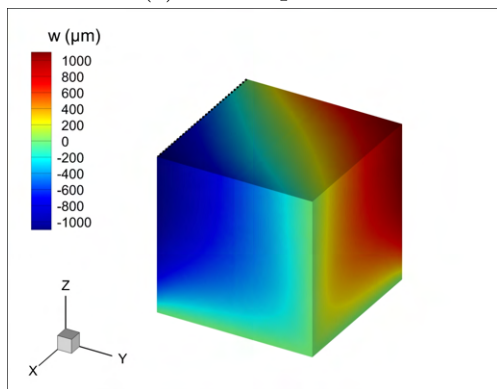
(b) u value COMSOL comparison.



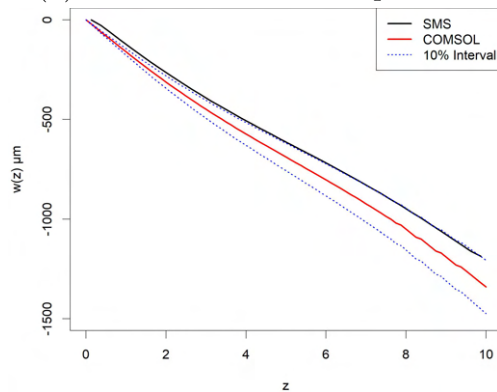
(c) SMS v profile.



(d) v value COMSOL comparison.

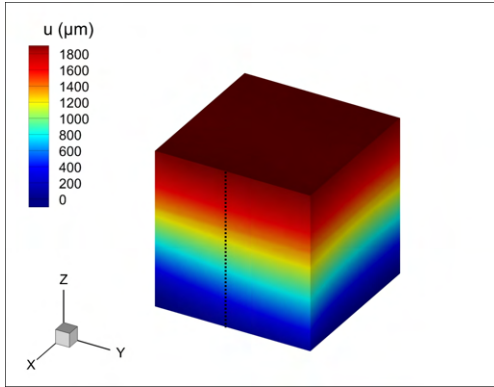


(e) SMS w profile.

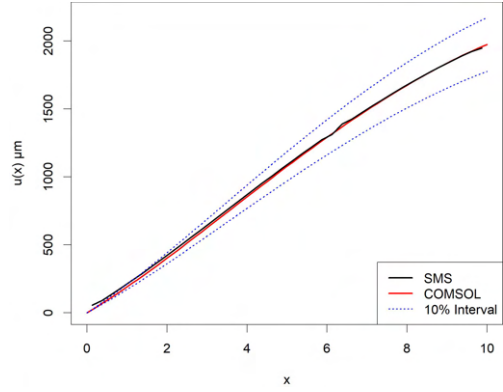


(f) w value COMSOL comparison.

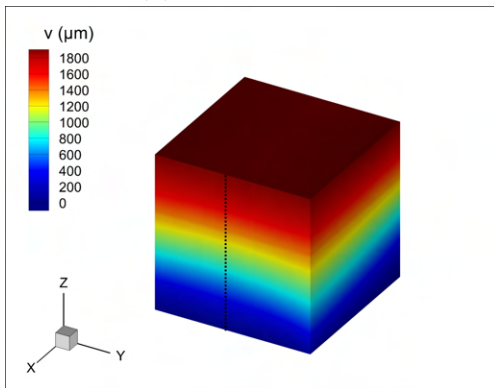
Figure B.6: Case 6 - Floor fixed block under positive body force in x and negative force in y .



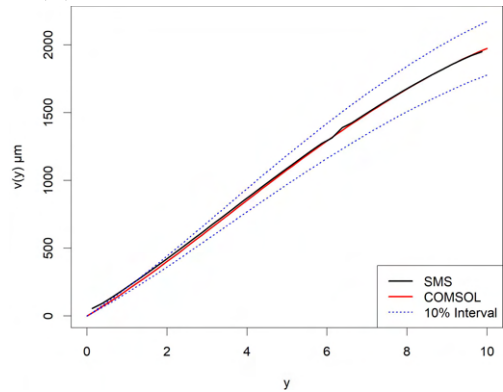
(a) SMS u profile.



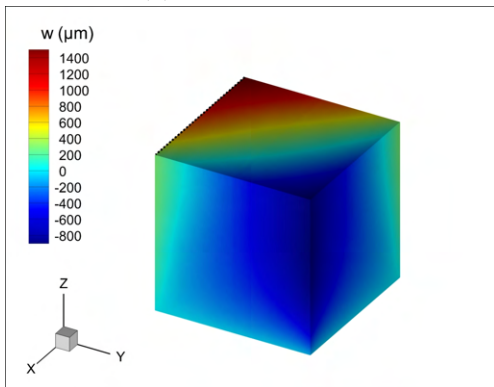
(b) u value COMSOL comparison.



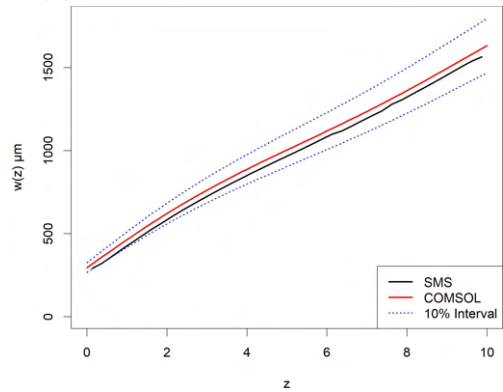
(c) SMS v profile.



(d) v value COMSOL comparison.

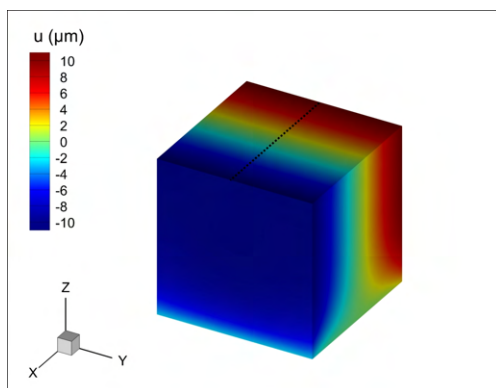


(e) SMS w profile.

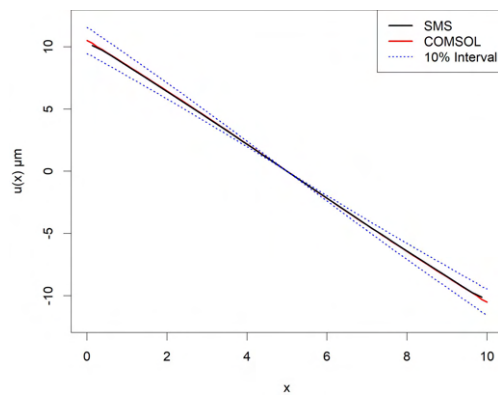


(f) w value COMSOL comparison.

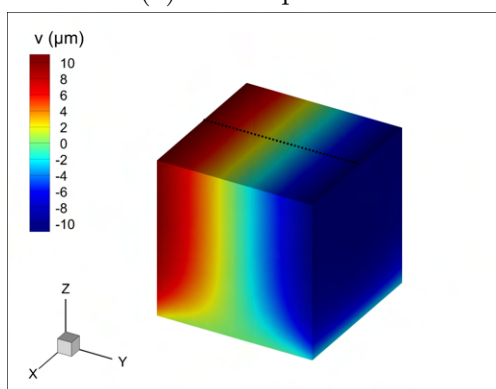
Figure B.7: Case 7 - Floor fixed block under positive body force in x , y and z .



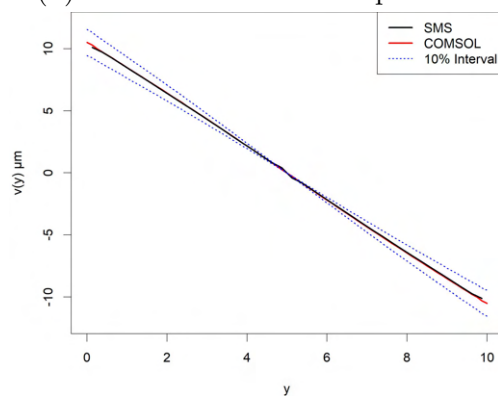
(a) SMS u profile.



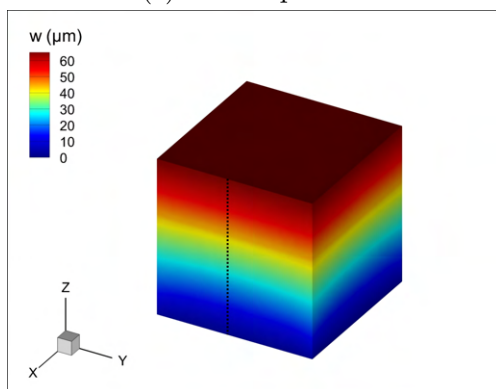
(b) u value COMSOL comparison.



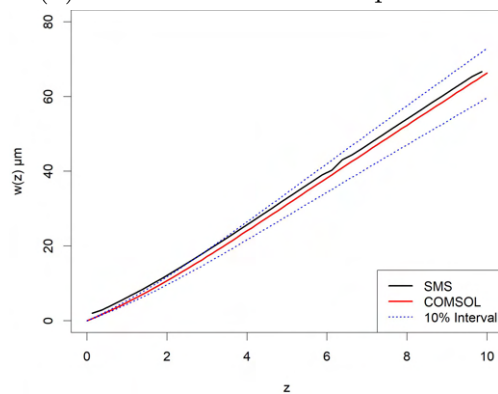
(c) SMS v profile.



(d) v value COMSOL comparison.

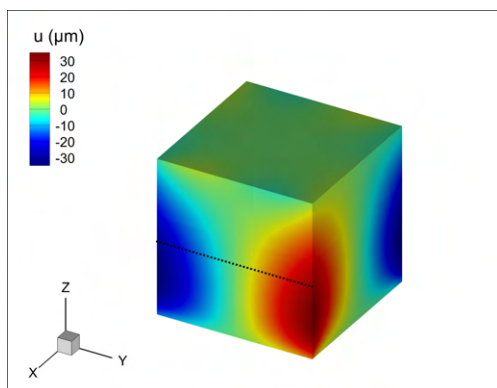


(e) SMS w profile.

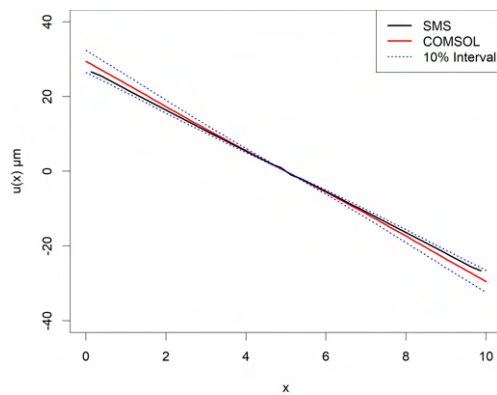


(f) w value COMSOL comparison.

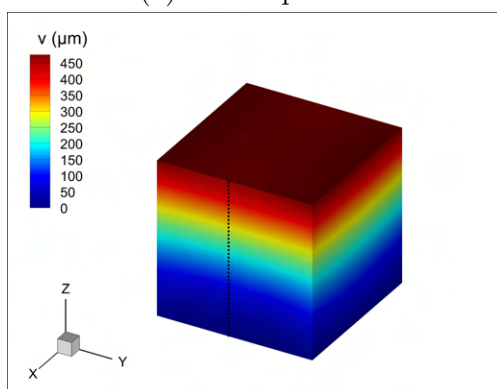
Figure B.8: Case 8 - Floor fixed block under positive facial force in z on high face.



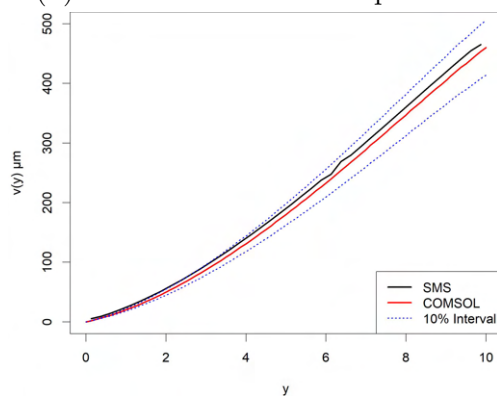
(a) SMS u profile.



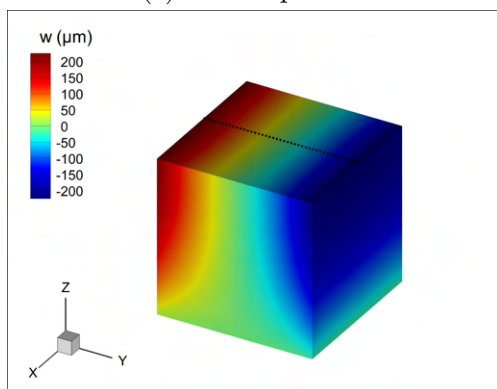
(b) u value COMSOL comparison.



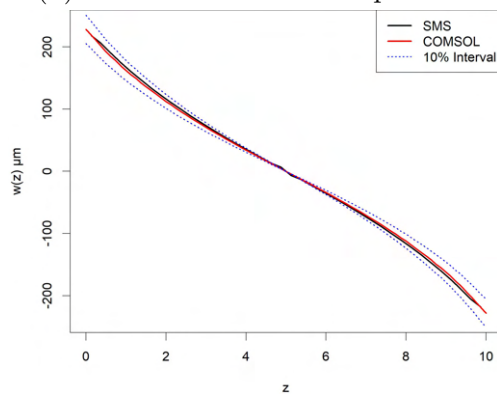
(c) SMS v profile.



(d) v value COMSOL comparison.

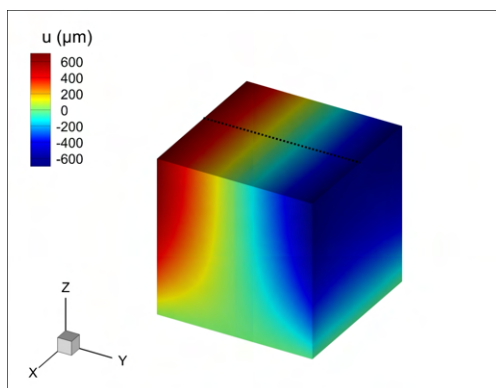


(e) SMS w profile.

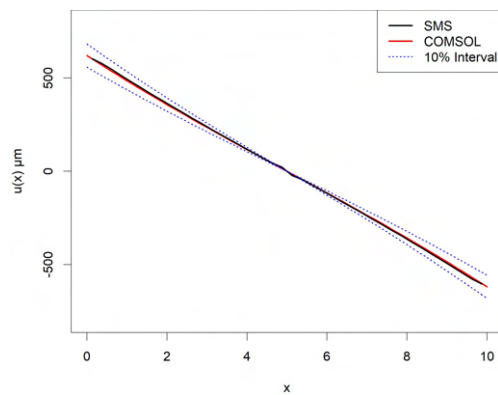


(f) w value COMSOL comparison.

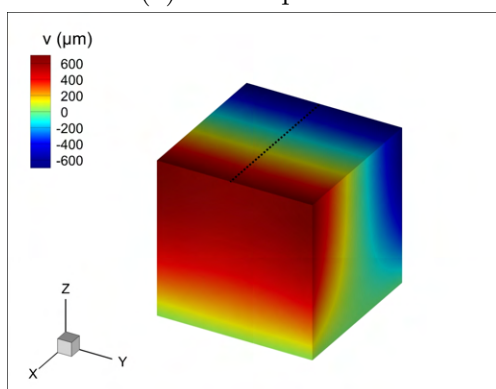
Figure B.9: Case 9 - Floor fixed block under positive facial force in y on high face.



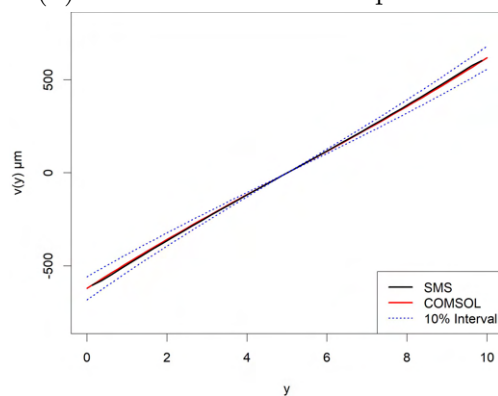
(a) SMS u profile.



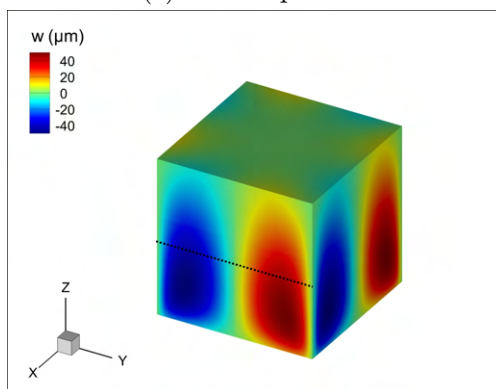
(b) u value COMSOL comparison.



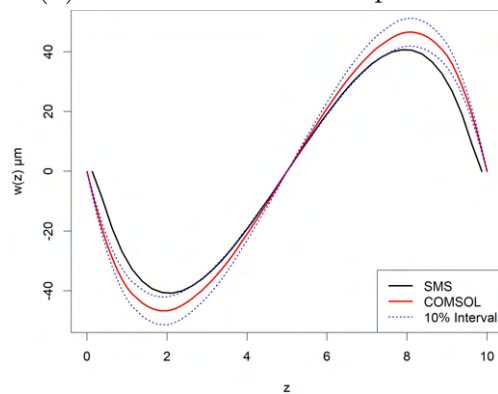
(c) SMS v profile.



(d) v value COMSOL comparison.

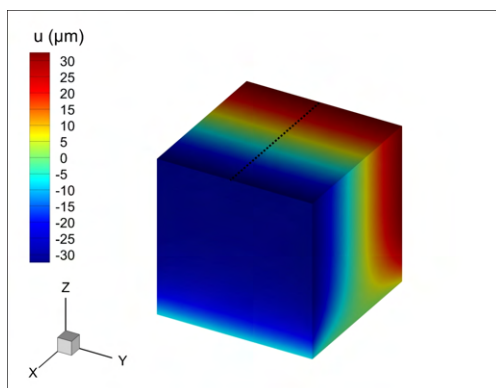


(e) SMS w profile.

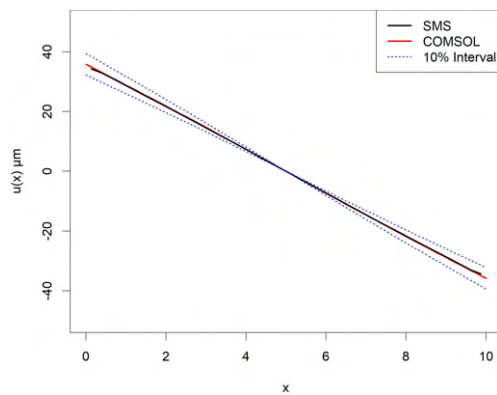


(f) w value COMSOL comparison.

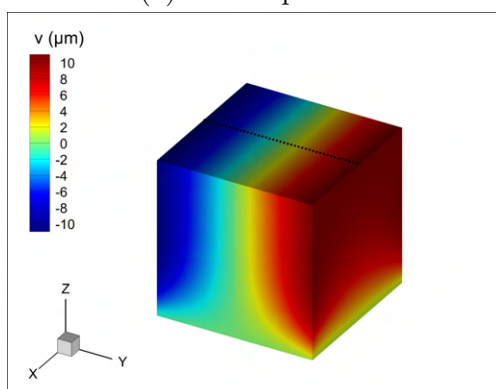
Figure B.10: Block Validation 10 – Floor block under rotational facial forces.



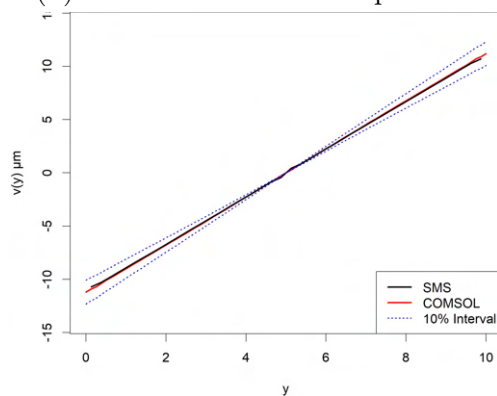
(a) SMS u profile.



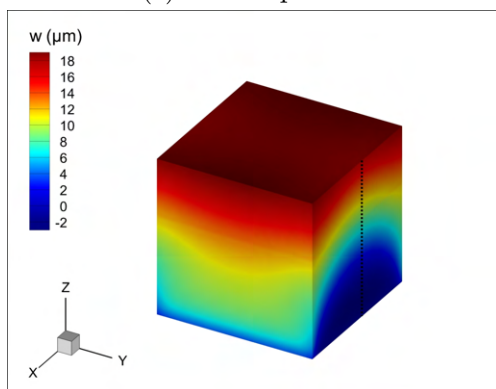
(b) u value COMSOL comparison.



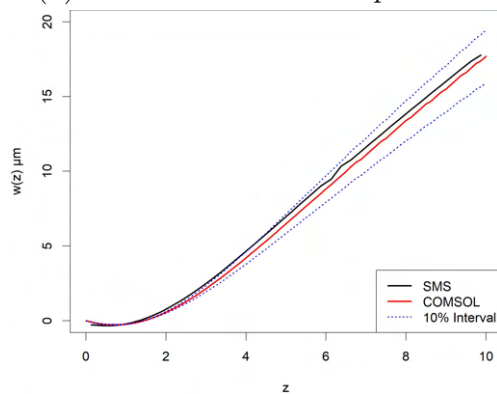
(c) SMS v profile.



(d) v value COMSOL comparison.

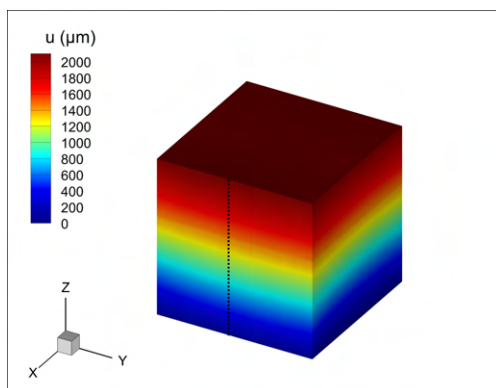


(e) SMS w profile.

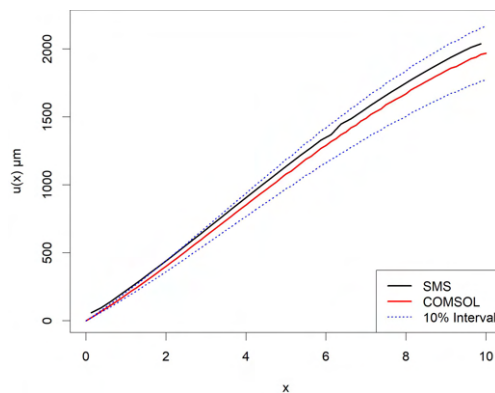


(f) w value COMSOL comparison.

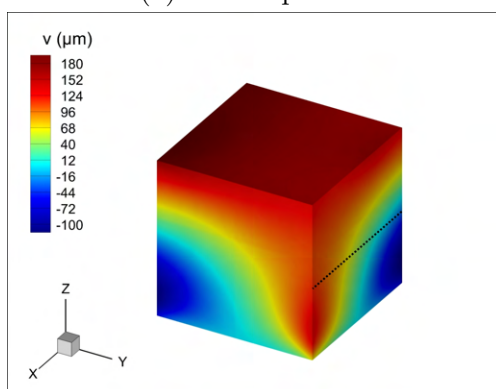
Figure B.11: Case 11 - Floor fixed block under opposing facial forces.



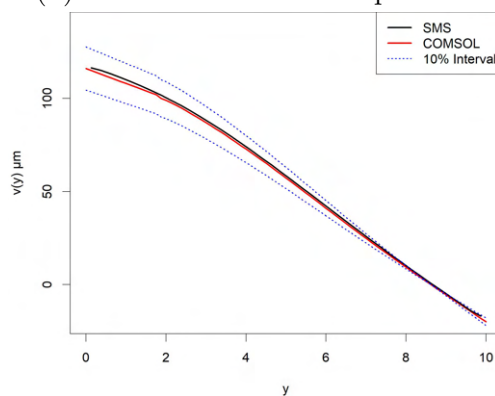
(a) SMS u profile.



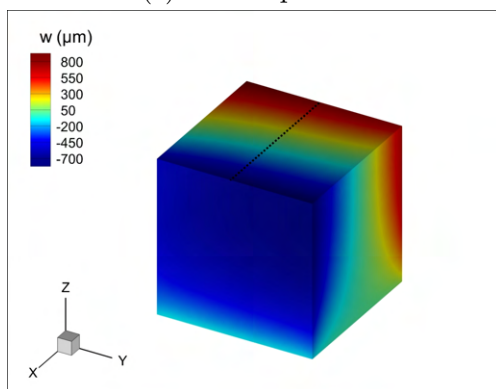
(b) u value COMSOL comparison.



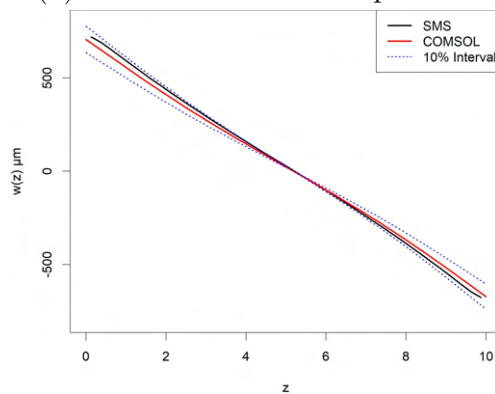
(c) SMS v profile.



(d) v value COMSOL comparison.

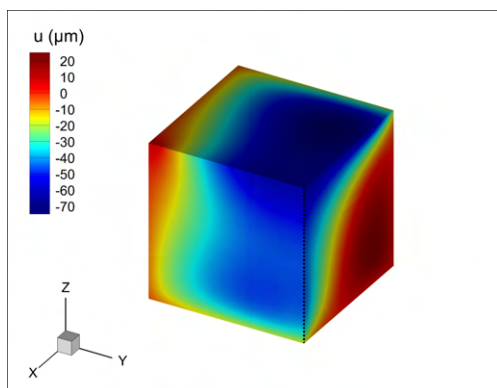


(e) SMS w profile.

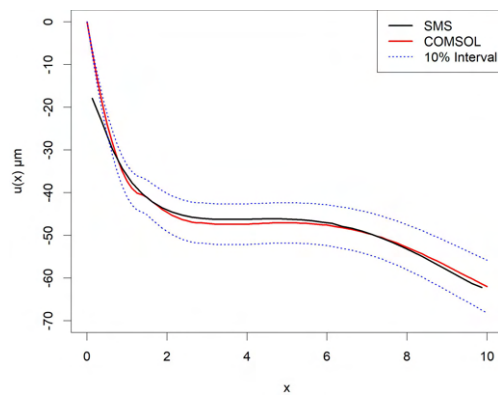


(f) w value COMSOL comparison.

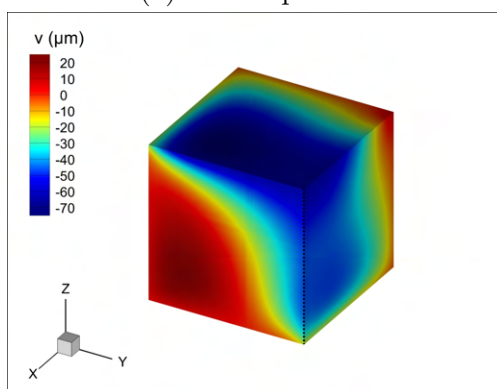
Figure B.12: Case 12 - Floor fixed block under positive body force in x and a facial force in z on side face.



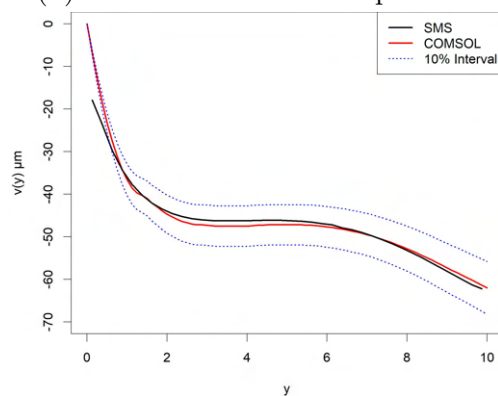
(a) SMS u profile.



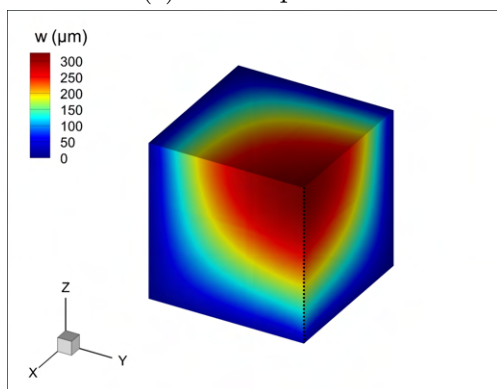
(b) u value COMSOL comparison.



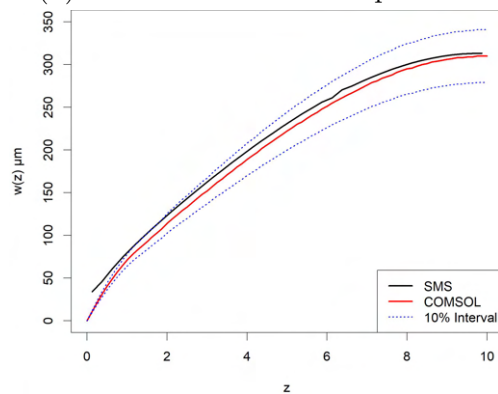
(c) SMS v profile.



(d) v value COMSOL comparison.

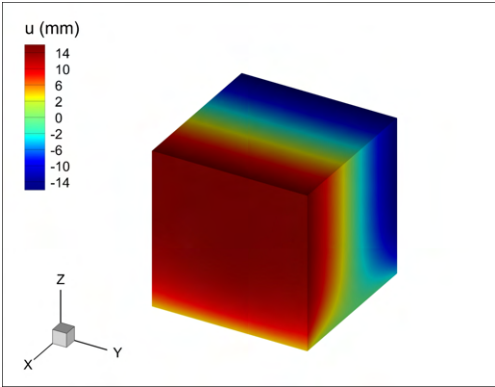


(e) SMS w profile.

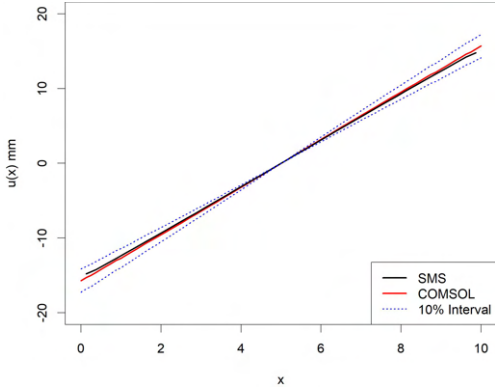


(f) w value COMSOL comparison.

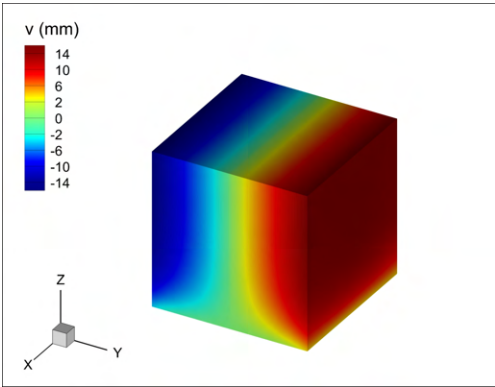
Figure B.13: Case 13 - Floor & wall fixed block under body force in z .



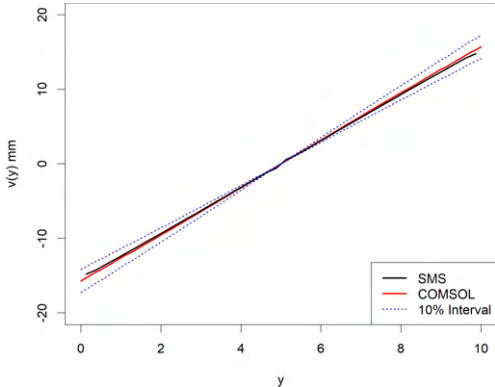
(a) SMS u profile.



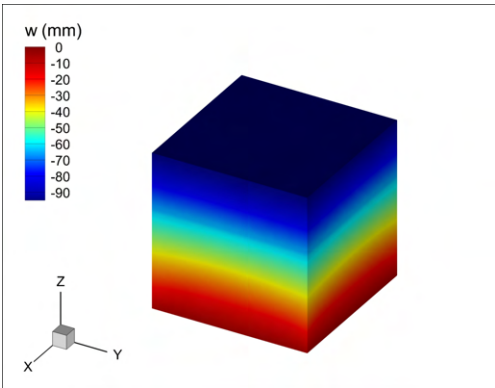
(b) u value COMSOL comparison.



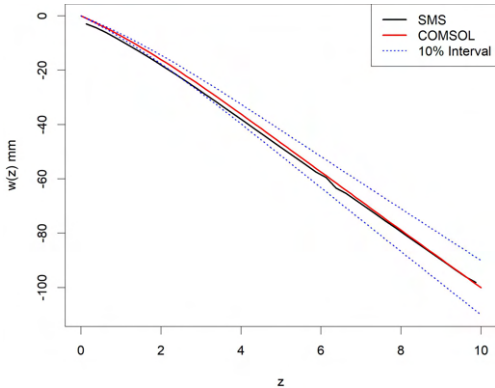
(c) SMS v profile.



(d) v value COMSOL comparison.

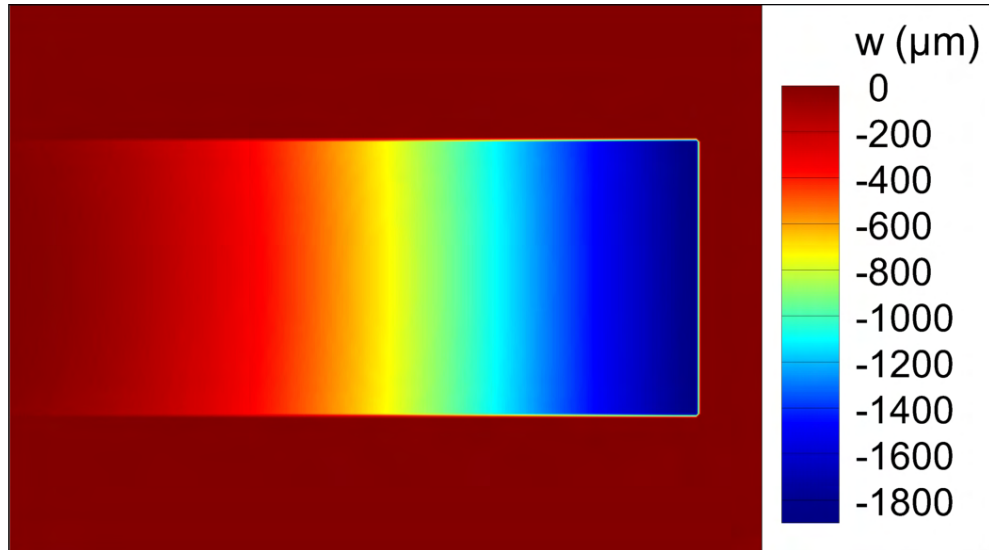


(e) SMS w profile.

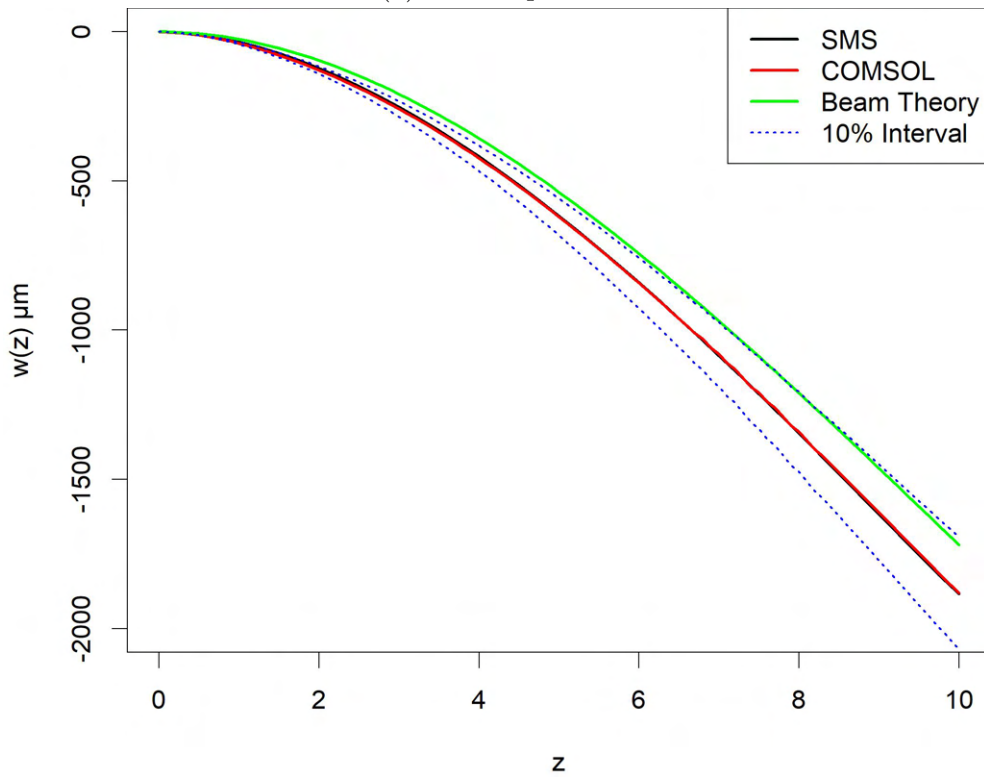


(f) w value COMSOL comparison.

Figure B.14: Case 14 - Floor block with fixed displacement.

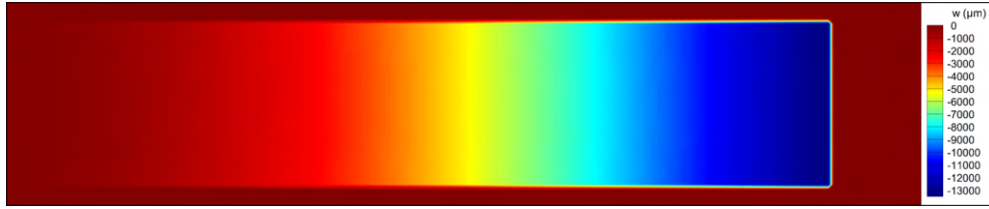


(a) SMS w profile.

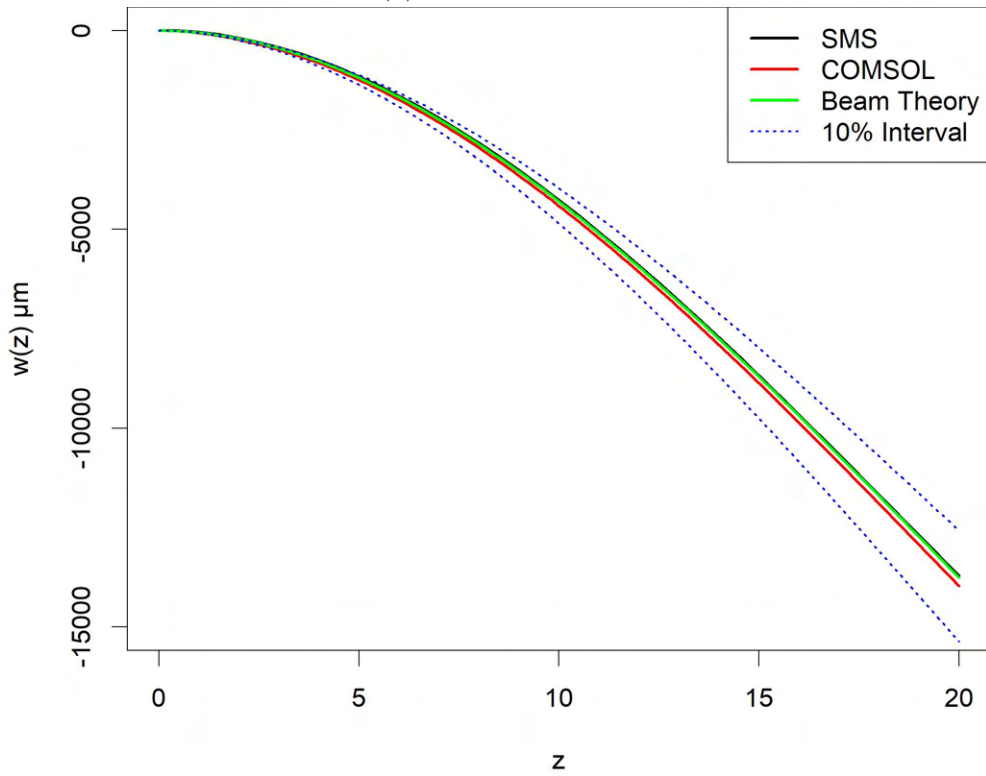


(b) w value COMSOL And Beam Theory comparison.

Figure B.15: Case 15 - $4 \times 4 \times 10$ cantilever beam with point load.

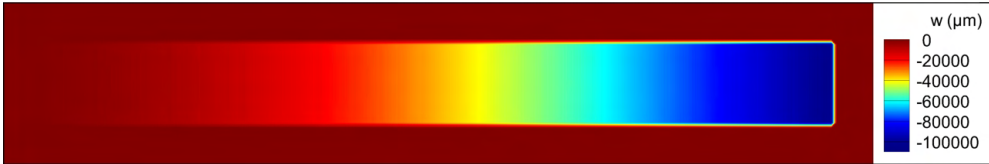


(a) SMS w profile.

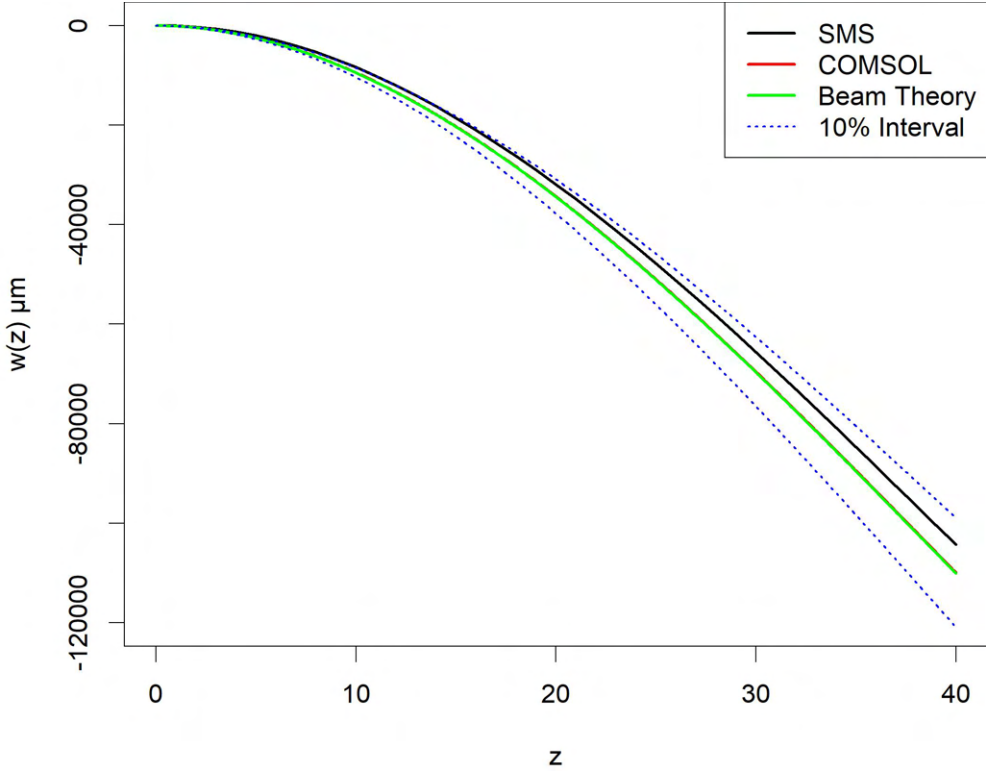


(b) w value COMSOL And Beam Theory comparison.

Figure B.16: Case 16 - $4 \times 4 \times 20$ cantilever beam with point load.

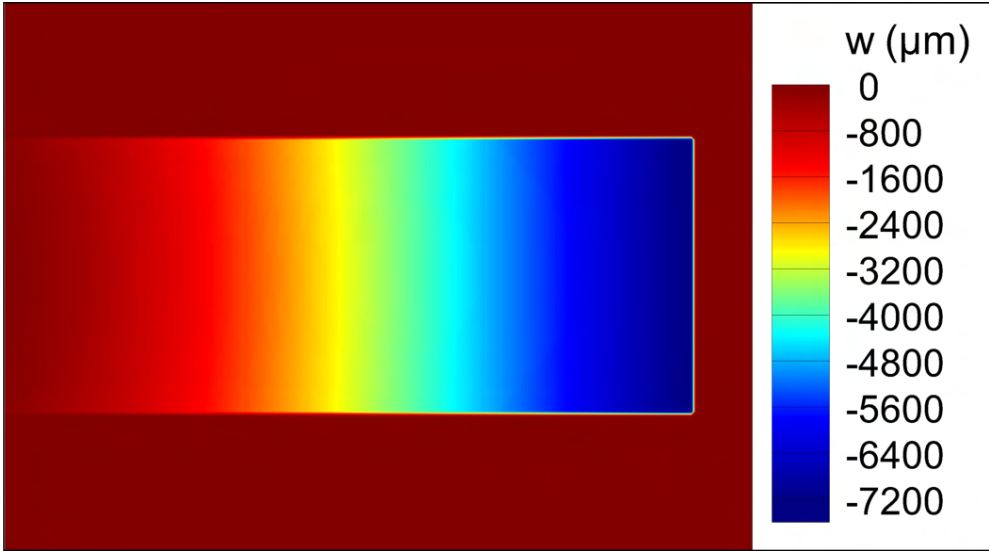


(a) SMS w profile.

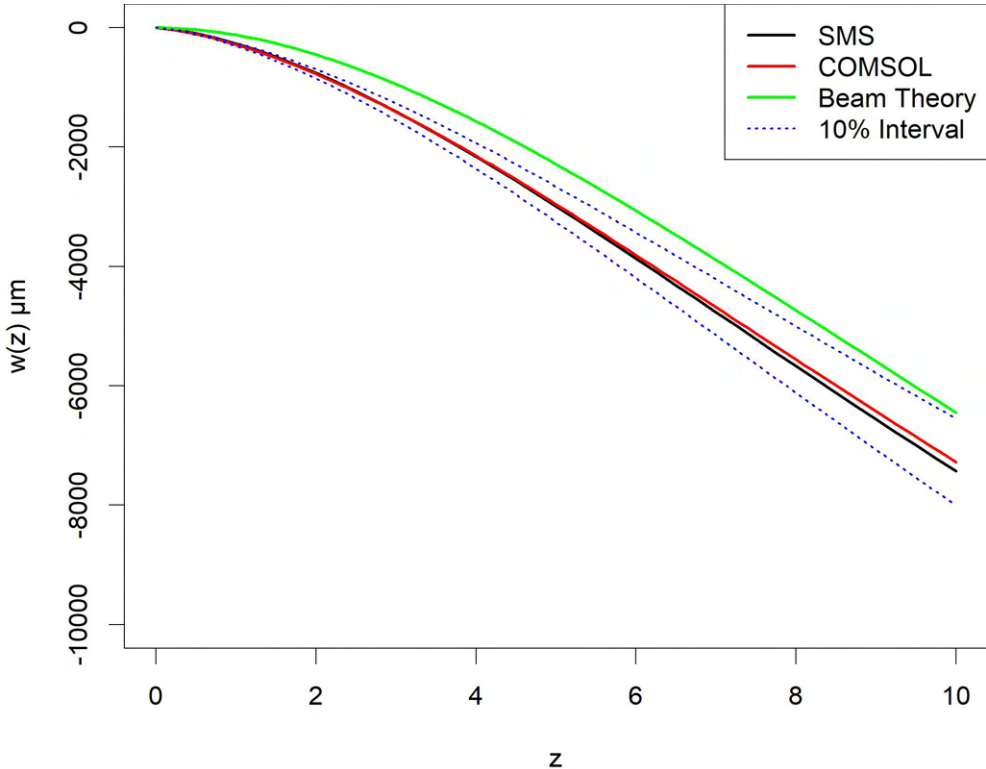


(b) w value COMSOL And Beam Theory comparison.

Figure B.17: Case 17 - $4 \times 4 \times 40$ cantilever beam with point load.

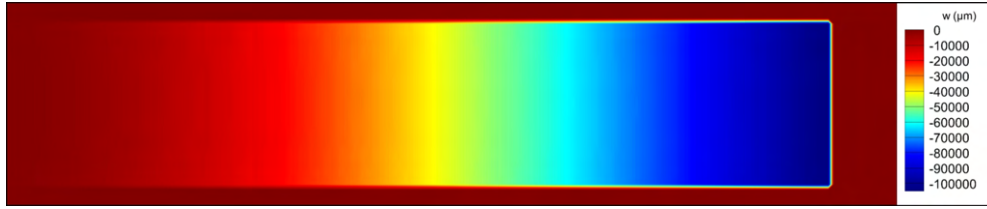


(a) SMS w profile.

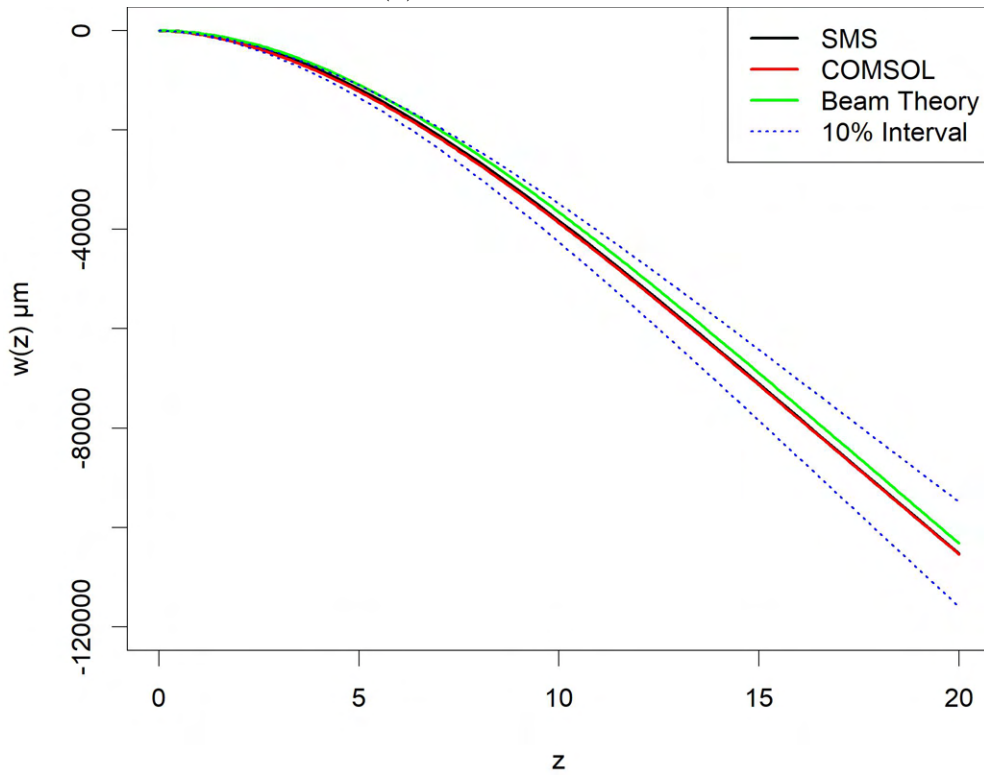


(b) w value COMSOL And Beam Theory comparison.

Figure B.18: Case 18 - $4 \times 4 \times 10$ cantilever beam with distributed load.

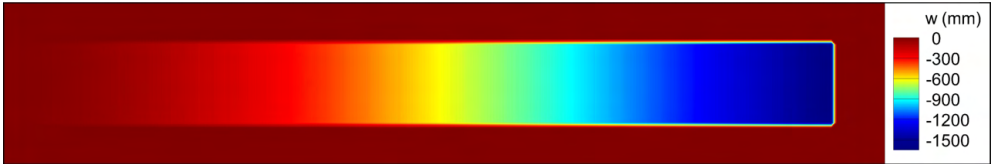


(a) SMS w profile.

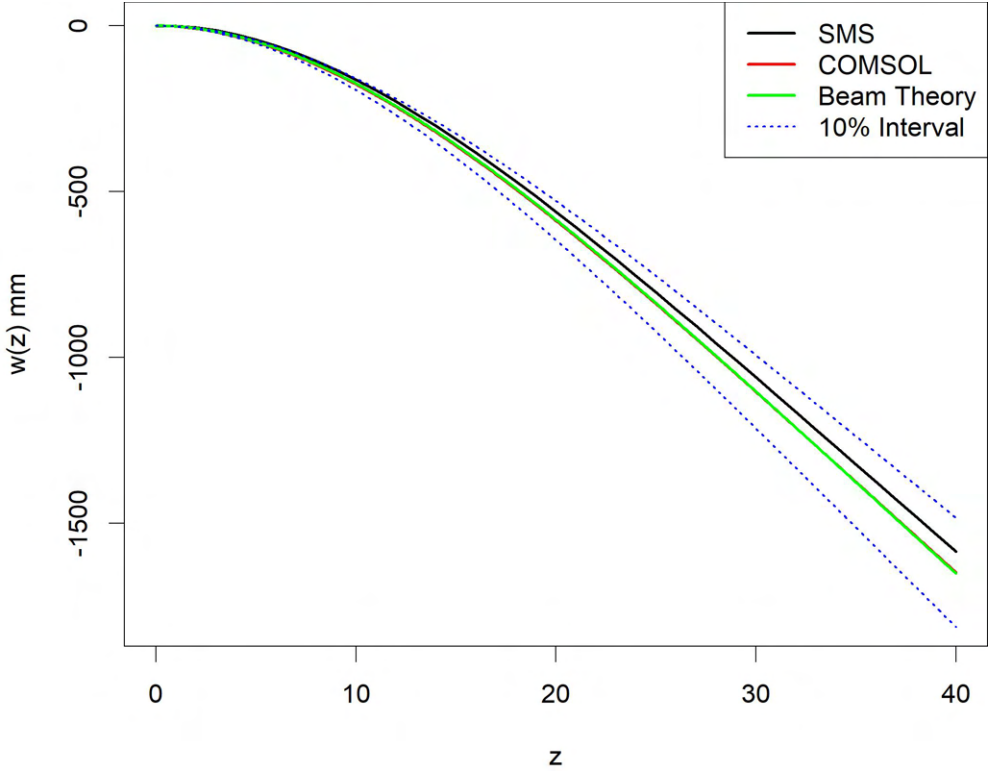


(b) w value COMSOL And Beam Theory comparison.

Figure B.19: Case 19 - $4 \times 4 \times 20$ cantilever beam with distributed load.

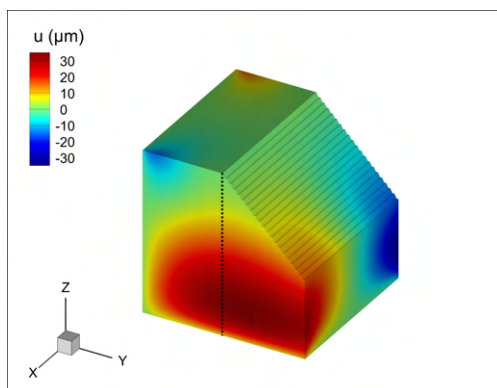


(a) SMS w profile.

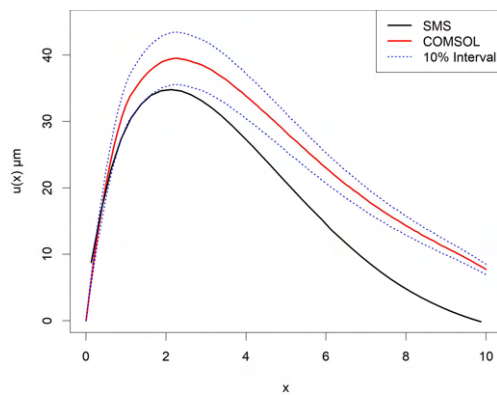


(b) w value COMSOL And Beam Theory comparison.

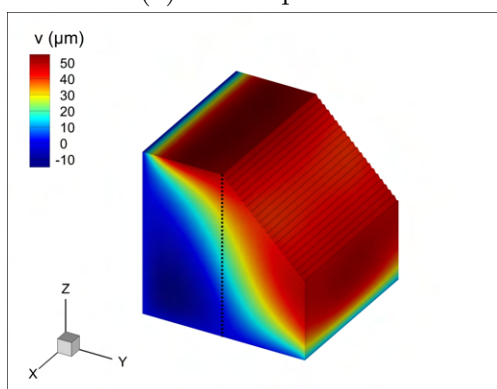
Figure B.20: Case 20 - $4 \times 4 \times 40$ cantilever beam with distributed load.



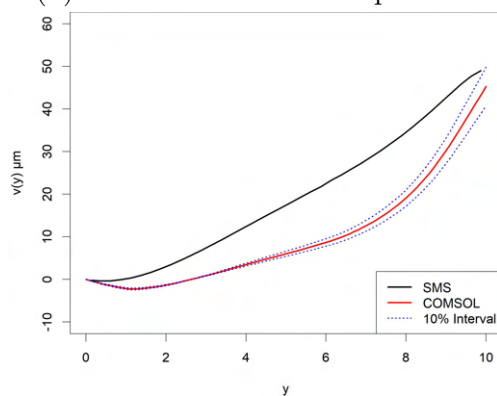
(a) SMS u profile.



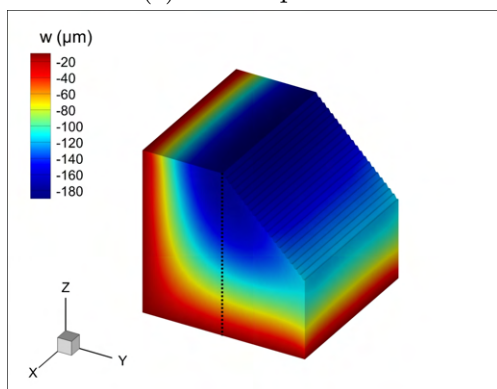
(b) u value COMSOL comparison.



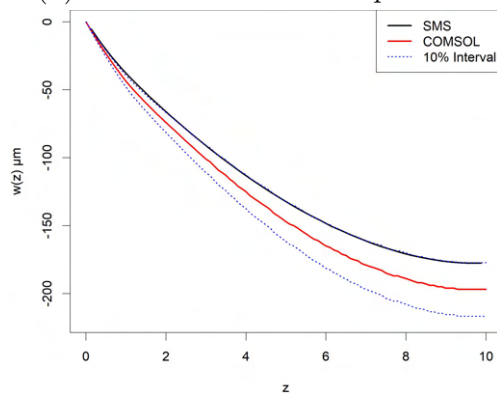
(c) SMS v profile.



(d) v value COMSOL comparison.

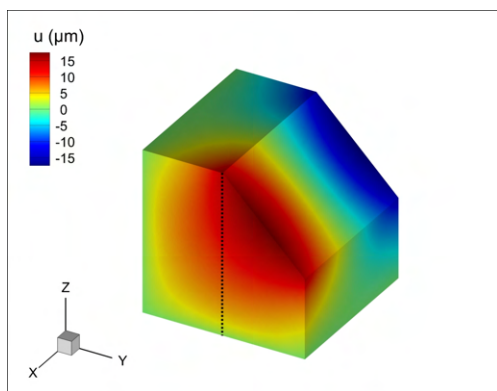


(e) SMS w profile.

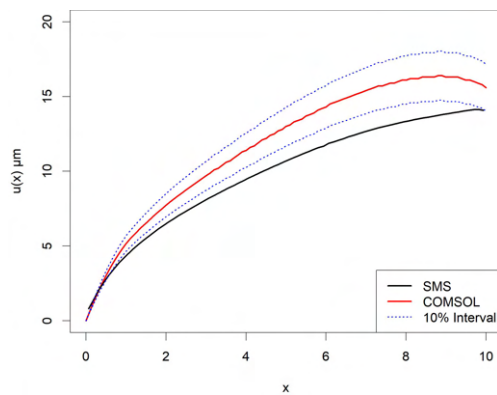


(f) w value COMSOL comparison.

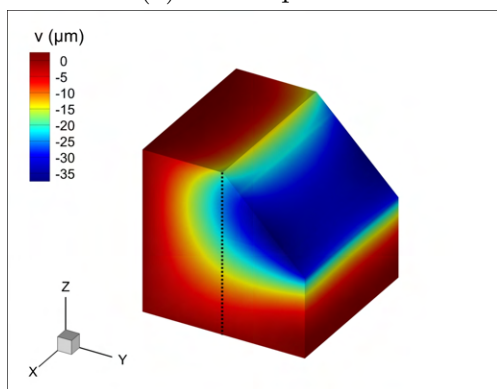
Figure B.21: Case 21 - Floor fixed block with diagonal edge under negative body force in z .



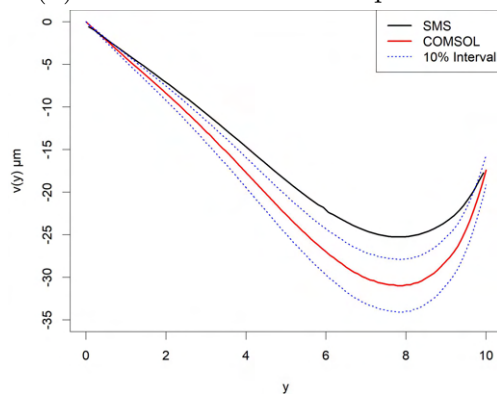
(a) SMS u profile.



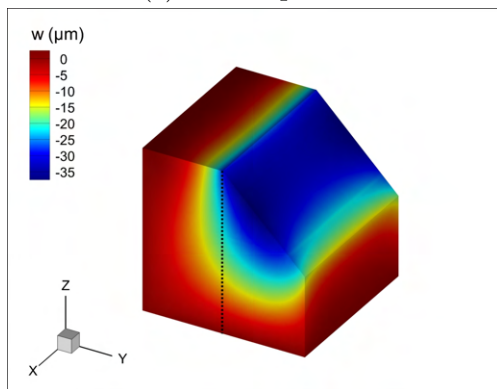
(b) u value COMSOL comparison.



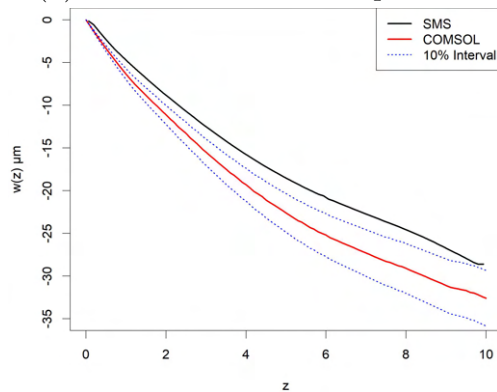
(c) SMS v profile.



(d) v value COMSOL comparison.

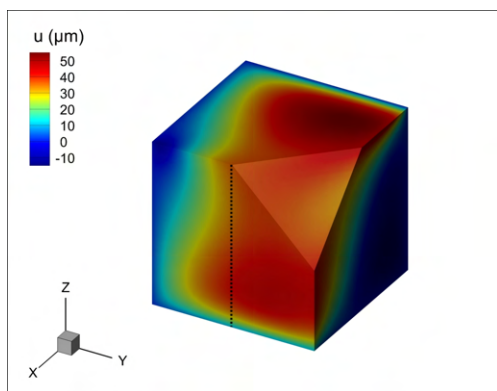


(e) SMS w profile.

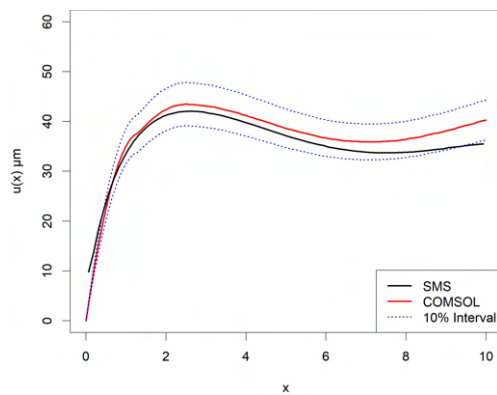


(f) w value COMSOL comparison.

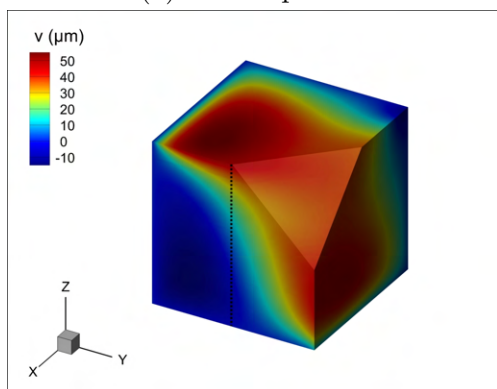
Figure B.22: Case 22 - Floor fixed block with diagonal edge with facial force applied to diagonal edge.



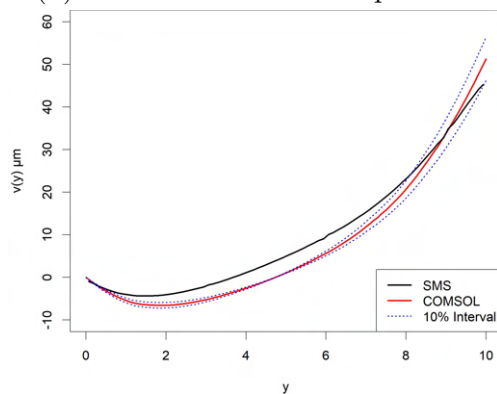
(a) SMS u profile.



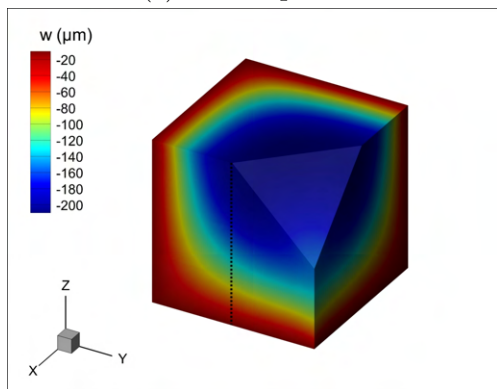
(b) u value COMSOL comparison.



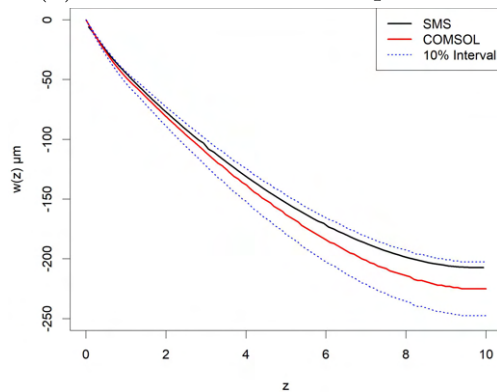
(c) SMS v profile.



(d) v value COMSOL comparison.

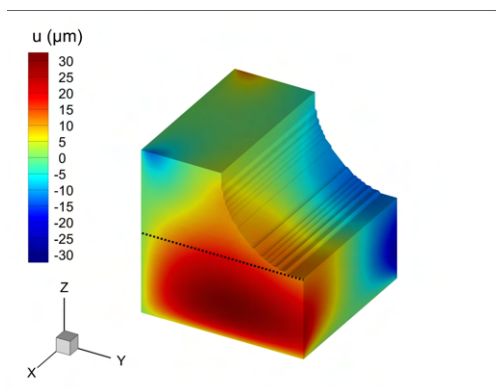


(e) SMS w profile.

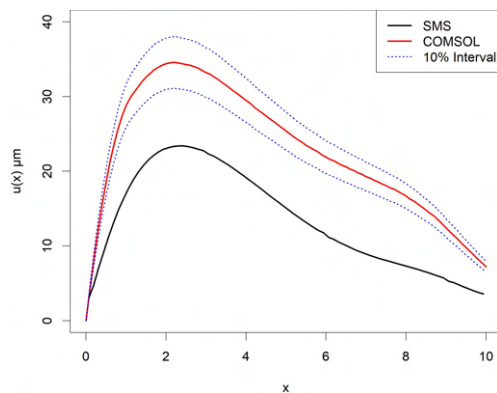


(f) w value COMSOL comparison.

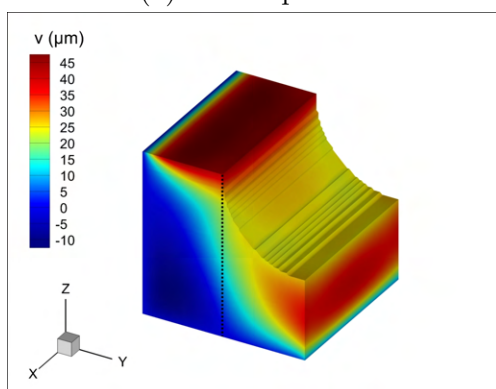
Figure B.23: Case 23 - Floor & wall fixed block with triangular corner under negative body force in z .



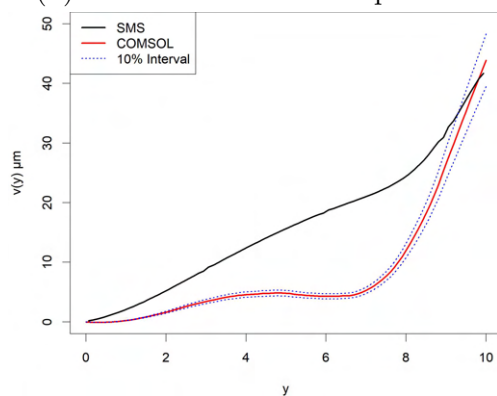
(a) SMS u profile.



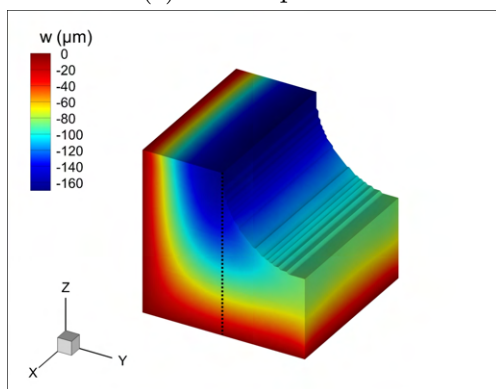
(b) u value COMSOL comparison.



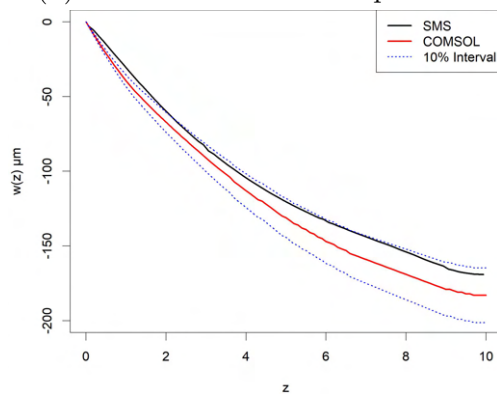
(c) SMS v profile.



(d) v value COMSOL comparison.

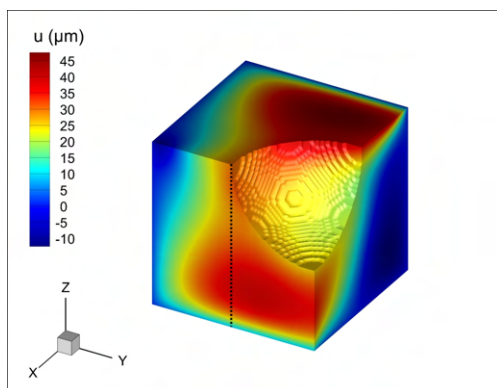


(e) SMS w profile.

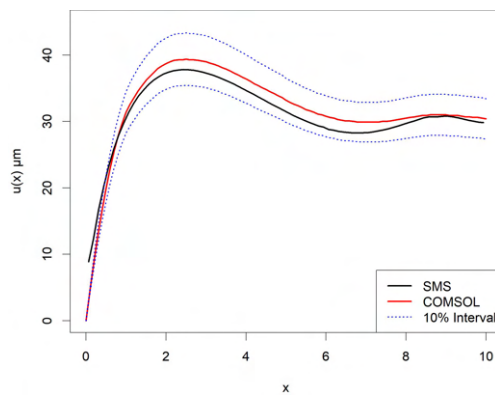


(f) w value COMSOL comparison.

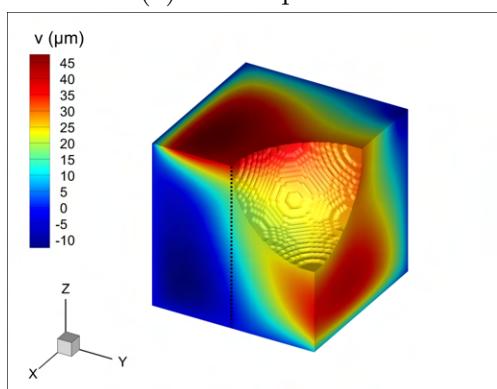
Figure B.24: Case 24 - Floor fixed block with curved edge under negative body force in z .



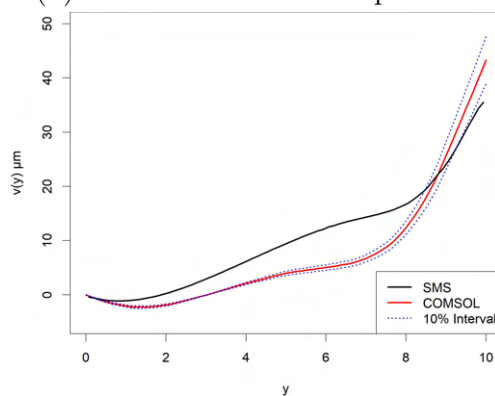
(a) SMS u profile.



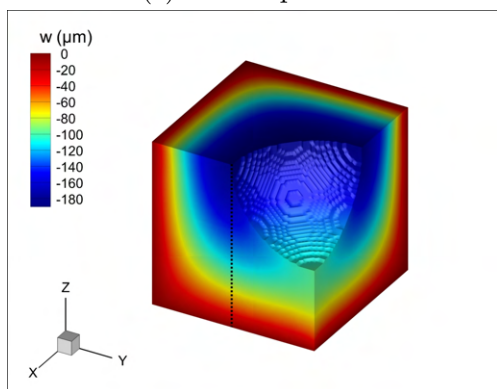
(b) u value COMSOL comparison.



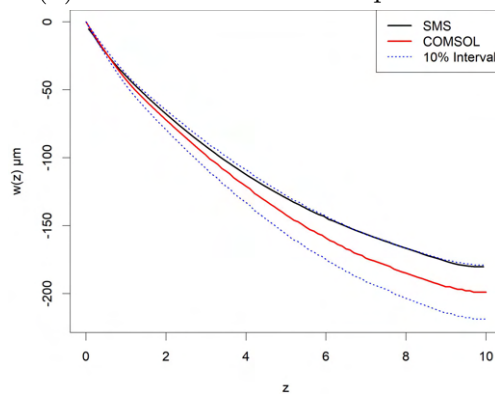
(c) SMS v profile.



(d) v value COMSOL comparison.

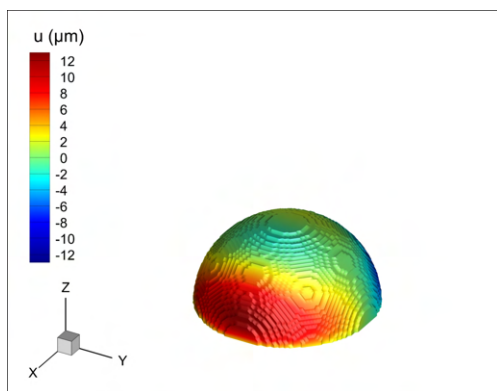


(e) SMS w profile.

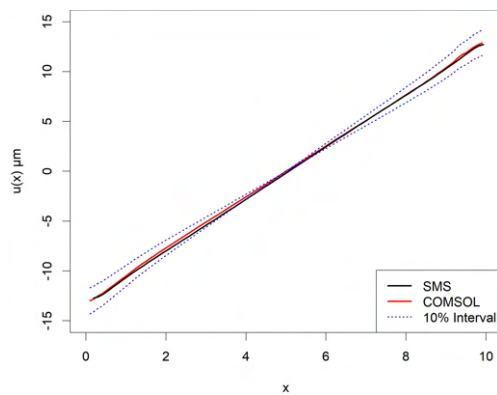


(f) w value COMSOL comparison.

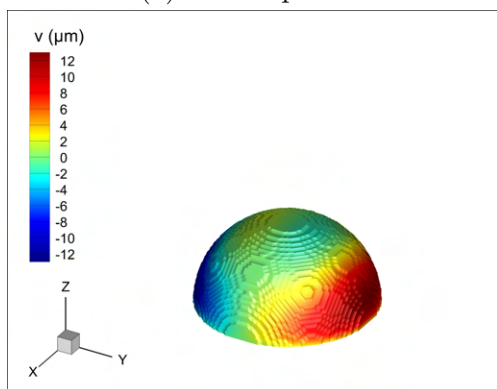
Figure B.25: Case 25 - Floor fixed block with concave corner under negative body force in z .



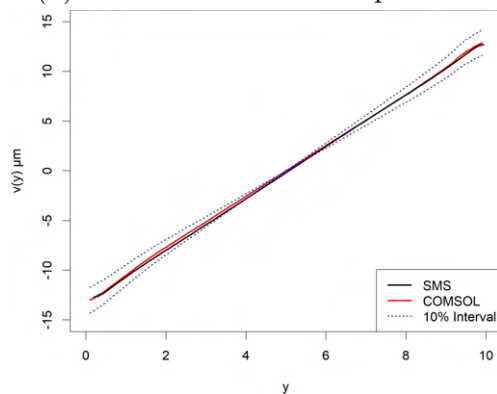
(a) SMS u profile.



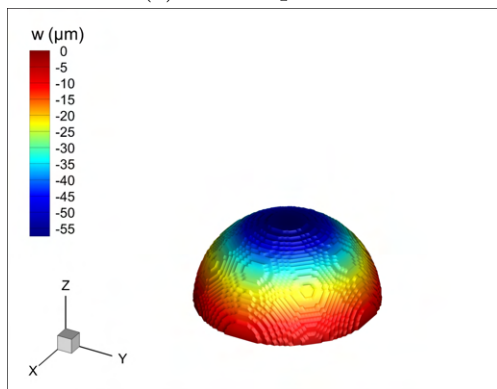
(b) u value COMSOL comparison.



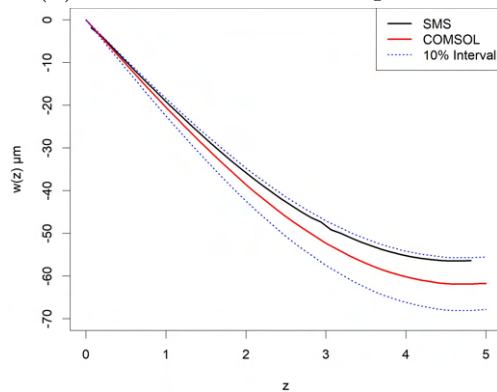
(c) SMS v profile.



(d) v value COMSOL comparison.

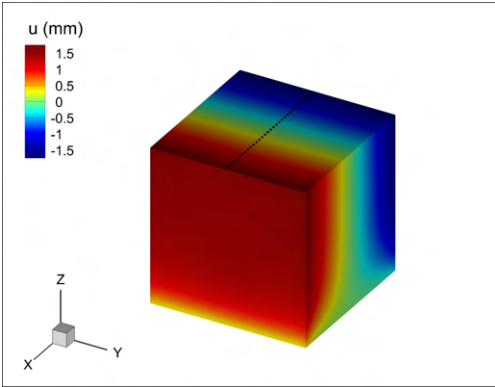


(e) SMS w profile.

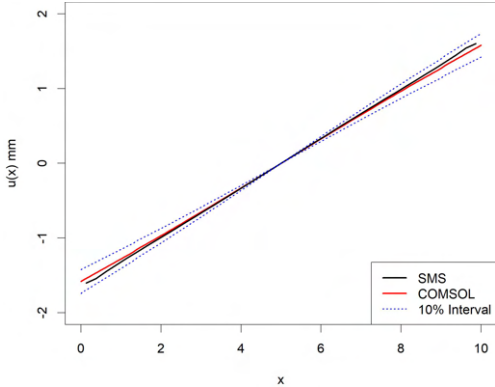


(f) w value COMSOL comparison.

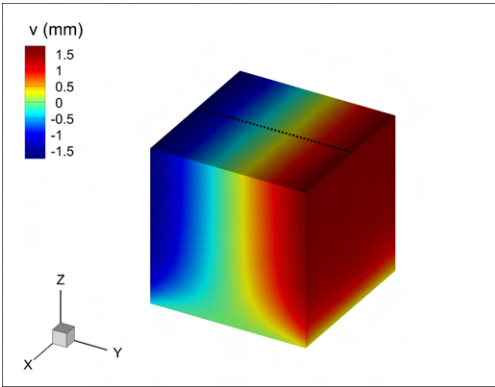
Figure B.26: Case 26 - Floor fixed hemispherical structure under negative body force in z .



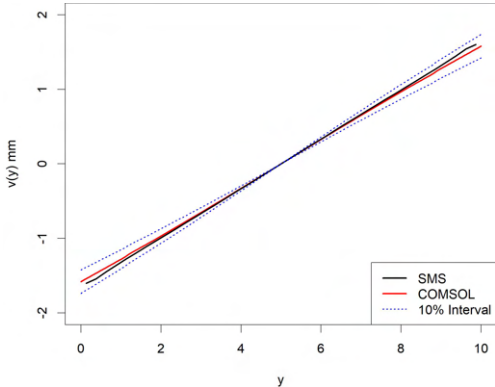
(a) SMS u profile.



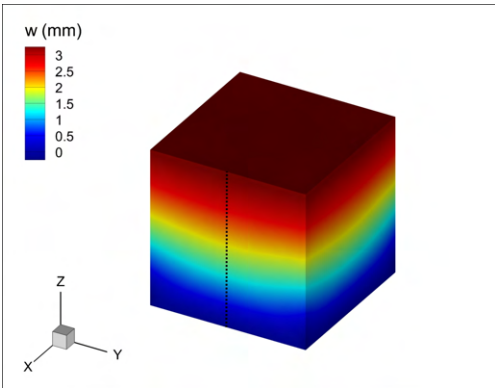
(b) u value COMSOL comparison.



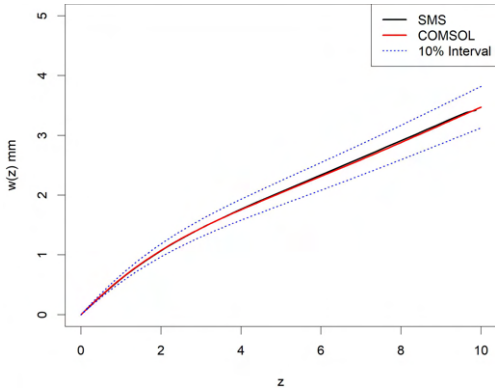
(c) SMS v profile.



(d) v value COMSOL comparison.

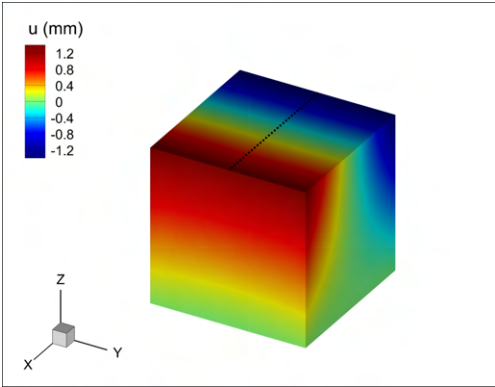


(e) SMS w profile.

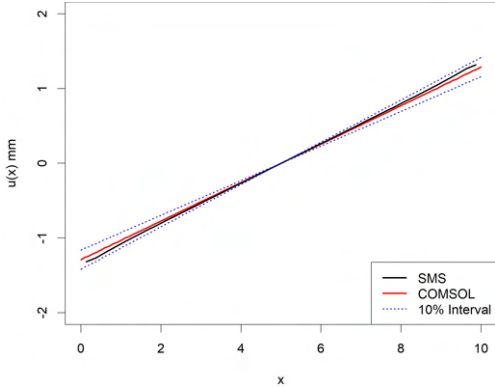


(f) w value COMSOL comparison.

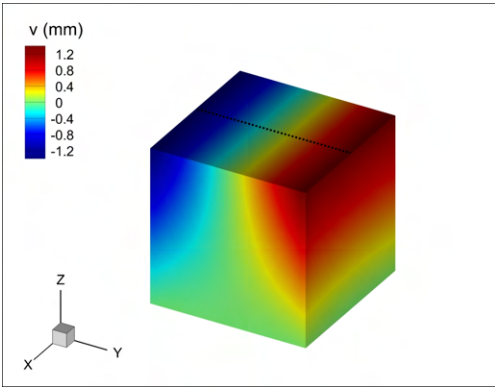
Figure B.27: Case 27 - Floor fixed block structure under uniform temperature increase causing thermoelastic expansion.



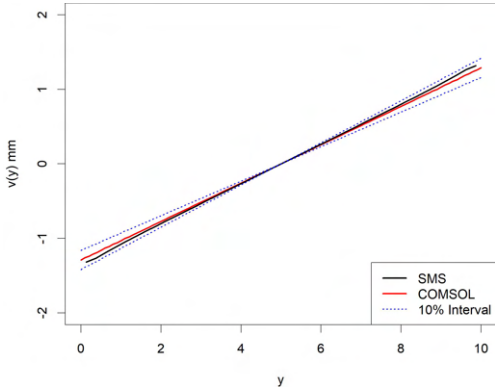
(a) SMS u profile.



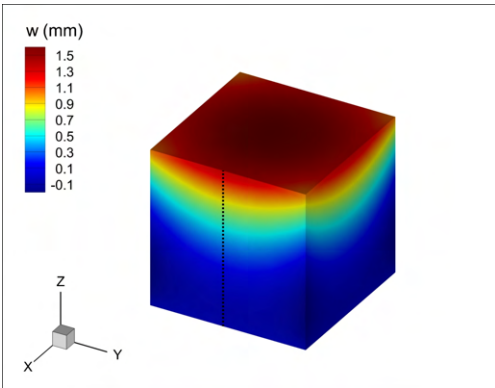
(b) u value COMSOL comparison.



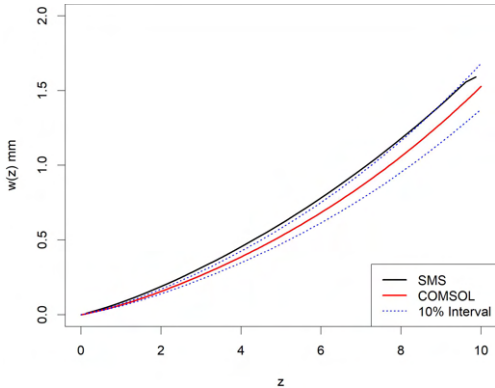
(c) SMS v profile.



(d) v value COMSOL comparison.

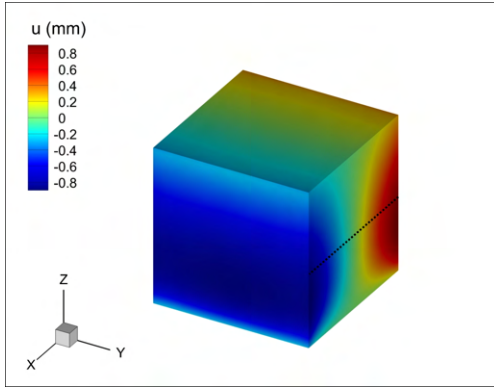


(e) SMS w profile.

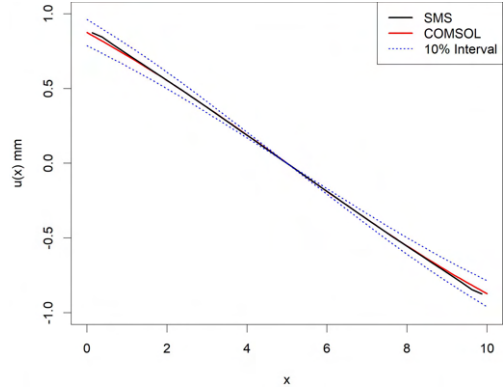


(f) w value COMSOL comparison.

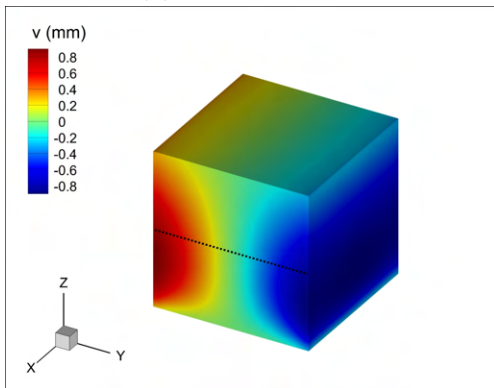
Figure B.28: Case 28 - Floor fixed block structure under increasing temperature gradient causing thermoelastic expansion.



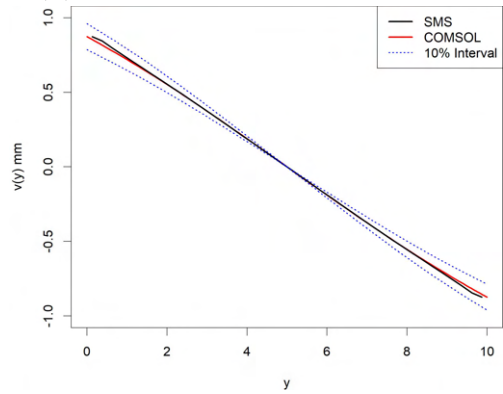
(a) SMS u profile.



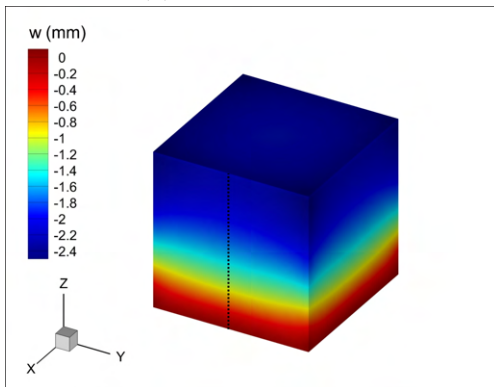
(b) u value COMSOL comparison.



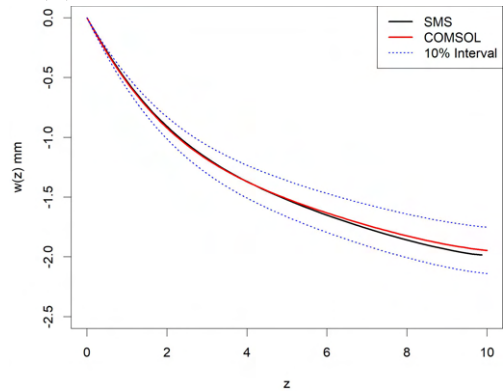
(c) SMS v profile.



(d) v value COMSOL comparison.

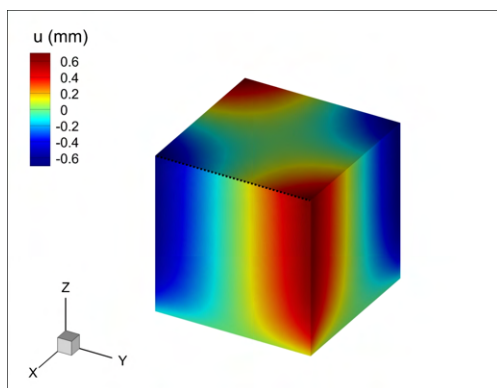


(e) SMS w profile.

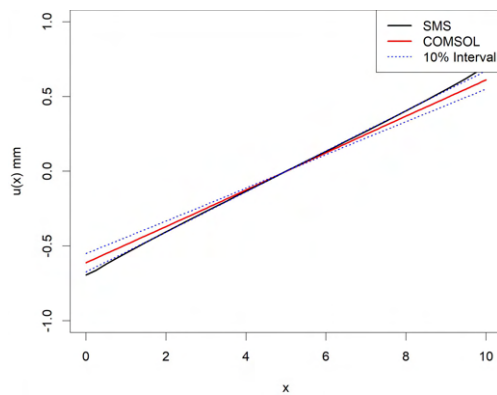


(f) w value COMSOL comparison.

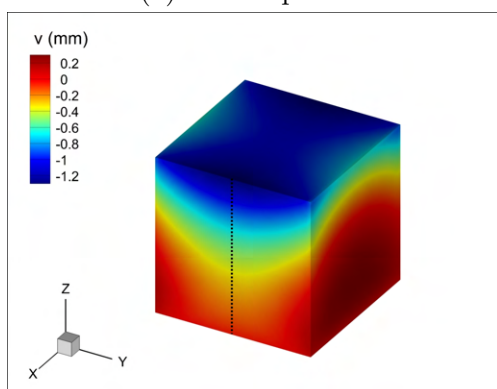
Figure B.29: Case 29 - Floor fixed block structure under decreasing temperature gradient causing thermoelastic contraction.



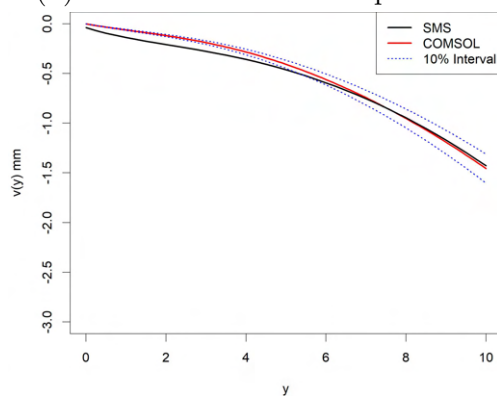
(a) SMS u profile.



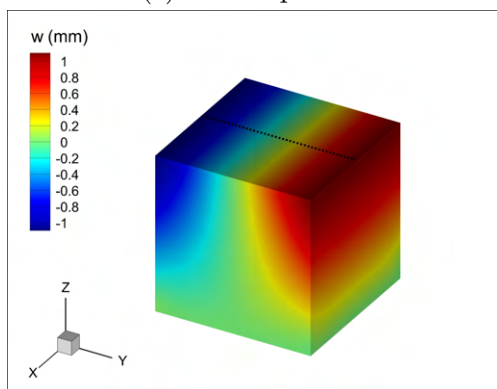
(b) u value COMSOL comparison.



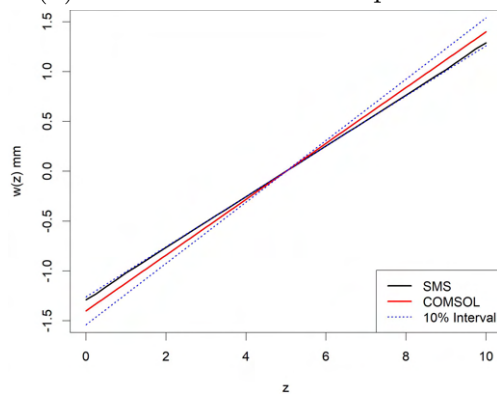
(c) SMS v profile.



(d) v value COMSOL comparison.



(e) SMS w profile.



(f) w value COMSOL comparison.

Figure B.30: Case 30 - Floor fixed block structure under temperature gradient causing thermoelastic expansion & contraction.

Appendix C

Dissemination

C.1 Publications

- Soar, P., Kao, A., Shevchenko, N., Eckert, S., Djambazov, G. and Pericleous, K., 2022, Predicting concurrent structural mechanical mechanisms during microstructure evolution, In *Philosophical Transactions of the Royal Society A* (Vol. 180, No. 2217, p. 20210149).
- Soar, P., Kao, A., Djambazov, G., Shevchenko, N., Eckert, S. and Pericleous, K., 2020, The integration of structural mechanics into microstructure solidification modelling. In *IOP Conference Series: Materials Science and Engineering* (Vol. 861, No. 1, p. 012054). IOP Publishing.

C.2 Prizes & Awards

- Inspiring researcher award - University of Greenwich (May 2021)
- Faculty winner of PGR poster competition - University of Greenwich (November 2019)
- Runner up in ‘Elevator Pitch’ competition - UK Solidification Workshop, hosted by BCAST at Brunel University (October 2019)
- People’s choice winner for faculty Three Minute Thesis (3MT) competition - University of Greenwich (April 2019)
- Faculty winner of PGR poster competition - University of Greenwich (November 2018)
- Faculty winner of Three Minute Thesis (3MT) competition - University of Greenwich (June 2018)